Study of Small Scale Processes on the Sun using High Resolution Techniques

A THESIS

submitted for the Award of Ph.D. degree of

MOHANLAL SUKHADIA UNIVERSITY

in the

Faculty of Science

BY

Rohan Eugene Louis

Under the Supervision of

Professor P. Venkatakrishnan

SENIOR PROFESSOR

UDAIPUR SOLAR OBSERVATORY

PHYSICAL RESEARCH LABORATORY, UDAIPUR

MOHANLAL SUKHADIA UNIVERSITY
UDAIPUR

Year of Submission : 2010

DECLARATION

I hereby declare that the work incorporated in the present thesis entitled *“Study of Small Scale Processes on the Sun using High Resolution Techniques”* is my own work and is original. This work (in part or in full) has not been submitted to any University for the award of a Degree or a Diploma.

Rohan Eugene Louis

CERTIFICATE

I feel great pleasure in certifying that the thesis entitled *"Study of Small Scale Processes on the Sun using High Resolution Techniques"* embodies a record of the results of investigations carried out by **Rohan Eugene Louis** under my guidance. I am satisfied with the analysis of data, interpretation of results and conclusions drawn.

He has completed the residential requirement as per rules.

I recommend the submission of thesis.

DATE: **Professor P. Venkatakrishnan**

SUPERVISOR

To Mom, Dad, Julian & Mumu

Contents

List of Figures viii

List of Tables xiv

Acknowledgements xv

Abstract xix

1 Introduction 1

1.1 Introduction . . . 1

1.2 Sunspot Fine Structure . . . 4

1.3 Means of High Resolution Sunspot Observations . . . 15

1.4 Organization of the Thesis . . . 16

2 Scientific Data from *Hinode* and SIR 21

2.1 Introduction . . . 21

2.2 *Hinode* and the Solar Optical Telescope (SOT) . . . 22

2.3 Stokes Inversion based on Response Functions (SIR) . . . 28

2.3.1 Synthesis Module . . . 29

2.3.1.1 Spectral synthesis . . . 29

2.3.1.2 Response functions . . . 31

2.3.2 The inversion module . . . 32

2.3.2.1 Error estimation . . . 35

2.3.3 Executing SIR . . . 35

2.3.4 User Intervention . . . 43

3 Photospheric and Chromospheric Observations of Sunspot Light Bridges **49**
3.1 Introduction 49
3.2 Data 51
3.3 Data Processing 51
3.4 General Properties of LBs 57
3.5 Horizontal Flows in LBs 57
3.6 Chromospheric Observations 64
3.7 Magnetograms from the far line-wing positions 67
3.8 Summary and Discussion 71

4 Detailed Investigation of a Chromospherically Active Sunspot Light Bridge **75**
4.1 Introduction 75
4.2 Observations 77
4.3 Results 77
4.3.1 Magnetic Configuration of LB and its Neighbourhood . . . 77
4.3.2 Strong Downflowing Patches 84
4.3.3 Implications of Anomalous Polarization Profiles 86
4.3.3.1 Supersonic Downflows in the Light Bridge 86
4.3.3.2 Mixing of Light Bridge and Umbral Fields 90
4.3.3.3 Supersonic Downflows at the Umbra-Penumbra Boundary 90
4.3.4 Chromospheric Activity 93
4.3.5 Photometric Variation in the Photosphere and Chromosphere 100
4.3.6 The decay phase of the LB 104
4.4 Summary and Discussion 110

5 Structure of Penumbra in the Context of the Evershed Flow **116**
5.1 Introduction 116
5.2 Observations 120
5.3 Inversions using a single component atmosphere 120
5.4 Defining the Normalized Radial Distance 121

5.5 Results . . . 126
5.5.1 Penumbral Spine and Intraspine Structure . . . 126
5.5.2 Radial Variation of Parameters . . . 133
5.5.3 Characteristics of Spines, Intraspines and Evershed Clouds 135
5.5.4 Perturbative Nature of ECs . . . 138
5.5.5 The Long Term Horizontal Flow Field . . . 143
5.5.6 Coherence of Penumbral Fine Structure . . . 146
5.6 Summary and Conclusion . . . 149

6 Results Pertaining to the Development of Adaptive Optics at Udaipur Solar Observatory 154
6.1 Introduction . . . 154
6.2 Concept of Adaptive Optics . . . 158
6.3 Membrane based Deformable Mirror: Intrinsic Aberrations and Alignment Issues . . . 168
6.3.1 Experiment . . . 170
6.3.1.1 Optical Setup . . . 170
6.3.1.2 Intrinsic Aberrations and Image quality . . . 170
6.3.2 Dealing with Induced and Intrinsic Astigmatism . . . 176
6.4 DM Performance in Compensating Real Time Aberrations . . . 176
6.4.1 Optical Setup . . . 176
6.4.2 Experiment and Results . . . 178
6.4.2.1 Mapping of the DM Actuator Surface with the Lenslet Array . . . 178
6.4.2.2 Generating the Influence Matrix . . . 181
6.4.2.3 DM in Real-Time Correction Mode . . . 181
6.4.3 Simulations Demonstrating the Effectiveness of Phase Diversity on AO Corrected Images . . . 185
6.5 Choosing the Optimal Shack Hartmann Wave Front Sensor for the Adaptive Optics System at USO . . . 190
6.5.1 Proposed Optical Setup for the prototype AO System . . . 190
6.5.2 Shift Estimation Algorithms . . . 192
6.5.3 Performance of SH Wave Front Sensors . . . 195

6.5.3.1 Constructing the Influence Matrix 197
6.5.3.2 Random Test Wave Fronts 199
6.5.3.3 Realistic Seeing Conditions 202
6.6 First Light Observations using the Prototype Adaptive Optics System 208
6.6.1 Optical Setup of the Prototype AO system 209
6.6.2 Determination of the Influence Matrix 211
6.6.3 Performance of the Prototype AO system 211
6.7 Summary and Discussion 219

7 Summary, Discussion and Future Work 223
7.1 Photospheric and Chromospheric Observations of Sunspot Light Bridges 224
7.2 Detailed Investigation of a Chromospherically Active Sunspot Light Bridge 225
7.3 Penumbral Fine Structure in the Context of the Evershed Flow . 227
7.4 Results Pertaining to the Development of Adaptive Optics at Udaipur Solar Observatory 228
7.5 Synthesis 230
7.6 Future Work 233

Appendix - A 236

Appendix - B 238

Bibliography 241

List of Publications 255

List of Figures

1.1 Full disk continuum image of the Sun taken by *SoHO* 3
1.2 G band image of sunspot 5
1.3 Ca II H image of sunspot 6
1.4 High resolution image of a sunspot light bridge 9
1.5 Dark cores in penumbral filaments 11
1.6 Narrowband filtergram and Dopplergram of a sunspot illustrating the Evershed Flow 13

2.1 Optical Telescope Assembly (OTA) and Focal Plane Package (FPP) of *Hinode* 24
2.2 Level-0 and Level-1 G band filtergrams 27
2.3 Schematic explanation on the choice of nodes 33
2.4 Observed and inverted Stokes profiles for an umbral pixel 44
2.5 Stratification of the physical parameters based on a single node SIR inversion 44
2.6 Observed and inverted Stokes profiles for a penumbral pixel using two different model atmospheres 45
2.7 Stratification of the physical parameters for the model atmosphere with and without gradients 46

3.1 The four sunspots containing the light bridges 53
3.2 Removal of Limb Darkening from G band filtergrams 55
3.3 Deprojected image of sunspot in NOAA AR 10961 56
3.4 Horizontal flows in LBs determined from LCT 59
3.5 Tracks of granular cells identified in each light bridge 61

3.6 Histograms of grain lifetimes and average speeds 62
3.7 Snapshots of Ca II H brightness in the four light bridges 65
3.8 Ca II H time sequences starting at 4:08 UT illustrating the propagation of a brightness enhancement along the light bridge 66
3.9 Average quiet Sun profiles for the four days 69
3.10 Magnetograms constructed at different positions on the blue wing of the Fe 6302.5Å line 70
3.11 Magnetograms constructed at different positions on the red wing of the Fe 6302.5Å line 71

4.1 Continuum image of NOAA AR 10953 at 630 nm 79
4.2 Physical parameters derived from SIR inversions of the light bridge 81
4.3 Physical parameters derived from SIR inversions of the light bridge 82
4.4 Transverse component of the magnetic field in the light bridge . . 83
4.5 Anomalous Stokes profiles in the light bridge and their spatial distribution 85
4.6 Results from inversions of Type-I profiles based on a two-component atmosphere 87
4.7 Results from inversions of Type-I profiles based on a two-component discontinuous atmosphere 88
4.8 Results from inversions of Type-I profiles based on a two-component discontinuous atmosphere 89
4.9 Results from inversions of Type-II profiles 91
4.10 LOS velocities along a slit passing through the umbra-penumbra boundary 92
4.11 Stokes profiles along the slit passing through the umbra-penumbra boundary 94
4.12 Ca II H filtergram acquired during the spectropolarimetric scan of the light bridge 96
4.13 Chromospheric event map constructed during SP2 98
4.14 G band and Ca II H filtergrams taken during the spectropolarimetric scan of the light bridge 99

4.15 Photospheric and chromospheric light curves at two different locations on the light bridge . . . 101
4.16 G band filtergram taken before and after the spectropolarimetric scan of the light bridge . . . 102
4.17 Photospheric and chromospheric light curves for a pixel on the light bridge . . . 103
4.18 Space time maps constructed from the slit along the axis of the light bridge . . . 105
4.19 Time sequences of Ca II H filtergrams . . . 106
4.20 Time sequences of Ca II H filtergrams . . . 108
4.21 Time sequences of G band filtergrams . . . 109

5.1 G Band image of sunspot in NOAA AR 10944 . . . 119
5.2 Maps of physical parameters derived from SIR-1 inversions . . . 122
5.3 Maps of physical parameters derived from SIR-2 inversions averaged between the logτ = 0 and logτ = -0.5 layers . . . 123
5.4 Maps of physical parameters derived from SIR-2 inversions averaged between the logτ = -0.5 and logτ = -1.0 layers . . . 124
5.5 Maps of physical parameters derived from SIR-2 inversions averaged between the logτ = -1.0 and logτ = -1.5 layers . . . 125
5.6 Physical parameters corresponding to sequence 20 . . . 127
5.7 Distribution of physical parameters with LOS velocity . . . 128
5.8 Mean Spine and Intraspine stratifications . . . 132
5.9 Radial variation of physical parameters averaged over different heights . . . 134
5.10 Stokes profiles corresponding to the spine, intraspine and EC . . . 136
5.11 Stratification of spine, intraspine and EC pixels . . . 137
5.12 Temporal evolution of an EC . . . 139
5.13 Stokes profiles emanating from an EC pixel for different time sequences . . . 140
5.14 Histogram of physical parameters corresponding to intraspines and ECs . . . 141

5.15 Mean radial variation of the physical parameters corresponding to the intraspines and the ECs 142
5.16 Average transverse flow field derived using LCT 144
5.17 Radial distribution of the transverse velocity 145
5.18 Average maps of the physical quantities 147
5.19 Radial distribution of the linear correlation co-efficient between LOS velocity and other physical parameters 148

6.1 Concept of an Adaptive Optics System 159
6.2 The concept of the Shack-Hartmann wave front sensor 160
6.3 Sub-aperture images produced by a hexagonal lenslet array 161
6.4 WFSC at USO 163
6.5 Tip-Tilt Mirror 166
6.6 37 channel Micro Machined Deformable Mirror 167
6.7 Actuator Geometry of the Deformable Mirror 167
6.8 Interferometric pattern of the 37 channel 15mm MMDM 168
6.9 f#15 Coudé refractor 171
6.10 Optical setup with the DM at different angles of incidence 172
6.11 Change in focus w.r.t change in voltage to DM and intrinsic astigmatism 173
6.12 Comparison of image quality using a plane mirror and DM 174
6.13 Change in astigmatism with radius of curvature for different angles of incidence 174
6.14 Images corresponding to different angles of incidence 175
6.15 Optical Setup using the two DMs in the lab 177
6.16 Mapping the DM actuators to the lenslet array 179
6.17 Shifts in the central sub-aperture for voltages applied to different actuators 180
6.18 Comparison of open and closed loop shifts for different time delays 182
6.19 Performance of AO system when global tilt is generated using the DM 183
6.20 Performance of AO system when global tilt is generated using the DM 184

6.21 Image Reconstruction using Phase Diversity for different seeing conditions . . . 186
6.22 Image Reconstruction using Adaptive Optics and Phase Diversity 189
6.23 Tentative Optical setup of the prototype AO system . . . 191
6.24 Comparison of different shift estimation routines in retrieving random shifts using a point source . . . 194
6.25 Comparison of different shift estimation routines in retrieving random shifts using a sunspot . . . 194
6.26 Comparison of different shift estimation routines in retrieving random shifts using solar granulation . . . 195
6.27 Lenslet configurations considered for the simulations . . . 196
6.28 First 30 Zernike Polynomials . . . 198
6.29 Histogram of the residual wave front errors using the four lenslet arrays . . . 199
6.30 Comparison between input random wave front and estimated wave front using Hx(360) . . . 200
6.31 Phase screen derived from a Kolmogorov spectrum corresponding to an r_0 of 3 cm . . . 201
6.32 Histogram of the fractional increase in the azimuthally averaged MTF area . . . 203
6.33 Azimuthally averaged MTF before and after AO compensation under different seeing conditions . . . 204
6.34 AO corrected images using Sq(340) and Hx(360) lenslet arrays for an $r_0 = 3$ cm seeing . . . 206
6.35 AO corrected images using Sq(340) and Hx(360) lenslet arrays for an $r_0 = 5$ cm seeing . . . 207
6.36 Optical setup of the prototype AO system . . . 208
6.37 Sub-aperture images using the square 500μm lenslet array . . . 209
6.38 Constructing the Influence Matrix . . . 212
6.39 Constructing the Influence Matrix . . . 213
6.40 Verification of the Influence Matrix . . . 214
6.41 Performance of the Image Stabilization system . . . 215
6.42 Comparison of uncorrected and AO corrected images . . . 216

6.43 Spatial resolution of the AO corrected image 217

List of Tables

2.1 Example of a SIR control file 37
2.2 Illustration of the LINEAS file 38

3.1 Details of observations used for the analysis of the light bridges . 52
3.2 Comparison of general physical properties of the light bridges . . 58
3.3 Number of grains sorted by different ranges of the mean relative azimuth 63

4.1 Details of the data used in the analysis of the light bridge 78
4.2 Physical parameters derived along the slit passing through the umbral-penumbral boundary 95

5.1 Mean errors in the physical parameters at different optical depths 129
5.2 Mean value of physical parameters and their r.m.s values corresponding to spines and intraspines 130

6.1 A list of successful Adaptive Optics systems 157
6.2 List of Shack Hartmann wave front sensors at USO 162
6.3 Performance of the code for atmospheric turbulence of varying wave front error 188
6.4 Performance of the Phase Diversity code vs no. of corrected terms 188
6.5 Performance of the code for various values of the defocusing parameter 189

Acknowledgements

It is said that the success of a movie is governed by the people behind the scenes, guiding and molding the actors to achieve the perfect shot. At this juncture, it gives me tremendous joy in thanking and acknowledging all the people who helped me in realizing this thesis. I am grateful to Prof. P. Venkatakrishnan for giving me this wonderful opportunity to work at the Udaipur Solar Observatory for my doctoral thesis. I could not have asked for a better place to do my research. He was magnanimous in providing the necessary infrastructure and encouraged me to think out-of-the-box and to develop a lateral independent approach to a problem. I also appreciate his interest in allowing me to pursue instrumentation and for involving me in the Adaptive Optics project. I thank Prof. J. N. Goswami, Director, PRL, for providing me the necessary funds to travel to Spain and Japan, thereby giving me an exposure to the international Solar Physics community. I am also grateful to the Academic Committee of PRL, whose suggestions allowed me to improve my thesis and work on two additional problems.

Dr. Shibu K. Mathew has been at the helm of developing instruments and I have learnt immensely from him. He was always eager to help and provided valuable suggestions whenever I was faced with uncertainty. I appreciate his efforts for helping me at various stages of my thesis including the many light-hearted moments that we shared. His never-rest just-do-it attitude is something that I have tried to imbue in my life. I am extremely grateful to Dr. Nandita Srivastava for her kind presence and words of advice. She has been a friend who always supported me and encouraged me during my troubled times. I enjoyed working with her and thank her for her patience and her timely anecdotes. Raja Bayanna, or 'Bava' as I fondly call him, has been an inspirational friend, counselor and teacher and whatever little Optics that I know, I owe to him. I will always remember the many wonderful and delicious meals both at his home as well as outside, when the fear of offending his wife Mahima was overwhelming. I shall always cherish their pleasant company.

I would like to express my sincere gratitude to the *Hinode* team for the high resolution data without which this thesis would not have been possible. *Hinode* is a Japanese mission developed and launched by ISAS/JAXA, collaborating with NAOJ as a domestic partner and NASA and STFC (UK) as international partners. Scientific operation of the *Hinode* mission is conducted by the *Hinode* science team organized at ISAS/JAXA. This team mainly consists of scientists from institutes in the partner countries. Support for the postlaunch operation is provided by JAXA and NAOJ (Japan), STFC (UK), NASA, ESA, and NSC (Norway).

I thank Prof. Ashok Ambastha for his inputs and suggestions during my thesis. If there is one person who patiently and surprisingly tolerated me the most, it is Mr. Raju Koshy, who put up with my antics on the badminton court as well with my dumb jokes. The friendly and hospitable staff at Udaipur Solar Observatory consisting of Mr. Sudhir Gupta, Mr. Naresh Jain, Mr. Rakesh Jaroli, Mr. Pinakin Shikari, Mr. Shankarlal Paliwal, Mr. Lakshmilal Suthar, Mr. Dalchand Purohit, Mr. Ramchander Carpenter and Mr. Jagdish Chauhan provided a very homely environment. I also thank Ram Ajor Maurya, Anand Joshi and Vema Reddy for their company and assistance. I extend my appreciation to Vikram, Maulik, Manish and Niraj for helping out with the AO acquisition software. I am also grateful to Mahima, Sanjukta, Hari Ram, Ratanlal, Husna Bano, Divya Mathew, Aaditya and Kuldeep for their pleasant company. I am grateful to Mr. Mukesh Saradava for speedily fabricating opto-mechanical mounts at the USO workshop. The security staff at USO was very friendly and always greeted me with a smile even in the wee hours of the morning. I wish to thank the staff at the USO canteen for providing good, hygienic and nutritious meals that enabled me to stay fit and healthy.

I wish to thank Dr. R. Sridharan for his meticulous efforts in preparing the Kolmogorov phase screens that were useful for my thesis. I acknowledge Dr. Ravindra who was extremely helpful in providing useful tips on Local Correlation Tracking.

Dr. Luis Bellot Rubio has been a proficient and patient teacher and gave me a lot of attention during my initial stint in understanding and executing the SIR code despite his extremely busy schedule. I thank him for his valuable inputs on Stokes polarimetry and on inversion codes. Dr. Horst Balthasar was very helpful during my stay at the VTT and explained the working of TIP in great detail. I also thank Prof. Dr. Carsten Denker and Torsten Waldmann for allowing me to work on the VTT AO system. I also thank Dr. Jürgen Rendtel and Thomas Hederer for assisting me during the observations. I am grateful to Prof. Oskar von der Lühe and Prof. Rolf Schlichenmaier for giving me the opportunity to visit the VTT. I acknowledge the KAOS team for an extremely user friendly interface which allowed me to operate the AO system with great ease.

Fr. Roger Lesser has been a spiritual advisor and a personal friend who lovingly and patiently guided me ever since I came to Udaipur. He has taught me to appreciate the many wonderful things beyond the purview of Science. I am deeply honoured to have lent my assistance during the preparation and publication of two of his books. I also thank Sheena for helping me in preparing the manuscript of his book. I acknowledge all the Reverend Fathers at St. Paul's for their kind and supportive company. A special word of appreciation to Ms. Celina Joy for graciously inviting me to several wonderful trips to her home at the Trident. I would like to express my gratitude to Varun Bhaiya and Joona Bhabhi for their love, support and encouragement and for making me feel at home with their warm hospitality.

My friends Sandeep Nanda, Pradeep Shankar, Srinivas Pradeep, Immanuel Anna and Lokesh Dewangan were always supportive of my research and chipped in with motivating words and lifted my spirits when I was feeling low. I am eternally grateful to Rev. Fr. Mudiappasamy Devadoss and Rev. Fr. Stephen Kulandaiswamy for giving me the educational support that enabled me to pursue research as a career. Rev. Fr. Stanislaus, Rev. Fr. Aloysius Xavier and the late Rev. Fr. Joseph always kept me in their prayers and I am truly thankful to them. My coming to PRL would have been impossible had it not been for the love, affection and care of Catherine Akka, Rajan Anna, Kulandaiswamy Uncle and Aunty, Victor Mama, Rosey Athai, Caro Akka, Thiru Anna, Pappy Athai and Uncle, Rev. Sr. Nirmala, my most loving grandmothers - Ammachi and Appai and my late grandfather.

The excellent LaTeX class file used for preparing this thesis document is based on Harish Bhanderi's PhD/MPhil template at Cambridge University. Parts of this template have been extended and corrected by Jakob Suckale to whom I am very grateful. I would like to acknowledge the thousands of individuals who have coded for the LaTeX project for free.

My parents, my brother Julian and my wife Soumita have stood by me through thick and thin and gave me all the love, moral support and motivation to carry out my research and work towards my PhD. The innumerable sacrifices that they made for me is beyond comprehension. It is thus only fitting that I dedicate my thesis to them for believing in me and my aspirations. I also acknowledge the support of Soumita's family who helped and encouraged me. The Almighty Lord has been most gracious with His abundant blessings and I thank Him for guiding me and protecting me at every step of the way.

Rohan Eugene Louis

Abstract

Magnetic fields are ubiquitous on the Sun and are organized on a large range of spatial scales. The magnetic field is responsible for the solar activity and is manifest as different structures in the solar atmosphere. Sunspots, which are the largest and most conspicuous concentrations of magnetic fields on the Sun, are produced by a global dynamo that governs the 22 year periodicity of the solar magnetic field. While a sunspot is a highly stable and coherent object with typical lifetimes of the order of days, its global properties arise from the organization and evolution of the ensemble of small scale structures, which constitute a sunspot and evolve on much shorter time scales. Moreover, the interplay between convection and the orientation of magnetic fields within sunspots gives rise to different structures or processes whose diagnosis is crucial for understanding the formation, evolution and decay of sunspots. Understanding the global magnetic field on the Sun, thus requires investigation of sunspot fine structure at the highest spatial resolution. This can be facilitated through space based telescopes which can carry out observations in a 'seeing-free' environment as well as with instruments coupled to large ground based telescopes, equipped with on-line and off-line techniques to combat and correct image degradation introduced by atmospheric turbulence. The motivation of the thesis is to investigate the nature and evolution of small scale magnetic and velocity inhomogeneities in sunspot light bridges and the Evershed flow, while also assisting in developing the means to carry out such a study at high spatial resolution from Udaipur. The thesis is organized as follows.

Chapter 1 describes the physical, magnetic, thermal and dynamic properties of a sunspot which is followed by a similar description of sunspot fine structure.

The importance of the small scale processes in sunspots in the context of a scale-free flux producing mechanism is established. Furthermore, the means of studying such processes from space as well as from ground is described. A brief chapterwise description of the thesis is presented.

The high resolution scientific data used extensively in the thesis comprises of filtergrams and Stokes spectra obtained from the Japanese space satellite *Hinode*. In Chapter 2, the spacecraft and the instruments are briefly described and the different data processing steps are illustrated. This chapter also details the inversion code SIR, that was employed to extract the thermal, magnetic and kinematic information from the *Hinode* spectropolarimetric data. The concept and importance of nodes while inverting actual data, is discussed.

In Chapter 3, high resolution photospheric and chromospheric filtergrams as well as spectropolarimetric observations of a set of four sunspot light bridges are utilized to investigate the association of velocity inhomogeneities in the photosphere to the chromospheric activity, if any, above light bridges. The physical properties and long term flows of the four light bridges are described and the dynamic nature of the brightness enhancements in the light bridges is presented.

Following the results of Chapter 3, the sunspot light bridge in NOAA AR 10953 was selected for a detailed investigation of its magnetic and kinematic properties and their possible role in the persistent and enhanced activity observed in the chromosphere. The rapid evolution of the photospheric magnetic field is described and the corresponding changes in the organization of velocity inhomogeneities is presented. The relationship between the photospheric magnetic and velocity sub-structures to the chromospheric phenomena is attempted. Furthermore, the impact of the evolution of the light bridge on the photometric throughput at the two heights in the solar atmosphere is established. The association of the light bridge to other structures such as penumbral filaments and umbral dots is discussed.

Chapter 5 highlights the penumbral fine structure in the context of the Evershed flow. The spatial and vertical distribution of the Evershed flow is obtained from the inversions assuming a spatially resolved magnetic structure. The existence of two distinct magnetic and thermal components in the penumbra and the presence of strong fields in the continuum layers is established. The spectral characteristics of the two penumbral components is presented. The temporal evolution of Evershed clouds and their perturbative effects on the intraspine channels is investigated. The coherence of the thermal and magnetic structure of the penumbra, over time scales much greater than that of the small scale features, is determined.

The developmental aspects of designing an Adaptive Optics system at Udaipur Solar Observatory are described in Chapter 6. A component wise study was conducted that included the estimation of the intrinsic and induced aberrations in the Deformable Mirror, determination of the influence matrix with real time correction of wave front errors induced by a second Deformable Mirror and determination of the optimal wave front sensor for the prototype Adaptive Optics system through computer simulations. The possibility of employing post-processing methods such as Phase Diversity on Adaptive Optics corrected images is also presented. First light observations with the prototype Adaptive Optics are highlighted and the improvement in image quality is discussed.

Chapter 7 presents a summary of the thesis work and conclusions drawn therein. Future scientific and instrumentation projects are briefly described.

Chapter 1

Introduction

1.1 Introduction

The Sun is the closest star to planet Earth and is an interesting and fascinating celestial object. The Sun is essential for sustenance of life on Earth since we are primarily dependent on it for heat and light. From an astrophysical point of view, the Sun is a colossal laboratory in space where one observes the interaction of plasma, magnetic fields and radiation. All solar activity is essentially governed by the magnetic field (Stix, 2002) whose manifestation is seen as different structures throughout the solar atmosphere. The magnetic field couples the dynamics in the interior of the Sun to the energetics in the outer atmosphere, namely the corona. In fact, it does not stop in the corona but extends far into the interplanetary medium. These open[1] magnetic field lines originating from coronal holes on the Sun, provide a means for plasma and particles or "solar wind" to flow into the heliosphere (Jones, 2005). The more violent and visible consequences of the dynamical magnetic field however, are observed in the form of Mass Ejections and Flares - energetic phenomena that are accompanied by emission of energetic particles and the release of electromagnetic energy. The energetics in the corona are caused by the de-stressing of magnetic fields, which are driven into a highly

[1] $\nabla.\mathbf{B}$ implies that there are no open magnetic lines of force, however the terminology refers to a domain where magnetic field lines extending from the Sun into the heliosphere are untraceable because of their vast distance

non-linear state by the continuous convective motion of plasma in the photosphere where the magnetic fields are anchored. What makes the Sun truly remarkable, is that despite its enormity, it can be regarded as an egalitarian when it comes to the size distribution of its magnetic flux and in turn, all associated structures/features throughout the solar atmosphere. This wide distribution of spatial scales, range from sunspots which are large, conspicuous manifestations of the magnetic field, to small magnetic bipoles or ephemeral concentrations, that cover the bulk of the Sun at any given time.

Sunspots have been observed since the invention of the telescope in the 17$^{\text{th}}$ century because they appear as dark regions on the Sun's visible surface, namely the photosphere. The discovery of a magnetic field in sunspots was made in 1908 (Hale, 1908) which revolutionized our perspective and understanding of the Sun. Sunspots are dark objects having a radius of 10-20 Mm with a central dark core called the *umbra* and surrounded by a less dark filamentary *penumbra*. The umbra radiates only 20% of the normal photospheric intensity, corresponding to a temperature deficit of 2000 K, whereas the average penumbral intensity is about 75% of that outside the spot (Solanki, 2003a, and references therein). The magnetic field is almost vertical at the center of the spot (where it has a strength of upto 3500 G, or 0.35 T) but its inclination to the vertical increases with increasing radius, reaching an average value of 70° at the edge of the spot, where the field strength drops to less than 1000 G (Bellot Rubio et al., 2004). Sunspots appear darker because the strong magnetic fields inhibit convective transport of energy which results in a decrease temperature. This property leads to the "Wilson Depression" where the geometrical height corresponding to unit optical depth varies by a few hundred kilometers (Wilson & Cannon, 1968; Balthasar & Wöhl, 1983; Mathew et al., 2004).

Sunspots are the result of a global dynamo (Parker, 1955; Choudhuri, 1998; Dikpati & Gilman, 2006; Weiss & Thompson, 2009) that resides at the base of the convection zone, called the tachocline, where there is an abrupt change in the rotation profile. Beyond the tacholine the solar surface exhibits differential rotation unlike its interior which is closer to a solid-body rotation. Sunspots are seen when magnetic fields rise through the convection zone due to buoyancy, and cross the photosphere. The dynamo is responsible for the 11-year solar cycle of

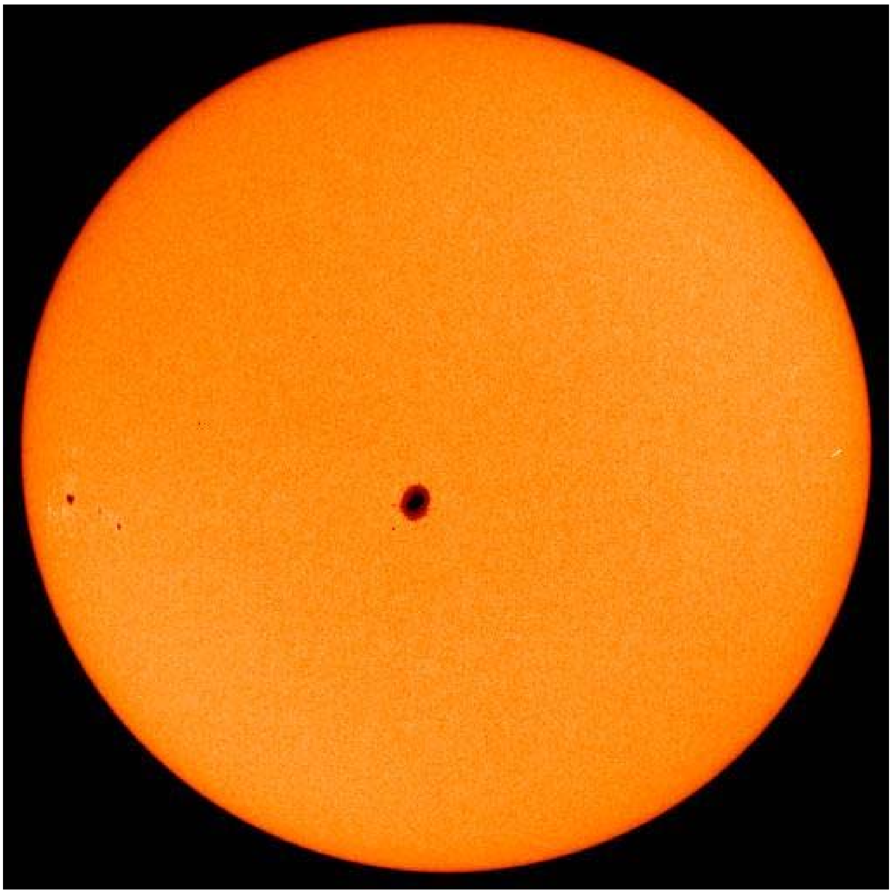

Figure 1.1: Full disk continuum image of the Sun taken by the MDI (Michelson Doppler Imager; Scherrer et al., 1995) on board the *SoHO* satellite on 14$^{\text{th}}$ Nov. 2006. Seen close to disk center is the sunspot in NOAA AR 10923.

sunspots. The number of sunspots varies strongly with the solar activity cycle (Komm et al., 1992) which was discovered by Heinrich Schwabe in 1843. Sunspots typically have a bipolar magnetic structure and are usually restricted to latitudes of 40° on either side of the equator (Carrington, 1858). During the start of a cycle they are seen in the higher latitudes and progressively appear at the lower latitudes as the cycle advances. The inclination between the preceding polarity and the following polarity increases with increasing latitude, according to A. H. Joy in Hale et al. (1919).

While the global dynamo is responsible for sunspots, a second (local) dynamo just beneath the photosphere drives the small scale magnetic fields that are ubiquitous on the Sun (Hagenaar , 2001). These small scale magnetic features also show the same trends of tilt in the axis of emergent bipoles, similar to that seen in sunspots, albeit with greater statistical variation. Thus to a certain extent, the production of these tiny flux elements is directly or indirectly influenced by the global dynamo (De Rosa, 2005). These tiny magnetic bipoles evolve on time scales of 10-40 hr and tend to fragment, merge or cancel with each other. Ephemeral regions as well as active regions (single sunspot or a group of sunspots) strongly influence the dynamics in the corona. The former, which carpet the solar surface, are constantly jostled by photospheric convective motions. This in turn creates an entanglement of loops which can produce electric currents higher up in the solar atmosphere that is believed to contribute to coronal heating (Parker, 1983; Priest et al., 2002). Large scale filament eruptions with accompanying coronal mass ejections, more often than not, are observed in the vicinity of complex active regions. Although the active-region and quiet Sun fluxes appear to be unrelated from the above description, Parnell et al. (2009) determined a single power law distribution of flux features on all observable scales, which strongly suggest that the mechanism generating magnetic fields on all scales is the same.

Figure 1.1 depicts a large sunspot close to disk center during the minima of solar cycle 23. Sunspots can be regarded as a coherent entity which remain in dynamic equilibrium over large spatial as well as temporal scales. However, a closer look at sunspots reveals a number of small scale features that evolve on much shorter time scales. These 'sub-structures' constitute an ensemble that together account for the global properties and coherence of the sunspot (Schlichenmaier, 2009). To illustrate the fine structure in the sunspot, I present a high resolution image of the same sunspot in Figure 1.2 which was taken by the Japanese space satellite, *Hinode* (Kosugi et al., 2007) in the G band. Figure 1.3 shows the same sunspot in the chromospheric Ca II H line.

1.2 Sunspot Fine Structure

This section describes the structure of a sunspot when viewed through a "magnifying glass" and illustrates them with figures wherever necessary.

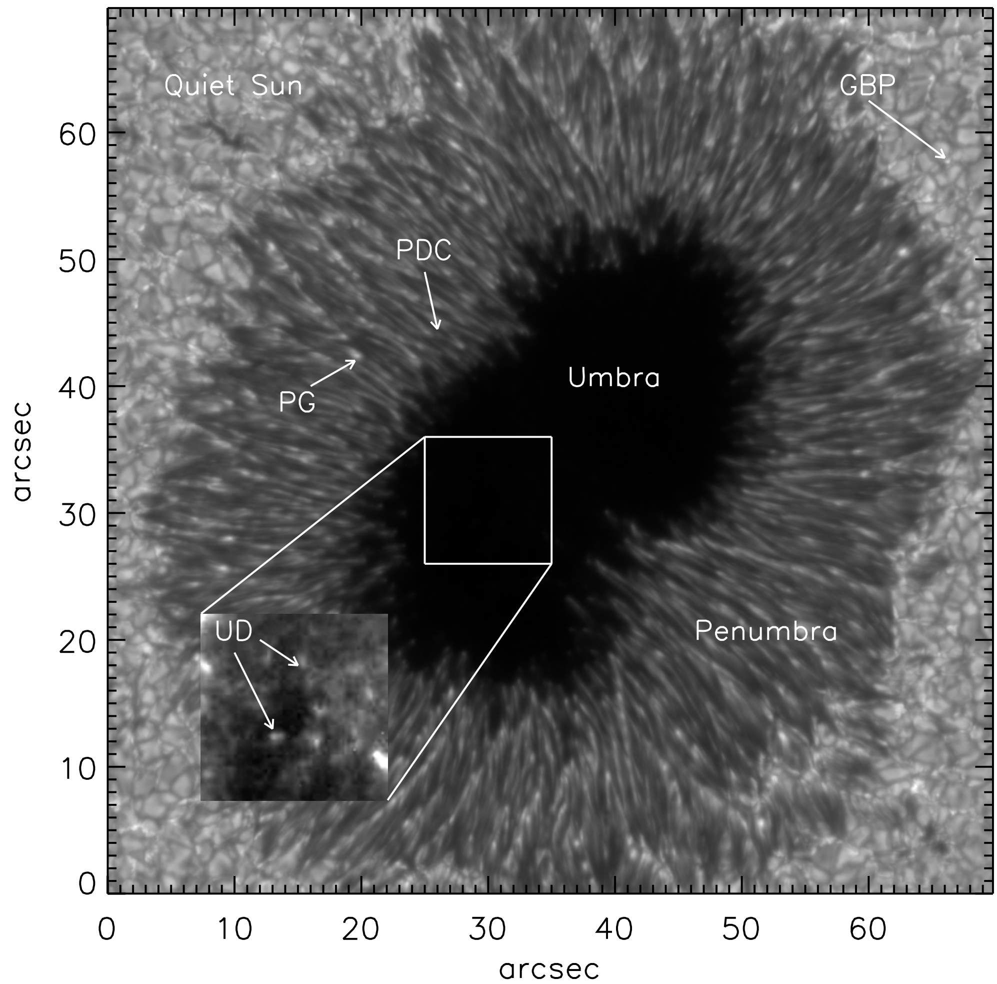

Figure 1.2: G band image of sunspot in NOAA AR 10923 taken by *Hinode*. UD-umbral dot, PG-penumbral grain, PDC-penumbral dark core, GBP-G band bright point.

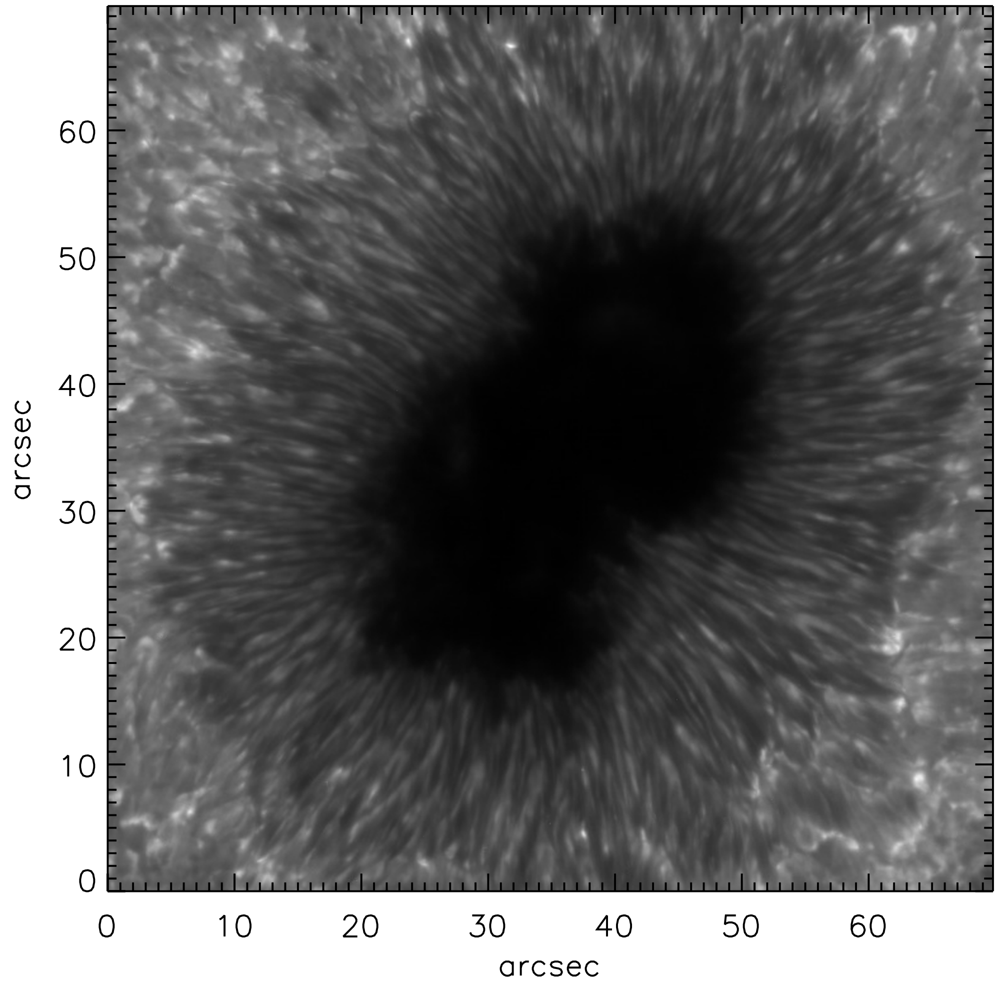

Figure 1.3: Ca II H image of sunspot in NOAA AR 10923 taken by *Hinode*.

1. **Umbral Dots(UDs):** The dark umbral background is populated by small, bright features called umbral dots (UDs). The size of UDs ranges from 0.″8 down to the current resolution limit of about 0.″2 (Sobotka et al., 1997a; Tritschler & Schmidt , 2002) while a recent work by Riethmüller et al. (2008b) shows that the size distribution of UD diameters is a maximum around 225 km, suggesting that most of the UDs are spatially resolved. Sobotka et al. (1997a) also observed that the larger, long lived UDs are seen in regions of enhanced umbral background intensity. The darkest parts of the umbral core, referred to as dark nuclei, are often devoid of UDs. Based on their relative location, UDs can be classified as "central" and "peripheral". While the former are seen in the inner regions of the umbra, the latter dominate the umbra-penumbra boundary. The peripheral UDs are usually brighter than the central ones. The intensity of UDs ranges from about 0.2 to 0.7 times the normal photospheric intensity at visible wavelengths. The typical speeds of UDs are $\approx$ 400 m s^{-1} (Sobotka et al., 1997b; Kitai et al., 2007; Riethmüller et al., 2008b; Sobotka & Jurcak, 2009). Most mobile UDs emerge near the umbra-penumbra boundary and move towards the centre of the umbra (Riethmüller et al., 2008b) with speeds of 700 m s^{-1}. UDs do not have a typical lifetime, with values ranging from 10 min (Sobotka et al., 1997a) to 2.5 min (Riethmüller et al., 2008b). The spread in the values of the lifetimes however, is subject to the identification and tracking algorithm.

   Parker (1979) proposed that UDs are manifestations of hot non-magnetized plasma pushing its way in the gappy umbral field. While the detection of such weak fields in the umbra remains elusive, recent *Hinode* observations indicate a reduction of 500 G in UDs with the contrasted ones residing in locations where the magnetic field is $\approx$ 2000 G and is inclined more than 30° (Watanabe et al., 2009). Central and peripheral UDs exhibit an enhancement in temperature of 550 K and 570 K respectively (Riethmüller et al., 2008a). The measurements of Doppler velocities in umbral dots show that peripheral UDs have an upflow (Sobotka & Jurcak, 2009) and can be as large as 0.8 km s^{-1} (Riethmüller et al., 2008a). Central UDs on the other hand exhibit very weak downflows (Sobotka & Jurcak, 2009) while Hartkorn & Rimmmele (2003) detected downflows of upto 0.3 km s^{-1}. Recent observations by Ortiz Carbonnel et al. (2010) detect downflows at the edge of UDs measuring 400 to 1000 m s^{-1} at a spatial resolution of 0.14 arcsec. 3D MHD simulations of Schüssler & Vögler (2006), which model UDs as narrow upflowing plumes, predicted a central dark lane in UDs, which has been observed from ground (Rimmele, 2008) as well as from space (Bharti et al., 2007b).

2. **Sunspot Light Bridges (LBs):** During the lifetime of a sunspot, its umbra may be crossed by one or more narrow bright bands known as "light bridges" which follow fissures that separate the umbra into individual pores during its decay phase (García de La Rosa, 1987). They can have penumbral or photospheric like conditions (Muller, 1979) and it is not unusual to see LBs of different structures in the same sunspot (Lites et al., 2004; Louis et al., 2008). At the photosphere, it has long been debated that they represent an intrusion of "field-free" material into the gappy umbral field (Parker, 1979; Choudhuri, 1986; Spruit & Scharmer, 2006) while some believe that they are manifestations of magneto-convection (Rimmele, 1997, 2004). In the chromosphere they are usually accompanied by brightness enhancements and ejections (Asai et al., 2001; Berger & Berdyugina, 2003; Louis et al., 2008) arising from the sheared magnetic topology created by the light bridge within the umbra. The few magnetic field measurements of LBs indicate weak, inclined magnetic fields (Rüedi et al., 1995; Leka, 1997; Jurčák et al., 2006) that support the idea of the weakly magnetized plasma emerging into the umbra. The lack of co-temporal multi-height observations of sunspot LBs eludes a complete understanding of its structure as well as the dynamics seen in the chromosphere.

3. **Filamentary Penumbra and Penumbral Grains :** The filamentary structure surrounding the dark umbra is called the penumbra. Even with moderate spatial resolution the penumbra is seen to consist of radially aligned bright and dark filaments, although the terms "bright" and "dark" have only local meaning - as an individual bright filament, can in fact, have

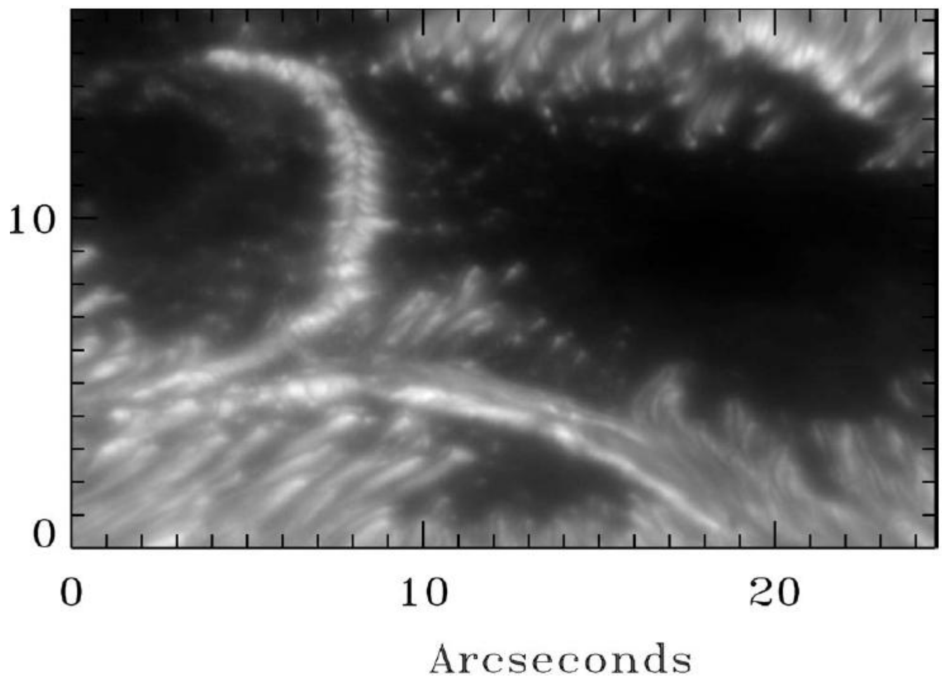

Figure 1.4: High resolution image of one of the light bridges in NOAA AR 10036 imaged by the 1 m Swedish Solar Telescope in La Palma, Canary Islands, Spain. Figure adapted from Lites et al. 2004, Sol. Phys. 221, 65.

lower intensity than a dark filament elsewhere. Even with the present resolution, the filaments are believed to have widths less than 100 km. There exists a dark core surrounded by two lateral brightenings (Scharmer et al., 2002), as well as comet/bead shaped local brightenings at the tips of the penumbral filaments. The latter are referred to as penumbral grains (PGs). PGs can also appear extended (Rouppe van der Voort et al., 2004), in which case, the term, 'grains', is confusing. It has been shown that the dark core is a result of hot plasma streaming along a horizontal tube that is surrounded by a stronger, vertical background field. This flow causes an increase in gas density which shifts the optical depth unity-level upwards to more cooler temperatures, which subsequently produces the dark core (Ruiz Cobo & Bellot Rubio, 2008). The penumbral filaments can exhibit an overall twisting motion with the twist being from the limb side to the centre side (Ichimoto et al., 2007b) and are only observed in those regions of the penumbra which are perpendicular to the line of symmetry. Although penumbral filaments appear to be radially oriented, their spatial extent along the sunspot radius is far from a linear one. This is one of the reasons why, an individual filament can exhibit opposite signs of helicity (Su et al., 2009).

The intensity of some bright PGs can exceed the temperature of the brightest granules outside the sunspot by some 150 K, the intensity ranging from about $0.85 I_{\rm phot}$ to $1.10 I_{\rm phot}$ (Tritschler & Schmidt , 2002). Observations of extremely bright grains were made by Denker et al. (2008), who reported typical intensities of $1.58 I_{\rm phot}$ with the brightest ones having an intensity of 1.8-2.0$I_{\rm phot}$. The PGs exhibit a near radial motion which is typically inward in the inner penumbra and outward in the outer penumbra (Sobotka et al., 1999). There also lies a dividing line (DL), located at about 60% of the radial distance from the inner to the outer edge of the penumbra, inside of which the grains move radially inward at speeds of about 0.5 km s^{-1}, and outside of which the grains move outward with a speed of 0.75 km s^{-1} (Sobotka & Sütterlin, 2001). The inward moving PGs often penetrate the umbra-penumbra boundary where they can no longer be distinguished from

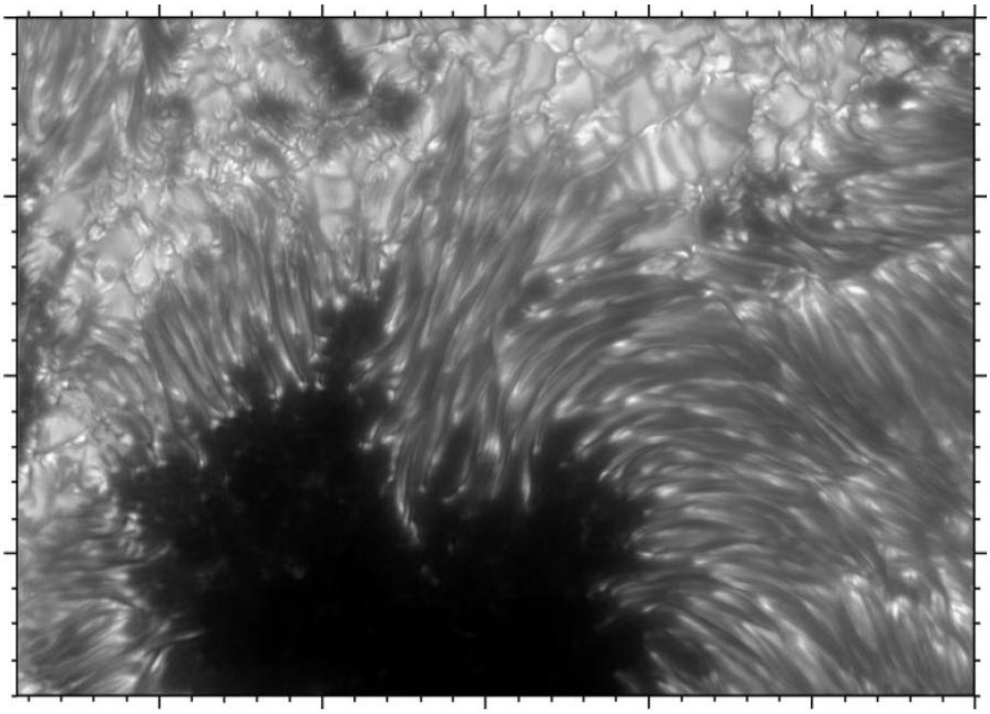

Figure 1.5: High resolution image of sunspot penumbra showing the existence of dark cores in penumbral filaments. Each tickmark corresponds to 1000 km on the Sun. Figure adapted from Scharmer et al., 2002, Nature, 420, 151.

peripheral UDs. Sobotka & Jurcak (2009) showed that the properties of peripheral UDs are closer to PGs than central UDs. The filamentary structure of the penumbra persists even after averaging white-light filtergrams over 2-4 hr(Balthasar et al., 1996; Sobotka et al., 1999), which illustrates a long-term stability of the magnetic field configuration. The paths of new PGs tend to follow trajectories of their predecessors at a given location (Sobotka et al., 1999).

4. **The Evershed Flow and the Two Component Magnetic Configuration:** The Evershed Flow (EF) can be considered as the oldest and most important property of sunspot penumbrae. The EF is seen as a shift in the spectral lines due to the radial, nearly horizontal outflow of plasma (Evershed, 1909) that starts in the inner or mid penumbra and returns to

the surface just outside the outer penumbral boundary or even within the penumbra (Westendorp Plaza et al., 1997; Ichimoto et al., 2007a; Sainz Dalda & Bellot Rubio, 2008). The spectral lines are blue shifted in the center side penumbra while they are red shifted in the limb side. The EF is seen as elongated upflows predominately in the inner penumbra (Franz & Schlichenmaier, 2009) and can even be supersonic in the mid and outer penumbra as well as beyond the sunspot boundary (del Toro Iniesta et al., 2001; Bellot Rubio et al., 2004). The EF is believed to be confined to bright filaments in the inner penumbra but in dark filaments in the outer penumbra (Schlichenmaier et al., 2005; Bellot Rubio et al., 2006a) and is an integral part of the penumbral structure. The dark central core between two lateral penumbral brightenings is believed to harbour the EF (Bellot Rubio et al., 2005, 2007). One of the models of the penumbra is the uncombed model of Solanki & Montavon (1993). This model takes into account the azimuthal fluctuation of the field inclination and proposes nearly horizontal flux tubes embedded in a uniform background field. In this scenario, the flux tubes are essentially weaker than the background field which is fairly more vertical. These two penumbral components are sometimes referred to as “intraspines” and “spines” respectively (Lites et al., 1993). At a spatial resolution of $\sim 0.''7$, the penumbral structure is well reproduced by inversions based on a two-component model (Bellot Rubio et al., 2004) that reinforces the uncombed geometry.

The surplus brightness of the penumbra is a natural consequence of the EF (Bellot Rubio, 2010) which also serves as an effective magnetic flux transport mechanism from the sunspot into the photosphere. The magnetic and kinematic properties of the EF have been extensively studied both in the optical and infrared wavelengths (Westendorp Plaza et al., 1997, 2001a,b; Mathew et al., 2003) and it is believed that the EF is a component of the convective flow that results from anisotropy introduced by the presence of inclined magnetic fields (Rempel et al., 2009b). Although numerical simulation of 3D MHD have progressed tremendously (Rempel et al., 2009b), they do not produce a mature penumbra and the associated EF. It is difficult to fit all the observations into a single model that can explain all

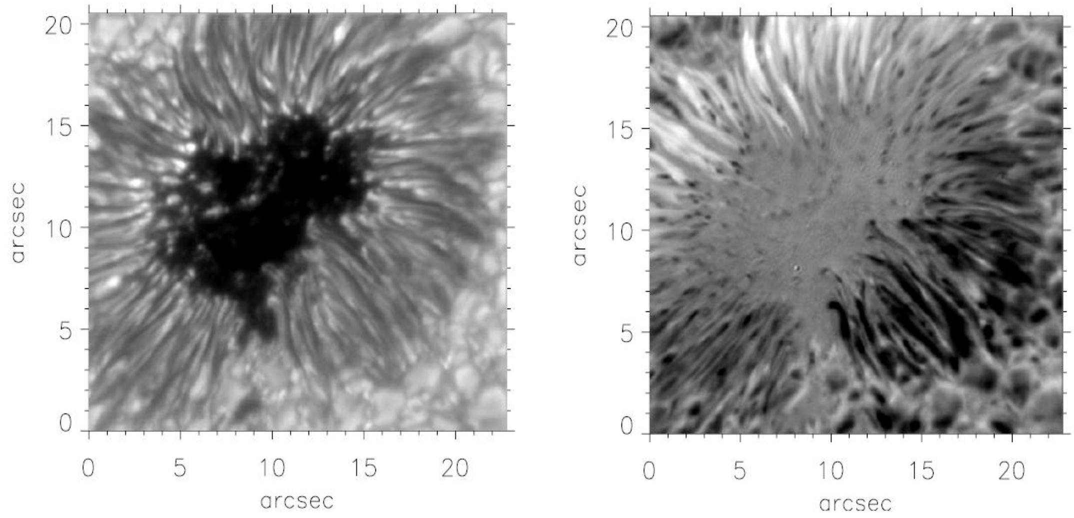

Figure 1.6: Left: Narrowband filtergram of a sunspot in NOAA AR 10605 on May 6, 2004, taken at the 76 cm DST, in Sunspot, New Mexico. **Right:** Dopplergram illustrating the Evershed Flow. *Dark*-blueshift/upflows, *Bright*-redshifts/downflows. The images were derived from the Fe I 5576 Å line. Figure adapted from Rimmele & Marino 2006, ApJ, 646, 593.

the properties of the penumbra simultaneously. The origin and nature of the EF thus appears to hold the key for all available interpretations of the penumbral fine structure (Solanki & Montavon, 1993; Schlichenmaier et al., 1998a; Sánchez Almeida, 2005; Spruit & Scharmer, 2006; Borrero et al., 2007). The interpretation of the penumbral structure, in particular, depends on the set of spectral lines which have different levels of sensitivity to different physical parameters (Cabrera Solana et al., 2005; del Toro Iniesta et al., 2010), the spatial resolution and polarimetric accuracy achieved by the polarimeter and finally the inversion code that appropriately describes the physical scenario (del Toro Iniesta, 2003b; Bellot Rubio et al., 2003b; Bellot Rubio, 2006b).

5. **Moving Magnetic Features (MMFs):** The decay of sunspots which is seen as a loss of magnetic flux, has been attributed to moving magnetic features (MMFs) - magnetic elements that move from the outer penumbra to the surrounding moat around a sunspot. Early observations of MMFs

showed them as bright points in CN spectroheliograms (Sheeley, 1969), flowing radially into the moat with a speed of ~ 1 km s^{-1} having a diameter of ≈ 1000 km. Vrabec (1971) observed that the magnetic field outside sunspots consisted of essentially vertical fields clumped together, with a stream of magnetic knots moving outwards from the sunspot. They are also seen as inward and outward patterns in LOS magnetograms observed by MDI (Ravindra, 2004). Subsequent observations showed that MMFs are extensions of penumbral filaments (Sainz Dalda & Martínez Pillet, 2005; Cabrera Solana et al., 2006; Ravindra, 2006) and are driven by 'Evershed clouds' (Cabrera Solana et al., 2007, 2008). Hagenaar & Shine (2005) have studied some of the statistical properties of MMFs such as flux content, lifetimes, sizes, point of origin in the penumbra/moat and horizontal speeds.

A number of models have been proposed for the formation of MMFs which include the sea-serpent model of Harvey & Harvey (1973), Ω Loop model of Ryutova et al. (1997) and the U-Loop model (Zhang et al., 2003; Zhang, 2007). Loop models suggested by Wilson (1973) and Spruit et al. (1987) predict an appearance of MMFs everywhere in the moat, which is not supported by observations (Lee, 1992). Recent observations made from LOS magnetograms reveal that the orientation of MMFs is strongly correlated with the large scale twist of sunspots (Yurchyshyn, 2001) which has also been supported by Zhang et al. (2003). Kubo et al. (2007a) suggest that MMFs are extensions of the uncombed penumbral structure which is corroborated by Sainz Dalda & Bellot Rubio (2008). Kubo et al. (2007b) reported a redshift greater than the sonic photospheric velocity in MMFs from spectropolarimetric observations from *Hinode*. Spectropolarimetric measurements made by Cabrera Solana et al. (2006) revealed abnormal circular polarization profiles with 3 or 4 lobes occurring in MMFs. This has been observed by Choudhary & Balasubramaniam (2007) who also recorded the Stokes profiles in the lower chromosphere. They found that the Stokes V profile was normal and antisymmetric in comparison to the anamolous profiles obtained in the photosphere which they suggest could be due to relaxation of loops from an initial twisted configuration.

It is well known that fluid motions occurring on the smallest spatial and temporal scales affect the transport of magnetic fields within the solar interior, and cause the field to be continually regenerated and redistributed (De Rosa, 2005). Consequently, small scale dynamics influence large scale structures. The optimum spatial resolution required to study these structures is decided by 2 spatial scales, namely the pressure scale height and the photon mean free path, both being $\approx$ $0.''1$ or 70 km in the photosphere. Sunspots are ideal candidates to probe the Sun's magnetic field. The assortment of fine structure observed in sunspots indicate small scale processes at work within them. If the mechanism responsible for flux generation is indeed scale free (Parnell et al., 2009), then the investigation of sunspot fine structure would account for a sunspot's formation, stability and decay. Although sunspots have a general magnetic, thermal and velocity structure, the uniqueness of each sunspot lies in the organization and statistics of its fine scale features. This small-to-big approach is thus justified in the context of understanding the global behaviour of magnetic fields on the Sun.

1.3 Means of High Resolution Sunspot Observations

Over the last decade, there has been a tremendous effort on all fronts to carry out photometric, polarimetric and spectroscopic observations at the highest possible resolution with space and balloon based missions, as well as ground based instrumentation. Although the former has the unique advantage of carrying out observations in the absence of the Earth's atmosphere, the main limitation comes from its limited life time, as decided by mission objectives, number of scientific instruments and wavelength coverage. *Hinode* (Kosugi et al., 2007) and *SDO* (Solar Dynamics Observatory; Scherrer et al., 2006) are some of the large space based missions, while *Sunrise* (Solanki et al., 2003b) is a 1 m telescope that will be flown on a balloon and has already completed one of the 2 proposed flights.

Solar observations from the ground inevitably suffer from seeing effects due to atmospheric turbulence. Ground based facilities are important because they are the only means of carrying out synoptic observations and can probe different heights in the solar atmosphere. It also offers an opportunity to constantly upgrade and modify existing instruments. In order to carry out high resolution observations from the ground, online compensation methods such as Adaptive Optics (AO) and a number of offline processing tools such as speckle imaging (Denker, 1998; Denker et al., 2005; Sridharan, 2001), phase diversity (Löfdahl & Scharmer, 1994) and Multi Object Multi Frame Blind Deconvolution (MOMFBD; van Noort et al., 2005) have been employed to further improve the image quality. The combination of AO and post processing techniques have significantly improved the image quality (Scharmer et al., 2003b; Rimmele et al., 2003; Keller et al., 2003; von der Lühe et al., 2003; Langhans et al., 2007; Denker et al., 2007; Wöger et al., 2008; Miura et al., 2008) of ground based telescopes and it is not surprising that modern telescope facilities around the world insist on having an AO system in tandem with the back-end instruments.

A 50 cm Multi Application Solar Telescope (MAST) will soon be installed at the lake site of the Udaipur Solar Observatory, which will be equipped with an AO system along with several back-end instruments. In preparation to this a prototype AO system is being designed on a 15cm Coudé telescope at the office site. MAST is proposed to deliver sub-arcsec resolution and will be the first large solar telescope in the Indian longitude to carry out high resolution solar observations. AO systems are not commercially available and their development offers challenges to the experimental physicist. The Indian Institute of Astrophysics, Bangalore, is planning to commission a 2 m NLST (National Large Solar Telescope) in the Leh area within the next 5 years, which will be equipped with an AO system.

1.4 Organization of the Thesis

The formation of a sunspot is initiated by the creation of its umbra. The umbra is formed by the coalescence of several smaller magnetic elements/pores which are driven towards one another (Solanki, 2003a). These individual magnetic fragments/pores can be thought of as being part of a larger flux tube that is rooted deep in the convection zone. This idea is analogous to several balloons being held together by strings. If buoyancy is strong enough to overcome the random convective motions, then these fragments will tend to come together. Parker (1992) proposed that attraction between vortices drives the coalescence of individual magnetic fibrils, wherein each flux tube is surrounded by a vortex flow. The vortices could attract one another if the inward directed aerodynamic drag exerted by a downdraft vortex is strong enough to overcome the magnetic stresses that tend to keep the fibrils apart. The coalescence of pores leading to sunspots are often accompanied by the presence of light bridges (Bumba, 1965) that tend to demarcate individual magnetic elements. The reversal of this process is also seen during the fragmentation of a sunspot (Bumba, 1965; García de La Rosa, 1987). The formation of the penumbra commences when the average inclination at the umbra-photosphere boundary exceeds a critical value of $\approx 35°$ which is related to the total magnetic flux of the pore. The penumbra develops very rapidly, with pieces of penumbra being completed within an hour (Bumba, 1965; Leka & Skumanich, 1998; Keppens & Martínez Pillet, 1996). The formation of a sector of the penumbra is abrupt, and according to Leka & Skumanich (1998) a newly formed penumbral segment is practically indistinguishable from a more mature one in terms of field strengths, inclination angles and continuum intensities. Recent high resolution observations by Schlichenmaier et al. (2010) illustrate the sector wise formation of the penumbra which spans half the umbral circumference within 4 hr. The formation of the rudimentary penumbra initiates the Evershed Flow (EF), that starts in the inner or mid penumbra and returns to the surface just outside the outer penumbral boundary.

This thesis comprises of two parts. In Part-I, I present high resolution observations and analysis of sunspot light bridges and the Evershed Flow taken from *Hinode*. These structures/processes have a more direct association to the formation and stability of a sunspot which warrant their investigation. Moreover, both phenomena are manifestations of inclined magnetic fields which would facilitate convective transport of energy, either as field free intrusions or elongated structures/rolls respectively. Part-II describes the developmental aspects of Adaptive Optics at the Udaipur Solar Observatory which is required for high resolution imaging and illustrates some of the experiments carried out during the calibration of the different AO components. The chapterwise details are briefly described below.

- Since its deployment in Nov. 2006, *Hinode* has been providing high resolution filtergrams in the photosphere and chromosphere as well as full Stokes spectra for inferring the vector magnetic field. One of the motivations of this thesis is to look for observational evidences of photospheric inhomogeneities in sunspot light bridges (LBs) and their association to the activity in the chromosphere. This would provide clues to as how LBs co-exist in the presence of strong fields in the photosphere and their role in heating the lower chromosphere above sunspots. This chapter utilizes high resolution *Hinode* observations of four ARs namely, NOAA AR 10953, AR 10961, AR 10963 and AR 10969 that consisted of one or more LBs. Filtergram observations in the photosphere and chromosphere and a set of Stokes spectra mapping the entire active region, were employed. Using photospheric images, the physical properties of the LB, as well as the transverse flow/motion of intensity features were studied. This was complemented with chromospheric observations to detect signatures of jets/enhancements. The Stokes V spectra was employed to construct magnetograms at different positions in the line profile to determine magnetic and velocity inhomogeneities. These observations of all ARs together was required to investigate the association of the photospheric structure to the overlying chromosphere and to look for similarities/differences in the light bridges of all four ARs. Based on the results of the multi-wavelength analysis, it was found that, although chromospheric brightness enhancements appear to be a common phenomena of LBs, one of them, NOAA AR 10953, in particular, exhibited persistent chromospheric enhancements for nearly three days, with a complex set of strong brightenings. This AR also showed strong signals in the magnetograms constructed in the far red wing of the line profile. In comparison, the magnetogram signals at this wavelength range in the other LBs was comparatively weaker or negligible. From these results, a more detailed analysis of the LB in NOAA AR 10953 was carried out in the following chapter.

- The Stokes spectra obtained from two polarimetric scans of the LB in NOAA AR 10953 at two different instances on the same day, were inverted using an inversion code to infer the magnetic, thermal and dynamic structure of the LB and its neighbourhood. These observations were complemented with photospheric and chromospheric filtergrams acquired close to the time of the scan. This chapter looks at the following aspects of the LB. Are there signatures of field-free intrusions in the magnetic field? What role does the vector magnetic field have to play with the observed enhancements in the chromosphere? What causes the strong signals in the magnetograms derived in the previous chapter? How are they related to the chromospheric observations? How does the global magnetic structure of the LB evolve with time? Does its evolution influence the photometric throughput in the photosphere and chromosphere?

- Chapter 5 deals with high resolution observations of a portion of the disk side penumbra that was repeatedly scanned in time. Using these observations, I first attempt to investigate if the penumbra is spatially resolved by the spectropolarimeter on board *Hinode*. In order to verify this, the inversion code was allowed to synthesize the observed Stokes profiles with a single magnetic component with gradients along LOS in the physical parameters. The properties of the EF were verified with those in the literature using a statistical distribution of the physical parameters. Having convincingly demonstrated the above aspect, a general stratification for the two penumbral components was derived. The radial variation in the physical parameters at different heights was used to locate the point of emergence of the EF in the penumbra. The Evershed cloud (EC) phenomenon was investigated and it was concluded that they have the same properties as intraspines along which they move. The stability and persistence of the overall penumbral geometry is illustrated by deriving a time averaged map of the physical parameters. These were then employed to study the radial distribution of correlations between the physical parameters and the time averaged continuum intensity. I also discuss the reasons for differences in some of the results obtained with previous as well as a few *Hinode* observations. Some of the limitations and drawbacks in the model atmosphere are presented and improvements to be implemented in the future are discussed.

- Chapter 6 forms Part-II of the thesis and describes the influence of atmospheric turbulence on the resolution of ground based telescopes and the importance of an Adaptive Optics (AO) system. The functionality of the system and description of the various components are presented. My contribution to the development of AO at the Udaipur Solar Observatory, involved i) determining the intrinsic and induced aberrations in the Deformable Mirror (DM), ii) using the DM to correct controlled aberrations in real time, where the perturbations were created by a second DM and iii) estimating the optimum Shack Hartmann wavefront sensor for the prototype system using simulations and demonstrating the effectiveness under seeing conditions prevalent at our site. Finally, photospheric observations of a sunspot using the Adaptive Optics system will be presented, demonstrating the improvement in image quality and resolution.

The results obtained from high resolution observations taken by *Hinode* will be summarized in the final chapter. In addition, the performance and limitations of the prototype AO system will be described and possible strategies for implementing the same on MAST will be presented. Future directions include - carrying out a similar analysis on more chromospherically active sunspot light bridges and using more complex magnetic atmospheres to explain the nature of the EF and comparing it with numerical simulations. On the instrumentation front, development of certain crucial modules for the dual Fabry Perot narrow band filter imager, one of the back end instruments for MAST, will be undertaken that will be briefly mentioned.

Chapter 2

Scientific Data from *Hinode* and SIR

2.1 Introduction

The last decade has witnessed a remarkable progress in space and ground based instrumentation, thereby setting up a platform to carry out observations at high spatial resolution. On the ground, photometric and longitudinal magnetograms have been achieved at a resolution of $\approx 0.''1$ and $\approx 0.''2$ respectively at the 1 m Swedish Solar Telescope (SST; Scharmer et al., 2003b), while spectropolarimetric observations at the German Vacuum Tower Telescope (VTT; Bello González et al., 2005) and the Dunn Solar Telescope (DST; Lites, 1996) have reached a resolution of $\approx$ 0.4-0.$''$6. These telescopes are 70 cm and 76 cm respectively in diameter. The Japanese Space Satellite *Hinode* (Kosugi et al., 2007), on the other hand can provide a resolution of $\approx$ 0.2-0.$''$3 for an extended duration, of the order of days, under "seeing-free" and highly stable operating conditions. This is critical for understanding the ever-changing photospheric and chromospheric phenomena on the Sun. This chapter consists of two parts. In the first part, a brief overview of the *Hinode* spacecraft and its instruments, namely the filtergraph and spectropolarimeter, are presented. The details of the instruments and optical components have been referred from Tsuneta et al. (2008) which gives an elaborate presentation of the spacecraft, instruments and recording of scientific data. The second part focuses on the SIR inversion code that was used extensively in the thesis for the determination of the magnetic, thermal and kinematic maps from the spectropolarimetric data of *Hinode*.

2.2 *Hinode* and the Solar Optical Telescope (SOT)

Hinode, was launched on 22 September 2006 from the Uchinoura Space Center, Japan. It has three basic payloads, a 50 cm Solar Optical Telescope (SOT), an EUV Imaging Spectrograph (EIS) and a Soft X-Ray Telescope (XRT). The SOT (Tsuneta et al., 2008), which is a 50 cm aperture, consists of the Optical Telescope Assembly (OTA; Suematsu et al., 2008) and the Focal Plane Package (FPP; Tarbell et al., 2008). The FPP comprises of three back-end instruments: a Broad-band Filter Imager (BFI), a tunable Narrow-band Filter Imager (NFI) and a Spectropolarimeter (SP; Lites et al., 2001; Ichimoto et al., 2008).

The schematic of the OTA and FPP is shown in Figure 2.1. The OTA consists of the primary mirror, secondary mirror, Heat Dump Mirror (HDM), Collimator Lens Unit (CLU), secondary Field Stop (2FS), Tip-tilt fold mirror (CTM-TM), and the Polarization Modulator Unit (PMU). The 50 cm primary and the secondary mirrors are manufactured from ULE (Ultra Low Expansion substrate materials) with the weight of the primary being 14 kg. Both mirrors have a protective silver coating. The distance between the primary and secondary is 1.5 m, with the HDM placed at the prime focus of the primary, that removes sunlight outside the 400$''$ FOV into space. The central obscuration ratio is 0.344 in radius with an effective f-ratio of 9.055 at the secondary focus. The optical tests simulating the in-orbit condition of the OTA on the ground included a temperature cycle test, a vignetting test, a scattered light measurement, a focus test and throughput measurement. It was demonstrated that the OTA had a Strehl ratio better than 0.9 at 500 nm while the measured FPP Strehl ratio averaged over the field of view is very close to or exceeds 0.9, thus meeting post-launch requirements. The total weight of the OTA is about 103 kg, and the FPP is about 46 kg. The CLU has a focal length of 37 cm which delivers a 3 cm exit pupil and provides a collimated beam to the FPP. The CLU comprises of six lenses in which the first two lenses are radiation-robust fused silica, and protect the four inner lenses that are more susceptible to radiation. There is an IR rejection filter placed at the entrance of the CLU which is nearly devoid of instrumental polarization and is also achromatic.

The PMU, which is located near the exit pupil, is a continuously rotating waveplate that has a rotation rate of 1.6s to provide the polarization modulation. The thermal dependence of the PMU retardation is minimized by using two birefringent crystals, namely quartz and sapphire, whose thermal co-efficients compensate one another. Although the retardation is wavelength-dependent, it has been optimized for observations at 630.2 nm (with a retardation of 1.35 waves) and 517.2 nm (1.85 waves), such that the Stokes vectors Q, U, and V have an equally high modulation efficiency of nearly 0.5. The Stokes vector (I, Q, U, V) represent the different states of polarization. The linear polarization signals Q and U as well as the circular polarization signal V are converted into sinusoidal variations of intensity by the polarizing beam splitters in the FPP. Demodulation of the signals are done by sampling the intensity 16 times per revolution of the PMU waveplate. The I, Q, U, and V spectra are subsequently obtained by either adding or subtracting each sample into the four memories allotted for the four Stokes states in the FPP.

The FPP has a reimaging lens followed by a beam splitter. The effective combined focal length is 1550 cm corresponding to an f#31 beam which results in a depth of focus of 400 μm in the FPP focal plane. On the downstream side of the beam splitter are the broadband and narrowband filter channels, which share a common CCD camera, the spectropolarimeter, and the correlation tracker. While a non-polarizing beam splitter divides the light between the SP and the filtergraph, a polarizing beam splitter in the filter channel transmits the p-polarized light to the NFI and the s-polarized light to the BFI. The FPP electrical box (FPP-E) has a computer for controlling the FPP and performs onboard data processing such as Stokes demodulation. The other electrical box (FPP-PWR) contains the power supply for the entire FPP subsystem.

The Mission Data Processor (MDP) controls FPP observations, which are decided by the observing tables uploaded from the ground, and processes housekeeping and science data from the FPP as well. The housekeeping data and the image data with header information are separately sent to the MDP from the

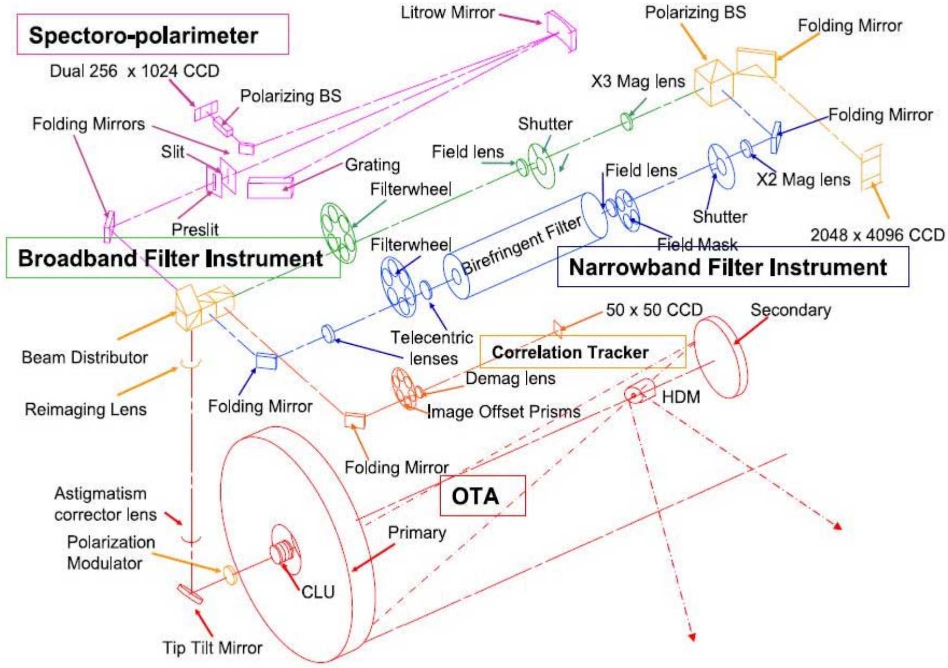

Figure 2.1: Optical Telescope Assembly (OTA) and Focal Plane Package (FPP) of *Hinode*. Figure adapted from Tsuneta et al. 2008, Sol. Phys., 249, 167.

SOT. The image data are compressed, if instructed to do so, combined with the final header information, packetized, and sent to the spacecraft data recorder through the spacecraft central Data Handling Unit (DHU).

1. **The Broad band Filter Imager (BFI):** The BFI produces photometric images with broad spectral resolution in 6 bands (CN band (450.45 nm), Ca II H line (396.8 nm), G-band (403.5 nm) and 3 continuum bands) at the highest spatial resolution (0.0541 arcsec/pixel) and cadence (<10 sec typical) over the full FOV (218×109 arcsec). This allows accurate measurements of the horizontal flows and temperature of the solar surface and to identify sites of strong magnetic fields. These BFI filters have an FWMH bandwidth of 0.3 - 0.7 nm and obtain images not subject to Doppler motion. The CCD consists of 4k×2k pixels which is also shared by the NFI. The exposure times are typically 0.03 - 0.8 s, but longer exposure times are also possible.

2. **The Spectropolarimeter (SP):** The SP is an off-axis Littrow Echelle spectrograph that records line profiles in all Stokes parameters with high spectral resolution (30mÅ) and a sampling of 21.5mÅ, in two magnetically sensitive lines of Fe I at 6301.5 Å and 6302.5 Å. The SP operates in four different modes: Normal Mapping mode, Fast mode, Dynamics mode and Deep Magnetogram mode. Normal mapping observation produces a polarimetric accuracy of 0.1%. The FOV along the slit for the normal mapping and fast mode is 164″ while in the dynamics mode it is 32″. The spatial sampling for the first three modes are 0.″16, 0.″32 and 0.″16 respectively while the time taken to map a 1.6″ area are 50 s, 18 s and 18 s respectively. The SP takes 83 min to cover a 160″ wide area in the normal mapping mode. In the Deep Magnetogram mode, photons may be accumulated over many rotations of the polarization modulator, which enables high polarization accuracy in very quiet regions, but at the expense of temporal resolution. For a typical exposure time, the sensitivity of the SP is 1-5 G in the longitudinal direction and 30-50 G in the transverse direction.

3. **The Correlation Tracker (CT):** The correlation tracker (CT) on board the FPP is essential for compensating spatial fluctuations arising from the spacecraft's jitter, possible wobbling associated with the PMU rotation, and slow drifts caused by opto-thermal deformation of the instrument structure. The stabilization is necessary for obtaining crosstalk-free polarization and magnetic maps. The CT comprises of a 50×50 pixel CCD that has a frame rate of 580 Hz. The spatial sampling is $0.''22$/pixel. The error signal generated from the cross correlation of solar granulation is fed to a Tip-Tilt mirror that consists of three piezo actuators manufactured by Queensgate Instruments Ltd. The in-flight stability is an impressive $0.''007$ and the closed loop bandwidth is 14 Hz.

   A lot of effort was made to characterize and cope with the effects of microvibrations on the OTA, resulting from instrument mechanisms, satellite gyroscopes and momentum wheels which could excite severe resonances with the telescope structure. This could have severely limited the bandwidth of the image stabilization system. The effect of microvibration was decreased by relocating noise sources, spacecrafts gyroscopes and by minor structural improvements.

The recorded data is compressed to 3 bits pixel^{-1} and 1.5 bits pixel^{-1} for the filtergrams and Stokes data respectively. The spacecraft data recorder on board *Hinode* has a storage capacity of ≈ 8 Gbits of which ≈ 70% is allocated to SOT, subject to increase if required. Using a nominal 4-Mbps high-telemetry channel in one ground station pass, ≈ 1.7 Gbits of SOT data can be downloaded. If the number of stations scheduled in a day are 15, the SOT can acquire 25.5 Gbits data per day, and the corresponding post-compression average data rate from the SOT is ≈ 300 kbps. The maximum data rate during post-compression is ≈ 1.3 Mbps. The 5.6 Gbits space spacecraft recorder can be filled in 1 hour during the burst observation mode which subsequently requires about three station passes for complete downlink.

The *Hinode* data is available at a number of data retrieval sites[1]. Data can

[1] *http://darts.isas.jaxa.jp/solar/hinode/query/start.do, http://sdc.uio.no/search/API, http://sot.lmsal.com/sot-data?cmd=search-events*

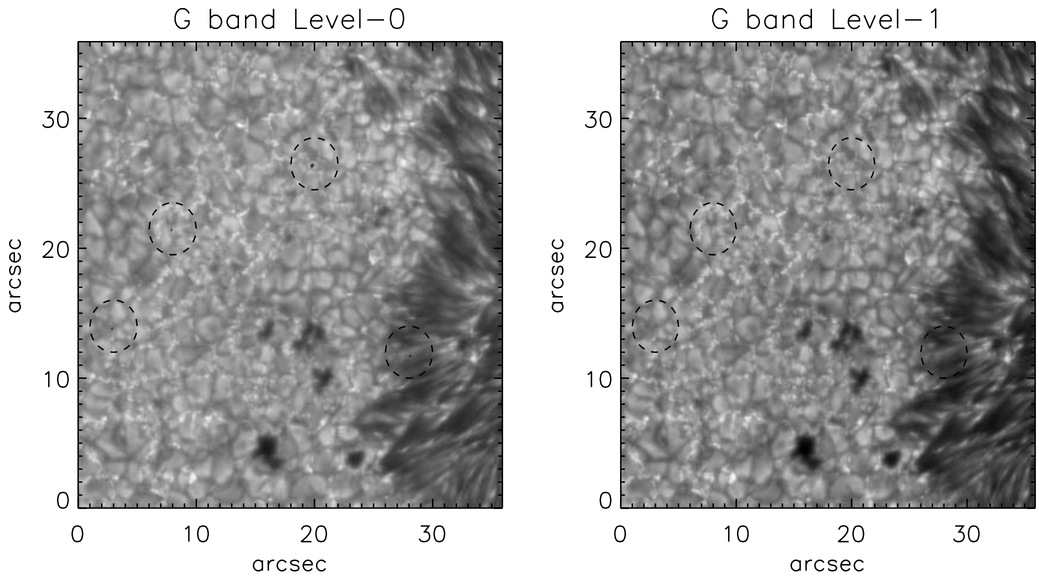

Figure 2.2: Illustration of Level-0 and Level-1 G band filtergrams. The dashed circle highlights regions in the image which are corrected in the Level-1 image (**right**). Note the improvement in image contrast.

be requested via anonymous ftp in which the files are made available through a tar container file. After decompression, the individual filtergrams/Stokes spectra, which are written in the FITS (Flexible Image Transport System) format, have to be processed to Level-1 data from Level-0. This processing is done using standard algorithms and routines in the *Solarsoft* package[1] which include correction of CCD row readout anomalies, dark pedestal and current subtraction, flat fielding, removal of bad pixels and application of a radiation despike. The Stokes spectra are also corrected for instrumental polarization and thermal flexures. The header structure is unique to each image and contains all the parameters pertaining to the observation. These include the date and time of observation, the instrument recording the data, exposure time, image scale, size and dimension, units of the image axes, observing wavelength, slit position, spacecraft pointing coordinates etc. The naming convention of the Level-1 data are 'yyyymmdd_hrmnsc.fits' with 'FG' and 'SP3D' prefixed for filtergrams and Stokes spectra respectively. While an individual broadband filtergram consists of a single image, the Level-1 Stokes data

[1] *http://www.lmsal.com/solarsoft/sswdoc/index_menu.html*

consists of the four individual spectra stacked one over the other, in the order of I, Q, U and V. The difference between the Level-0 and Level-1 data is illustrated in Figure 2.2 wherein the dashed circle highlights regions in the image which need to be corrected in the Level-0 image (*left*) and are subsequently corrected in the Level-1 image (*right*). The Level-1 products can be used for scientific analysis.

2.3 Stokes Inversion based on Response Functions (SIR)

This section describes the SIR package and its execution for the inversion of the Stokes spectra recorded by the spectropolarimeter on board *Hinode*. Detailed description, formulation and solution of the radiative transfer equation for polarized light is beyond the scope of the thesis and the interested reader may refer del Toro Iniesta (2003a) and Landi Degl'Innocenti & Landolfi (2004). Sections 2.3.1.1 to 2.3.3, describe very briefly the manner in which SIR operates and its execution, using the input Stokes profiles and the user supplied initial model atmosphere. Section 2.3.4 is important from the thesis point of view as it discusses the significance of nodes to the application of actual spectral data and emphasizes the need for the optimum model atmosphere.

SIR (Stokes Inversion based on Response functions) is a package that is capable of synthesis and inversion of spectral lines that are formed in the presence of magnetic fields. The SIR code utilizes the Zeeman-induced polarization states (I, Q, U, V) arising from any electric dipole transition and atomic species. The analysis of solar spectra is carried out automatically under the assumption of LTE (Local Thermodynamic Equilibrium). When SIR is executed in the synthesis mode, Stokes spectra[1] emerging from any specified model atmosphere are derived. The model atmosphere can consist of up to two different components (either magnetized or non-magnetized). This is done by numerically solving the radiative transfer equation (RTE) for polarized light. In the inversion mode, SIR fits any combination of observed Stokes parameters for any arbitrary number of spectral lines. In order to achieve this, an initial (user-provided) model

[1]Stokes spectra or Stokes profiles implies the dependence of I, Q, U and V on wavelength.

atmosphere is iteratively modified until the synthetic Stokes profiles match the observed ones. This results in the thermal, dynamic and magnetic structure of the atmosphere similar to the conditions in which the observed profiles were formed.

The inversion module of SIR utilizes the Levenberg-Marquardt (LM) nonlinear least-squares algorithm (Press et al., 1993) for the minimization of the differences between the observed and synthetic Stokes spectra. The LM technique converts the nonlinear problem into a linear one, the solution of which is carried out by means of a modified singular value decomposition (SVD) algorithm (Ruiz Cobo & del Toro Iniesta, 1992). The success of the SIR inversion critically depends on the Response Functions (RFs), which are the partial derivatives of the Stokes parameters with respect to the atmospheric parameters. Thus, the synthesis module of SIR calculates all the necessary RFs.

Westendorp Plaza et al. (1998) quantified the performance of SIR with that of the Milne-Eddington based inversion code of Skumanich & Lites (1987) in various numerical experiments. SIR has been successfully applied to the study of different solar structures observed in polarized light, such as sunspots (Collados et al., 1994; Westendorp Plaza et al., 1997), unresolved magnetic elements (Bellot Rubio et al., 1996), to structures such as penumbrae (del Toro Iniesta et al., 1994), solar granulation (Ruiz Cobo et al., 1996), and solar oscillations (Ruiz Cobo et al., 1997). The model atmospheres were retrieved from the observed Stokes spectra in the above analyzes.

2.3.1 Synthesis Module

2.3.1.1 Spectral synthesis

Spectral synthesis is carried out by solving the radiative transfer equation for Zeeman split lines

$$\frac{\mathrm{d}\boldsymbol{I}(\tau_5)}{\mathrm{d}\tau_5} = \mathsf{K}(\tau_5)\ [\boldsymbol{I}(\tau_5) - \boldsymbol{S}(\tau_5)] \tag{2.1}$$

where τ_5 represents the continuum optical depth at 5000 Å along the line of sight (hereafter LOS), K is the total absorption matrix (a 4×4 matrix describing the absorption properties of the atmosphere), and $\boldsymbol{S} = (S_I, S_Q, S_U, S_V)^\dagger$ the source function vector. Since LTE conditions are assumed, the source function vector is given by $\boldsymbol{S} = (B_\nu[T], 0, 0, 0)^\dagger$, with $B_\nu[T]$ the Planck's function at the local temperature T.

The physical parameters needed to compute K are specified in the model atmosphere, which need to be discretized in an equally spaced logarithmic scale of the continuum optical depth at 5000 Å. At each grid point, the temperature, electron pressure, microturbulence, magnetic field strength, azimuth and inclination of the magnetic field vector, and LOS velocity are specified. The model atmosphere is completed with a set of depth-independent parameters: macroturbulent velocity, stray light contamination and filling factor (for two component atmospheres). Magneto-optical effects leading to linear and circular birefringence are fully considered. The continuum absorption coefficient k_c is evaluated for a given wavelength, temperature and electron pressure by taking into account contributions from H, He, H^-, He^-, H_2^-, H_2^+, C, Mg, and Na, as well as Rayleigh scattering by H, H_2 and He, and Thomson scattering by free electrons. Other atomic and molecular line opacity sources, which are neglected in the present version of SIR, can be included in a straightforward manner.

SIR assumes hydrostatic equilibrium. After each iteration step, the electron pressures of the already perturbed model atmosphere are put into hydrostatic equilibrium by using the equation of state of an ideal gas with variable mean molecular weight to take into account the partial ionization of the various atomic elements. Gas pressures are computed from temperatures and electron pressures on the assumptions of LTE and chemical equilibrium. In this process, the partial pressures of H, H^+, H^-, H_2, H_2^+ and other 83 elements are determined following the strategy outlined by Mihalas (1967). The synthesis is carried out under the assumption that the predominant broadening mechanisms are van der Waals broadening Γ_6 and radiation broadening Γ_rad. Stark broadening is neglected. Γ_6 can be multiplied by a user-specified enhancement factor E that is usually in the range 1-3. Once K and $\boldsymbol{S}$ have been calculated, SIR solves the RTE by means of a Hermitian algorithm (Bellot Rubio et al., 1998). The Hermitian algorithm is based on the Taylor expansion of the Stokes vector to fourth order in optical depth. It provides an approximation to the evolution operator (see Section 2.3.1.2) at no extra cost, which is crucial for the calculation of response functions. The main advantages of the Hermitian method are accuracy and speed.

The various steps through which SIR calculates simulated Stokes spectra are:

1. The files containing the model atmosphere and the atomic parameters of the lines to be synthesized are read.

2. The RTE is integrated numerically for the wavelengths specified in a wavelength grid file. If the atmosphere consists of two different components, the Stokes spectra emerging from each component, $\boldsymbol{I}_1(\lambda)$ and $\boldsymbol{I}_2(\lambda)$, are computed individually and then mixed according to their filling factors f_1 and f_2, with $f_1 + f_2 = 1$. In this case, the emergent Stokes spectrum is

$$\boldsymbol{I} = f_1\,\boldsymbol{I}_1 + f_2\,\boldsymbol{I}_2 \tag{2.2}$$

3. The same height-independent macroturbulent velocity $v_{\rm mac}$ is assumed for all spectral lines. The effect of the macroturbulence is simulated by convolving $\boldsymbol{I}$ with a gaussian

$$M(\lambda - \lambda_0, v_{\rm mac}) = \frac{1}{\sqrt{2\pi}\;\sigma}\mathrm{e}^{-\frac{(\lambda-\lambda_0)^2}{2\sigma^2}} \tag{2.3}$$

   where $\sigma \equiv \lambda_0 v_{\rm mac}/c$, λ_0 is the central wavelength of the transition and c is the speed of light. Additionally, the macroturbulent-broadened profiles ($\boldsymbol{I}^* = \boldsymbol{I} * M$) may be convolved with the PSF of the spectrograph if it is available.

4. The last step in simulating the observed profiles $\boldsymbol{I}_{\rm obs}$ is to add a user-provided stray light spectrum $\boldsymbol{I}_{\rm str}$ that contributes a fraction α to $\boldsymbol{I}_{\rm obs}$:

$$\boldsymbol{I}_{\rm obs} = (1-\alpha)\,\boldsymbol{I}^{*} + \alpha\boldsymbol{I}_{\rm str} \tag{2.4}$$

2.3.1.2 Response functions

Response functions (RFs) to the various atmospheric parameters $x(\tau)$, $\boldsymbol{R}_x(\lambda,\tau)$, are calculated at every optical depth and wavelength according to the formula

$$\boldsymbol{R}_x(\tau) = \mathsf{O}(0,\tau)\left\{\mathsf{K}(\tau)\frac{\partial \boldsymbol{S}(\tau)}{\partial x} - \frac{\partial \mathsf{K}(\tau)}{\partial x}\left[\boldsymbol{I}(\tau) - \boldsymbol{S}(\tau)\right]\right\} \tag{2.5}$$

where $\mathsf{O}(0,\tau)$ represents the evolution operator from τ to the surface. By definition, the modification of the emergent Stokes spectrum $\delta\boldsymbol{I}(\lambda)$ after perturbations $\delta x(\tau)$ of the atmospheric parameter x at optical depth τ is given by

$$\delta\boldsymbol{I}(\lambda) = \int_0^\infty \boldsymbol{R}_x(\lambda,\tau)\,\delta x(\tau)\,\mathrm{d}\tau \tag{2.6}$$

If a nonzero macroturbulence is used to synthesize the emergent Stokes spectrum, all the RFs have to be convolved with M as well. The same applies if the spectrograph profile is taken into account.

2.3.2 The inversion module

The inversion of Stokes profiles proceeds by minimizing a merit function which is the sum of the squared differences between observed and synthetic data weighted by the uncertainties of the observations and by some factors w_{ki}^2. The merit function is defined as

$$\chi^2 \equiv \frac{1}{\nu}\sum_{k=1}^{4}\sum_{i=1}^{M}\left[I_k^{\mathrm{obs}}(\lambda_i) - I_k^{\mathrm{syn}}(\lambda_i)\right]^2 \frac{w_{ki}^2}{\sigma_{ki}^2}, \tag{2.7}$$

where index $k = 1,\ldots,4$ samples the 4-component vectors containing the observed (obs) and synthetic (syn) Stokes profiles, $i = 1,\ldots,M$ sample the wavelengths at which the spectrum has been measured, ν is the number of degrees of freedom (i.e., the number of observables minus the number of parameters to be inverted) and σ_{ki} are the uncertainties of the observations. SIR automatically adjusts the factors w_{ki}^2 so as to give the same relative weight to the Stokes parameters of different spectral lines, independently of their amplitudes. The user may specify that more weight is to be assigned to a particular Stokes parameter. For example, more weight could be desired for Stokes V when analyzing magnetic regions. By default, SIR assumes that the uncertainties σ_{ki} are all equal to a constant value σ given by the signal-to-noise ratio of the observations. When SIR finds values smaller than -1.0 for any of the Stokes parameters, the corresponding σ_{ki} are set to 10^{15}, the consequence being that such data points are not taken into account in the fit.

The minimization of Eq. (2.7) is carried out iteratively by modifying an initial user-provided model atmosphere. This process yields the perturbations of the

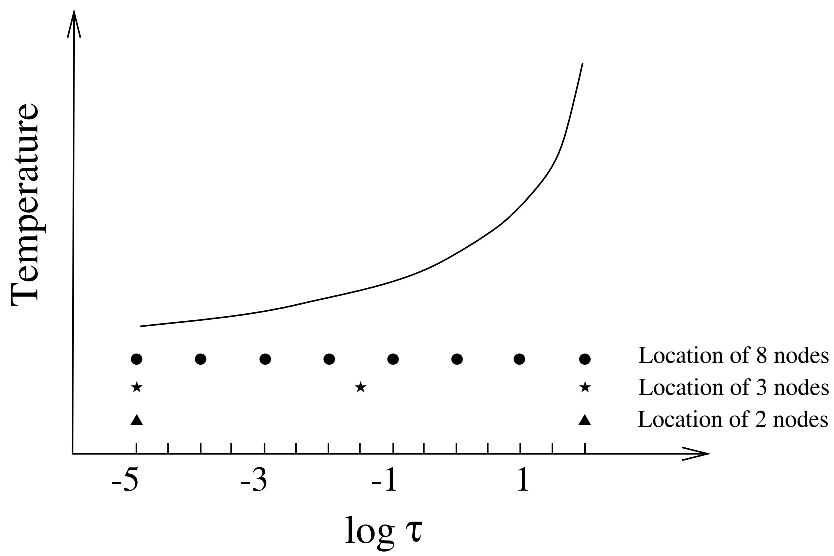

Figure 2.3: Schematic explanation of how the nodes are chosen. The particular case of temperature (T) is considered. The atmosphere is discretized in the logarithmically evenly spaced grid shown in the x–axis, the step size being $\Delta \log\tau = 0.5$ in this particular example. The optical depths at which perturbations of the temperature will be sought are determined by the number of nodes selected. If the user specifies two nodes, perturbations of T at $\log\tau = -5.0$ and $\log\tau = 2.0$ will be found. With three nodes, perturbations will be found at $\log\tau = -5.0$, $\log\tau = -1.5$ and $\log\tau = 2.0$. The same scheme applies with a larger number of nodes. Five nodes cannot be used here because there are no sufficient spatial points in the grid to produce an even distribution of the nodes through the whole atmosphere.

guess atmosphere required for the synthetic spectrum to match the observed one. However, the minimization of χ^2 is complex because $\boldsymbol{I}^{\rm syn}$ depends nonlinearly on the various atmospheric parameters. To handle this problem, SIR implements a Levenberg-Marquardt algorithm (Press et al., 1993). LM makes use of the derivatives of χ^2 with respect to the model parameters. It turns out that these derivatives can be expressed in terms of RFs (Ruiz Cobo & del Toro Iniesta, 1992), which explains the relevance of the RFs for the inversion.

In order to reduce the number of free parameters, the perturbations of the depth-dependent physical quantities characterizing the initial guess model atmosphere are calculated only for a few grid points (called *nodes*) of the spatial grid in which the atmosphere is discretized. For each physical quantity (e.g., temperature, LOS velocity, etc), the atmosphere is represented by a different set of nodes. The perturbations of the various parameters in all the remaining grid points are approximated by linear or cubic-spline interpolation of the perturbations at the nodes.

Figure 2.3 explains in more detail the concept of nodes introduced by SIR. Once the number of nodes has been specified for a given physical quantity, the code locates the optical depths at which perturbations will be sought. If only one node is allowed, the perturbation suggested by LM is added to the values of the physical quantity under consideration at all heights (i.e., its depth stratification is modified by a constant perturbation). With two nodes, the perturbations at the nodes are interpolated linearly to the whole atmosphere. With three nodes, either linear or parabolic interpolation is used. With four or more nodes, linear or cubic-spline interpolation is applied.

SIR allows the user to specify the number of nodes for each physical quantity. The number of free parameters equals the sum of the number of nodes adopted for the various physical quantities. The set of iterations carried out without modifying the number of nodes is called a *cycle*. Usually, SIR needs two or three cycles to arrive at the final solution. In each iteration cycle, the number of free parameters is normally increased to permit more flexibility to the solution.

2.3.2.1 Error estimation

For the computation of errors in the retrieved parameters a simple physical argument is followed. According to Eq. (2.7), the weighted squared difference between the observed and synthetic spectra can be written as

$$\sum_{i,k} \delta I_{ki}^2 \frac{w_{ki}^2}{\sigma_i^2} = \nu\chi^2, \tag{2.8}$$

with $\delta I_{ki} \equiv I_k^{\rm obs}(\lambda_i) - I_k^{\rm syn}(\lambda_i)$. It is assumed that m model parameters are to be inverted, each one being responsible of a fractional part $1/m$ of the observed differences δI_{ki}^2. With these hypotheses one can find a set of perturbations $\delta x(\tau)$ to the original parameters that minimize χ^2. Using the definition of the RFs (see Eq. 2.6) one gets

$$\frac{\delta I_{ki}}{\sqrt{m}} = R_{x,k}(\lambda_i, \tau)\delta x(\tau)\Delta\tau, \tag{2.9}$$

and so

$$\sigma_{x(\tau)}^2 \equiv [\delta x(\tau)]^2 = \frac{\nu\chi^2}{m(\Delta\tau)^2 \ \sum_{i,k} R_{x,k}^2(\lambda_i,\tau)\ w_{ki}^2/\sigma_i^2}. \tag{2.10}$$

It is implicitly assumed that all model parameters are independent, so changes in a given parameter do not influence the remaining ones. As it might have been expected, uncertainties $\sigma_{x(\tau)}$ are proportional to the inverse of the RF to changes in $x(\tau)$. Therefore, parameters that have little influence on the emergent Stokes spectrum show the largest uncertainties. This is the case for most parameters outside the region where the spectral lines are formed.

2.3.3 Executing SIR

The SIR distribution is available freely on the internet[1] as a container file called 'sir.tar' which consists of the following directories.

- `default`. This subdirectory keeps default files.
- `idl`. Several IDL procedures for visualizing model atmospheres and Stokes profiles. There are also some utilities for extracting observed profiles from the IDL FTS spectral atlas.

[1] *http://www.iaa.es/hinode_europe/index.php/gb/inversion_codes*

- `manual`. This subdirectory contains the user manual.
- `models`. Some standard model atmospheres which may be of use in real inversions are provided in this folder. A number of utilities for modifying these models or others are provided as well.
- `program`. This subdirectory keeps the source programs and the macros needed to compile SIR.
- `test`. This subdirectory contains a particular inversion intended to test the degree of success of the installation.

Once all the routines have been compiled, the 'sir.f' main program has to be linked to the SIR library. This results in the 'sir.x' executable file which is now ready to be used for inversions. The user input to SIR is through the 'sir.trol' file which is the control file, an example of which is shown in Table 2.1. I now proceed to elaborate some of the important fields in the control file.

- `Number of cycles`. This parameter indicates the number of iteration cycles to be carried out. In the above example, SIR performs three cycles. For synthesis of Stokes spectra (without inversion), the number of cycles should be set to zero.
- `Observed profiles`. This is the name of the file containing the observed profiles (in inversion mode) or the name of the file where the synthesized profiles will be stored (in synthesis mode). The files are suffixed with '.per' and must consist of 6 columns while the number of rows depends on the wavelength points for each spectral line. In the case of the *Hinode* SP data, the number of rows are 112. The first column consists of the spectral line index that is present in the LINEAS file (see below). The second column is the relative wavelength with respect to the laboratory rest wavelength i.e. $(\lambda - \lambda_0)$. Columns 3 to 6 are the I, Q, U and V spectral points at each wavelength position. These must necessarily be normalized to the quiet Sun continuum intensity, since the thermal structure of the model atmosphere is inferred from this.

Table 2.1: Example of a SIR control file

Number of cycles	(*):3	! (0=synthesis)
Observed profiles	(*):profiles.per	
Stray light file	:stray.per	! (none=no stray light contam)
PSF file	:psf.dat	! (none=no convolution with PSF)
Wavelength grid file	(s):grid.grid	! (none=automatic selection)
Atomic parameter file	:LINEAS	! (none=DEFAULT LINES file)
Abundance file	:THEVENIN	! (none=DEFAULT ABUNDANCES file)
Initial guess model 1	(*):guess1.mod	
Initial guess model 2	:guess2.mod	
Weight for Stokes I	:1	! (DEFAULT=1; 0=not inverted)
Weight for Stokes Q	:1	! (DEFAULT=1; 0=not inverted)
Weight for Stokes U	:1	! (DEFAULT=1; 0=not inverted)
Weight for Stokes V	:10	! (DEFAULT=1; 0=not inverted)
AUTO SELECT. OF NODES?	:	! (DEFAULT=0=no; 1=yes)
Nodes for temperature 1	:1,5,10,12	
Nodes for electr. press. 1	:	
Nodes for microturb. 1	:0,1	
Nodes for magnetic field 1	:1	
Nodes for LOS velocity 1	:	
Nodes for gamma 1	:	
Nodes for phi 1	:	
Invert macroturbulence 1?	:1	! (0 or blank=no, 1=yes)
Nodes for temperature 2	:	
Nodes for electr. press. 2	:	
Nodes for microturb. 2	:	
Nodes for magnetic field 2	:	
Nodes for LOS velocity 2	:	
Nodes for gamma 2	:	
Nodes for phi 2	:	
Invert macroturbulence 2?	:	! (0 or blank=no, 1=yes)
Invert filling factor?	:	! (0 or blank=no, 1=yes)
Invert stray light factor?	:1	! (0 or blank=no, 1=yes)
mu=cos (theta)	:	! (DEFAULT: mu=1.)
Estimated S/N for I	:200	! (DEFAULT: 1000)
Continuum contrast	:	! (DEFAULT: not used)
Tolerance for SVD	:	! (DEFAULT value: 1e-4)
Initial diagonal element	:	! (DEFAULT value: 1.e-3)
Splines/Linear Interpolation	:	! (0 or blank=splines, 1=linear)
Gas pressure at surface 1	:	! (0 or blank=Pe boundary cond.)
Gas pressure at surface 2	:	! (0 or blank=Pe boundary cond.)
Magnetic pressure term?	:	! (0 or blank=no, 1=yes)
NLTE Departures filename	:	! blank= LTE (Ej. depart_6494.dat')

Table 2.2: Illustration of the LINEAS file.

Line=Ion	Wavelength	E	Exc.Pot	log(gf)	Transition	α	σ
1=FE 1	6301.5012	1.0	3.654	-0.75	5P 2.0- 5D 2.0	0.243	2.3520e-14
2=FE 1	6302.4936	1.0	3.686	-1.236	5P 1.0- 5D 0.0	0.240	2.3976e-14
3=FE 1	5576.0888	1.0	3.428	-0.910	7D 1.0- 7D 0.0	0.232	2.3912e-14

- `Stray light file`. Name of the file containing the stray light intensity profile ($\boldsymbol{I}_{\mathrm{str}}$). If no name is specified, the synthetic profiles will be computed with $\alpha = 0$ (i.e., no stray light contamination). The wavelengths of the stray light profile must coincide with those in the observed profiles, otherwise an error message will be issued and the program will abort. This file too must be suffixed with '.per'.

- `PSF file`. Name of the file containing the spectrograph profile. If no name is specified, the synthetic profiles are not convolved with the PSF of the spectrograph.

- `Wavelength grid file`. Compulsory in synthesis mode, optional otherwise. This is the name of the file specifying the wavelengths at which the profiles are known. In inversion mode, the wavelengths can be read from the profiles themselves, so there is no need to specify any wavelength grid. This file is of particular importance in the synthesis mode, while deriving the convective blue shift in the photosphere.

- `Atomic parameter file`. Name of the file containing the atomic data for the spectral lines considered. If no name is specified, SIR will look for the default `LINES` file in the ∼`/sir/default/` directory. The LINEAS file contains the atomic parameters of the transitions to be considered (Table 2.2). Valid atomic parameter files have eight columns as follows:

  The first column gives the index with which the line is identified in the profile and the wavelength grid files. The index is separated by a `=` sign from the atomic symbol of the element. The ionization stage is specified by a number: 1 means neutral atom, and 2 singly ionized atom. At present, SIR can handle only the two first ionization stages.

The second column specifies the (laboratory) central wavelength of the transition (in Å). The third column gives the enhancement factor to the van der Waals coefficient Γ_6. The fourth and fifth columns give the excitation potential of the lower level (in eV) and the logarithm of the multiplicity of the level times the oscillator strength, respectively. The sixth column specifies the atomic transition. The transition is used only if magnetic fields are present, since it determines the number and strength of the various Zeeman components, but it is always necessary to avoid error messages. In the absence of magnetic fields, one need not know the exact transition to be able to synthesize or invert the corresponding intensity spectrum. Finally, the last two columns specify the collisional broadening parameters α and σ σ is expressed in cm^2.

- `Abundance file`. Name of the file containing the abundances A_x of the various chemical species in the solar atmosphere and is defined as $A_x = 12 + \log{[x]/[H]}$. If no name is specified, the default `ABUNDANCES` file in the `~/sir/default` directory will be used. The THEVENIN abundance file (Thévenin, 1989) is normally used. Valid abundance files have two columns. The first one indicates the atomic number and the second, the abundance in logarithmic scale already mentioned.

- `Initial guess model 1`. Compulsory. This is the name of the model atmosphere to be used for synthesis (if in synthesis mode) or the name of the initial guess model (if in inversion mode). In the example, the starting model is called `guess1.mod`. The improved model resulting from the first iteration cycle will be called `guess1_1.mod`, and will be read as the initial guess model for the second iteration cycle. After this new cycle, the improved model is `guess1_2.mod`, and so on. An inversion run may be started with an initial guess model called `model_4.mod`, for instance. In this case, SIR will take care of updating the subindex whenever an iteration cycle has finished. Thus, the improved model resulting from the first cycle will be called `model_5.mod`.

  Valid model atmosphere files have a first line with three numbers written in free format. These numbers indicate the macroturbulent velocity (in km s^{-1}), the filling factor (ranging from 0 to 1), and the stray light contamination (in percent), respectively.

After the first row, n_τ lines follow. There are eleven columns providing the logarithm of the **line-of-sight** continuum optical depth at 5000 Å, the temperature (in K), the electron pressure (in dyn cm^{-2}), the microturbulent velocity (in cm s^{-1}), the magnetic field strength (in G), the line-of-sight velocity (in cm s^{-1}), the inclination and azimuth of the magnetic field vector (in deg), the geometrical height (in cm), the gas density (in g cm^{-1}), and the gas pressure (in dyn cm^{-2}), respectively. The inclination γ of the magnetic field vector is measured with respect to the line of sight, and ranges from 0 to 180 degrees (these values corresponding to longitudinal fields pointing to and away from the observer, respectively). Negative inclinations should be avoided. The azimuth ψ is reckoned from the direction where Q is maximum and $U = 0$ (which is defined by the polarimeter), and increases counterclockwise as seen by the observer. The azimuth varies between 0 and 360 degrees.

The model atmospheres must run from larger to smaller optical depths, otherwise an error message will be issued. If two components are used, the optical depths of the two models must coincide. In this case, it is also necessary that the sum of the two filling factors provided in the first line of the files be equal to unity. If not, SIR will adopt the filling factor of the first component (f_1) to calculate the corresponding filling factor of the second component as $f_2 = 1 - f_1$.

In inversion mode, the optical depths must be equally spaced, since the nodes are evenly distributed through the whole atmosphere. When constructing a given model atmosphere, it is important to make sure that the number of depth points, n_τ, permits the selection of a wide set of nodes. This is possible if $n_\tau - 1$ has a large number of divisors. Adequate values of n_τ are, for example, 13, 25, 37 and 49.

For an accurate integration of the radiative transfer equation, spacings of the order of 0.1 in the logarithm of the optical depth are recommended. Spacings larger than 0.5 may lead to inaccurate integrations. Spacings smaller than, say, 0.05 does not imply greater precision but increase the computation time. Typically, the depth grid should extend from 1.0 to −4.0 for photospheric lines and from 1.0 to −6.0 for chromospheric lines.

- `Initial guess model 2`. Same as above, but only if a two-component model atmosphere is being used. The name of the initial guess model for the second component does not need to coincide with that of the first component. Thus, for instance, one might start the inversion with an initial second component called `model2_7.mod`. The number of depth points in model 2 must coincide with that in model 1. Otherwise, the program is aborted.

- `Weights for Stokes I, Q, U and V`. These parameters indicate the relative weight of Stokes I, Q, U and V in the χ^2 merit function. In the example of Table 2.1, Stokes V is given ten times more weight than Stokes I, Q and U. If no weight is specified, a default weight equal to unity will be assigned. Zero weights imply that the corresponding Stokes parameters will not be inverted.

- `AUTO SELECT. OF NODES?` If this parameter is set to zero (the default), the user must specify by hand the number of nodes to be used for each physical quantity in all the iteration cycles. If this parameter is set to one, then a simple pattern for the automatic selection of nodes is adopted. Such a pattern takes advantage of the fact that the Stokes profiles are most sensitive to temperature, while the other physical quantities are less important to first order. Then, the temperature is given more flexibility (i.e., more nodes) right from the very beginning. To this end, the divisors of $n_\tau - 1$ (where n_τ is the number of grid points in the discretized atmospheres) are found. Let $d(i)$ denote the i^{th} divisor (from the smallest to the largest one).

  The automatic sequence of nodes for temperature would be: $d(3)$, $d(4)$, $d(5)$, and so on. Thus, for the jth cycle, the number of nodes assigned to temperature would be $d(j+2)$. For the other depth-dependent physical quantities, the number of nodes assigned at j^{th} cycle is $d(j)$.

Even if automatic selection of nodes is in effect, the user can decide which parameters are to be determined. For instance, if the temperature of model 1 is to be improved right from the first cycle, while the temperature of the second component is desired to improve only after the first cycle, then with the automatic selection of nodes the user should write `1` in the field `Nodes for temperature 1`, and `0,1` (or `0,3`, for example) in the field `Nodes for temperature 2`. The zero in the second field instructs SIR not to invert the temperature of model 2 in the first cycle. The numbers one or three indicates that the temperature of the second component will be modified already in the second cycle (with the number of nodes being determined automatically).

- `Nodes for the various atmospheric parameters in models 1 and 2`. The following eighteen fields specify the number of nodes to be used in each iteration cycle (only if manual selection of nodes has been chosen). Consider the following example from the control file in Table 2.1:

```
Nodes for temperature 1       : 1,5,10,12
Nodes for electron pressure 1 :
Nodes for microturbulence 1   : 0,1
Nodes for magnetic field 1    : 1
```

  In the first cycle, temperature will be given one node, microturbulence zero nodes, and magnetic field one node. In the second cycle, temperature is given 5 nodes, microturbulence 1 node and magnetic field 1 node. In the last cycle (the third one), ten nodes will be used for temperature and one for microturbulence and magnetic field, respectively. The electron pressure must **never** be inverted, since there is no sufficient information in the profiles to estimate it reliably.

  Some physical parameters are considered to be height-independent, so that they can be given only zero or one node. These include macroturbulence, filling factor and stray light factor.

2.3.4 User Intervention

Once the observed profiles and initial guess files are ready, SIR can proceed to derive the model atmosphere. The most crucial aspect of human intervention in the execution of SIR comes in the choice of nodes for the physical parameters. While the retrieved model atmosphere should produce synthetic profiles that resemble the observed ones, the number of degrees of freedom must always be kept to a minimum. This implies that the user must have an idea of the type of magnetic and thermal structure from where the profiles emanate prior to the inversion. The inversion procedure does not intend to find a new model, rather it tries to find the proper values for the free parameters of a given model (Ruiz Cobo, 2007). To illustrate this, I invert 2 sets of profiles, one in the sunspot umbra and the other in the penumbra. For the first profile, I assume that all the physical parameters remain constant with height, except temperature which I provide with 2 nodes. Figure 2.4 shows a satisfactory fit between the observed and inverted profile with a χ^2 of 3.16 resulting from the inversion. The depth-independent parameters are shown along with their 1σ error bars in Figure 2.5. Note the complete splitting of the Fe 6302.5Å line into the two σ components as well as the unshifted π component which is an indication of strong fields that are marginally inclined. This is also why the linear polarization signals Q and U are much weaker, measuring less than 1.5 %.

In the case of the penumbral profile, two separate sets of inversion are carried out. In the first, I allow 5 nodes for Temperature and 3 nodes for the magnetic field strength as well as LOS velocity. Inclination and azimuth are provided 2 nodes each. The second inversion is similar to that of the umbral profile, with 1 node for all parameters except temperature. The comparison of the two inversions is depicted in Figure 2.6. I would like to draw your attention to a few subtle characteristics in the profiles. The blue wings of the two lines in the I profile appear a little extended in comparison to the red wing. There is a slight asymmetry in the amplitude of two lobes in the Q as well as U profile. In addition, the blue lobe of the V profile is remarkably different from the red lobe which was not seen in the case of the umbral profile. The two sets of inversion, shown side-by-side in

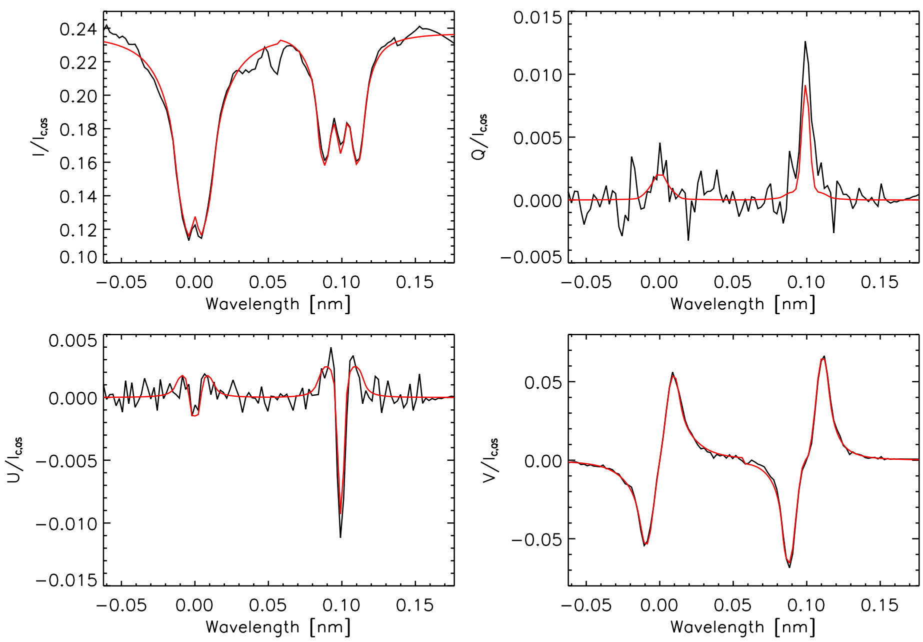

Figure 2.4: Observed (*black*) and inverted (*red*) Stokes profiles for an umbral pixel.

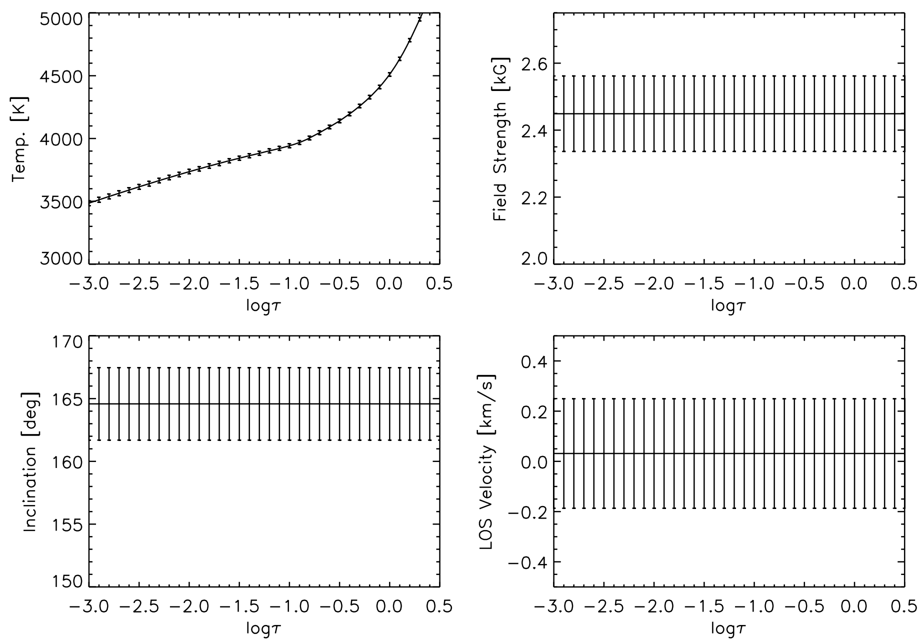

Figure 2.5: Stratification of the physical parameters based on a single node SIR inversion of the umbral pixel.

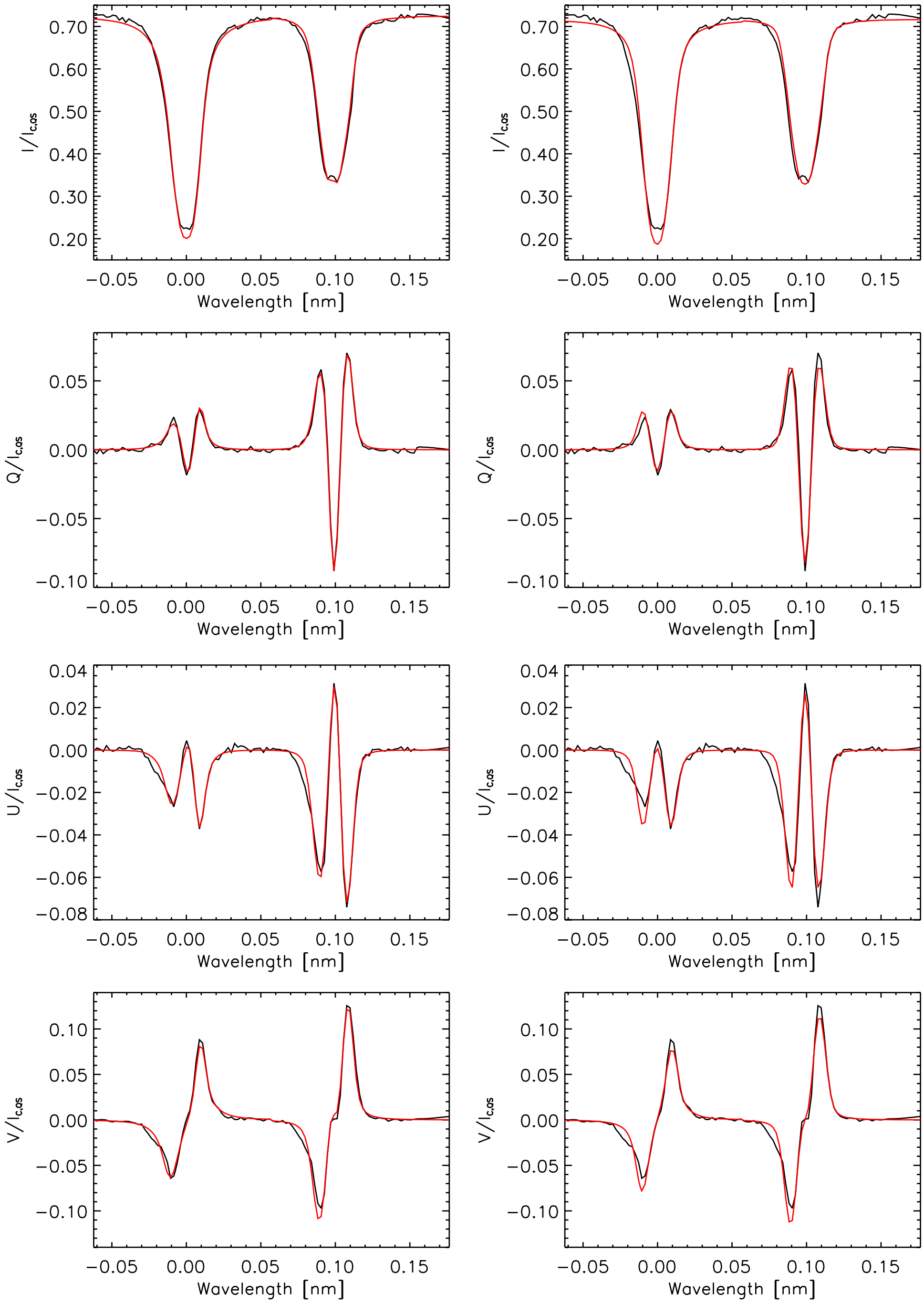

Figure 2.6: Observed (*black*) and inverted (*red*) Stokes profiles for a penumbral pixel using two different model atmospheres. The **left** column illustrates inversions in which gradients are present in the model atmosphere, while the **right** column is based on a homogeneous atmosphere similar to the umbral pixel in Figure 2.4. The Merit Function χ^2 retrieved from the two inversions are 4.5 and 9.8 respectively.

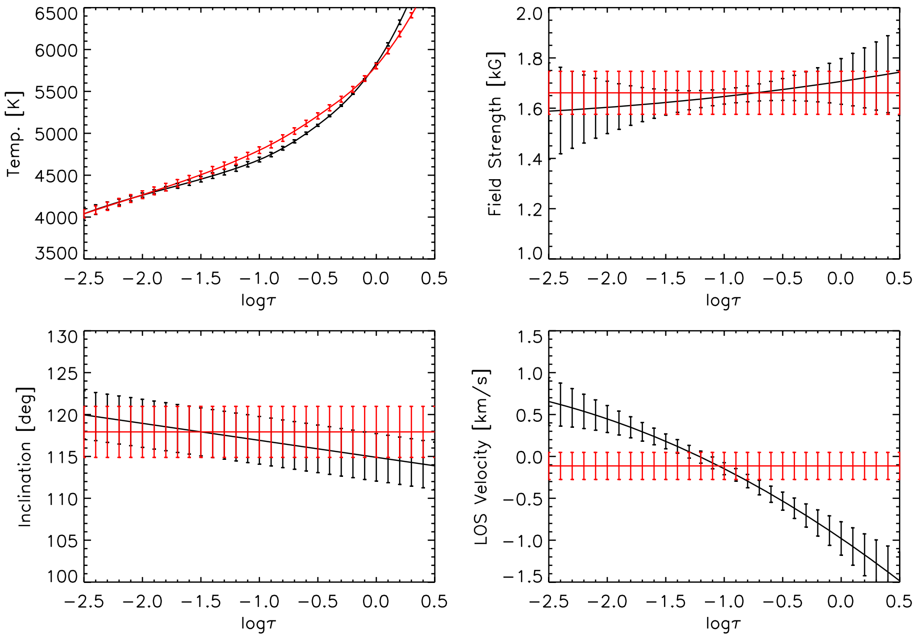

Figure 2.7: Stratification of the physical parameters for the model atmosphere with (*black*) and without gradients (*red*). The error bars correspond to $\pm 1\sigma$.

Figure 2.6, demonstrate the differences resulting from the different model atmospheres. While the presence of gradients arising from a larger number of nodes is able to reproduce the asymmetries, the single node inversions do not, because of the restriction imposed on the model atmosphere. For a majority of structures in the solar atmosphere, the concept of a homogeneous model atmosphere is only an approximation. This is also seen from the stratification derived by SIR in the two cases and is shown in Figure 2.7. While the field strength, inclination and azimuth do not vary by a large amount along optical depth, the LOS velocity shows downflows of the order of 1 km s^{-1} in the deep layers and subsequently decreases with height with weak upflows in the higher layers. The LOS velocity derived from the second inversion does not reflect this trend and appears to be an average value of the actual stratification observed in the range of $\log\tau$=-1.0 to -1.5 in optical depth, which roughly coincides with the formation height of the Fe lines.

Of particular importance is the Milne-Eddington (ME) approximation. This approximation assumes a model atmosphere in which the physical parameters remain constant with height while the Source function changes linearly with optical depth. The solution of the RTE in a ME atmosphere is also called the Unno-Rachkovsky (Unno, 1956; Rachkovsky, 1967) solution and is very useful because of its analytical character. The total absorption matrix K can be written as a function of 9 parameters namely, the line-to-continuum absorption coefficient, η_0, the Doppler width, $\Delta\lambda_D$, the damping constant, a, magnetic field strength, B, field inclination, γ, field azimuth, ϕ, LOS velocity, v_{LOS}, and two parameters that describe the Source function S_0 and S_1. There are a number of inversion codes (ICs) that are based on the ME approximation - HELIX (HElium Line Information eXtractor; Lagg et al., 2004), MELANIE (Milne Eddington Line Analysis using a Numerical Inversion Engine; Socas Navarro, 2001) and MILOS (MILne-Eddington inversion of the pOlarized Spectra; Orozco Suárez & del Toro Iniesta, 2007).

ME inversion codes are very fast and are robust, in the sense that the results are user independent. Besides, LTE approximation or Hydrostatic Equilibrium are not needed, thus ME ICs can be even applied when the knowledge of the atmospheric structure or about the physics involved in the line formation is poor. However, it is important to notice that the Milne-Eddington approximation is reliable as long as no net circular polarization (Chapters 4 and 5) is observed, since this is an indicator that no gradients along the line of sight are present (condition for the absorption matrix to be constant along the ray path). Another important point is that the Milne-Eddington approximation neglects much of the thermodynamics of the atmosphere: first assuming that the level populations and continuum opacity are such that η_0 is constant, and constraining the real temperature stratification of the atmosphere assuming that the source function changes linearly with optical depth. While single node SIR inversions, such as that of the umbral profile, are similar to a ME inversion, they are **not the** same.

In the general case, the RTE has to be solved numerically because the absorption matrix is no longer constant. The line absorption coefficient is calculated by means of the Boltzmann equation. This has to be done for each atmospheric layer since the temperature changes continuously from the $\tau_c = 1$ level (not necessarily following a linear trend). In addition, the damping parameter changes with depth in the atmosphere. This is produced by changes in the temperature itself and by changes in the collisional damping, which depends on the density (or partial pressures) of neutral species such as hydrogen and helium[1]. The above arguments suggest that ME inversions should be used as a first order tool to derive the overall magnetic and kinematic structure and then use it to probe interesting/exotic regions with complex model atmospheres. This approach has been extensively followed in the thesis and will be elaborated in the succeeding chapters.

[1]In the photosphere of the sun and of cool stars the main contribution to the collisional broadening are neutral species. Other contributions, such as linear or quadratic Stark effect can be neglected

Chapter 3

Photospheric and Chromospheric Observations of Sunspot Light Bridges

3.1 Introduction

Light bridges (LBs) are conspicuous bright intrusions in the dark umbral core of sunspot umbra and are often seen during the evolution of sunspots. This would suggest that the processes responsible for the formation of LBs are linked to the structure of sunspots. Korobova (1966) classified LBs that differed in structure, localization with respect to height, and temperature range and on the basis of this, identified three classes: i) photospheric LBs, which are associated with sunspot fragmentation, ii) facular LBs, in which facular structures penetrate the umbra, and iii) arch bridges, which are projections of prominences near sunspots. Light bridges could also be classified as "photospheric," "penumbral," and "umbral" according to Muller (1979) and he concluded that their morphology is the same as photospheric structures. Light bridges are usually seen along "fissures" where a sunspot forms or decays (García de La Rosa, 1987). High-resolution observations also show LBs breaking into a string of umbral dots, indicating a similar formation mechanism between the two phenomena. Sobotka (1989) derived a semiempirical model from spectroscopic observations of LBs and found that the temperature of LBs was lower than the penumbra as well as bright umbral dots. Spruit & Scharmer (2006) proposed that LBs are essentially "field-free" intrusions of plasma in a "spaghetti" of magnetic flux tubes (Parker, 1979; Choudhuri, 1986) similar to umbral dots, wherein the intrusion is elevated above the continuum $\tau = 1$ line. On the other hand Rimmele (2004) observed small-scale convection patterns in a light bridge using adaptive optics corrected images at the Dunn Solar Telescope. Magnetic field measurements of LBs reveal more reduced, inclined magnetic fields (Rüedi et al., 1995; Leka, 1997; Jurčák et al., 2006). Schleicher et al. (2003) reported a slight blue shift in LBs, which are interrupted by short events characterized by strong blue or red shifts from line-of-sight velocity measurements while proper motions of upto 1.5 km s^{-1} have been reported in a granular light bridge in a large solar pore (Hirzberger et al., 2002). The existence of a central dark channel in light bridges has been reported by Sobotka et al. (1994); Hirzberger et al. (2002), and Berger & Berdyugina (2003). Using high-resolution images from the Swedish 1-m Solar Telescope, Lites et al. (2004) estimated the height of the central dark channel to be in the range 200 - 450 km.

Berger & Berdyugina (2003) studied the dynamics of LBs and observed enhanced brightening along the light bridge, which they attribute to the stressed magnetic configuration overlying the light bridge. Observations of LOS magnetograms by Bharti et al. (2007a) revealed the presence of an opposite polarity in a light bridge, which they speculate to be a driver for low-altitude reconnection and subsequently serve as a mechanism for heating the overlying chromosphere. Recently, Katsukawa et al. (2007a) studied the formation process of a light bridge using the spectropolarimeter onboard *Hinode*. Their observations clearly show bright umbral dots and penumbral filaments gradually penetrating the umbra as deep as 4 Mm resulting in a LB. In this chapter I attempt to address the following issues. How do the photospheric properties and dynamics of various LBs compare with one another? Is the chromospheric activity in sunspot LBs a common phenomena? What are the general conditions, and in particular the photospheric counterparts, that could be responsible for the observed activity? For the above analysis, photospheric and chromospheric filtergrams were utilized to study the properties of four sunspot LBs that were observed by *Hinode* (Kosugi et al., 2007) in 2007. In addition, magnetograms were constructed from spectropolarimetric observations of the above candidates to look for small-scale velocity inhomogeneities. The rest of the chapter is organized as follows. The details of the observations are presented in Section 3.2. Standard data processing steps and the determination of some general properties of the LBs are described in Section 3.3 and 3.4 respectively. The long term as well as irregular horizontal flows of intensity features are determined in Section 3.5 using two different optical flow algorithms. Section 3.6 depicts the chromosphere above the respective LBs while the presence of small-scale velocity inhomogeneities, determined from line-wing magnetograms, is described in Section 3.7. The results from the analysis are summarized in Section 3.8.

3.2 Data

G-band filtergrams were obtained for NOAA ARs 10953, 10961, 10963 and 10979 from the BFI (Broadband Filter Imager), of the 50-cm Solar Optical Telescope (SOT; Tsuneta et al., 2008) onboard *Hinode*. These observations were made on May 1, June 29, July 12 and August 23, 2007 respectively. The duration of the filtergrams were 45 min, 88 min, 46 min and 69 min respectively. Ca II H filtergrams with a sampling of $0.''1$ and a cadence of ≈ 5 min for the entire day were also utilized. The data from the archives were Level 0 products and were processed to Level 1 by standard routines written in IDL. This included dark correction, flat-fielding, and removal of bad pixels. In addition to the filtergrams, the spectropolarimeter (SP) of the SOT provided full Stokes spectra of the Fe I line pair at 630 nm for all four active regions. The spectra have a sampling of 21.5 mÅ . The spatial sampling along the slit for AR 10953 was $0.''16$ while for the others it was $0.''32$. These observations were also corrected for dark current, flat field, thermal flexures, and instrumental polarization using routines included in the Solar-Soft package. The observations are summarized in Table 3.1.

3.3 Data Processing

Figure 3.1 shows the four sunspots comprising of one or more LBs. As the sunspots are located at different positions on the solar disk, the images will exhibit an overall intensity gradient which is referred to as limb darkening. This

Table 3.1: Details of observations used for the analysis of the LBs.

Date	Instrument	Wavelength (nm)	Time	Spatial Sampling	Size	Cadence
01 May 2007	SOT-BFI	430.5 G band	11:50 - 12:34 UT	0.″11	1024×1024	1 min
01 May 2007	SOT-BFI	396.8 Ca II H	2:00 - 5:00 UT	0.″11	1024×1024	1 min
			11:50 - 12:34 UT	0.″11	1024×1024	1 min
01 May 2007	SOT-SP	630 Fe I	10:46 - 12:25 UT	0.″16 along slit	1000 slit positions	4.8 s at each slit position
29 June 2007	SOT-BFI	430.5 G band	00:33 - 01:38 UT	0.″11	1024×1024	45 sec
29 June 2007	SOT-BFI	396.8 Ca II H	00:35 - 22:59 UT	0.″11	1024×1024	$\sim$ 5 min
29 June 2007	SOT-SP	630 Fe I	01:00 - 01:32 UT	0.″32 along slit	512 slit positions	4.8 s at each slit position
12 July 2007	SOT-BFI	430.5 G band	00:27 - 3:11 UT	0.″11	2048×1024	3 min
12 July 2007	SOT-BFI	396.8 Ca II H	00:30 - 19:39 UT	0.″11	2048×1024	$\sim$ 5 min
12 July 2007	SOT-SP	630 Fe I	03:44 - 04:47 UT	0.″32 along slit	1000 slit positions	4.8 s at each slit position
23 Aug 2007	SOT-BFI	430.5 G band	20:41 - 21:48 UT	0.″11	2048×1024	1 min
23 Aug 2007	SOT-BFI	396.8 Ca II H	13:35 - 23:54 UT	0.″11	2048×1024	$\sim$ 5 min
23 Aug 2007	SOT-SP	630 Fe I	22:00 - 22:32 UT	0.″32 along slit	512 slit positions	4.8 s at each slit position

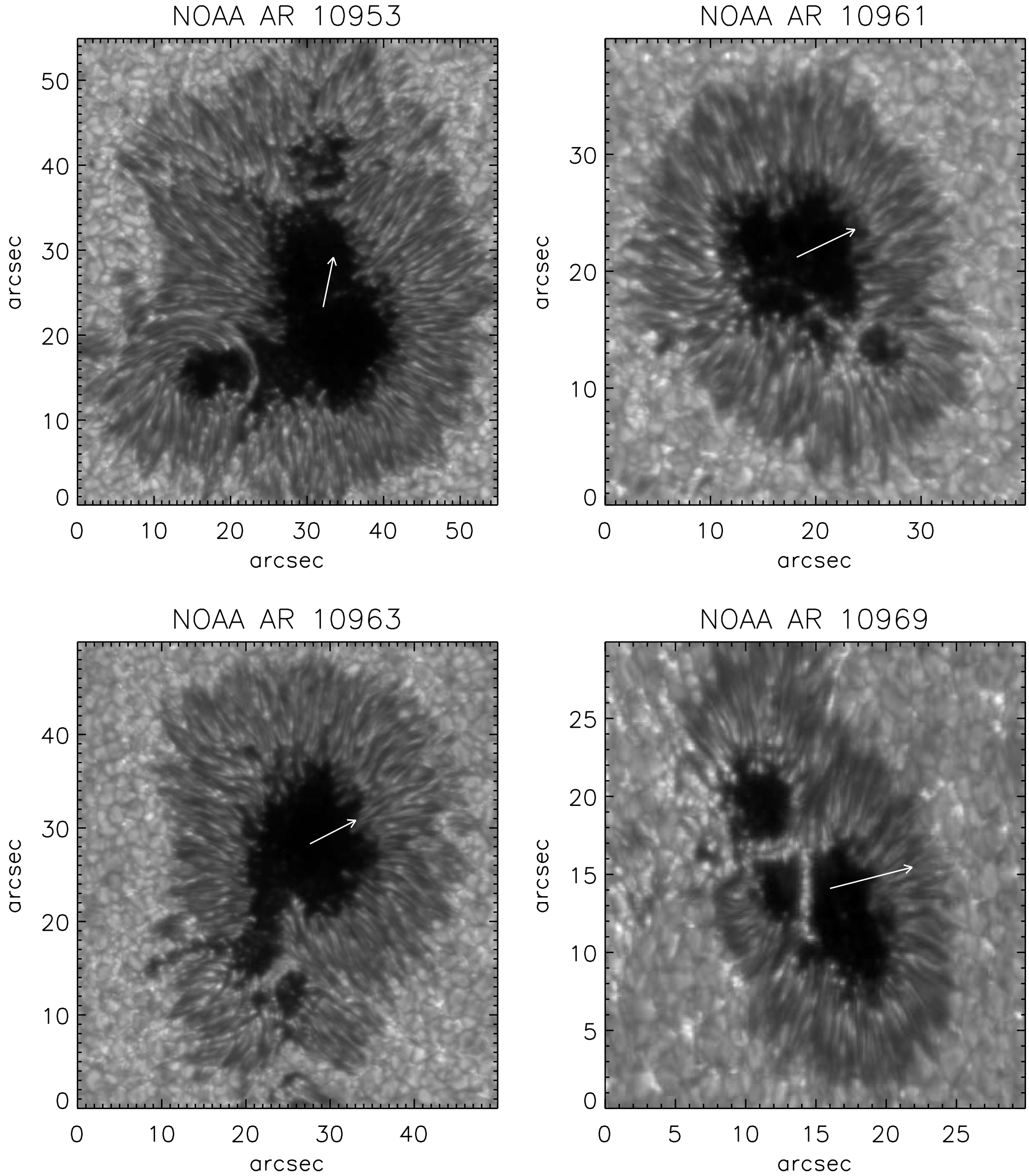

Figure 3.1: The four sunspots observed in the G band, containing one or more LBs. The white arrow points to disk centre.

phenomena arises due to the fact that radiation has to pass through larger layers of the stellar atmosphere due to the oblique viewing angle near the limb (Milne, 1921; Böhm-Vitense, 1997). In addition to limb darkening, geometric foreshortening renders a projected image of the sunspots which is seen when a sunspot traverses the solar disk from the East to West. Both these effects are first removed from the G band filtergrams before making any quantitative estimates of the LB and sunspot properties. I adopted the procedure described by Tan et al. (2009) for the removal of limb darkening. First a calibration line (CL) had to be chosen for each filtergram. This CL, that runs along the horizontal direction or the x-axis of the image, should sample only pure granulation. However, magnetic fields on small scales are present everywhere on the Sun and this is seen as internetwork fields or bright points in the G band which is a temperature sensitive molecular band. Thus, along with the granular intensity fluctuations there will be a number of pixels that have an enhanced intensity arising from the G band bright points or faculae. From the entire image, the CL was chosen for which the rms intensity along it was a minimum. Before computing the rms intensity the mean was subtracted from the overall intensity. The intensity profile from the resulting CL was then plotted as function of μ, where $\mu = \cos\Theta$ (Θ is the heliocentric angle), as shown in the top panel of Figure 3.2 for the sunspot in NOAA AR 10969 observed by *Hinode* on August 23, 2007. A polynomial fit was then carried out to the intensity along the CL using the variable μ. Tan et al. (2009) used a fifth-degree polynomial, whereas I found that the degree had to be changed for the four set of sunspots, because of their relative heliocentric positions. Thus, degrees of 1, 2, 2 and 4 were utilized for the four sunspots respectively which resulted in a successful fit. The resulting intensity was then determined by subtracting the computed intensity as function of μ from the original image. A bias value was then added so that the intensities in the resulting image were positive, as well as close to the observed intensity. The removal of limb darkening is illustrated in the bottom panel of Figure 3.2.

After correcting for the limb darkening, the images were deprojected to compensate the foreshortening effect. Using the standard keywords in the FITS header list that is present in each filtergram, the values ρ and θ were computed for each pixel. These variables correspond to the location of the pixel on the Solar

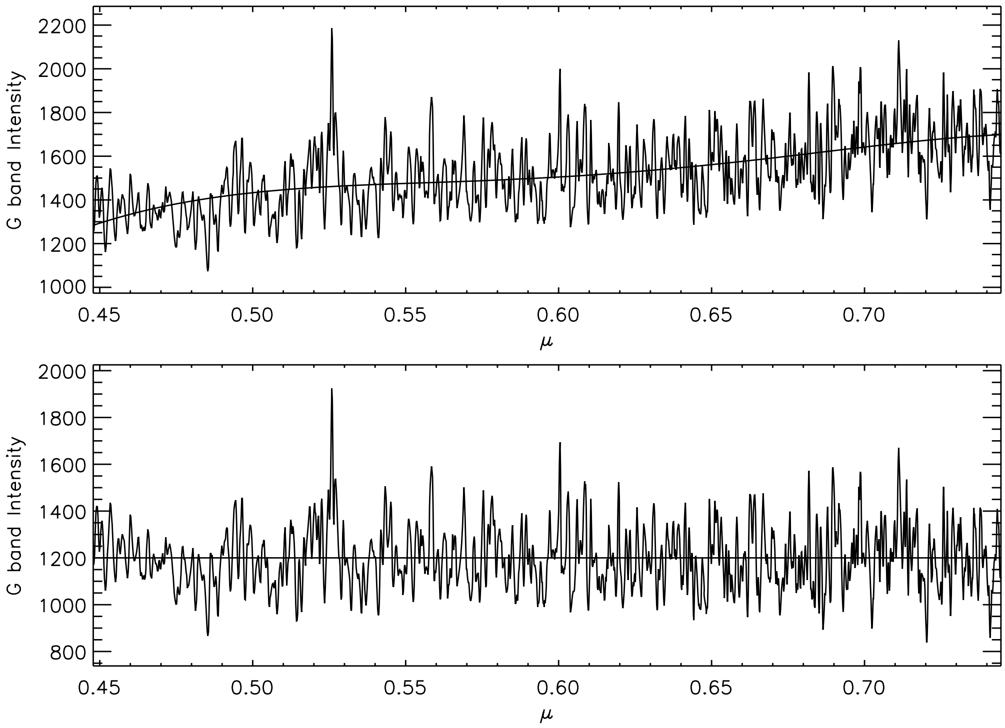

Figure 3.2: Top panel: Observed intensity from the calibration line for sunspot in NOAA AR 10969. The solid line is the fourth-degree polynomial fit to the intensity. **Bottom panel:** Resulting intensity after correcting for limb darkening and the best fit.

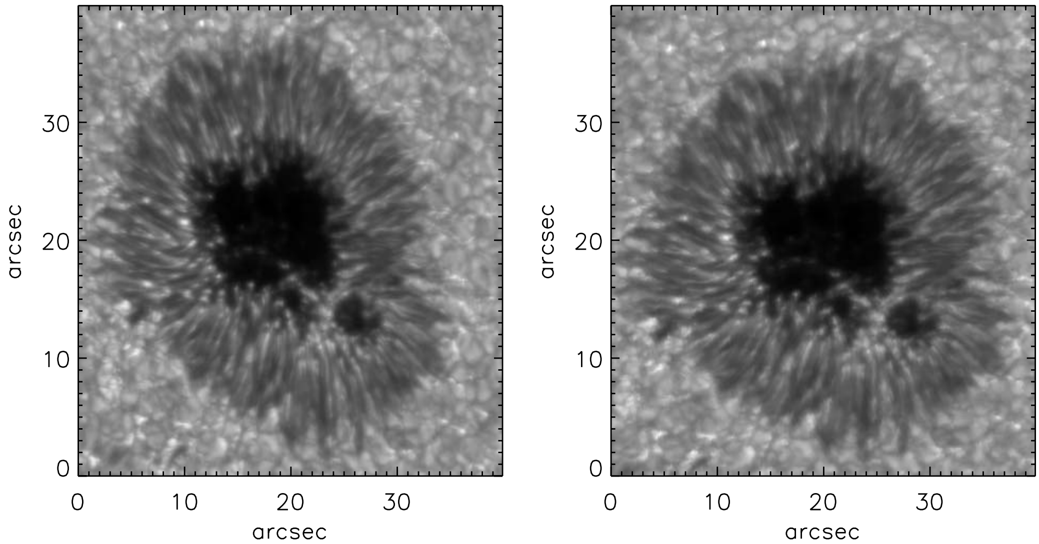

Figure 3.3: Left: Sunspot in NOAA AR 10961 on June 29, 2007. **Right:** Deprojected image of sunspot.

disk, where ρ is the radial distance and θ is the angle measured from the solar north to the line joining the sunspot to disc centre, in the counterclockwise direction. Using the heliographic latitutde (B_0), longitude (L_0) and position angle (P) from the Almanac, the values B and L were determined. The transformation from the image coordinates to the heliographic coordinates was carried out using Eqn. 2 of Gary & Hagyard (1990). Since this transformation will not result in spatial locations that are integral values, the gaps in the resulting image were filled by carrying out an interpolation based on a weighted average (Shepard, 1968). The weighting is a function of the distances of the neighbouring data points to the point where the intensity has to be determined. After trial and error, a search grid of 2×2 pixels centered on the data point was chosen. Figure 3.3 illustrates the resulting deprojection of the sunspot in NOAA AR 10961. The sunspot in NOAA AR 10953 was only corrected for limb darkening and not deprojected as it was very close to disk centre. The corrected filtergrams were then registered using a 2D cross correlation routine.

3.4 General Properties of LBs

After carrying out the basic correction routines, I determined the following quantities for each LB. These were, the length, width, radius of curvature and the area of the sunspot in which the LB existed. The computation of the radius of curvature involved placing an arc of a circle along the axis of the LB and adjusting the radius till the arc became parallel to the LB. Two points were subsequently chosen at the two ends of the LB from which the angle subtended by the LB at its fictitious centre was determined. This angle along with the radius provided the length of the LB. The width of the LBs were determined at two or three locations by taking a cut perpendicular to the axis of the LB. The intensity along the cut was subsequently fitted with a Gaussian whose FWHM (Full Width at Half-Maximum) is used as the width of the LB.

In order to determine the area of the sunspot, the penumbra-photosphere boundary was first computed using the cumulative histogram (Mathew et al., 2007) of the intensity of the sunspot brightness and of the immediately surrounding quiet Sun. The quiet Sun intensity was then used to normalize the image. The boundary was determined as that intensity for which there was a steep rise around unit intensity. Linear fits to the flattest parts of the average histogram were determined. The boundary was chosen at the highest intensity at which the linear fit ceases to be a tangent to the histogram. All pixels lying within the boundary add up to the total area of the sunspot. The above mentioned quantities are summarized in Table 3.2.

3.5 Horizontal Flows in LBs

To measure the horizontal velocities on the light bridges I used Local Correlation Tracking (LCT) on the processed and registered G band images. LCT (November, 1986; November & Simon, 1988; Welsch et al., 2004) is a useful technique to study horizontal motions of tracers such as those of granules and moat flows. The Fourier-based LCT method described by (Fisher & Welsch, 2008) was adopted in this study. The main ingredients in implementing LCT are the width of the Gaussian window and the time interval between successive frames. The technique

Table 3.2: Comparison of general physical properties of the LBs.

Date	NOAA AR	Location	Heliocentric Angle (Θ)	Length (Mm)	Width (Mm)	Radius of Curvature (Mm)	Area of Sunspot (Mm^2)
01 May 2007	10953	E1.7 S7.3	7.5	6.36±0.45	0.66±0.04	4.62±0.32	4691
					0.68±0.04		
					0.85±0.02		
29 Jun 2007	10961	E34.7 S13.7	37	3.47±0.21	0.69±0.07	6.03±0.32	1903
					0.81±0.05		
12 Jul 2007	10963	E21.7 S9.7	23.7	4.97±0.21	1.66±0.09	15.67±0.32	2485
					0.96±0.18		
23 Aug 2007	10969	E51.6 S10.3	52.4	4.43±0.27	0.78±0.11	14.55±0.32	928
					0.74±0.09		
				3.84±0.44	0.66±0.03	24.78±0.32	
					0.80±0.02		

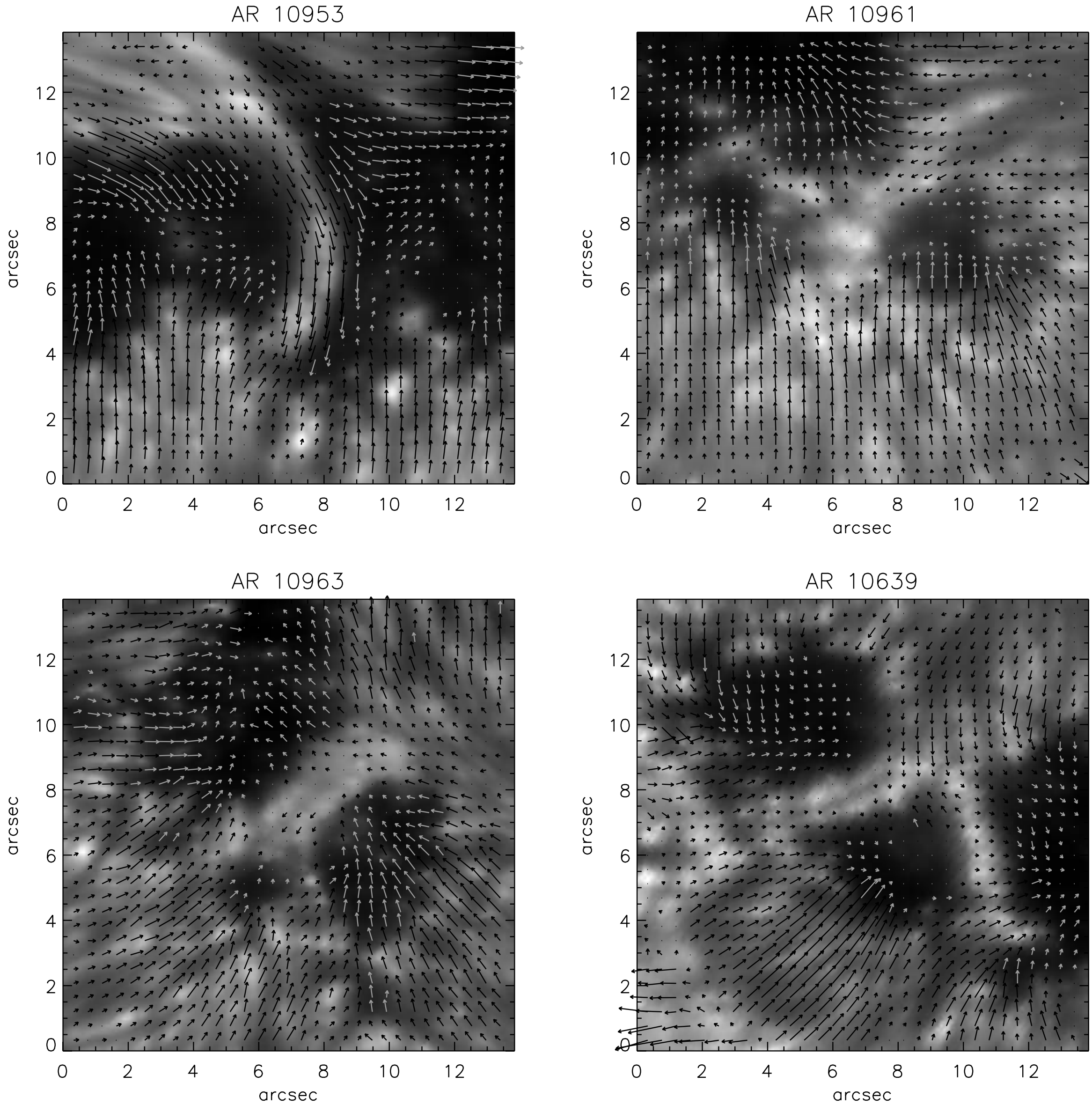

Figure 3.4: Horizontal flows in LBs determined from LCT. The arrows have been drawn for every fourth pixel. The white and black arrows signify pixels with an intensity less than and greater than 500 counts respectively.

involves locating the maximum correlation between two frames, each multiplied by the apodizing window function, centered on a particular pixel, for which the velocity is to be measured. Thus by knowing the shift value between the two frames, the time interval, and the image scale, the velocity can be determined. To track the motion, each frame (128×128 pixels) was smoothed by a $0.''5$ boxcar and subtracted from the original image. This yields the residual fine-scale features to be tracked. After several trials a Gaussian window with a standard deviation of $1''$ and a time interval of 3 minutes was chosen. An average flow map was then computed for the entire series. This was done to determine the steady motions and to remove the transients. The average flow maps for the four LBs are shown in Figure 3.4. The LB in NOAA AR 10953 is characterized by a non-uniform unidirectional flow that starts from the northern end of the penumbra and is directed southwards. The average speeds computed from LCT are ≈ 0.5 km s^{-1}. The other LBs surprisingly do not exhibit any long term flows. In fact, the LBs appear to be the only locations where the velocities are of the order of the estimated error. This could be attributed to the fact that these 3 LBs comprise of granular like structures with the central dark lane seen clearly in NOAA ARs 10963 and 10969. The granular-like cells/grains tend to evolve on time scales of 5-7 min and follow a random pattern during their motion. This would explain why the long term horizontal flow is not seen in these LBs. In order to confirm this scenario I implemented a center tracking algorithm on these small grains as described by Hirzberger et al. (2002) wherein the tracking was carried out automatically.

Each image is subtracted from its smoothed version which yields the isolated bright structures to be tracked. Within a 3×3 pixel area the local maxima is selected if the central pixel is brighter than the rest of the pixels. The grain is tracked in time if its shift in the next frame does not change by more than 1 pixel. Locations of all pixels in the previous and current frame are stored and used for determining the lifetimes and speeds. Figure 3.5 illustrates the tracks with black and gray denoting the start and birth of the grains respectively. The figure shows the tracks for those objects whose lifetimes exceed 5 frames. As expected, the grains do not appear to exhibit any preferred direction of motion and from the distribution of the lifetimes (Figure 3.6), it is evident that the

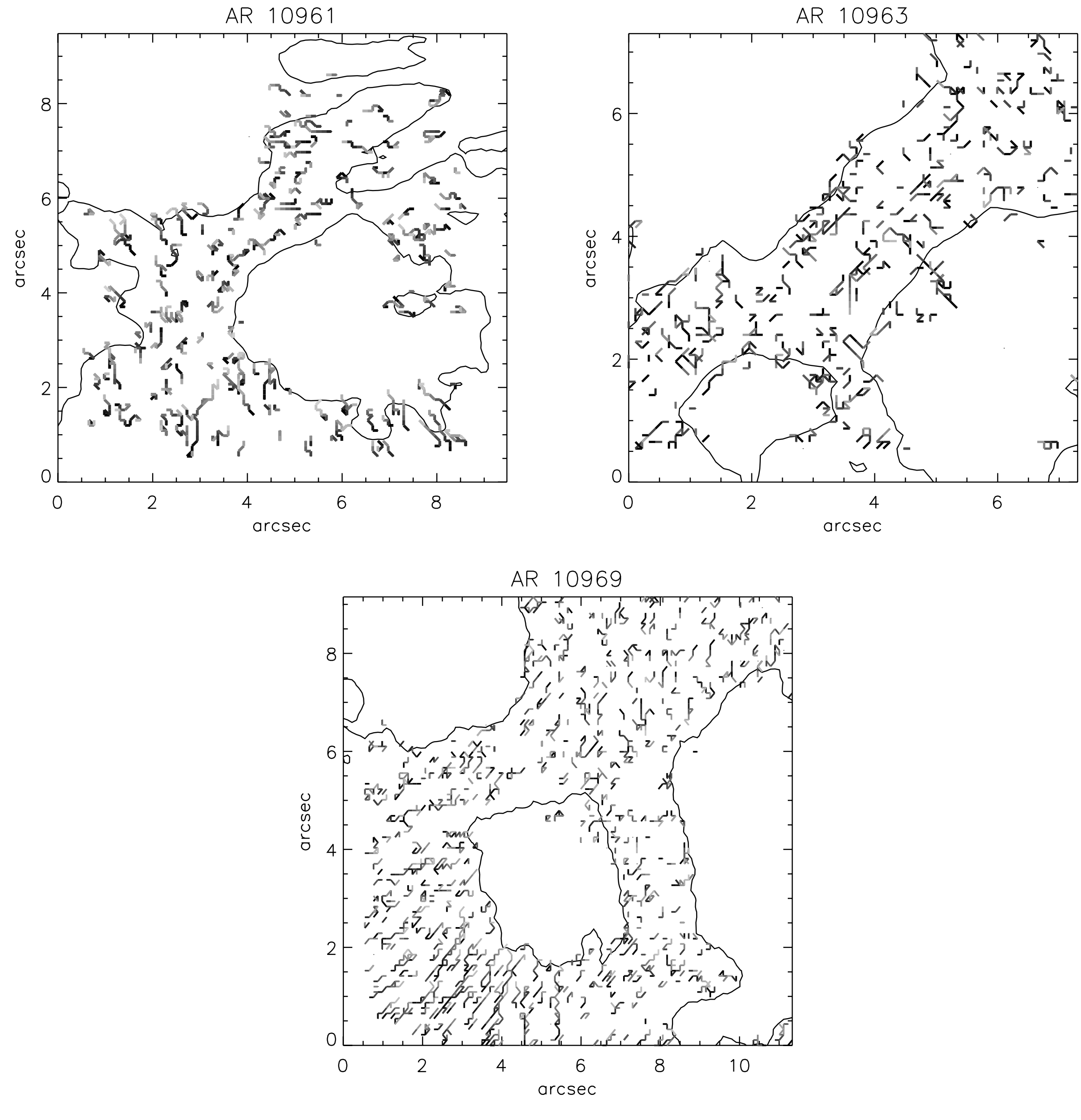

Figure 3.5: Tracks of granular cells identified in each LB. The black and gray colours indicate birth and death of the cells.

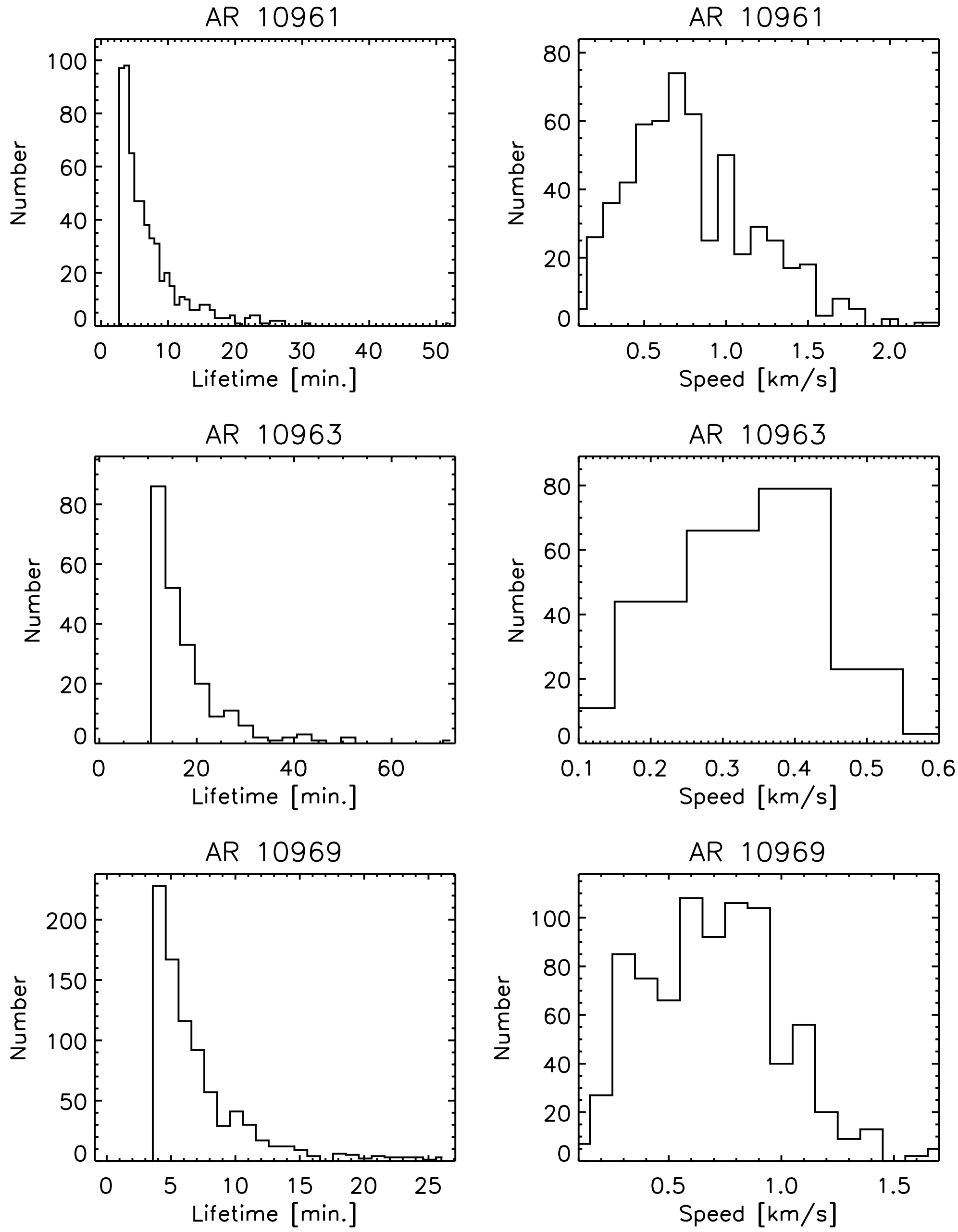

Figure 3.6: Histograms of grain lifetimes (**left**) and average speeds (**right**) for the 3 LBs shown from top to bottom.

Table 3.3: Number of grains for different ranges of the mean relative azimuth.

NOAA AR	No. of grains sorted by mean relative azimuth ϕ (deg)					Total
	$0° \leq \phi \leq 30°$	$30° < \phi \leq 60°$	$60° < \phi \leq 90°$	$90° < \phi \leq 120°$	$\phi > 120°$	
10961	20	75	70	26	3	194
10963	49	64	109	39	100	361
10969	120	160	234	114	47	675

granular cells/grains would not be detected from averaging the speeds computed by LCT. The median lifetimes for ARs 10961, 10963 and 10969 are 6, 18 and 7 min respectively. The average speeds for the 3 LBs are 720, 395 and 730 m s^{-1} respectively. The larger lifetime observed in NOAA AR 10963 is due to the larger time separation between successive frames as well as a relatively smaller number of grains that were identified and tracked. The random walk exhibited by the grains is further illustrated by computing the mean relative azimuth for each bright feature. Using the coordinates in each frame, the successive displacement is determined from which the azimuth or the direction of the displacement vector is calculated. Using the lifetime or the number of frames, the mean relative azimuth is then computed from the running difference of the azimuth values, which is subsequently sorted as shown in Table 3.3. The values of the mean relative azimuth peak around $30° \leq \phi \leq 90°$, as seen from Table 3.3. The large relative azimuths, along with the short lifetimes and irregular paths, render the grains from being detected by LCT. In addition to this, the grains do not reappear from earlier locations which is very similar to the way granules on the quiet Sun evolve, although long term flows are observed in the form of meso and supergranular motions.

3.6 Chromospheric Observations

Figure 3.7 illustrates the excess brightness observed in the Ca II H filtergrams for all the LBs in the four sunspots. The images were chosen by inspection from the entire time sequence to illustrate the magnitude as well as the nature of the chromospheric enhancement. The LB in NOAA AR 10953 is seen to exhibit rapid brightness changes that occur along the LB but also in the form of an arch type enhancement as depicted in the top left panel of Figure 3.7. In fact this enhancement is seen to persist in the mean image constructed from a 3 hr time sequence. The above changes in brightness enhancement are also seen in the root mean square (*rms*) image which depict locations of strong intensity variations on all time scales (Louis et al., 2008). The time sequence of images also shows some of the enhancements traveling along the LB in the same direction as the flow that was determined from LCT, and resembles a cascade effect following a Christmas tree pattern. Such an event is depicted in Figure 3.8 wherein, an enhancement that starts as a jet on the northern entrance of the LB propagates along the LB, downward. During its motion there appears to be a secondary brightening as seen in sequences in 3 and 6 of Figure 3.8. The mean speed of propagation of this strong enhancement is ≈ 4 km s^{-1}. Interestingly, there exist several bright thread like brightenings that appear to connect to the LB from the adjacent umbra, with brightenings traveling along such structures as well. The enhancements are also persistent and were observed on April 29 and 30 (Shimizu et al., 2009) and continued upto the end of May 1.

While brightness enhancements are seen in the other LBs too, they seem to confined to localized regions within the LBs. There also does not appear to be any signature of brightenings in the adjacent umbra that reach or connect to the LB as was seen in NOAA AR 10953. In NOAA AR 10961 however, there is a strong enhancement that is almost aligned with the axis of the LB starting from the nearby penumbra where the LB is attached. In particular this enhancement is seen to occupy or engulf the entire span/length of the LB. The LB in NOAA AR 10963 changes dramatically over a period of 20 hrs. This is seen as a continuous readjustment of the point of anchoring of the LB with the penumbra with the presence of two arms around 5:45 UT. One of them gradually retracts leaving a

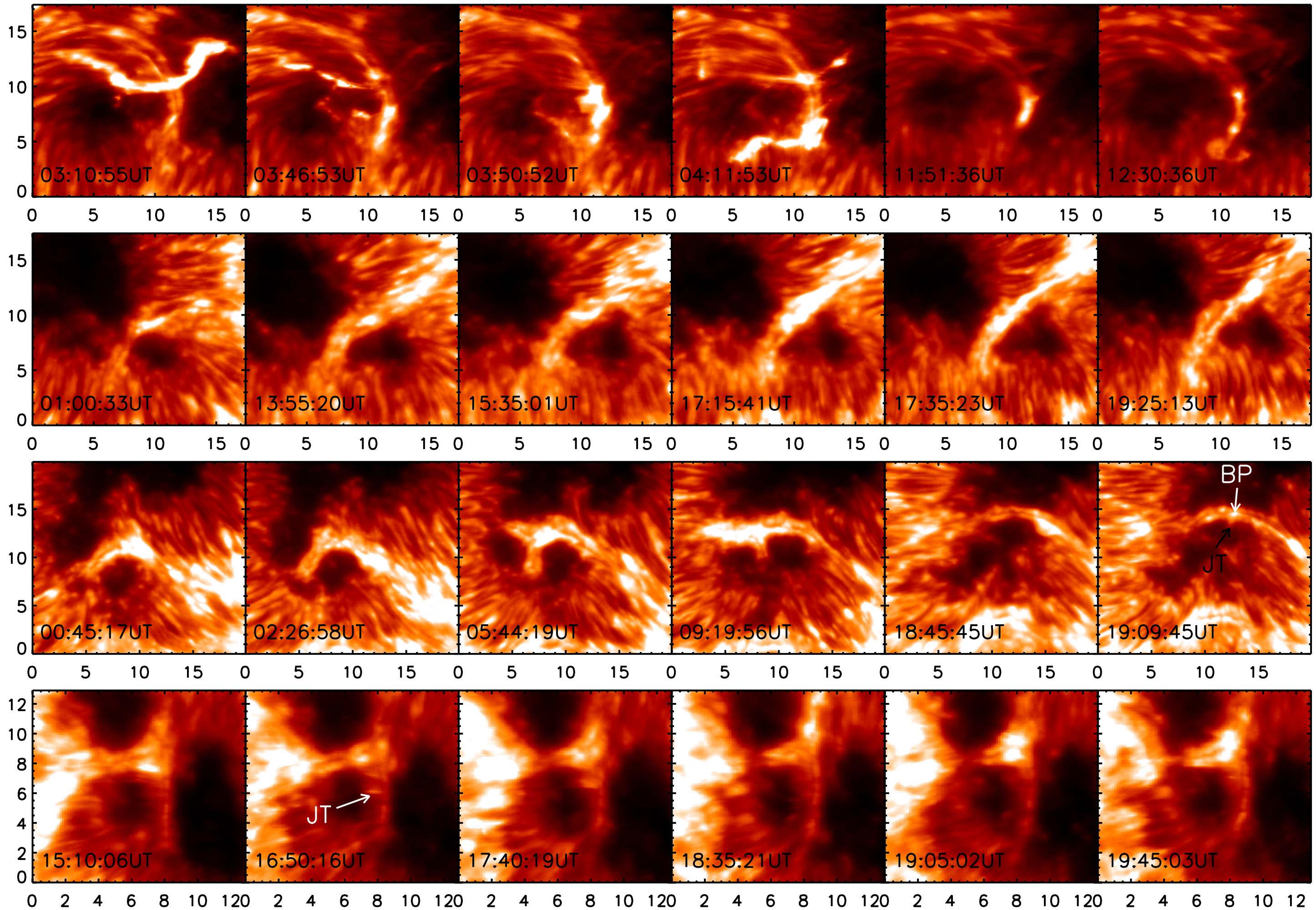

Figure 3.7: Top to Bottom: Ca II H images of the four LBs at different instances of time shown from left to right. **JT** - Jet like brightening, is shown in the right most column of the third row and in the second column from the left of the bottom most row. **BP** - Bright Patch close to the jet like feature. All images have been normalized to the quiet Sun intensity and saturated to the same intensity level.

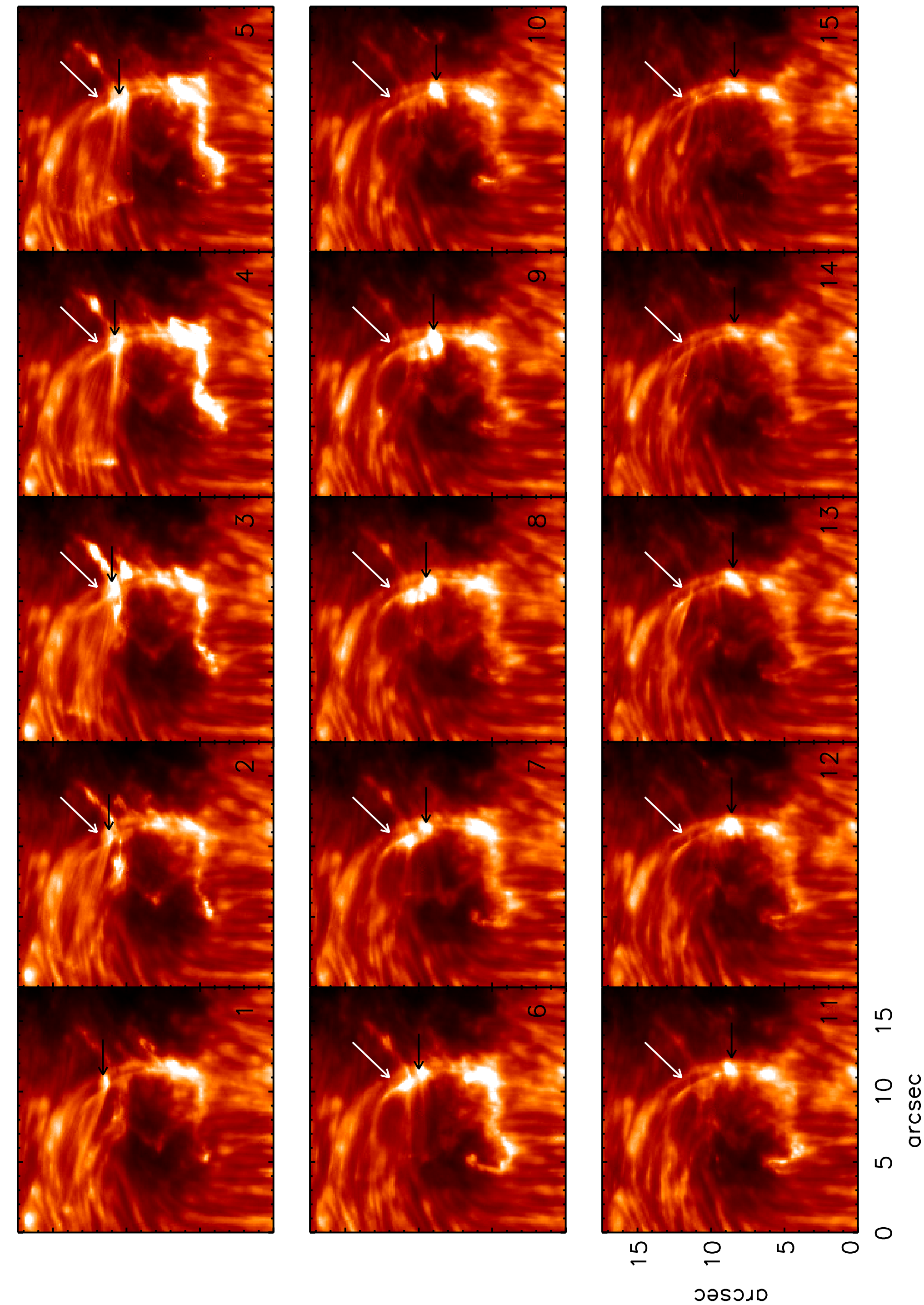

Figure 3.8: Ca II H time sequences starting at 4:08 UT illustrating the propagation of a brightness enhancement along the LB in NOAA AR 10953. The white and black arrow depict the brightness enhancement at the start of the sequence and during its motion respectively.

much more slender LB with both ends connected to either side of the umbra. In the early phase when the LB was broader with a more complex geometry, the brightness enhancements are seen in localized regions which do not appear to be connected elsewhere on the sunspot. In the latter half of the sequence the brightenings are much more subdued with instances of brightening seen near the penumbra where one end of the LB is connected. Very small jagged structures (JT, marked with the black arrow) are seen along the length of LB oriented nearly perpendicular to the axis of the LB, with one of them associated with a tiny bright feature (BP, marked with the white arrow) and are shown in the right most panel in the 3rd row of Figure 3.7. The chromosphere of NOAA AR 10969 appears to be brighter near the common point where the two LBs are connected to one another. While enhancements are predominantly seen at this location, there is noticeable chromospheric activity near the upper LB, while the lower one has similar jagged-like brightenings (JT) as seen in NOAA AR 10963. In this AR too, there do not appear to be any strong enhancements in the adjacent umbra that connect to either LB. In comparison to ARs 10953 and 10961, the chromosphere above the LBs in 10963 and 10969 is relatively subdued although isolated events of very strong enhancements that are extremely short lived might have been missed because of the longer cadence. Furthermore, the lifetime of the chromospheric events never exceeds 5 minutes with short lived ones lasting a single frame, while the mean lifetime is $\approx$ 1-2 min.

3.7 Magnetograms from the far line-wing positions

The spectropolarimetric observations by *Hinode* comprise of spectra of the four Stokes profiles at each slit position. The slit was subsequently incremented and in the process mapped the entire active region. In this Section, I illustrate how the magnetic and velocity inhomogeneities can be extracted for the four LBs using the Stokes V profile. Stokes V, is the difference of the right- and left-circularly polarized signals which conveys information on the LOS component of the magnetic field. In the weak field approximation, the ratio of the Stokes V and I is proportional to the LOS magnetic field. The normal V profile consists of two anti-symmetric lobes with the zero crossing value being a measure of the LOS velocity of the magnetized component. While Stokes I is affected by both magnetized and non-magnetized flows, Stokes V on the other hand reflects magnetized flows alone. Another useful diagnostic of the V profile, is the area asymmetry, referred to as the net circular polarization. The area asymmetry is defined as

$$\delta A = \frac{|A_b| - |A_r|}{|A_b| + |A_r|} \tag{3.1}$$

following Leka & Steiner (2001). A_b and A_r refer to the area under the blue and red lobe respectively. Solanki & Montavon (1993) showed that

$$\mathrm{sign}(\delta A) = \mathrm{sign}\left(-\frac{d|B|}{d\tau}.\frac{dv_{los}}{d\tau}\right) \tag{3.2}$$

$$\mathrm{sign}(\delta A) = \mathrm{sign}\left(-\frac{d|\cos\gamma|}{d\tau}.\frac{dv_{los}}{d\tau}\right) \tag{3.3}$$

wherein a non-zero area asymmetry is an indication of gradients in the magnetic field strength and LOS velocity, or inclination and LOS velocity. The complexity of the V profile increases when there are unresolved magnetic structures that have different velocity components. This property can be used to probe magnetic and velocity inhomogeneities. I constructed magnetograms at different positions in the blue and red wing of the V profile, moving outwards from the line centre, for the region of the sunspot containing the LB. This procedure is similar to that described by Ichimoto et al. (2007a) to detect the sources and sinks of the Evershed Flow. Before constructing the magnetograms, the initial wavelength for each data set was determined. All pixels for which the ratio of the total polarization to the intensity was less than 3 times the noise level (0.3 %) were averaged to yield the quiet Sun profile. Using the spectral sampling of 21.5mÅ and the rest wavelength of the 6302.5Å line, the starting wavelength was determined. I chose the second iron line because it forms in the lower half of the photosphere. The average quiet Sun profile for the four sunspots is shown in Figure 3.9. Since the V signal can only be extracted from integral pixel locations, there will be an offset from the line center position to the immediate neighbouring pixel. These offsets are -116, 47, 47 and 163 m s^{-1} for the four sunspots respectively. Here the negative sign indicates blue shifts. Magnetograms were derived from pixels 10 to

14 from the line center on the red and blue wing and are shown in Figures 3.10 and 3.11 respectively. A shift of 1 pixel is equivalent to 1.02 km s^{-1}.

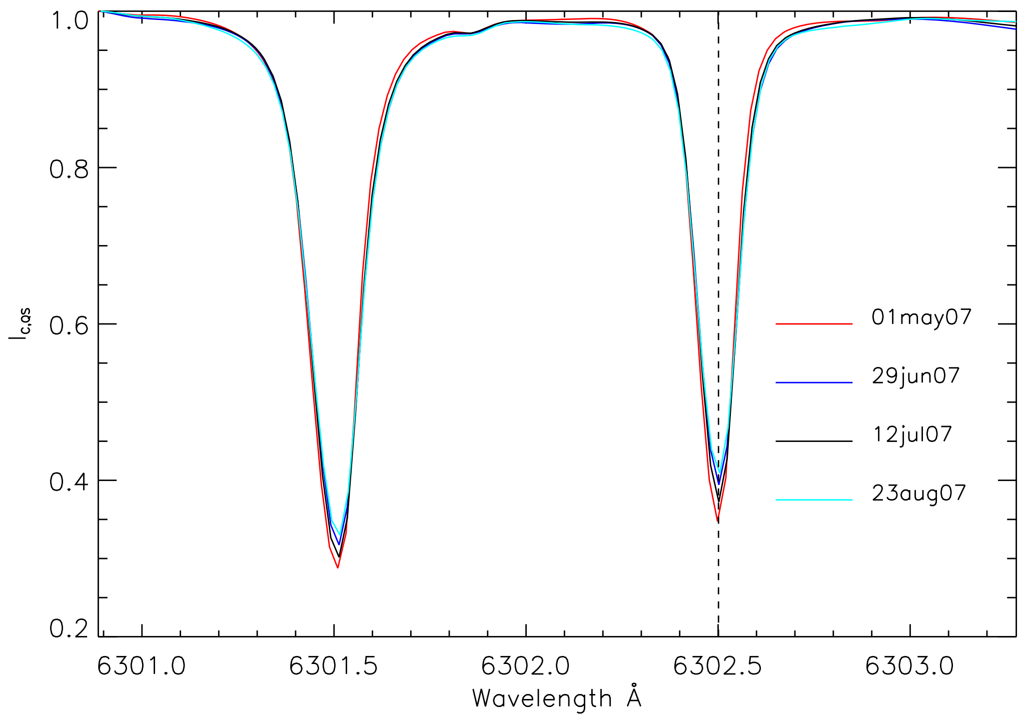

Figure 3.9: Average quiet Sun profiles for the four days shown in different colours which have been normalized to unity. The vertical dashed line denotes the rest wavelength of the iron 6302.5 Å line.

Blue wing magnetograms of NOAA AR 10953 show a relatively strong positive signal of ≈ 2% close to the entrance of the LB, with the V signal resembling a Q or U profile. Moreover, this patch is seen predominantly in pixels 10 and 11 from the line center position, becoming weaker as one moves to longer wavelengths. A small isolated region of positive polarity is seen in one of the two LBs in NOAA AR 10969 near the western edge with signals of ≈ 5%. The presence of positive signals in the far blue wings is suggestive of a second component in the resolution element of opposite polarity to that of the sunspot. Furthermore, the far blue wing magnetograms do not indicate any strong negative signal in all the LBs, in the event of the blue lobe of the V profile having a secondary lobe, or extended wings. The conspicuous patch of negative V signal at wavelength positions 10 and 11 in NOAA AR 10961 in the penumbra has a magnitude of ≈ 10%.

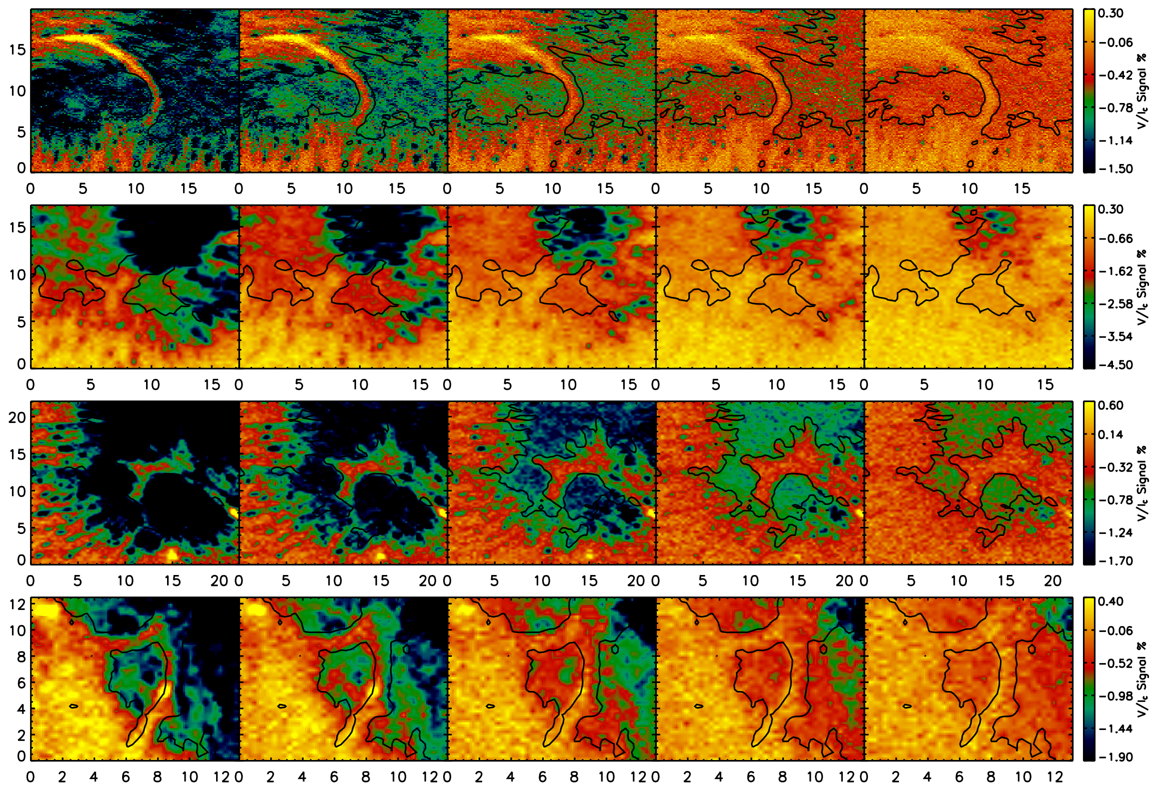

Figure 3.10: Magnetograms constructed at different positions on the blue wing of the Fe 6302.5Å line. **Left to right:** Wavelength positions 10 to 14 from line center. **Top to Bottom:** NOAA ARs 10953, 10961, 10963, 10969. The black contour denotes the continuum intensity. The images have been scaled as shown in the colour bar.

The red wing magnetograms show a very interesting feature on the LB in NOAA AR 10953. There are localized patches of very high positive signal that is not seen anywhere else in the vicinity of the LB. These patches are seen even in the far wavelength positions of 13 and 14 from the line center. In addition, the entrance of the LB consists of two localized patches of negative signal that are close to the positive signal patch that was seen in the blue wing magnetogram. Although strong signals are seen in the other LBs, with values of $\approx 9\%$ seen in NOAA AR 10961, they are not seen beyond pixels 11 from the line center. The strong patches seen in wavelength positions 12 for NOAA AR 10953, 10961 and 10963 and marked in white arrows in Figure 3.11, and measure $\approx 9\%$, 5% and

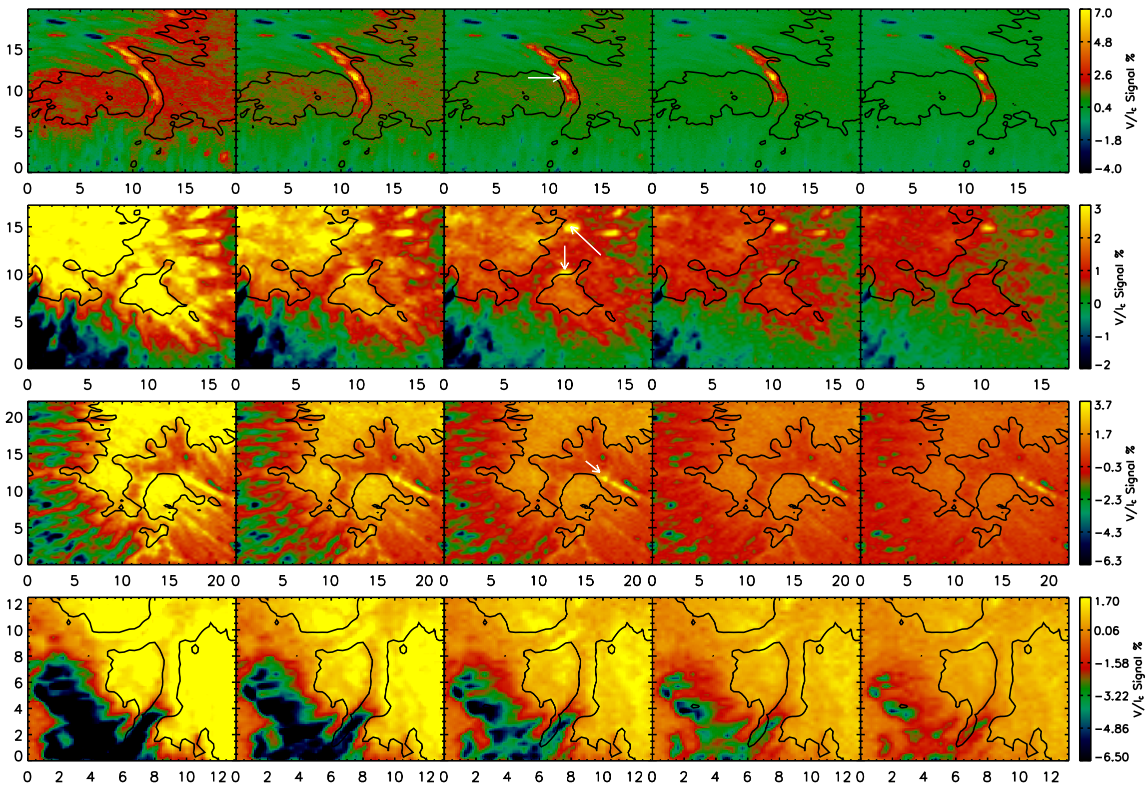

Figure 3.11: Same as Figure 3.10 but for different positions on the red wing of the Fe 6302.5Å line. The white arrows marked in the central column denote positive V signals measuring $\approx$ 9%, 5% and 4 % for NOAA ARs 10953, 10961 and 10963 respectively.

4% respectively. The difference between the signals seen in NOAA AR 10953 and the rest, is that the former has two distinct lobes in the red wing while the latter comprise of extended red wings at this range of wavelength. This aspect of the peculiar Stokes profiles in NOAA AR 10953 is dealt with in more detail in the following chapter.

3.8 Summary and Discussion

High resolution photospheric and chromospheric observations of a set of four sunspot light bridges (LBs) observed by *Hinode* are presented in this chapter. The observations comprise filtergrams taken in the G band and Ca II H line as well as Stokes spectra of the neutral Fe line pair at 630 nm. The G band filtergrams were corrected for limb darkening as well as projection effects and were subsequently co-aligned. These processed filtergrams were used to derive physical characteristics of the LBs, namely their length, width and radius of curvature. The LB in NOAA AR 10953 was observed to have the maximum length and minimum radius of curvature in comparison to the others. The sunspot in NOAA AR 10953 also was the largest amongst the four and was located close to the disc centre.

The corrected and registered time sequence of G band images of LBs in the four ARs were then subjected to LCT to derive the horizontal motion of intensity features. While the LB in NOAA AR 10953 was seen to exhibit a unidirectional non-uniform flow measuring $\approx$ 500 m s^{-1}, the other LBs did not show any indication of coherent long term flows. In order to verify the absence of a long term flow in the remaining LBs, a centre tracking algorithm was implemented to trace the motion of individual bright features/grains. The grains appear to follow an irregular trajectory in the LB with median lifetimes and velocities of $\approx$ 6 min and 700 m s^{-1} respectively for the LBs in NOAA AR 10961 and 10969. The corresponding values for the LB in NOAA AR 10963 are 13 min and 350 m s^{-1} owing to the longer cadence. The nature of the trajectories is also reflected in the mean relative azimuths which vary from 30° and 90°. The individual features do not reappear at previous locations of emergence which is similar to the behaviour of granules.

Chromospheric observations made in the Ca II H line show brightness enhancements in all the LBs although the magnitude and frequency of these phenomena vary from one to the other. Of the four LBs, the one in NOAA AR 10953 exhibits very strong and a highly complex set of brightenings which last for three days. The typical lifetimes of these enhancements vary from 1-2 min and never exceed 5 minutes. Some events last a single frame which suggest that a cadence of less than a minute is required to track the phenomena from start to finish. The chromospheric activity is observed in the form of an arch-type brightening that spans across the LB; as brightness fronts which propagate along the LB, occasionally leading to secondary enhancements; as localized enhancements which are directed along the axis of the LB and as tiny jets along the length of the LB which are oriented nearly perpendicular to the axis of the LB.

The set of Stokes profiles acquired by the spectropolarimeter on board *Hinode* was used to construct magnetograms of the LBs, from the far blue and red wing of the Stokes V signal which served as a useful diagnostic to detect small scale magnetic and velocity inhomogeneities. It is observed that there are extended regions in the vicinity of the LB in NOAA AR 10953 wherein the Stokes V signal resembles a linear polarization profile thereby producing a positive signal of $\approx$ 2% at -215 mÅ from the line centre of the Fe 6302.5Å line. For a negative polarity sunspot this profile is suggestive of a secondary unresolved component that has a polarity opposite to that of the sunspot. This feature in the blue wing is not seen in the other LBs, except for one of the LBs in NOAA AR 10969 wherein the positive V signals are confined to a very small region. The blue wing magnetograms far from line centre, however do not exhibit any strong negative signal in any of the LBs studied here. The far red wing magnetograms of NOAA AR 10953 display patches of positive polarity even at wavelength positions 13 and 14 while, a relatively weaker patch of a similar kind is seen in the other LBs, although they do not persist beyond wavelength positions 11.

The chromospheric brightness enhancements seen from the Ca II H filtergrams appears to be a common attribute of sunspot LBs and not necessarily confined to any specific kind of LB, namely photospheric or penumbral. These enhancements exceed the quiet Sun intensity by more than 50% which is significantly large given its proximity to the sunspot umbra. On the other hand, the detection of magnetic and velocity inhomogeneities on all the LBs has been possible due to the high resolution and stable operation of *Hinode*. While the magnetograms discussed in this chapter are insufficient to quantify the magnetic field vector and its stratification, it is apparent that one can qualitatively derive certain salient aspects of the magnetic nature of the LBs. The Stokes V signal is a measure of the LOS component of the magnetic field. In the case of NOAA AR 10953, which is fairly close to disc centre this is equivalent to the vertical component of the magnetic field. The existence of circular polarization signals on the LB, measuring nearly

8% at 301 mÅ from the line centre is suggestive of relatively[1] vertical and/or strong fields. In addition, the proximity of the sunspot to disc centre implies that the polarization signals emanate from deeper layers in the photosphere while for sunspots far from disc centre one samples higher layers. This is in contrast to the notion that LBs are weak field domains in the sunspot which harbor inclined fields. At the same time, linear polarization signals measuring greater than 10% are also present on the LB, which would point to relatively inclined fields. The fact that circular polarization signals are observed at this range of the line profile points to unresolved components within the pixel and/or strong gradients in the physical parameters along LOS. Furthermore, the presence of strong regular linear and anomalous circular polarization profiles makes the magnetic geometry of LB that much more complex. In comparison to NOAA AR 10953, the V signal in the other LBs is actually due to relatively inclined fields as these sunspots are located at fairly large heliocentric angles as is the case with NOAA ARs 10961 and 10969. Moreover, the amplitude and extent of the V signal is far smaller than the one seen in NOAA AR 10953. Nevertheless, the spectral characteristics seen from the magnetograms are evidence that small scale variations in the magnetic field and LOS velocity occur in LBs which was not reported earlier. One could speculate that these small scale variations could be related to the observed chromospheric activity which is investigated in the following chapter for NOAA AR 10953. The strong localized enhancements, which are more intense than the microjets that are ubiquitous in the penumbra (Katsukawa et al., 2007b), could play an important role in heating the lower chromosphere directly above sunspots. This could differentiate the observed chromospheric activity in one LB from another. The nature and extent of these small scale photospheric inhomogeneities needs to investigated with further spectropolarimetric observations of LBs taken in normal mapping mode by *Hinode* close to disc centre.

[1] I use the terms relatively vertical or horizontal with respect to the umbral fields which we know is vertical close to the centre of the spot and is inclined at $\approx 40°$ at the umbra-penumbra boundary

Chapter 4

Detailed Investigation of a Chromospherically Active Sunspot Light Bridge

4.1 Introduction

In the previous chapter, photospheric and chromospheric observations of a number of sunspot light bridges (LBs) were presented. Of all the cases, the LB in NOAA AR 10953, and in particular the penumbral LB, exhibited persistent brightness enhancements as seen from the Ca II H filtergrams, that lasted for nearly three days. In addition, magnetograms constructed in the far red wings showed a significant polarization signal over the LB which is a strong indication of velocity and magnetic inhomogeneities present within the resolution element. These results already point to a strong association of the magnetic field in the photosphere to the chromospheric activity over the LB. Although this has been suggested by some authors in the past (Berger & Berdyugina, 2003; Jurčák et al., 2006), simultaneous vector magnetic field measurements in the photosphere are necessary to diagnose these events. Furthermore, it is the magnetic field in the photosphere that determines the nature of a LB, which is perceived as a field-free intrusion in a gappy umbral field (Parker, 1979; Choudhuri, 1986) or manifestation of magneto-convection (Rimmele, 1997, 2004).

High resolution *Hinode* observations by Katsukawa et al. (2007a) illustrate the formation of a light bridge by several umbral dots emerging from the leading edges of penumbral filaments, and rapidly intruding into the umbra. The extent of the filament intrusion into the umbra was measured to be around 4000 km with a large number of umbral dots populating the neighborhood of the intruding LB. They however, did not find any substantial weakening in the magnetic field during/after the LB formation nor a large change in the field inclination. The intrusion of the penumbral filaments, they propose, is facilitated by the motion of umbral dots thereby weakening the adjacent umbral field. Their observations illustrate a strong association of umbral dots and the newly formed LB.

In this chapter high resolution spectropolarimetric and filtergram observations are employed to i) investigate the photospheric inhomogeneities in the LB in NOAA AR 10953 and their relationship to the chromospheric activity and ii) ascertain the phototmetric changes associated with evolution of the LB. To that extent the magnetic and kinematic structure of the LB was determined at two instances on the same day. The second set of observations were made just before the LB fragmented which was useful to determine the change in the spectral characteristics in the LB and its vicinity. Photospheric and chromospheric filtergrams taken in the G band and Ca II H line respectively, were utilized to evaluate the effect of the evolution of the LB on the photometric brightness in the photosphere as well as in the chromosphere. The vector magnetic field along with the chromospheric filtergrams at very high spatial resolution reveal for the first time, patches of supersonic downflows in the LB as well as at the umbral-penumbral boundary that lie close to the LB. Some of the strong downflows are co-spatial with chromospheric brightness enhancements while others lie in the immediate neighborhood of the enhancements. The rest of this chapter is organized as follows. Section 4.2 describes the data acquired from various instruments on-board *Hinode*. The spectropolarimetric scans were subsequently used to derive maps of physical parameters that are presented in Section 4.3.1. The strong downflows and magnetic inhomogeneities in the LB are described in Sections 4.3.2 while the implication of the presence of anomalous Stokes profiles on the LB are presented in Section 4.3.3. A comparison of the chromospheric activity during the evolution of the LB and its association with the downflows is described in Section 4.3.4. Section 4.3.5 illustrates the photometric change in the photosphere and chromosphere as the LB evolves. The decaying phase of the LB is depicted in Sections 4.3.6 and the results are subsequently summarized in Section 4.4.

4.2 Observations

On 2007 May 1, the leading spot of NOAA AR 10953 was observed with *Hinode* (Kosugi et al., 2007). Between 10:46 and 12:25 UT, the *Hinode* spectropolarimeter (SP; Lites et al., 2001; Ichimoto et al., 2008; Tsuneta et al., 2008) recorded the four Stokes profiles of the iron lines at 630 nm with a spectral sampling of 21.55 mÅ, a pixel size of 0.″16, and an exposure time of 4.8 s per slit position (normal map mode). A similar scan in the normal map mode was carried out by the spectropolarimeter from 21:00 to 22:24 UT. The sunspot was located close to disk-centre at S07E0.7 and S07W04 during the two scans respectively. The corresponding heliocentric angles were 7° and 8° respectively. These observations were corrected for dark current, flat field, thermal flexures and instrumental polarization using routines included in the SolarSoft package. The two SP scans will be hereafter referred to as SP1 and SP2 respectively. The Broadband Filter Imager (BFI) of *Hinode* took Ca II H and G band filtergrams with a cadence of 1 minute to monitor the chromosphere and photosphere of the LB. The effective pixel size of the filtergrams is 0.″11. The filtergrams were subsequently registered using a 2-D cross correlation routine. Due to the unavailability of data from the BFI during SP2, filtergrams acquired $\approx$ 1 hr before and after the scan were utilized. Table 4.1 summarizes the data used for the analysis in this chapter.

4.3 Results

4.3.1 Magnetic Configuration of LB and its Neighbourhood

Figure 4.1 shows a continuum map of the spot and the LB taken during SP1 and SP2. While the LB is intact and anchored at both ends in the penumbra during the time of SP1, it appears to have disintegrated at the lower end and retreating towards the north, during the time of SP2. The distance of separation of the lower end of the LB from the penumbra is $\approx$ 2400 km measured at the time of

Table 4.1: Details of the data used in the analysis of the light bridge.

Date	Instrument	Wavelength (nm)	Time	Spatial Sampling (arcsec)	Size	Cadence
01 May 2007	SOT-SP	630 Fe I	10:46 - 12:25 UT	0.″16 along slit	1000 slit positions	4.8 s at each slit position
01 May 2007	SOT-BFI	396.8 Ca II H	11:50 - 12:34 UT	0.″11	1024×1024	1 min.
01 May 2007	SOT-BFI	430.5 G band	11:50 - 12:34 UT	0.″11	1024×1024	1 min.
01 May 2007	SOT-SP	630 Fe I	21:00 - 22:24 UT	0.″16 along slit	1000 slit positions	4.8 s at each slit position
01 May 2007	SOT-BFI	396.8 Ca II H	20:00 - 20:58 UT	0.″11	1024×1024	1 min.
01 May 2007	SOT-BFI	430.5 G band	20:00 - 20:58 UT	0.″11	1024×1024	1 min.
01 May 2007	SOT-BFI	396.8 Ca II H	23:00 - 23:54 UT	0.″11	1024×1024	1 min.
01 May 2007	SOT-BFI	430.5 G band	23:00 - 23:54 UT	0.″11	1024×1024	1 min.

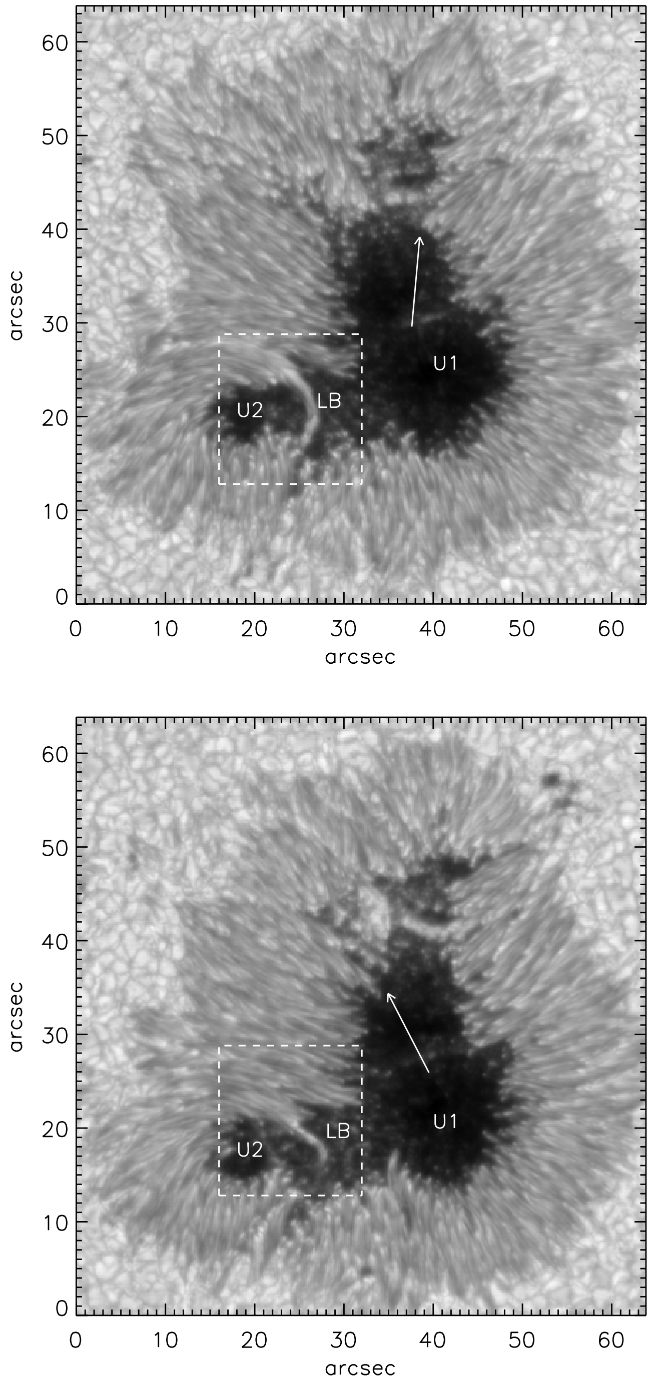

Figure 4.1: Continuum image of NOAA AR 10953 at 630 nm taken during SP1 (**top**) and SP2 (**bottom**). The white box represents the region containing the light bridge (LB), while U1 and U2 are the sunspot umbrae adjacent to the LB. North is up and West to the right. The arrow indicates the direction to disk center.

the second scan. A maximum retreating speed of 700 m s^{-1} is estimated from the time duration between the last available filtergram and the second SP scan. The continuum images at the two instances indicate that the LB is at different stages of evolution and it is imperative to derive the changes in the magnetic and kinematic parameters during these instances.

The observed Stokes profiles recorded from the two scans were inverted using the SIR code (Stokes Inversion based on Response Functions; Ruiz Cobo & del Toro Iniesta, 1992). SIR computes perturbations in the physical quantities at specific locations across the optical depth grid called *nodes*, and then carries out an interpolation to yield values at all grid points. To determine the global structure of the LB and the surroundings, I performed a one-component inversion setting the magnetic and dynamic parameters to be constant with depth. The temperature stratification was perturbed with two nodes. A total of 9 parameters were retrieved from the observed profiles, including height-independent micro- and macro-turbulent velocities and a stray-light factor.

The three components of the vector magnetic field (strength, inclination, and azimuth) deduced from the inversion of SP1 and SP2 are shown in Figures 4.2 and 4.3. All the angles are expressed in the local reference frame after a manual disambiguation of the line-of-sight (LOS) azimuths. As can be seen, the LB is characterized by weaker and more inclined fields than the umbra. This confirms earlier results by, e.g., Leka (1997) and Jurčák et al. (2006). Interestingly the LB shows very small, localized regions of extremely weak fields which are < 700 G. This is illustrated as the dark blue colour on the LB in the field strength maps of Figures 4.2 and 4.3. As shown in Figure 4.2, this weak field region appears to be concentrated at the lower end of the LB, while they are more diffuse and are seen towards the central part, close to the eastern edge, as depicted in Figure 4.3. The inclination maps for the two observations show a deeper intrusion of highly inclined fields in the former while it is less conspicuous in the latter.

The transverse magnetic field changes dramatically over the 10 hr period. Initially, the magnetic field is parallel to the axis of the bridge, in the upper half of the LB. Both photometrically and magnetically, the LB looks like an extension of the penumbra protruding into the umbra. Louis et al. (2008) detected a horizontal flow along the LB that starts in the adjacent penumbra, demonstrating that the

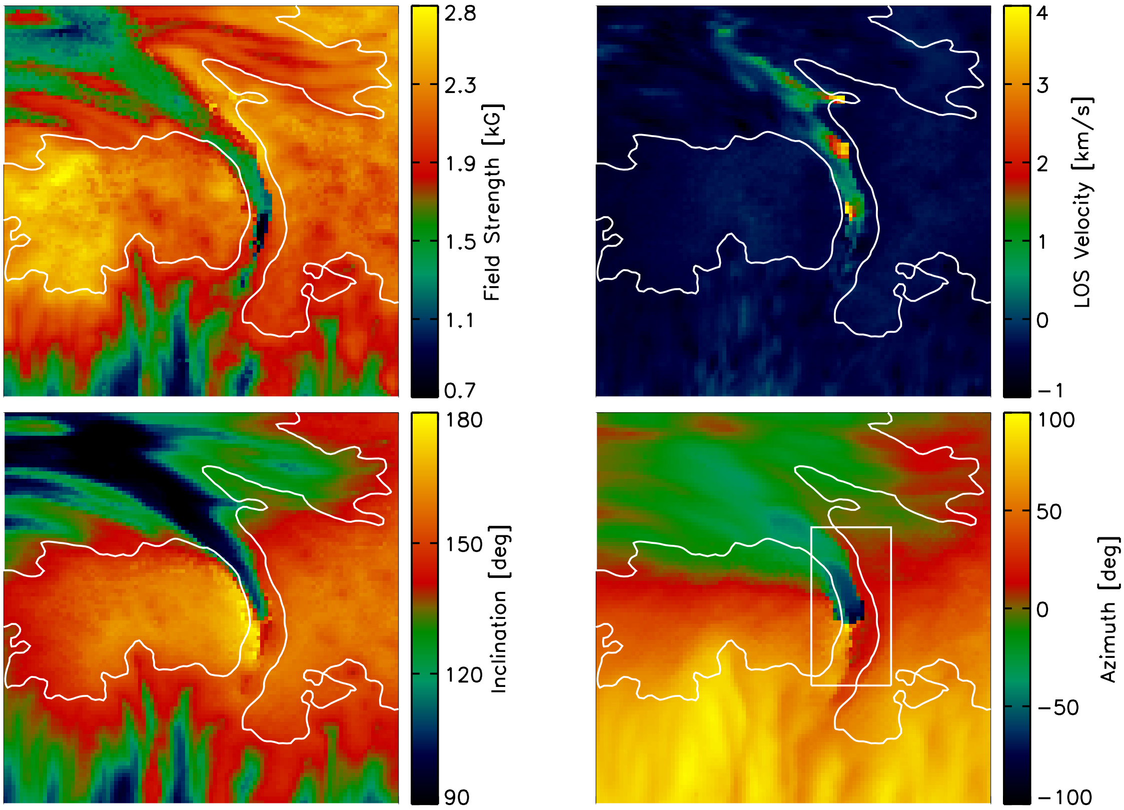

Figure 4.2: Anticlockwise from top left: Magnetic field strength, field inclination, field azimuth, and LOS velocity in the $16'' \times 16''$ sub-region containing the LB, as deduced from the inversion of SP1. The angles are expressed in the local reference frame. Azimuths increase counterclockwise, with zero representing fields pointing to solar West. Positive velocities indicate redshifts. The mean umbral velocity is zero.

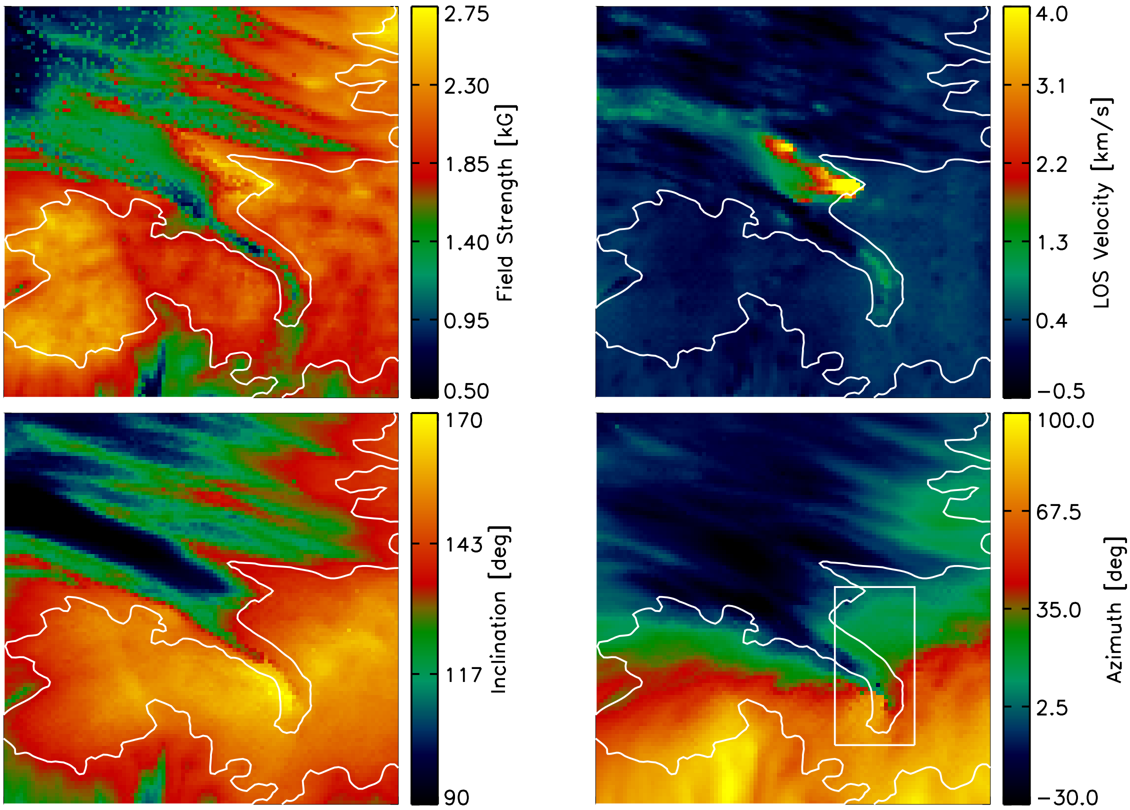

Figure 4.3: Same as Figure 4.2 but derived from inversions of SP2.

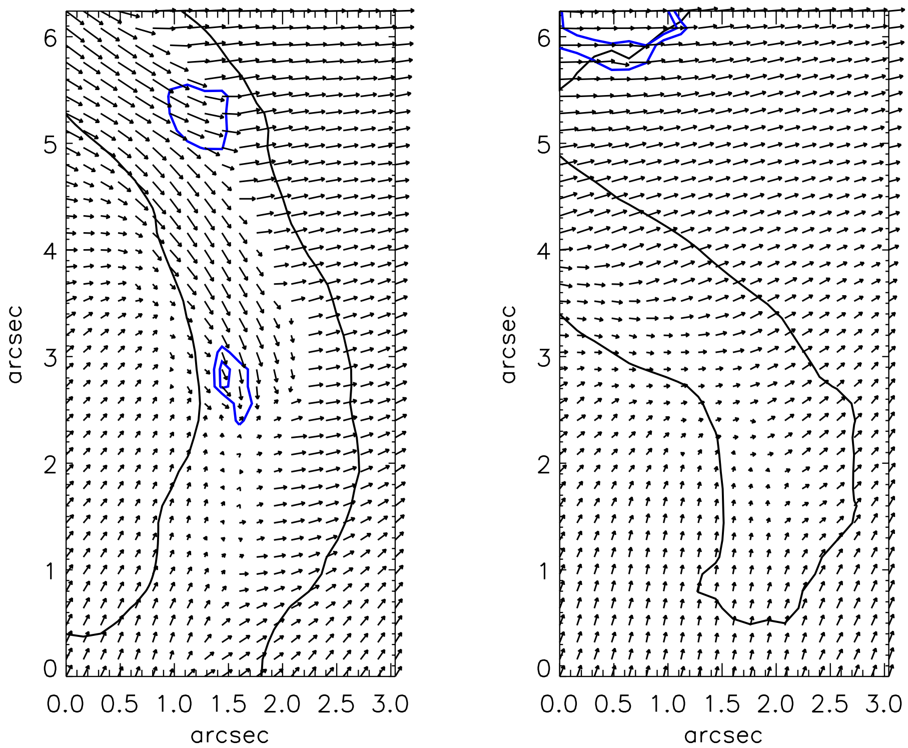

Figure 4.4: Transverse component of the vector magnetic field in the LB for the region marked as the white rectangle in Figures 4.2 and 4.3. The arrows have been drawn at each pixel. The blue contour lines mark LOS velocities of 2.5 and 4 km s^{-1}.

two structures are also connected dynamically. The isolated region with relatively weak magnetic fields lie at the lower end of the LB, where the LB fields pointing south, encounter sunspot fields oriented toward the north. In addition, there is a strong discontinuity in the field azimuth running parallel to the west edge of the LB which seems to separate the LB fields from the adjacent umbral fields. The azimuth in the LB changes from -100° during SP1 to -30° [1] during SP2. This is illustrated in the transverse magnetic field obtained from SP2 which depicts most of the transverse field vectors to be oriented across the LB while only a minority of them are parallel to its axis and lie predominantly in the upper half where the LB emerges (Figure 4.4).

4.3.2 Strong Downflowing Patches

The LOS velocity map displayed in the top right panel of Figure 4.2 reveals the existence of strong, localized downflows in the LB with velocities of upto 4 km s^{-1}. Similarly, very large velocities occupying a conspicuously large patch are seen at the umbra-penumbra boundary with velocities exceeding 5 km s^{-1} as seen in Figure 4.3. Although, this large patch is not on the LB, it is still in the vicinity of the northern part of the LB. The LOS velocity map corresponding to SP1 shows that these downflows occur close to the weak-field region and the azimuth discontinuity described in Section 4.3.1, i.e., at positions where the magnetic field changes its orientation very rapidly (Figure 4.2). There are essentially three strong downflowing patches as seen from Figure 4.2 which appear as islands. From the second scan the LOS velocity map shows two strong downflowing patches, with one of them essentially lying at the umbra-penumbra interface while the other is nearly 3″ further apart from the larger patch. While the downflows occupy a patch 0.″3–0.″5 wide for the first scan, the downflows obtained from the second scan occupy an area larger than 1 arcsec^2.

Inspection of the polarization signals emanating from the downflowing patches in the LB, derived from the first scan, reveal Stokes V profiles with two peaks in the red lobe, i.e., they exhibit a total of three peaks. Hereafter they will be labeled as Type 1. In the LB one also finds anomalous linear polarization profiles

[1] Negative azimuths imply angles measured in the clockwise direction from solar west

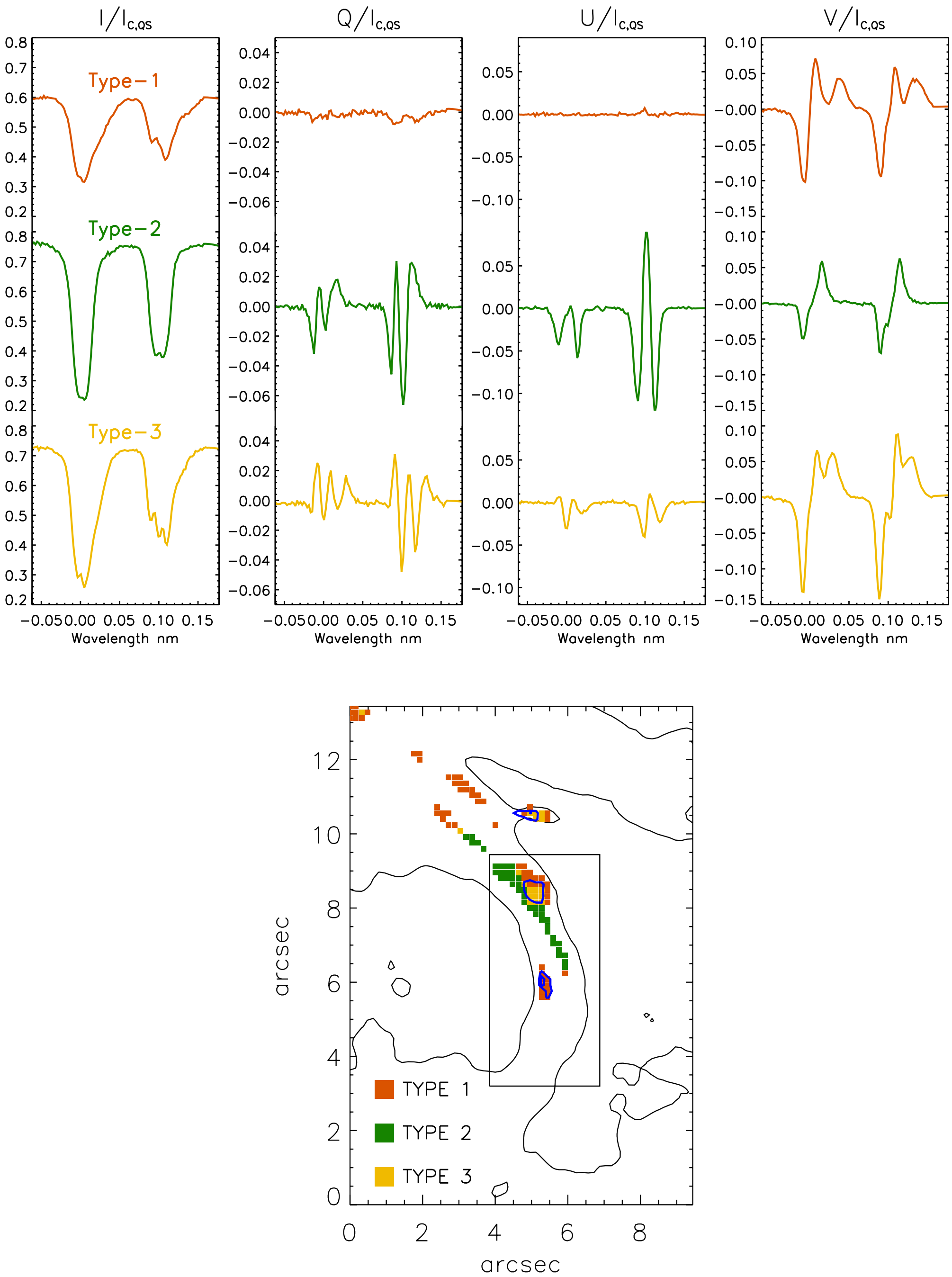

Figure 4.5: Top: Anomalous Stokes spectra observed in the LB. Type I, II, and III profiles are shown in orange, green and yellow, respectively. **Bottom:** Spatial distribution of the anomalous profiles. Blue contours mark velocities larger than 2.5 and 4 km s^{-1}.

with normal Stokes V signals which are designated as Type 2. Type 3 profiles are essentially a combination of the other two classes. Examples of these profiles are given in Figure 4.5, together with their spatial distribution. It is instructive to mention that polarization signals of this kind have previously not been reported in sunspot LBs.

4.3.3 Implications of Anomalous Polarization Profiles

4.3.3.1 Supersonic Downflows in the Light Bridge

The complex shapes of Type 1 profiles cannot be reproduced satisfactorily with Milne-Eddington-like atmospheres such as the ones used to determine the global structure of the LB. For this reason, the velocities given in Section 4.3.2 are only approximate. Here I obtain more reliable values with the help of two-component inversions.

I start with a simple two-component model in which the magnetic field and the LOS velocity do not vary with height. The results of this inversion are shown in Figure 4.6. As can be seen, one of the components has supersonic velocities of $\sim$10 km s^{-1}. Given that the strong downflows occur in patches 0.3–0.5 arcsec wide, it seems unlikely that the two magnetic components are unresolved horizontally. An alternative scenario is that they are stacked in the vertical direction, one on top of the other.

To investigate this possibility, I consider a different model atmosphere with two magnetic components. One of them has height-independent parameters and the other features a discontinuity in the stratifications at a certain optical depth. The amplitude and the location of the discontinuity are free parameters. These inversions have been carried out using SIRJUMP, an extension of the SIR code (Bellot Rubio, in preparation). The results show that the fast component always has velocities exceeding 10 km s^{-1}. As an example, Figure 4.7 displays the stratifications of one such model with the downflows occurring in the lower half of the photosphere, while Figure 4.8 illustrates the stratifications with the downflows occurring in the upper half of the photosphere.

While the two-component models used in this Section differ in complexity, all of them indicate supersonic velocities and magnetic fields of the same polarity. In

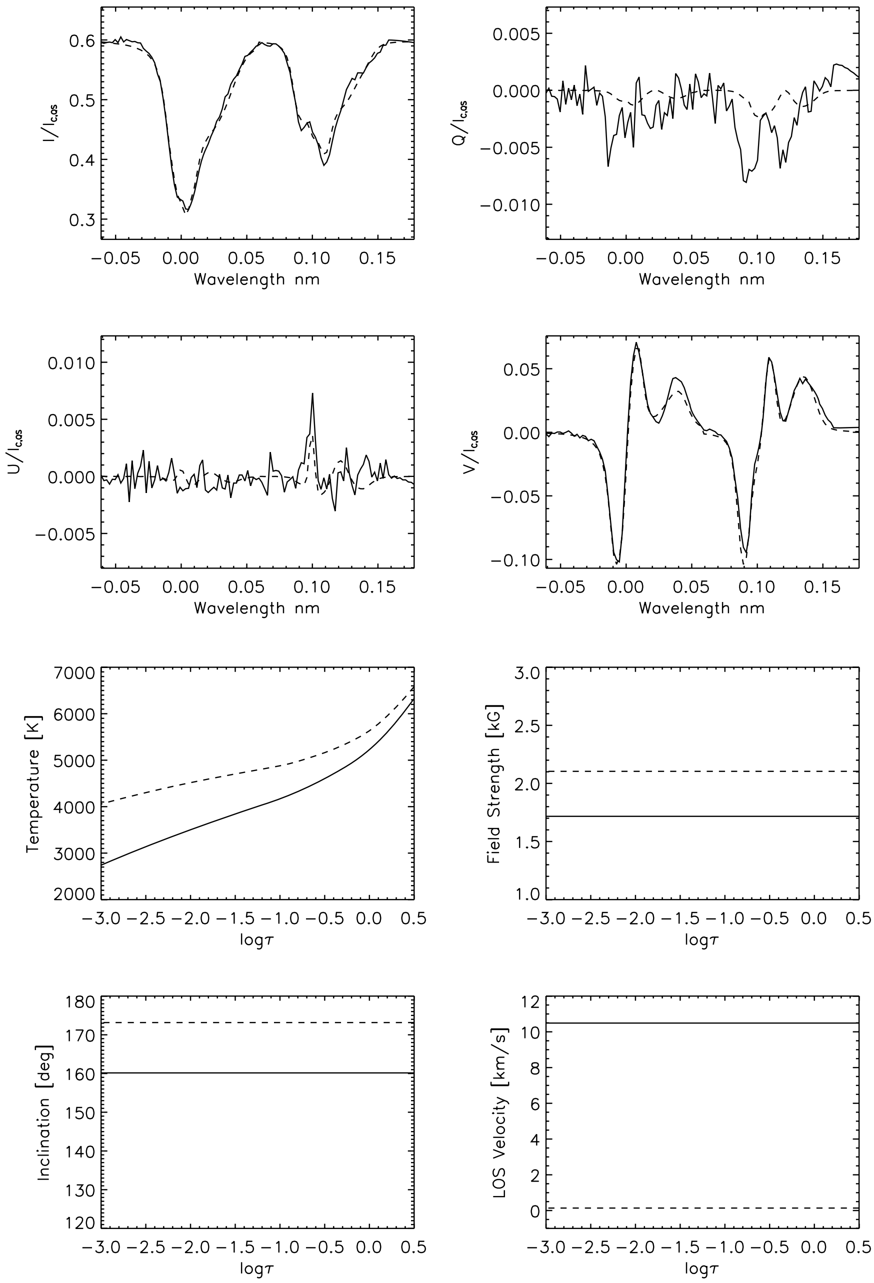

Figure 4.6: Top set of panels: Observed (*solid*) and best-fit (*dashed*) Stokes profiles using a simple two-component atmosphere. **Bottom set of panels:** Atmospheric stratifications for the two components (*solid* and *dashed lines*, respectively).

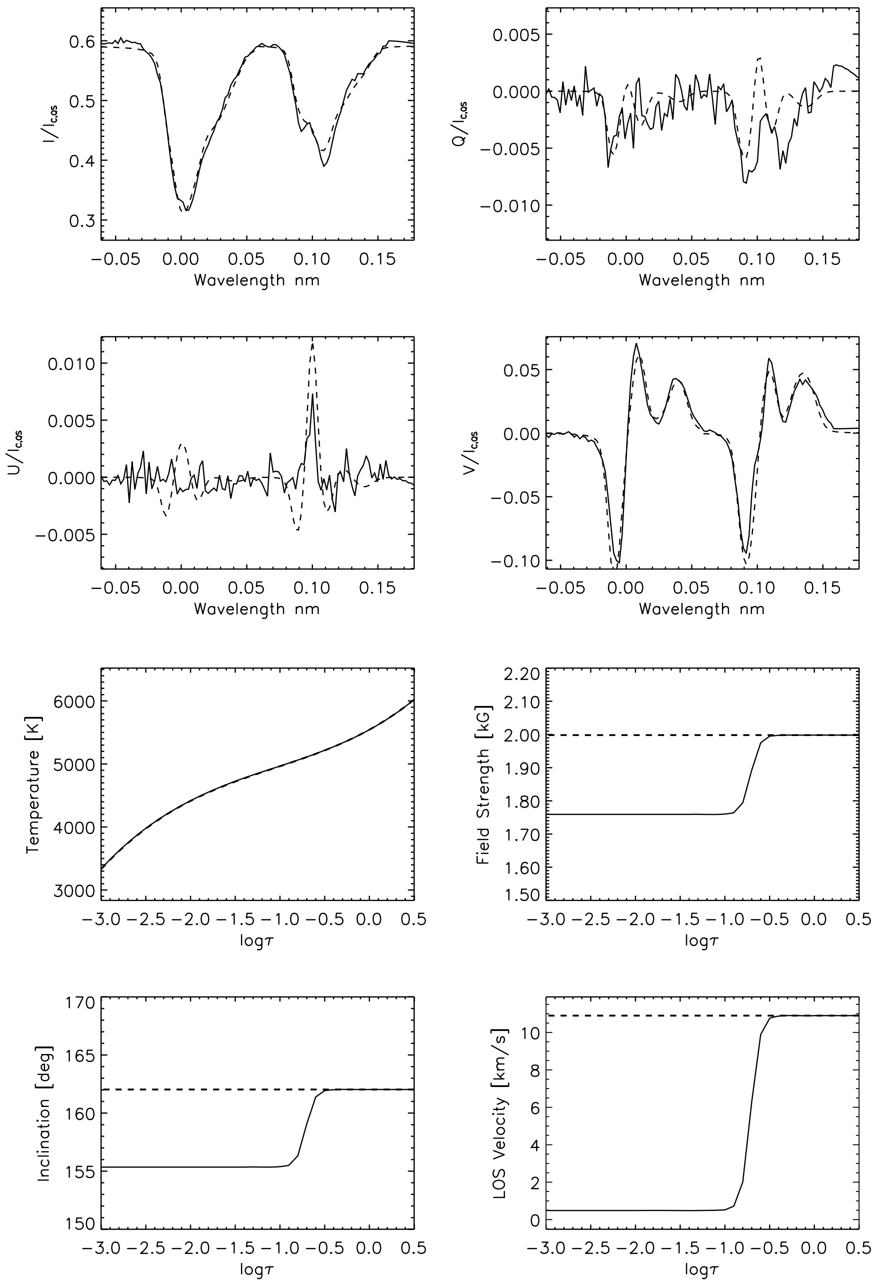

Figure 4.7: Same as Figure 4.6, for a two-component model in which one of the components has a discontinuous stratification with supersonic speeds in the deeper layers. **Bottom set of panels:** The constant background atmosphere is represented by the *dashed* lines, whereas the *solid* lines correspond to the discontinuous atmosphere.

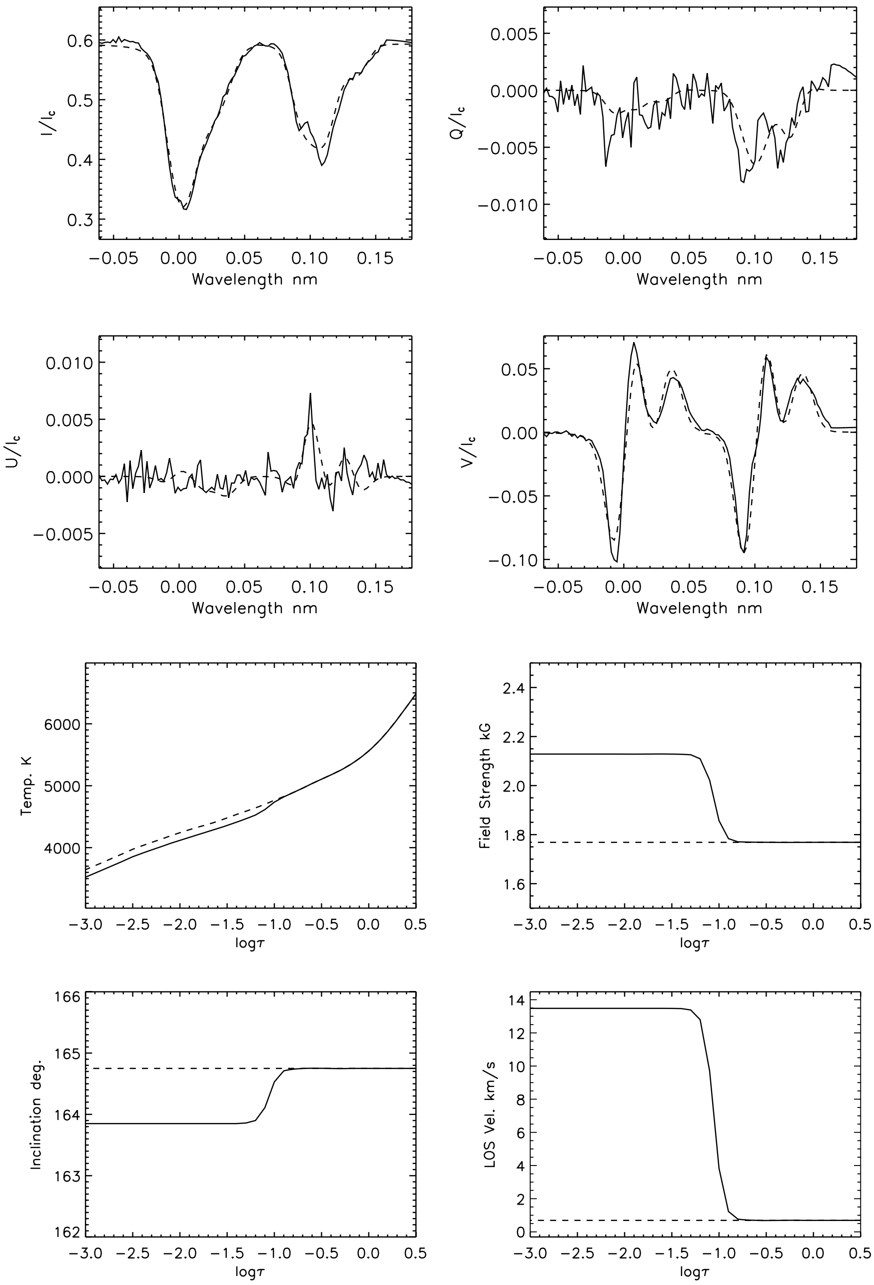

Figure 4.8: Same as Figure 4.7, for a two-component model in which one of the component has a discontinuous stratification with supersonic speeds in the upper layers.

fact, the existence of supersonic flows is obvious from the shapes of the observed Stokes V profiles, which are similar to those emerging from the outer part of the penumbra where the Evershed flow exceeds the sound speed. The inclined red wings of Stokes I also demonstrate the occurrence of strong velocities. All these spectral signatures are well reproduced by the two-component inversions. To the best of my knowledge, this is the first time that supersonic downflows are found in LBs. Subsonic speeds of $\sim$1 km s^{-1} have been reported earlier by Rüedi et al. (1995), Schleicher et al. (2003), and Bharti et al. (2007a).

4.3.3.2 Mixing of Light Bridge and Umbral Fields

The profiles from the azimuth discontinuity seen in SP1 consist of anomalous linear polarization profiles with normal Stokes V signals. The Stokes Q profile is seen to consist of 4 or even 5 peaks. The multiple peaks indicate that different magnetic components coexist in the resolution element. The azimuth discontinuity lies along a ridge on the west side of the LB possibly arising from a mixing of the umbral and LB fields (Figure 4.5).

To demonstrate the interaction of the polarization signals from the LB and the umbral, a single-component atmosphere with gradients in the physical parameters along LOS, is employed. The bottom set of panels in Figure 4.9 show the field to be fairly stronger and relatively inclined in the higher layers corresponding to logτ=-2 and -2.5, while it is weaker and more horizontal in the deeper layers close to logτ=0 to -0.5. The field azimuth is seen to be aligned along the light bridge in the deep layers while it is oriented across it in the higher layers. One could thus imagine the LB field dominating the deep layers with the overlying umbral field in the higher layers.

4.3.3.3 Supersonic Downflows at the Umbra-Penumbra Boundary

The LOS velocities derived from the inversions of SP2 show a large downflowing patch at the umbra-penumbra boundary. A horizontal slit passing through this patch along the umbra-penumbra boundary was chosen and is shown in the top panel of Figure 4.10. Pixels lying to the left of the umbra-penumbra boundary were inverted using a simple two-component model, setting the magnetic field and

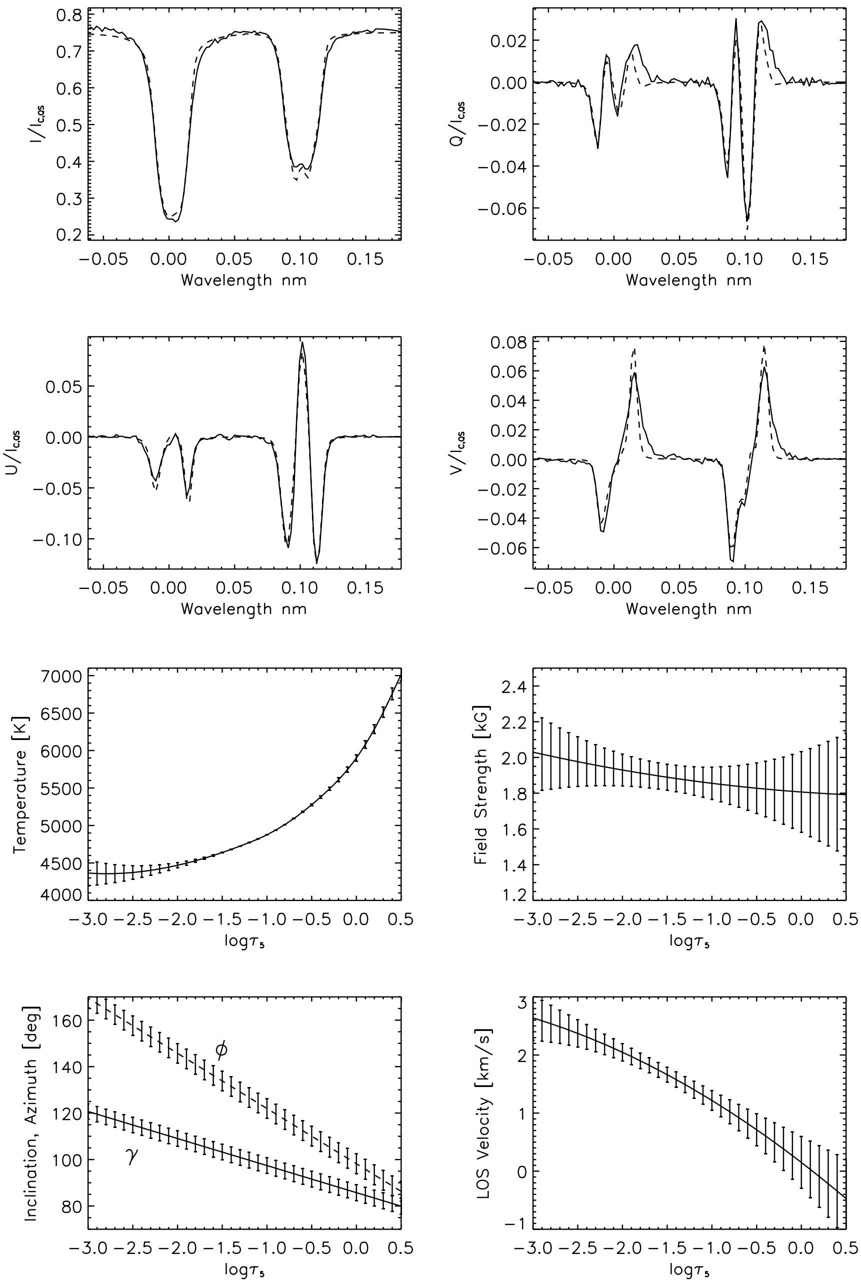

Figure 4.9: Top set of panels: Observed (*solid*) and best-fit (*dashed*) Stokes profiles using a one-component atmosphere with gradients along LOS. **Bottom set of panels:** Atmospheric stratifications of the physical parameters. The azimuth has been reduced by 190° so as to fit in the same plotting range as the inclination. The angles have not been converted to the local reference frame.

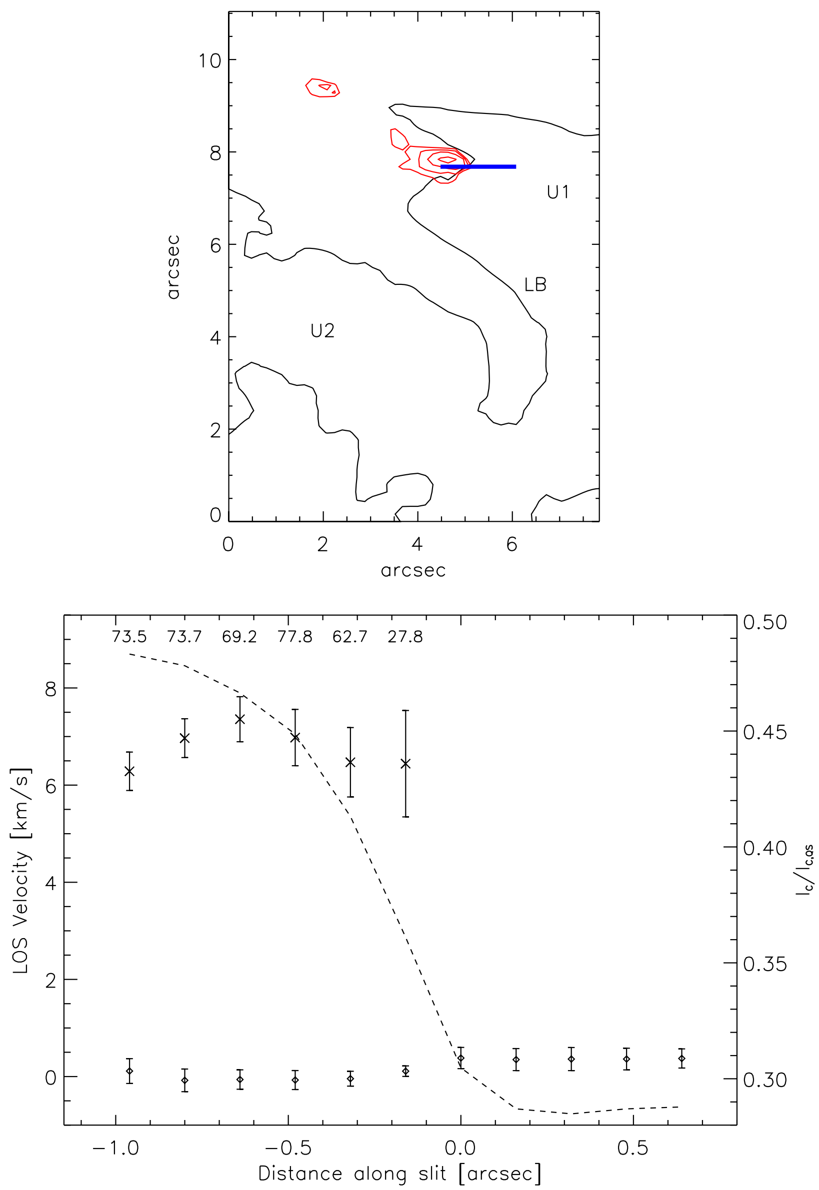

Figure 4.10: Top: Red contours depict LOS velocities ranging from 3, 4, 5 and 6 km s^{-1}. The blue line represents a slit across the strong downflows at the umbra-penumbra boundary. The distance along the slit increases from left to right with the umbra-penumbra boundary being zero. Pixels to the left are negative. **Bottom:** LOS velocities along the blue slit marked in the top panel. The velocities left of the umbra-penumbra boundary were determined from inversions using a two-component atmosphere. The numbers on the top represent the filling fraction of the faster moving component. The error bars correspond to $\pm 1\sigma$. The dashed line represents the normalized continuum intensity along the slit.

LOS velocity to be constant with height. This was done since the profiles from this patch resemble the ones described in Section 4.3.3.1. As the profiles lying on the right half of the slit, were regular profiles, no further inversions were done. The bottom panel of Figure 4.11 reveals very large velocities close to/exceeding the sound speed, adjacent to the umbra-penumbra boundary. Such large velocities are known to exist in the mid and outer penumbra, but observations presented here reveal for the first time very strong velocities adjacent to the umbra where magnetic fields are typically in excess of 2 kG. Thus, convection, of any kind, can be ruled as a possibility for producing the large velocities, because of the large field strengths. Figure 4.11 shows the variation in the Stokes profiles along the slit. At the umbra-penumbra boundary, one observes a distinct reduction in the continuum intensity. The highly inclined red wings in the I profile as well as the double-lobed V profile are reproduced by the simple two-component atmosphere. I would however like to mention, that given the large area of the downflows, it seems unlikely that the two components are a result of insufficient spatial resolution, as iterated in the Section 4.3.3.1. However, the emphasis is on the supersonic velocities at the umbra-penumbra boundary which is manifested as anomalies in the polarization signals. Table 4.2 summarizes the variation in the physical parameters along the slit, which illustrates strong fields not only in the umbra but also in the penumbra. The fields are inclined and oriented nearly radially to the umbra-penumbra boundary.

4.3.4 Chromospheric Activity

The left panel of Figure 4.12 shows that some, but not all, of the strong downflowing patches coincide with chromospheric Ca II H brightness enhancements. The filtergram displayed there was taken during the first of the two, spectropolarimetric scans of the LB and shows a strong Ca II H line-core brightening at the position and time of the largest photospheric velocities[1]. NOAA AR 10953 produced many other long-lasting chromospheric plasma ejections on April 29 and

[1]The other two patches do not exhibit significant brightness enhancements. However, they are located near the end of thread-like chromospheric structures that reach into the umbra U1 (see the white lines in Figure 4.12). These structures show brightenings, but not as intense as those associated with the strongest downflows.

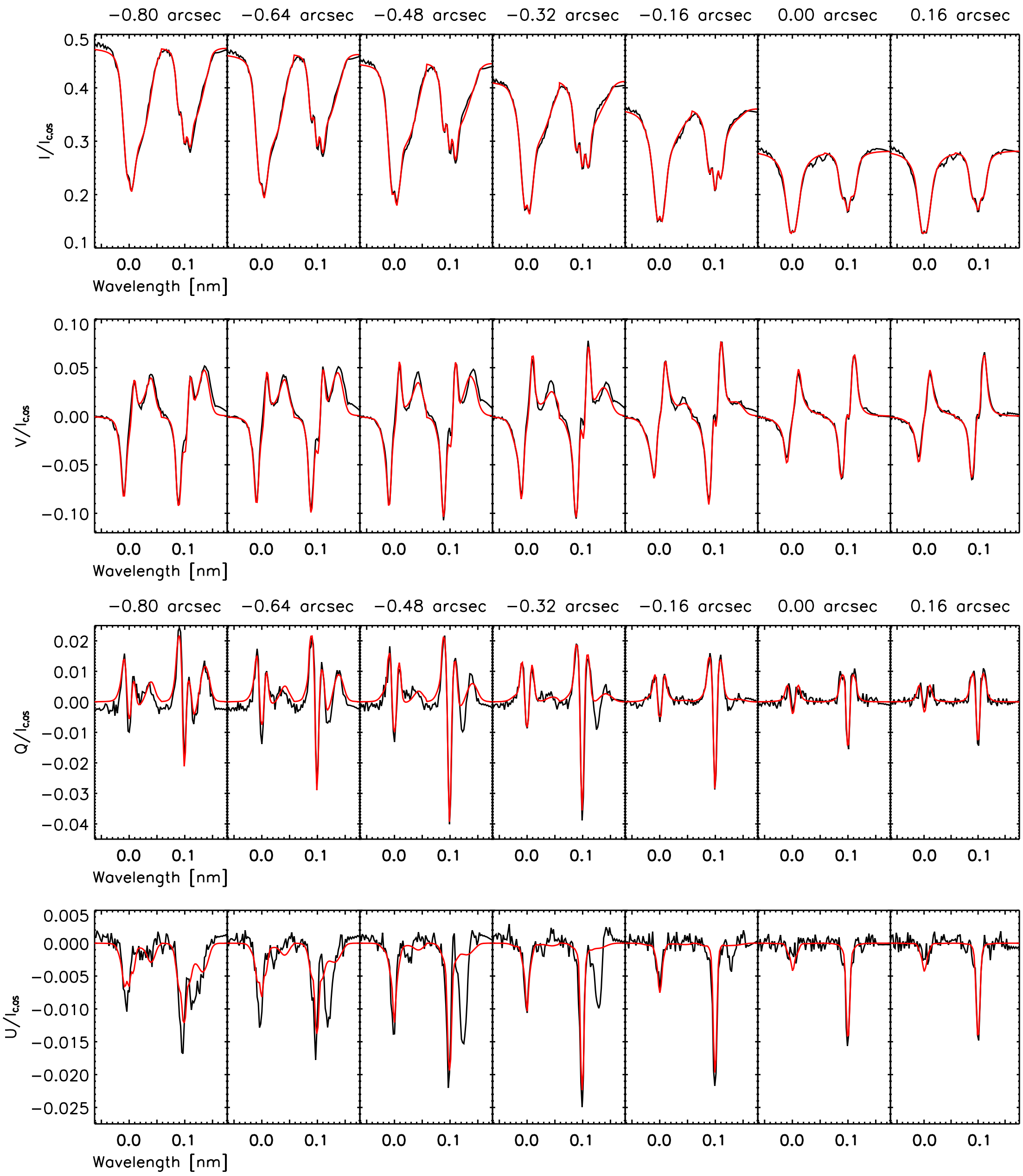

Figure 4.11: Top set of panels: Observed (*black*) and inverted (*red*) Stokes I and V profiles along the slit. **Bottom:** Observed (*black*) and inverted (*red*) Stokes Q and U profiles along the slit.

Table 4.2: Physical parameters derived along the slit passing through the umbral-penumbral boundary. The angles are expressed in the local reference frame.

Distance	LOS Velocity (km/s)		Field Strength (G)		Inclination (deg)		Azimuth (deg)		Fill Fraction %	
along the slit	C-1	C-2	C-1	C-2	C-1	C-2	C-1	C-2	C-1	C-2
-0.96	6.3±0.4	0.1±0.3	2420±221	2229±164	124±4	136±5	1±5	-3±5	73.5	26.5
-0.80	7.0±0.4	-0.07±0.2	2500±224	2244±152	128±4	137±5	3±6	0±5	73.7	26.3
-0.64	7.4±0.5	-0.06±0.2	2529±261	2292±131	131±5	136±4	5±8	2±5	69.2	30.8
-0.48	7.0±0.6	-0.07±0.2	2518±325	2310±126	135±7	134±4	7±13	5±4	77.8	22.2
-0.32	6.5±0.7	-0.04±0.2	2627±385	2313±97	141±9	136±3	9±24	6±4	62.7	37.3
-0.16	6.4±1.10	0.11±0.1	2666±589	2316±69	147±15	139±2	7±49	7±3	27.8	72.2
0.0		0.38±0.2		2350±124		133±4		11±8		100
0.16		0.35±0.2		2340±132		135±4		10±9		100
0.32		0.36±0.2		2309±137		135±4		10±9		100
0.48		0.36±0.2		2258±128		135±4		11±8		100
0.64		0.37±0.2		2243±113		136±4		10±8		100

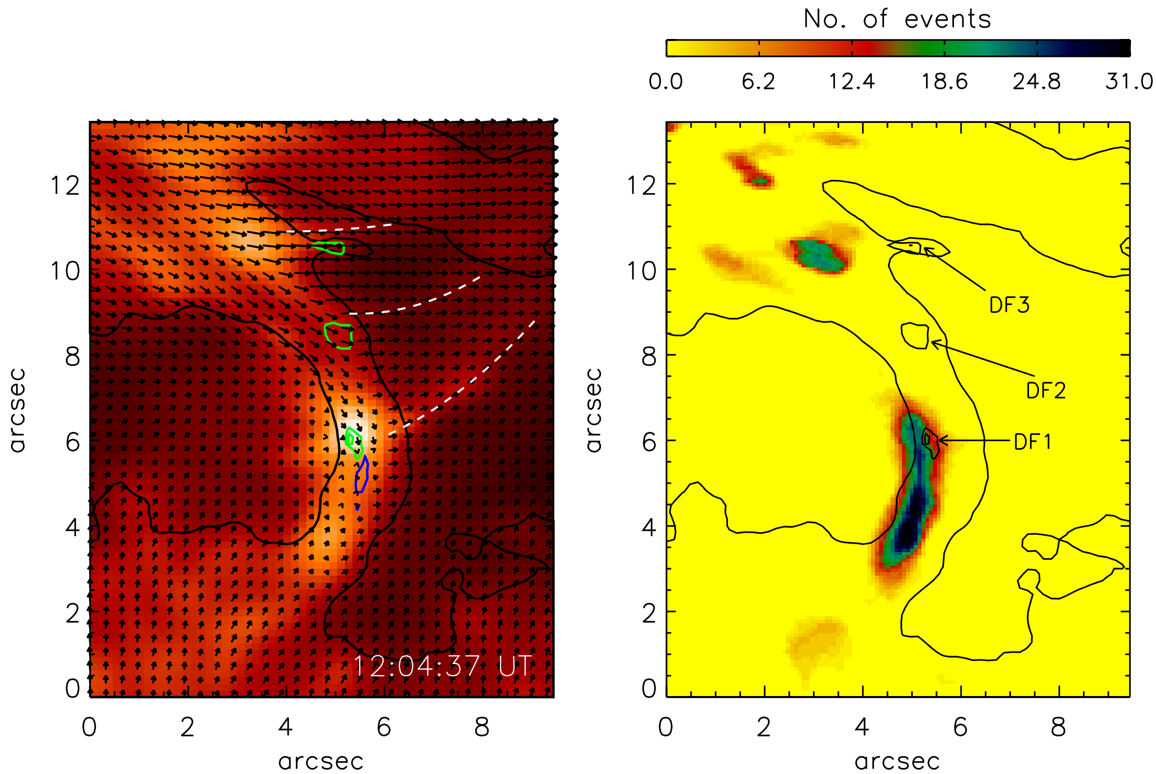

Figure 4.12: Left: Ca II H filtergram of the LB taken at 12:04:37 UT when the spectrograph slit was above the LB, with contours of LOS velocities corresponding to 2.5 and 4 km s^{-1} shown in green. The arrows indicate the transverse component of the field in the local reference frame for every alternate pixel, after solving the 180° azimuth ambiguity. Blue contours represent fields weaker than 750 G and black contours outline bright continuum structures. The white dashed lines mark thin chromospheric threads whose ends are located in or near the downflowing patches. **Right:** Chromospheric event map constructed during SP1. DF1, DF2 and DF3 indicate the downflowing regions with black contours drawn for 2.5 and 4 km s^{-1} respectively.

30 (Shimizu et al., 2009). In the previous chapter it was shown that the enhancements during the early part of May 1, exhibited transient flashes across the LB as well a strong brightening along a loop-like structure that was seen in the 3 hr mean image (Louis et al., 2008). It was also shown that the transient events are extremely fast and have lifetimes of 2-3 min. Simultaneous Ca filtergrams were available only during SP1 while the same was acquired ≈ 1 hr before and after SP2. In order to study the association of the downflows, both in the LB as well as at the umbra-penumbra boundary, to the chromospheric enhancements, events maps were constructed in the following manner. The 3 separate time sequence of Ca filtergrams corresponding to SP1, before SP2 and after SP2 cover periods of 44 min, 59 min, and 54 min respectively with a cadence of 1 min. For each of these sets a small region in the quiet Sun chromosphere was selected and the time averaged intensity was determined. This value was then used to normalize the intensity of each filtergram. A histogram of the intensities in the sub-region containing the LB was constructed to select a threshold value. From the trailing part of the histogram, a threshold value of 0.9 and 0.8 was chosen for SP1 and the two filtergram sets during SP2 respectively.

Using the threshold value, a binary image was created for each individual image in the time sequence, where all pixels with an intensity above the threshold were set to one and the rest to zero. These binary maps were then added in time, yielding at the end, a map with pixels having values indicating the number of chromospheric events. Figures 4.12 and 4.13 illustrate the event maps constructed from the manner described above, for the two sets of the SP scans. The chromospheric event map constructed during the time of SP1, shows the strongest downflowing patch DF1 lying within the sausage shaped region where a large number of events occurred. The figure illustrates that during the 44 min spectropolarimetric scan of the sub-region, the chromospheric enhancements were predominantly confined to the lower end of the LB close to the eastern edge. The top most downflowing patch DF3 is $\approx 1''$ away from the nearest chromospheric brightening, while DF2 appears somewhat devoid of any chromospheric association, with the distance of separation being $\approx 3''$. Although thread like-brightenings are seen in individual Ca images there does not seem any trace of such structures in the event maps, which could be attributed to the relatively

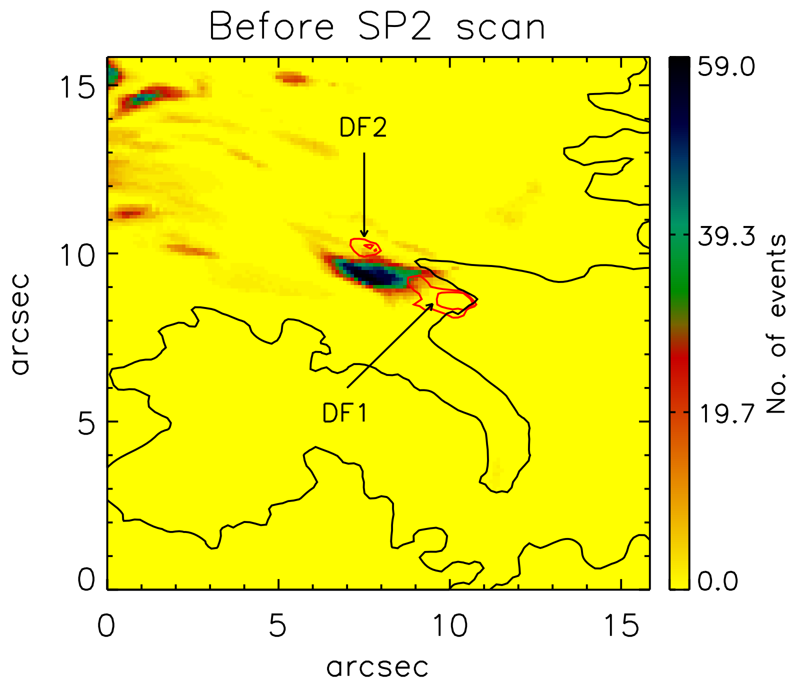

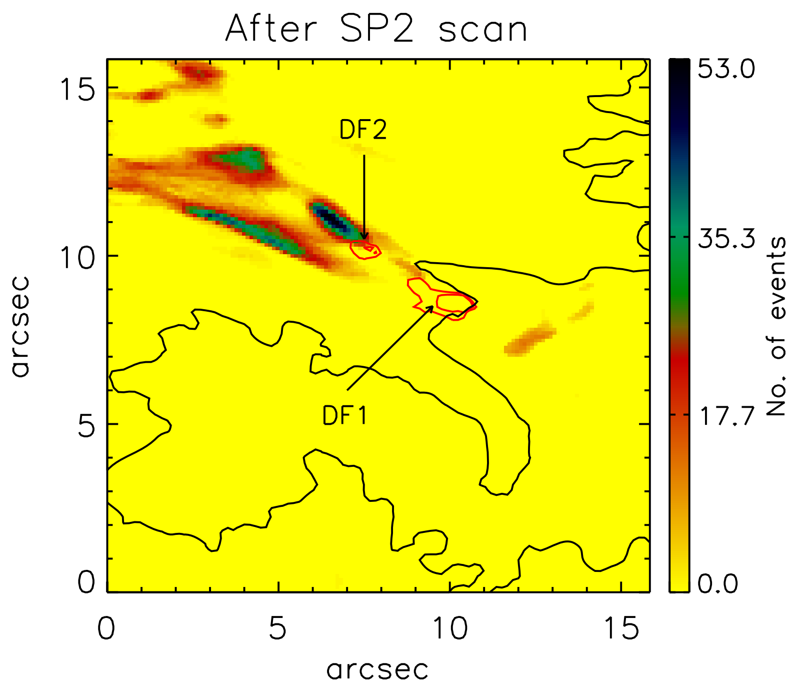

Figure 4.13: Same as Figure 4.13 but for Ca time sequences before (**top**) and after (**bottom**) SP2.

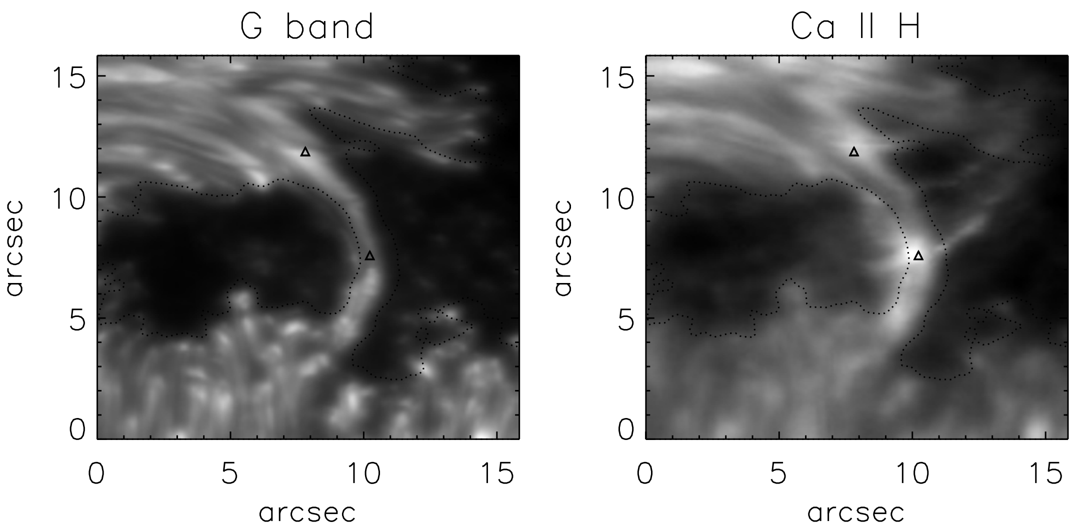

Figure 4.14: Left: G band image taken at the time of the spectropolarimetric scan of the LB at 12:04 UT. **Right:** Ca II H image taken at 12:04 UT. The black dotted line is the continuum intensity contour derived from the spectropolarimetric scan. The two triangles depict pixels for which light curves were determined.

high threshold value. This would also imply that the counts seen in the event maps represent the strongest brightening which persist in time.

The chromospheric event maps constructed before and after SP2 show a remarkable change in the counts pattern. There does not appear to be any brightening associated with the LB, but the strong chromospheric patch lies in the same radial direction and very close to the downflowing regions. Before the scan the events are concentrated in between the two downflowing patches while after the scan it appears to have shifted radially outward and lies closer to the second patch DF2 (Figure 4.13). There does, however, exist a small number of events in the umbra U1 seen in the bottom panel of Figure 4.13. This phase coincides with the disintegration of the LB, which is described in detail in Section 4.3.6.

4.3.5 Photometric Variation in the Photosphere and Chromosphere

In the following section the photometric variations in the LB and its surrounding, measured in the photosphere and chromosphere, are presented. This is an exercise to determine if the LB, which perturbs the magnetic field in the photosphere, and its evolution has any bearing to the photometric throughput in the solar atmosphere. In order to study this, light curves were constructed at the photosphere and chromosphere for the different filtergram data sets and at different locations on the LB. Figure 4.14 depicts a G band and Ca II H image acquired when the spectropolarimeter slit was above the LB. The two triangles marked in the figure represent pixels along which the light curves were determined. The pixel at the entrance of the LB lies below the barb-like structure described in Louis et al. (2008). The region immediately below the barb shows a strong intensity enhancement in the G band. The second pixel on the axis of the LB coincides with the chromospheric brightening that persistently occurred in that region. The intensity was averaged over two pixels and then plotted as a function of time as illustrated in Figure 4.15.

The top and bottom panels represent light curves at the entrance of the LB and its axis respectively. The top panel in Figure 4.15 shows the G band light curve with a distinct bump at 12:10 UT which is followed by a similar bump in the Ca light curve 8 min later. The variation of intensity in both heights appears to be identical after 12:20 UT. While the G band light curve appears fairly constant before the bump, the Ca light curve tends to increase steadily with time before decreasing. This increase exhibits two different trends which is illustrated by the two linear fits to the light curve shown by red lines. The second straight line is ≈ 4 times steeper than the other and the commencement of this second phase in the Ca light curve coincides with the same in the G band. The light curves from the pixel on the axis of the LB reveals a moderate correspondence between the G band and Ca intensities, with a linear correlation coefficient of 0.5. The G band intensity decreases initially followed by several intermediate bumps that coincide with the large increase in Ca intensity, particularly when the spectropolarimeter slit was above the LB. The G band intensity however, is much lower in the axis

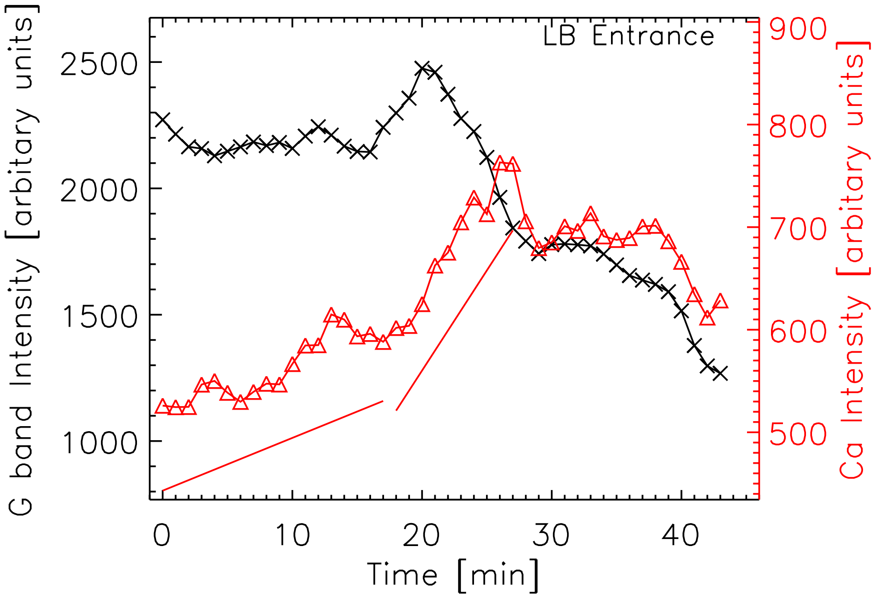

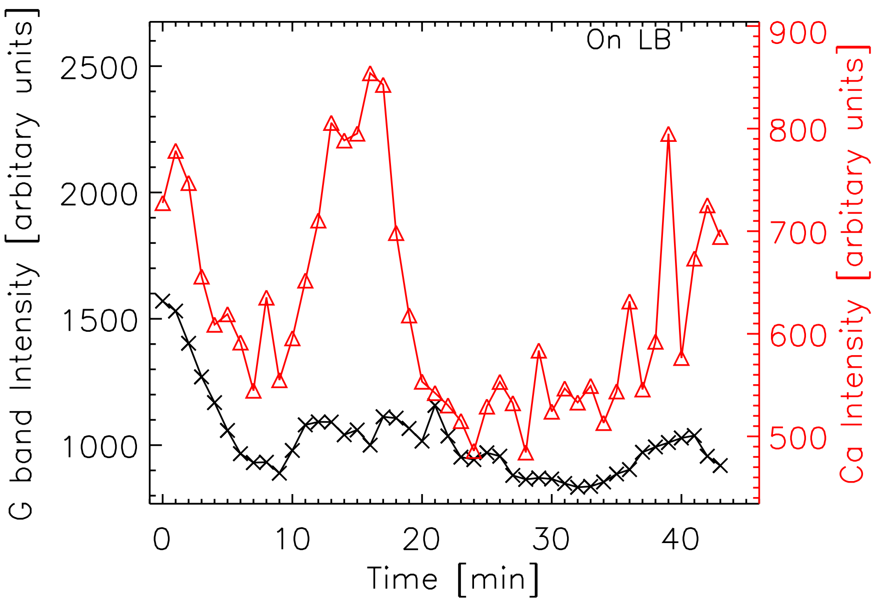

Figure 4.15: Light curves corresponding to the two pixels depicted in Figure 4.14. The red straight lines in the top panel are linear fits to the Ca light curve depicting two different slopes. The lines have been shifted downwards to emphasize the two phases of increase.

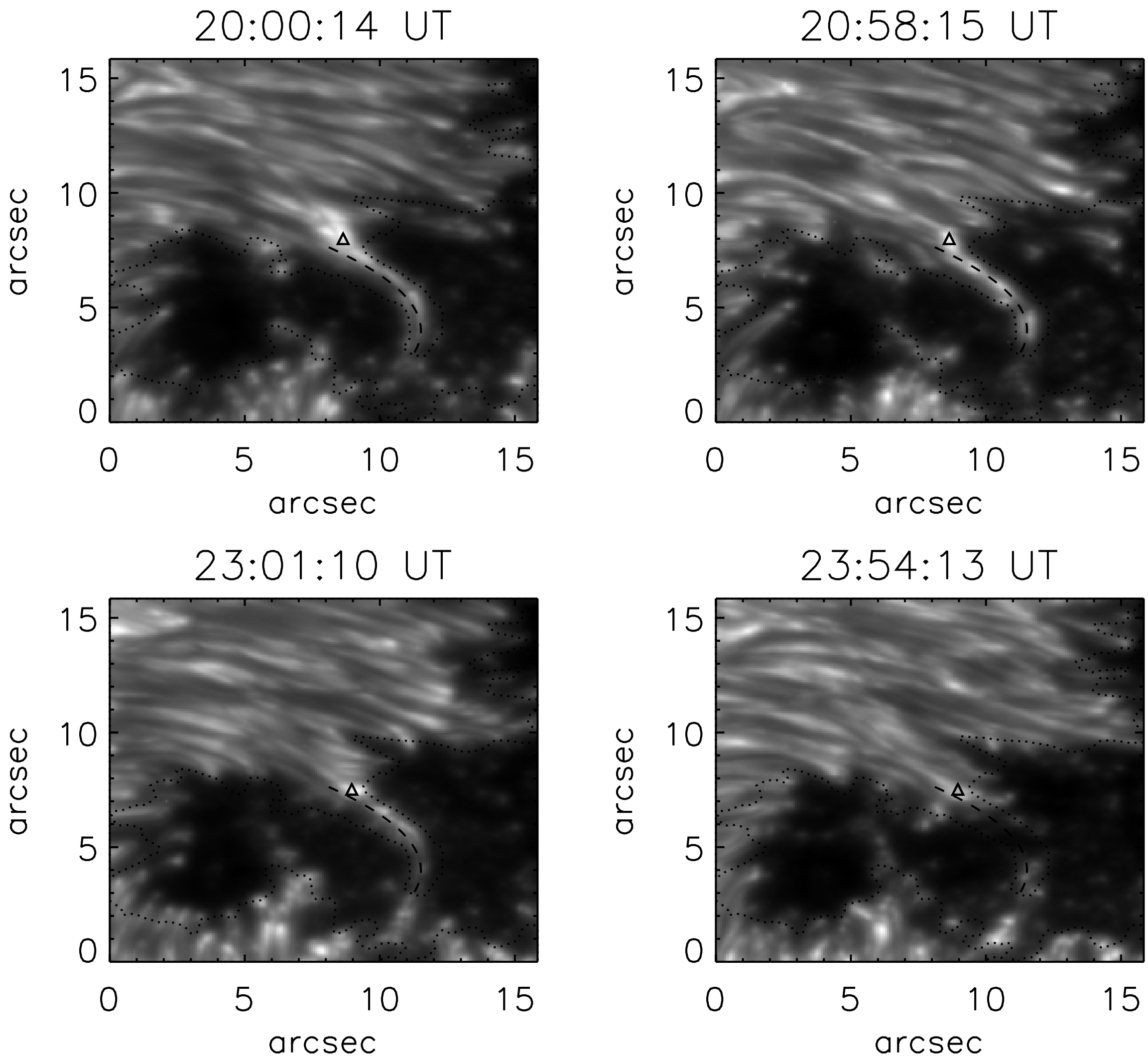

Figure 4.16: G band images taken at different instances of time namely, before (**top**) and after (**bottom**) the SP2 scan. The triangle depicts the pixel for which photospheric and chromospheric light curves were determined.

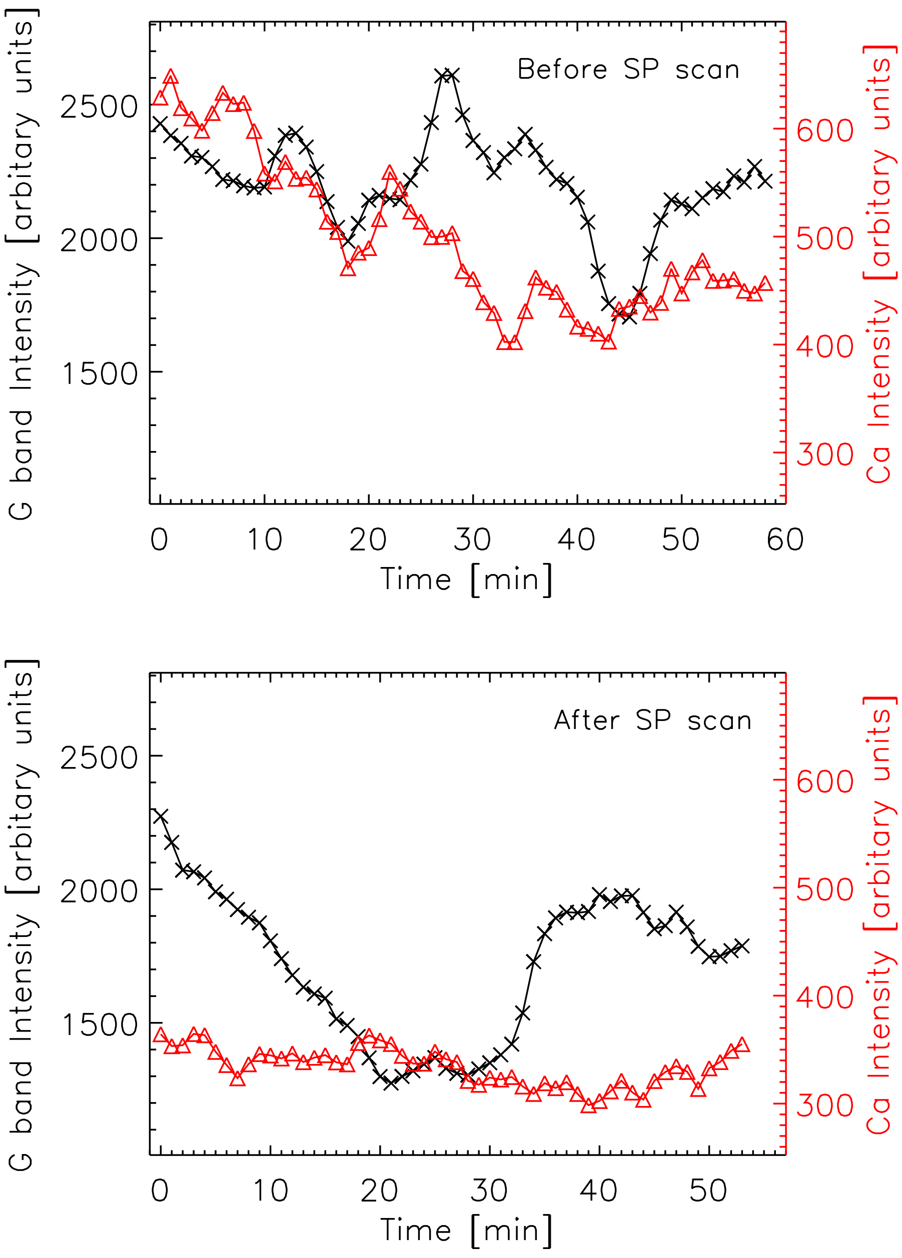

Figure 4.17: Light curves corresponding to the pixel depicted in Figure 4.16.

of the LB in comparison to the entrance, while the converse is seen in the Ca intensity at the two locations.

I carried out a similar exercise with the G band and Ca filtergrams taken during SP2, nearly 10 hrs later as depicted in Figure 4.16. As the LB was disintegrating, light curves were constructed only from the entrance of the LB and are shown in Figure 4.17. The G band light curve, prior to the SP2 scan, shows several bumps at 20:13 UT, 20:27 UT, 20:35 UT and a sudden dip in intensity around 20:45 UT, which was followed by an increase once again. The light curve in the chromosphere too shows a similar trend with peaks that appear to be shifted from the photospheric counterpart, similar to what was seen in the top panel of Figure 4.15. The Ca light curve however, tends to decrease with time suggesting a reduction in chromospheric activity in the entrance of the LB. The bottom panel of Figure 4.17 reveals a very interesting trend. The G band light curve monotonically decreases till 23:21 UT, and remains a constant till 23:30 UT after which there is a sudden increase. The decrease in the G band intensity till 23:30 UT coincides with the gradual weakening and disintegration of the LB. The chromosphere on the other hand does not exhibit any change with time and is greatly reduced as seen from the bottom panel of Figure 4.17. The subsequent increase in the photospheric brightness is attributed to the presence of penumbral structures, namely, bright penumbral grains, but this feature is not seen higher up in the chromosphere.

4.3.6 The decay phase of the LB

The G band space-time maps constructed for the two time sequences, before and after the SP2 scan respectively, summarize the episode of the LB's fragmentation. These maps were derived along the curved slit shown as the dashed line in Figure 4.16. The top panel of Figure 4.18 shows the motion of features along the LB and the measured speeds from the tracks, labeled B1, B2 and B3 are 170$\pm$24, 940$\pm$201 and 700$\pm$121 m s^{-1} respectively. The space-time map also shows that the motion of a feature outlined by B1 demarcates the upper brighter half of the LB from the lower half which is less intense. The space-time map constructed after the SP2 scan shows 2 phases of the LB's decay. There is an initial fast

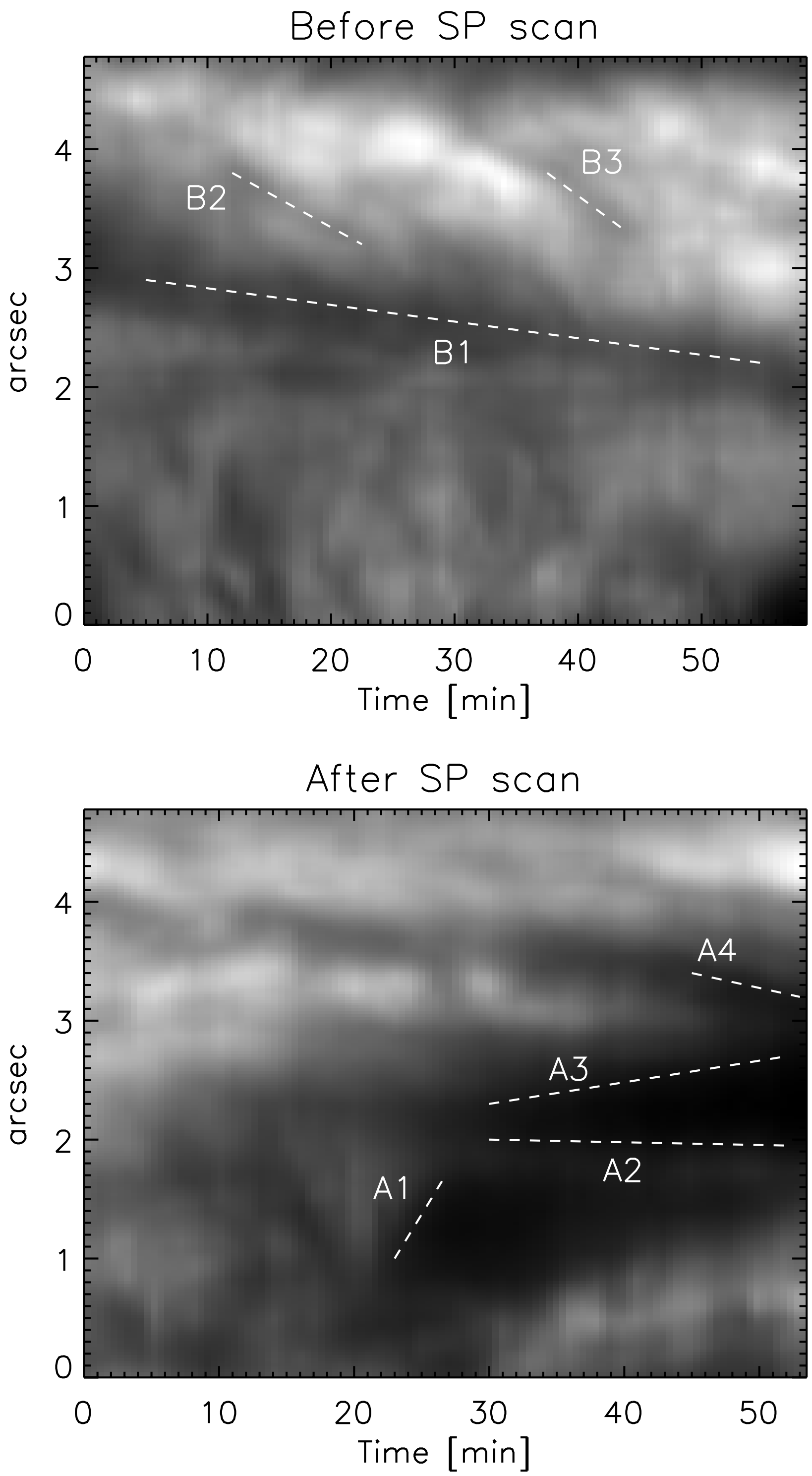

Figure 4.18: Space time maps constructed from the slit along the LB axis shown in Figure 4.16. The top and bottom panels correspond to the G band filtergrams acquired before and after SP2 respectively.

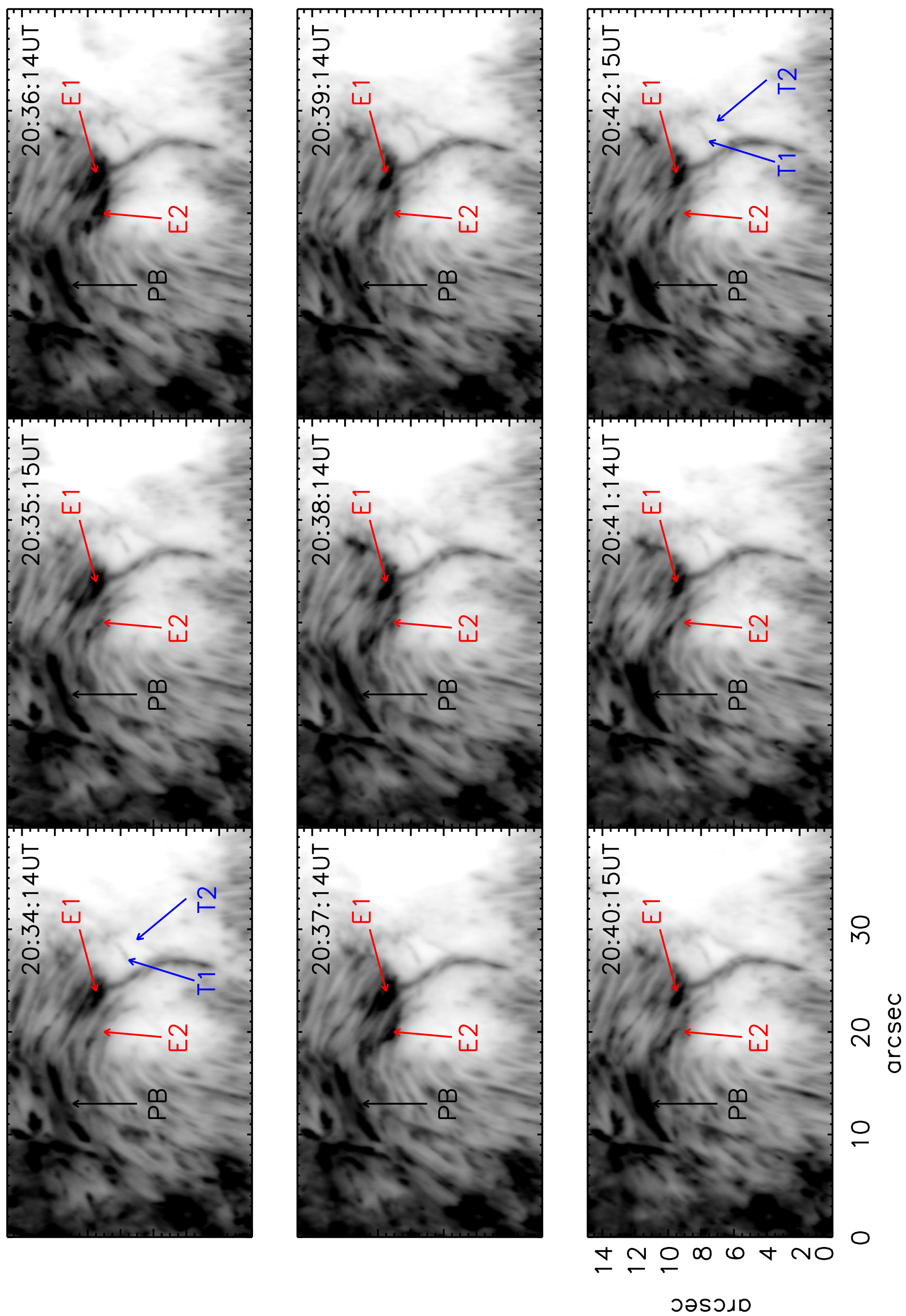

Figure 4.19: Time sequences of Ca II H filtergrams shown in negative. These set of images were taken before SP2. E1, E2-enhancements occurring close to the umbra, T1, T2-threads connecting the LB from the umbra, PB-penumbral brightness enhancement.

retreat of the lower end of the LB (track A1), with speeds measuring 2200±475 m s^{-1}, followed by a more gradual motion with speeds of 220±55 m s^{-1} (track A3). The instant the fast retreat changes to the slow retreat, diffuse structures resembling umbral dots are seen in the spatial location where the lower end of the LB had been earlier. This structure fairly remains motionless represented by the track A2. Meanwhile, the upper half of the LB or the penumbra continues to exhibit motion radially towards the umbra with speeds of 305±155 m s^{-1} (track A4).

The transient nature of the chromospheric enhancements associated with the LB and its neighborhood are presented below. A set of nine consecutive frames starting from 20:34 UT show chromospheric enhancements i) that occur close to the umbra-penumbra boundary (E1, E2), ii) brightenings seen in the form of threads reaching the LB from the adjacent umbra (T1, T2) and iii) arc-shaped enhancements that occur in the penumbra but far from the LB and appear to be connected to E1 (PB). E1 is a more stronger event compared to E2 and is seen to persist within the set of images shown in Figure 4.19. The area over which E1 is observed increases at 20:36 UT and within a span of 2 minutes reduces tremendously. E2 on the other hand is a weaker, smaller enhancement that lasts for a mere 3 frames. The thread-like enhancements (T1, T2) are extremely feeble and can be barely observed. These structures lack the intensity as seen in the earlier set of filtergrams acquired 10 hrs earlier. They however remain visible during the selected time duration. The strongest of the enhancements however, is PB which in fact is far from the LB as well as the umbra-penumbra boundary. These enhancements occupy a very large area and are observed to rapidly change in consecutive frames.

A similar set of images illustrate the chromospheric events associated with the fragmentation of the LB and is illustrated in Figure 4.20. I have chosen a longer time interval of 20 min to emphasize a very interesting observation. The enhancements close to the umbra-penumbra boundary, namely E1 is initially observed to encompass a very complex pattern of brightenings that last for 8 min, after which, it reduces to a much smaller region similar to what was shown in Figure 4.19. Another transient enhancement resembling a jet like brightening (J1) is ejected from the LB, eastward into the adjacent umbra U2. J1 is clearly

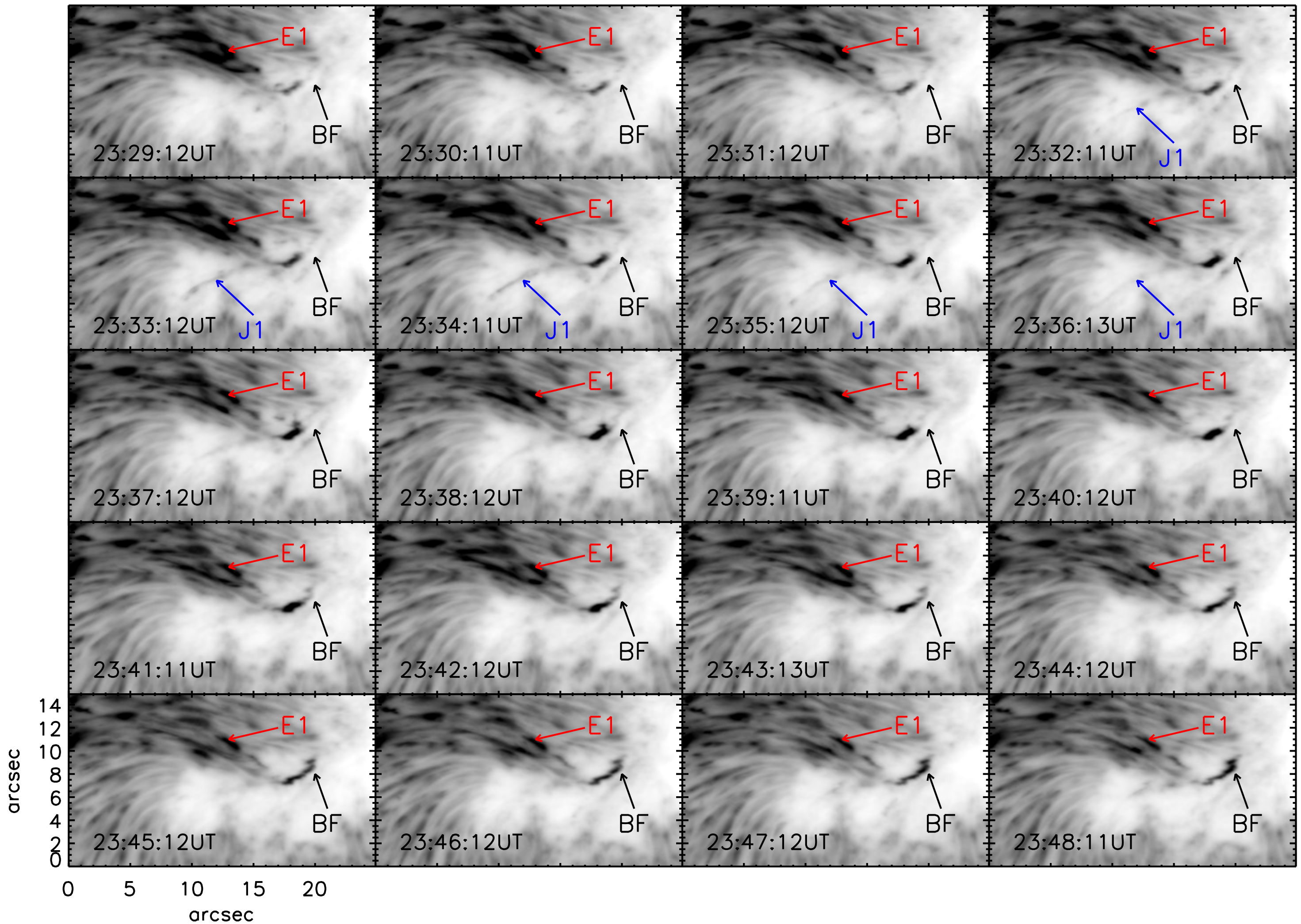

Figure 4.20: Time sequences of Ca II H filtergrams shown in negative. These set of images were taken after SP2. E1-enhancements occurring close to the umbra, J1-jet like brighening, BF-brightness front.

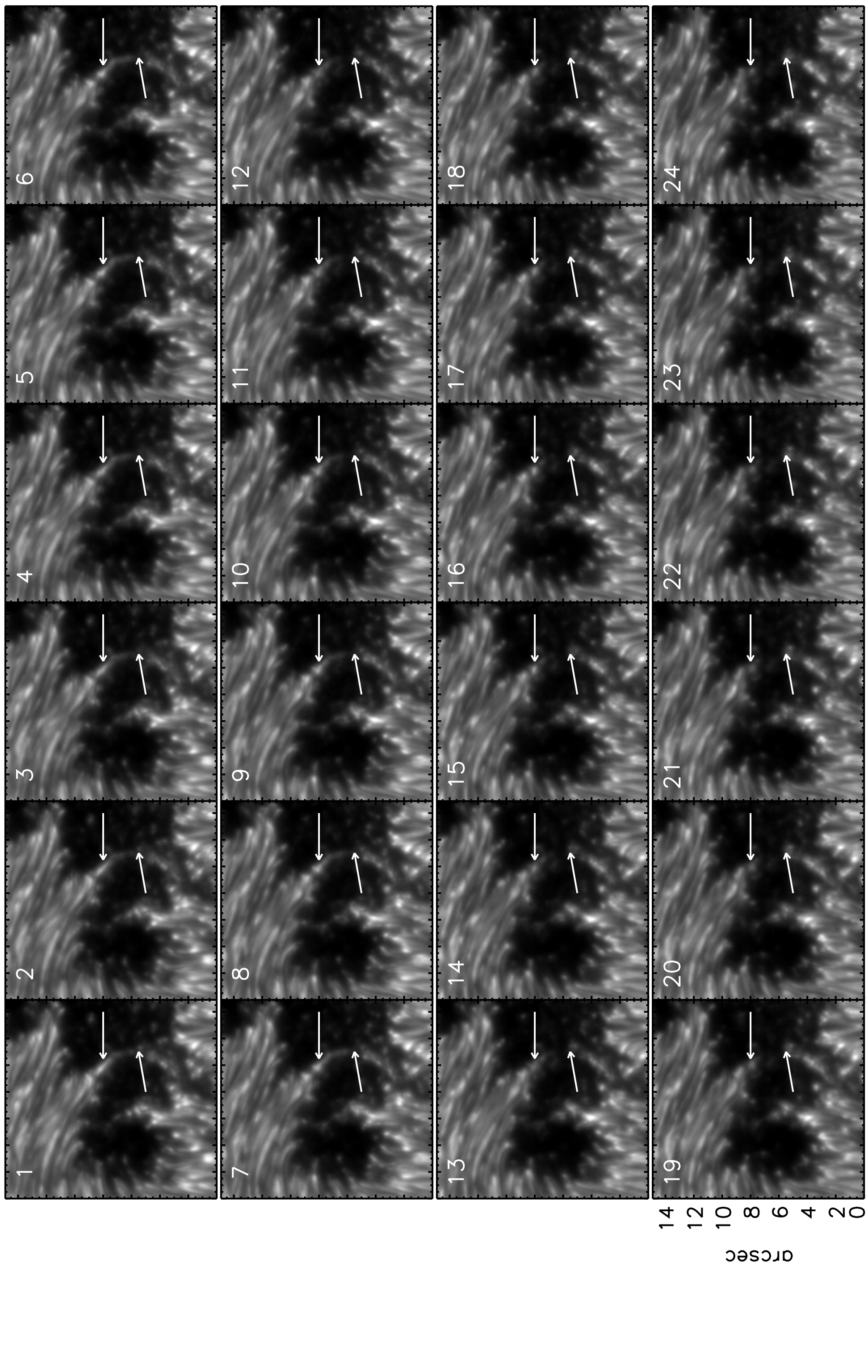

Figure 4.21: Time sequences of G band filtergrams starting at 23:15 UT, illustrating the fragmentation of the LB into a number of umbral dots. The two white arrows indicate the positions where the LB had previously existed

seen at 23:33 UT and 23:34 UT after which it gradually diffuses. Only one of the 2 thread-like brightenings, seen in Figure 4.19, is observed prominently in the present sequence of images. From the sequence of images, a brightness front is observed to move along this thread like structure in a direction toward the umbra U1. The length of the thread-like structure also increases with the passage of the brightness front. The initiation of this event commences with the last remaining part of the LB finally fragmenting.

The decay phase of the LB has a significant bearing to its constituent sub-structures. Figure 4.21 captures the final moments of the LB as its southern half gradually fragments leaving behind a string of umbral dots. The two arrows indicate the positions where the LB had previously existed. The space-time maps shown in Figure 4.18 as well as the sequence of G band images indicate that the umbral dots remain stationary after the fragmentation. In order to compare the photometric brightness before and after the LB fragmented, a light curve was derived from the pixel shown by the bottom arrow in Figure 4.18. The mean intensity before the LB fragmented is relatively weaker, than that after fragmentation. A similar behavior is seen with the intensity variation for the pixel marked by the top arrow, albeit the increase in intensity occurs nearly 15 min later. Thus the fragmentation of the LB is accompanied by a gradual decrease in brightness till it completely disintegrates, which is immediately replaced by relatively brighter umbral dots which appear to be co-spatial with the earlier LB.

4.4 Summary and Discussion

In this chapter the global magnetic and dynamic properties of a sunspot light bridge (LB) in NOAA AE 10953 were determined from high resolution spectropolarimetric and filtergram observations by *Hinode*. These observations were made on two occasions nearly 10 hr apart on 2007 May 1 and highlight important stages in the evolution of the LB. Broad band filtergrams were acquired, as and when they were available, in the proximity of the spectropolarimetric scans of the LB, to provide photometric measurements in the photosphere and chromosphere. A one-component model atmosphere with height-independent parameters (except for the temperature) was used in the inversions of the Stokes profiles to derive maps of the physical parameters. Continuum images of the LB, corresponding to the two SP scans, indicate a significant change in the structure of the LB. The latter captures the onset/progress of the decay of the LB. The corresponding maps of the magnetic field and LOS velocity obtained from the inversions, also reflect this characteristic. The reduction in field strength in the LB was initially confined to a larger area both along the axis as well as along its width. This however, dramatically changes as seen from the second set of maps. The LB shows very small, localized regions of extremely weak fields which are < 700 G on both occasions of the SP scan. The weak field region stands out clearly despite the model atmosphere being very simple, unlike the earlier work of Jurčák et al. (2006) which was based on a more complex model atmosphere that used more than 1 node in the SIR inversions. The fact that very weak fields are not observed anywhere else on the LB, does not in any way rule out the field-free nature of the LB. This simply could be attributed to the fact that the field-free intrusion may not be high enough to be seen in the line forming region. The transverse magnetic field which was initially aligned along the axis of the LB changes to one being oriented across it with time. This indicates the metamorphosis of the LB and could be used to classify strong and faint LBs (Sobotka et al., 1993, 1994). While the field strength in the LB is much stronger and relatively vertical during the formation (Katsukawa et al., 2007a) and decay phase as described in this paper, the trend changes to a weaker and more inclined configuration during the intermediate phase as seen from the first of the two scans. The following scenario is an attempt to explain this based on the intrusion of field free plasma into the umbral field. Let us assume that the intrusion starts very deep below the umbra. In the beginning the magnetic perturbation of the umbral field will not be detectable at the line forming region. Hence we will not see any weakening of field strength or change in field inclination. During the evolution of the light bridge, the hot material penetrates higher up in the umbra, thereby producing the changes of magnetic field observed in the intermediate phase. At the end of the lifetime of the light bridge, the intrusion subsides restoring the umbral field almost to its earlier configuration.

There exist patches of very strong downflows exceeding 4 km s^{-1} in the LB, which are associated with complex Stokes V spectra having double red lobes.

Two-component inversions of the profiles indicate supersonic velocities of 10 km s^{-1} or more. A Milne-Eddington inversion by Shimizu et al. (2009) of the same LB on the previous day shows a small downflow patch with velocities of only 0.7 km s^{-1}. In the LB, the supersonic downflows occur near regions where the magnetic field of the LB meets sunspot fields with rather different orientations. In those locations one observes anomalous linear polarization signals, but only when the field is relatively horizontal. Such profiles could arise from the mixing of the LB and umbral fields which are shown from the inversions using a one-component atmosphere with gradients along LOS. Similar observations of supersonic downflows were observed at the umbra-penumbra boundary, close to the LB, based on inversions of the Stokes profiles from the same region, nearly 10 hrs later. The LB on the other hand did not exhibit any large/supersonic downflows. The discovery of the supersonic downflows in the LB as well as at the umbra-penumbra boundary is one of the important results of this chapter.

The supersonic downflows in the LB as well as at the umbra-penumbra interface are sometimes associated with transient chromospheric brightenings. The spatial correspondence of the photospheric velocities and the chromospheric enhancements was studied using event maps. Although co-temporal chromospheric filtergrams were not available during the second SP scan, the event maps clearly show that the chromospheric enhancements lie very close to the downflows. The question that naturally arises from the above observations is the source/mechanism of the supersonic downflows and the brightenings? The strong downflows are similar to the Evershed Flow which can be supersonic in the mid and outer penumbra as well as beyond the sunspot boundary (del Toro Iniesta et al., 2001; Bellot Rubio et al., 2004, 2007). The 'siphon flow' model of Thomas & Montesinos (1993); Montesinos & Thomas (1997) and the 'moving tube' model of Schlichenmaier et al. (1998a,b) produce the Evershed flow by a gradient of the gas pressure at the ends of a tube. From the simple inversions described above it is difficult to identify the upflowing counterpart to the strong downflows. Moreover, if the downflows represent a mass flux returning to the surface as in the Evershed scenario, then the supersonic component should have an opposite polarity as that of the sunspot, which is clearly not the case here. In addition, the flow/tube models do not yield any information on the chromospheric phenomena associated with the downflows. It would thus appear that there lies an alternate physical process that should explain the observations.

In the first SP scan, the downflowing patches (at least some of them) are seen to be cospatial with chromospheric enhancements. In the LB, of the three downflowing patches, two of them on the upper half of the LB are associated with azimuth discontinuities which would imply different magnetic components in the resolution element. The resulting anomalous linear polarization profiles illustrate the overlying umbral field with the light bridge confined below. Such a configuration could facilitate a slingshot reconnection mechanism, as formulated by Ryutova et al. (2008a,b). This model was proposed as a possibel driver for the recently discovered penumbral microjet phenomena (Katsukawa et al., 2007b). As indicated by Ryutova et al. (2003), reconnection of magnetic field lines can occur, even if they have the same polarity. Additionally, one of the requirements of the model is that the parts of the flux tube participating in the reconnection should be as small as 150-200 km which is observed in the anomalous linear polarization profiles confined to a thin ridge along the LB. The question is where does the reconnection occur? If a reconnection geometry as depicted by Isobe et al. (2007) is assumed, then the height at which reconnection occurs can be estimated from the inclination of the magnetic field and the separation between the photospheric downflows and chromospheric brightenings. Let us consider the top most downflowing patch on the LB that is $\approx 2''$ or 1450 km, from the nearest chromospheric brightening. The inclination of the magnetic field is $\approx 120°$ to the vertical. Using these values, the height at which the reconnection occurs would be $1450 \times \tan 30°$ km or $\approx$ 840 km which is well within the formation height of the Ca II H line. This height is also well above the photosphere which is only 500 km thick. By the same argument, it can be shown that if reconnection occurs at a height of 840 km, then for fields which have an inclination of 165°, the distance between the chromospheric brightening and the downflows would be $\approx$ 225 km or $0.''3$, which is 2 SP pixels. This is precisely the case for the strongest downflowing patch that is co-spatial with the chromospheric brightenings. The chromosphere can facilitate reconnection as plasma β is less than unity at these heights. The photospheric downflows could be the result of downward propagating shocks resulting from the reconnection. Observations of the upper transition region and corona by EIS (EUV Imaging Spectrometer; Culhane et al., 2007) indeed show strong upflows in the He II 256 Å line above the LB (Matthews et al., 2010) which lends credence to the reconnection scenario. The supersonic downflows that occur at the umbra-penumbra boundary could be produced by a similar mechanism and it has been shown by Louis et al. (2010b) that such phenomena are common in sunspots, not necessarily having a light bridge. The chromospheric enhancements in the light bridge and its neighbourhood however, are much more stronger, long lived and persistent than the ubiquitous penumbral mircrojets.

The impact of the evolution of the LB on the photosphere and chromosphere was studied using light curves, from the G band and Ca II H filtergrams at two different locations. The time duration of 45 min encompasses the duration of the first SP scan of the LB. The light curve computed from the pixel at the entrance of the LB shows an increase in the Ca intensity that coincides with that in the G band. While the latter reaches a maximum, the former continues for 8 additional minutes before decreasing. One would expect this because of the fairly large height of formation of Ca which extends from the temperature minimum to around 10000 K at a height of $\approx$ 2000 km (Vernazza et al., 1981). The G band light curve from the pixel on the LB is much weaker in comparison to the one at the entrance. A correlation coefficient of $\approx$0.5 was measured between the Ca and G band light curves at this location. This is surprising since very strong enhancements occurred on the LB in the chromosphere but the corresponding intensity in the photosphere is only moderate. Similarly, light curves determined during the decay phase show the chromospheric intensity changing with time which is aptly seen before and after the LB disintegrated. The results presented here indicate that the LB could be responsible for an additional brightness of sunspots higher up in the atmosphere. Even though the photometric variations in the two heights are affected by the presence of the LB, the association is strictly not one-to-one. These have to be verified with additional cases as well as with more wavelengths to probe different heights.

The fragmentation of the LB is very similar to its formation (Katsukawa et al., 2007a) which is observed as a rapid retreat followed by a more gradual withdrawal. As the LB decays, it fragments into a number of umbral dots that appear brighter than the decaying LB. Even in the decay phase, the chromosphere displays a wide variety of brightenings both on the LB as well as in its immediate neighborhood although it is much more subdued in the LB as compared to observations seen by Louis et al. (2008), nearly 18 hrs earlier. The LB did not exhibit any strong velocities at this point of time. Observations by Shimizu et al. (2009) of the LB on April 29 and 30 show chromospheric jets on the eastern edge of the LB, but no strong velocities. It would thus imply that there are specific conditions under which strong downflows would be present along with the chromospheric brightenings.

The observations of supersonic downflows as well as the chromospheric and photospheric photometric analysis suggest that the LB is a highly dynamic entity that exhibits small scale magnetic and velocity inhomogeneities, that could play an important role in accounting for in-situ brightness of sunspots in the chromosphere. Moreover, the events leading to the fragmentation of the LB into umbral dots appear similar to its formation hinting at a specific sub-photospheric convective process powering it. The reconnection mechanism for producing the chromospheric enhancements and the supersonic downflows must be complemented with additional observations using *Hinode*, by acquiring high cadence (<10 sec) filtergrams, along with repeated spectropolarimetric scans of the LB.

Chapter 5

Structure of Penumbra in the Context of the Evershed Flow

5.1 Introduction

The Evershed Flow (EF) is an integral property of sunspot penumbrae. It is observationally seen as a shift of the spectral lines, due to the nearly horizontal, radial outflow of plasma (Evershed, 1909), that starts as upflows in the deep layers of the inner penumbra and ends in a ring of downflow channels at the outer edge of the penumbra (Schlichenmaier & Schmidt, 1999). Filter based velocity measurements indicate the quasi-periodic nature of the EF, wherein individual velocity packets are observed to propagate towards the periphery of the sunspot with velocities of 2 - 5.5 km s^{-1} (Rimmele, 1994) and vary on a time scale of 8-14 min (Rouppe van der Voort, 2003). The EF is believed to be closely associated to the fine structure of the penumbra (Solanki, 2003a). This association is seen in the form of the "uncombed geometry" (Solanki & Montavon, 1993) of the penumbra, wherein the radial outflow is predominantly confined to horizontal flux tubes embedded in a more stronger, vertical, background field which is essentially at rest (Westendorp Plaza et al., 2001b; Mathew et al., 2003; Bellot Rubio et al., 2003a). This model primarily accounts for the azimuthal as well as center-to-limb variations of the net circular polarization of sunspot penumbrae (Borrero et al., 2007). The background field and the embedded tubes are referred to as the "spines" and "intraspines" respectively (Lites et al., 1993). A natural ingredient of the "uncombed geometry" is the manner in which the spines tend to fold around the intraspines (Martínez Pillet, 2000), that was recently confirmed by Borrero et al. (2008a). According to Spruit & Scharmer (2006) the intraspines are a consequence of convection taking place in radially aligned field free gaps below the visible surface and thus coin the penumbra as a "gappy" structure. The MISMA hypothesis of Sánchez Almeida (2005) puts forth the argument that the manifestation of the EF in the form of upflows and downflows, arises from the unresolved structure of the penumbra. High resolution observations, however, have established that the bright penumbral filaments, in fact, consist of a central dark core (DC; Scharmer et al., 2002) which harbor the hot EF (Bellot Rubio et al., 2005; Langhans et al., 2007; Bellot Rubio et al., 2007). Langhans et al. (2007) point out that the visibility of the penumbral DCs degrades with increasing heliocentric distances which arise from a 3D geometrical effect and not due to the formation height effect.

Furthermore, the transport of energy from the sub-photosphere into the penumbra still remains one of the most intriguing problems in sunspot physics. It has been pointed out that overturning convection in the form of rolls (Zakharov et al., 2008; Scharmer, 2009) could explicate the radiative flux as well as the fine structure of the penumbra which was illustrated in the simulations of Scharmer et al. (2008). This aspect was recently demonstrated by realistic 3D MHD simulation of sunspots by Rempel et al. (2009a,b) who point out that the EF is a component of the convective flow that results from an anisotropy introduced by the presence of inclined magnetic fields. On the other hand, the surplus brightness can also be explained by the hot EF in the context of the "uncombed" model (Ruiz Cobo & Bellot Rubio, 2008) which accounts for the surplus brightness of the penumbra as well as DCs. The physical mechanism responsible for the EF has been described in terms of the "siphon-flow" model (Montesinos & Thomas, 1997; Montesinos & Thomas , 1993; Thomas & Montesinos, 1993) and the "moving-tube" model (Schlichenmaier et al., 1998a,b). While the former comprises of a flow along an arch that is essentially driven by a gradient in gas pressure at the footpoints, the latter describes the dynamic evolution of a flux tube that is initially located at the magnetopause and gradually rises and migrates towards the umbra. The "moving-tube model" is based on the concept of interchange convection (Jahn & Schmidt, 1994) wherein heat is distributed laterally through the magnetopause into the penumbra by an interchange of flux tubes. Both models have to a great extent explained several interesting observations. A consequence of the "siphon-flow" model is that the flux tubes can either return to the photosphere well within the penumbra (Westendorp Plaza et al., 1997), extend as far as 10 Mm beyond the visible sunspot boundary (Rimmele, 1995), produce supersonic velocities near the outer penumbral boundary (del Toro Iniesta et al., 2001; Borrero et al., 2005) or continue beyond the sunspot with supersonic velocities (Martínez Pillet et al., 2009). On the other hand the "moving-tube" model is validated by observations of supersonic flows well within penumbra (Bellot Rubio et al., 2004), with high resolution dopplergrams of the limb side penumbra (Rimmele & Marino, 2006), with magnetograms taken at the far blue wing of the Stokes V profile (Ichimoto et al., 2007a) and recent observations of Beck (2008). It has however, been pointed out by Schlichenmaier & Solanki (2003) that, while pure interchange convection is unable to account for the radiative flux of the penumbra, steady upflows along magnetic flux tubes are sufficient to explain the brightness as long as the magnetic return flux lies within the penumbra.

It is necessary to remember that the elucidation of the physical structure of the penumbra is strictly based on the manner in which the polarization signals are interpreted by the inversion codes (ICs). The result of using different model atmospheres, required for the spectral synthesis, could infer completely different scenarios, particularly, if the physical structure is not spatially resolved (Bellot Rubio et al., 2004; Cabrera Solana et al., 2008). In such scenarios a single component atmosphere with gradients along the LOS cannot be differentiated from a 2 component atmosphere without gradients (Borrero et al., 2004). One such instance is that of the Evershed clouds (ECs), enhanced LOS velocity signals, which can in fact be wrongly construed as perturbations to the magnetic structure along which they move, based on a single component atmosphere that uses height independent parameters (Cabrera Solana et al., 2008, refer to Cabrera Solana et al. (2007) for the general properties of ECs). In this chapter, I address the issue of field free/weak field intrusions in the penumbra as well as the physical properties of the Evershed flow, based on SIR inversions of the Stokes profiles from a small region of the disc side penumbra of a regular sunspot. Although Borrero & Solanki (2008b) had performed a similar analysis, for a region in the

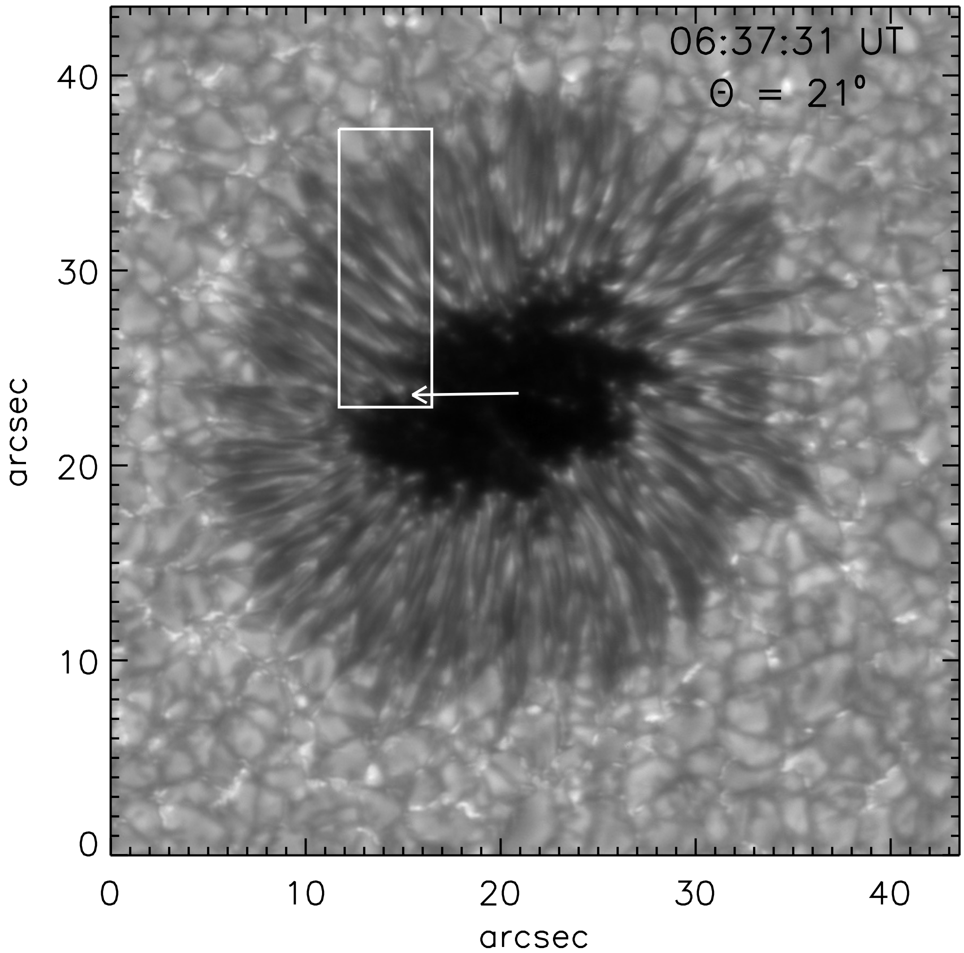

Figure 5.1: G band image of sunspot in NOAA AR 10944. The white box denotes the $4.8'' \times 14.4''$ area of the center side penumbra that was chosen for the analysis. The arrow points to disk center.

limb side of a different active region, the model atmospheres they chose are different from the ones described in this chapter. Sections 5.5.3 and 5.5.4 illustrate the spectral properties and temporal evolution of ECs, while the coherence of the time averaged penumbral fine structure and its association to the Evershed flow are presented in Sections 5.5.5 and 5.5.6.

5.2 Observations

Spectropolarimetric observations of the sunspot in NOAA Active Region 10944 were carried out using the Solar Optical Telescope (SOT; Tsuneta et al., 2008) on board *Hinode* (Kosugi et al., 2007), on 2007 March 2. The sunspot was located at a heliocentric angle of 20° ($\mu = 0.94$). Data pertaining to a 10.24″ wide area of the sunspot was used, that was mapped repeatedly by the spectropolarimeter (SP; Lites et al., 2001; Ichimoto et al., 2008) from 6:35 UT to 10:50 UT. This region included a part of the center side of the sunspot and the neighbouring photosphere. At each slit position, the four Stokes profiles of the neutral iron lines at 630 nm were recorded with a spectral sampling of 21.55 mÅ, a pixel size of 0.″16, and an exposure time of 4.8 s. The observations were corrected for dark current, flat field, thermal flexures, and instrumental polarization using routines included in the SolarSoft package. The Level-1 data thus consisted of 46 time sequence scans, each scan being 64×512 pixels in size which were subsequently registered using a 2D cross correlation routine. G band filtergrams acquired during the above time duration by the BFI (Broad band Filter Imager) were also utilized. The filtergrams have a sampling of 0.″1 and a cadence of 1 min.

5.3 Inversions using a single component atmosphere

The left panel of Figure 5.1 shows the G band image of the sunspot and the smaller sub-region (30×90 pixel) of the center-side penumbra that was scanned by the SOT-SP. A wavelength calibration was first performed in the following manner. The average quiet Sun profile was determined from those pixels where the polarization signal was less than 3σ. Using the wavelength sampling of 21.5mÅ and the rest wavelength of the 6302.5Å Fe line, the wavelength scale was determined. This was then used to compute the convective blue shift using the 2 component model of the quiet Sun, as described by Borrero & Bellot Rubio (2002) and subsequently corrected for the heliocentric position of the sunspot (Balthasar, 1988). This procedure yielded a value of -225 m s^{-1} and the corrected wavelength scale was used in the inversions. The Stokes profiles from each of the 46 time sequence scans were inverted using the SIR code (Stokes Inversion based on Response Functions; Ruiz Cobo & del Toro Iniesta, 1992). I assume that the penumbral region chosen for the analysis is spatially resolved and use a single component atmosphere in each pixel. Each of the 46 time sequences were subjected to two sets of inversion. In the first, the following parameters namely, field strength, inclination, azimuth, LOS velocity were provided one node each, i.e., they are assumed to be height independent. Apart from these, the code also retrieved a height independent micro and macro turbulent velocity and an additional parameter in stray light. Temperature alone was perturbed with two nodes. This set of inversions will be referred to as SIR-1. In the second set, temperature was provided with five nodes, while field strength and LOS velocity were given three nodes each. Inclination and azimuth were given two nodes each. This set of inversions, referred to as SIR-2, also retrieved height independent micro and macro turbulent velocities and a stray light factor similar to the SIR-1 inversions. As can be seen, SIR-1 is similar to inversions based on a Milne-Eddington atmosphere which provide parameters that are essentially averaged along LOS (Westendorp Plaza et al., 1998). These are particularly useful in providing an overall view of the spatial organization of the penumbra and in particular, to identify regions that essentially harbor the EF. Figure 5.2 illustrates the physical parameters retrieved by SIR-1 for each time sequence, while Figures 5.3 to 5.5 depict the parameters derived from the SIR-2 inversions. In what follows, a detailed analysis of the penumbral structure is derived from the results of SIR-2 inversions.

5.4 Defining the Normalized Radial Distance

G band filtergrams were used in order to determine the radial position of each pixel. Since each sequence mapped by the spectropolarimeter takes ≈ 5.2 minutes, there are five G band images acquired by the BFI during that time which were subsequently scaled and aligned with the continuum maps. First the visible part of the penumbra was chosen from the continuum maps, after which the umbra-penumbra boundary and penumbra-photosphere boundary were selected. This was also done with the G band image, acquired closest to the start of each sequence, so as to match the same in the continuum map. The following

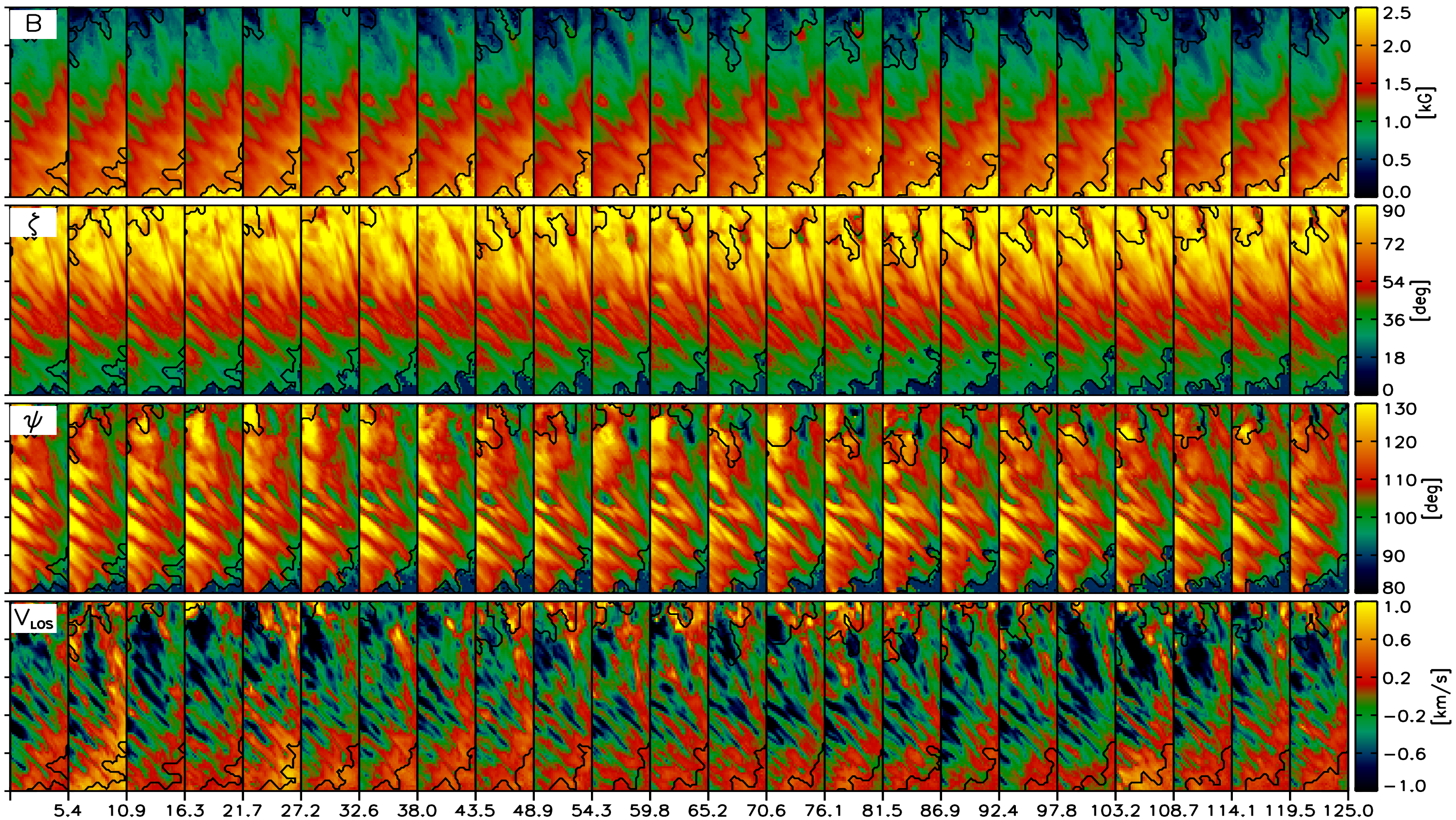

Figure 5.2: Maps of the physical parameters derived from the SIR-1 inversion. *From top to bottom:* Field Strength, zenith angle, azimuth and LOS Velocity respectively. The numbers along the x-axis at the bottom panel indicate time in min. The images have been scaled as shown in their respective colour bars. The angles have been transformed to the LRF. Solar west is to the right and north is up. The azimuth increases in the counterclockwise direction from the west. The black contours denote the umbra-penumbra and penumbra-photosphere boundary.

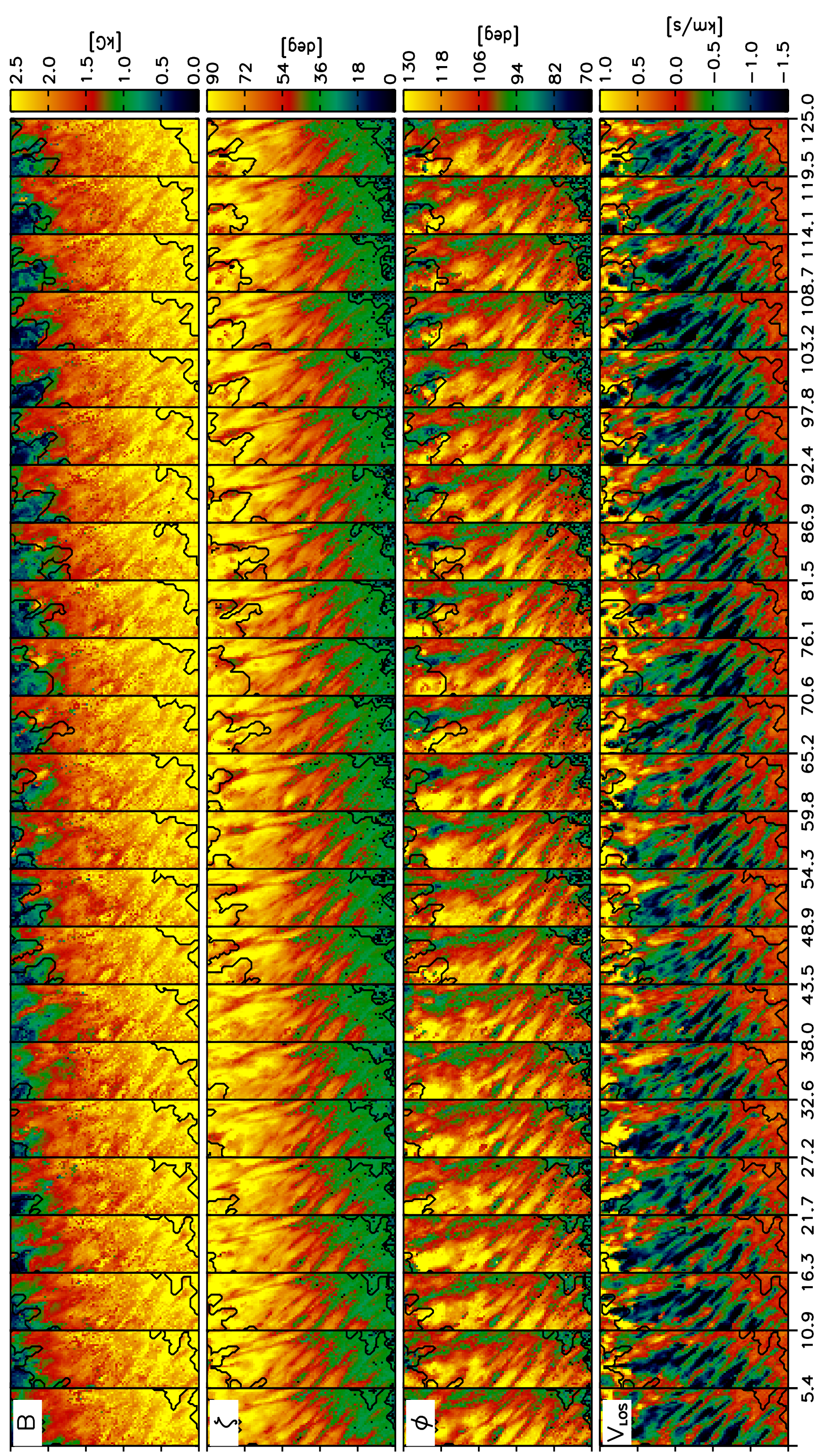

Figure 5.3: Same as Figure 5.2 but derived from the SIR-2 inversion. The physical parameters have been averaged between the $\log\tau = 0$ and $\log\tau = -0.5$ layers.

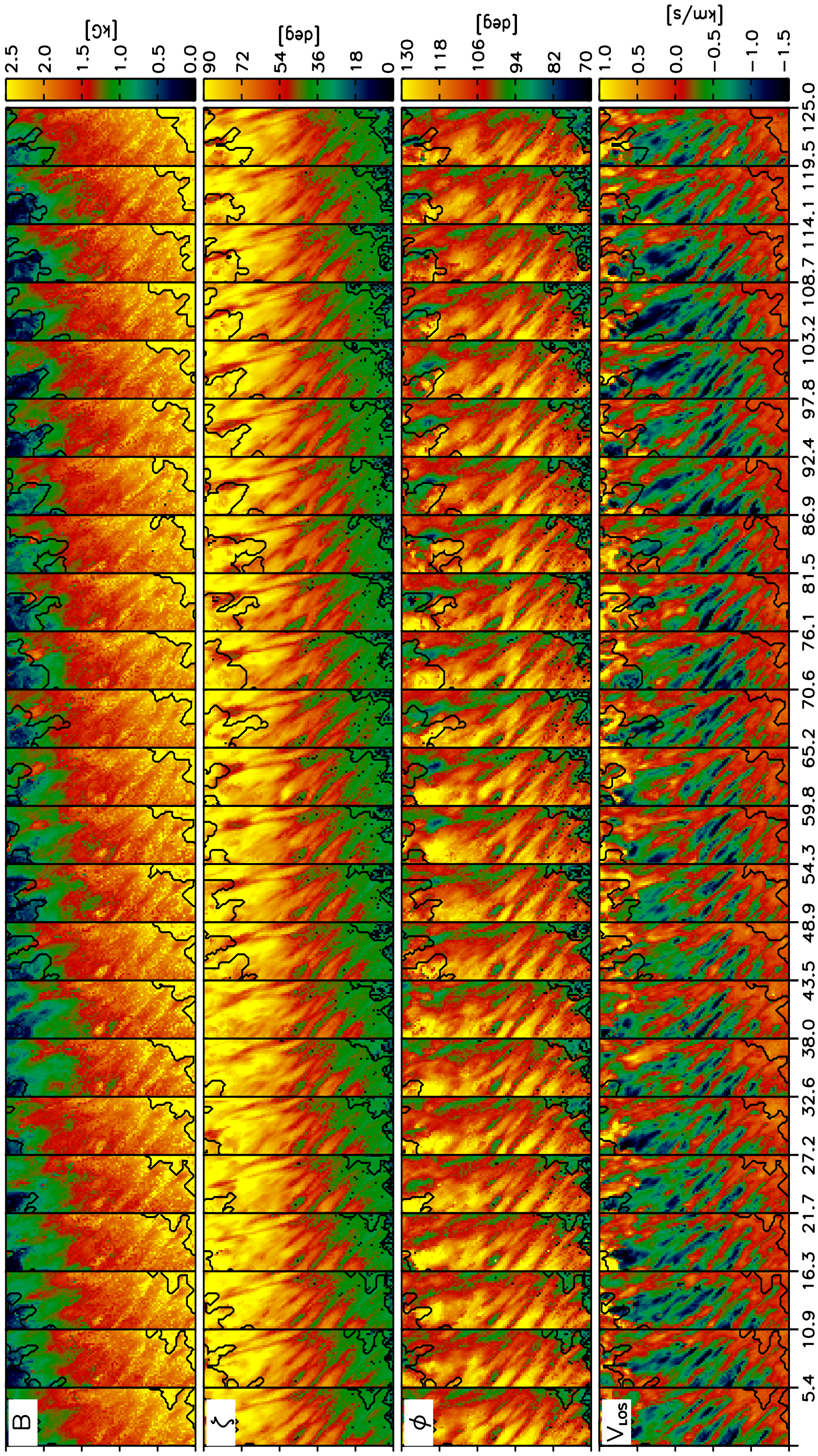

Figure 5.4: Same as Figure 5.3 but the physical parameters have been averaged between the logτ = -0.5 and logτ = -1.0 layers.

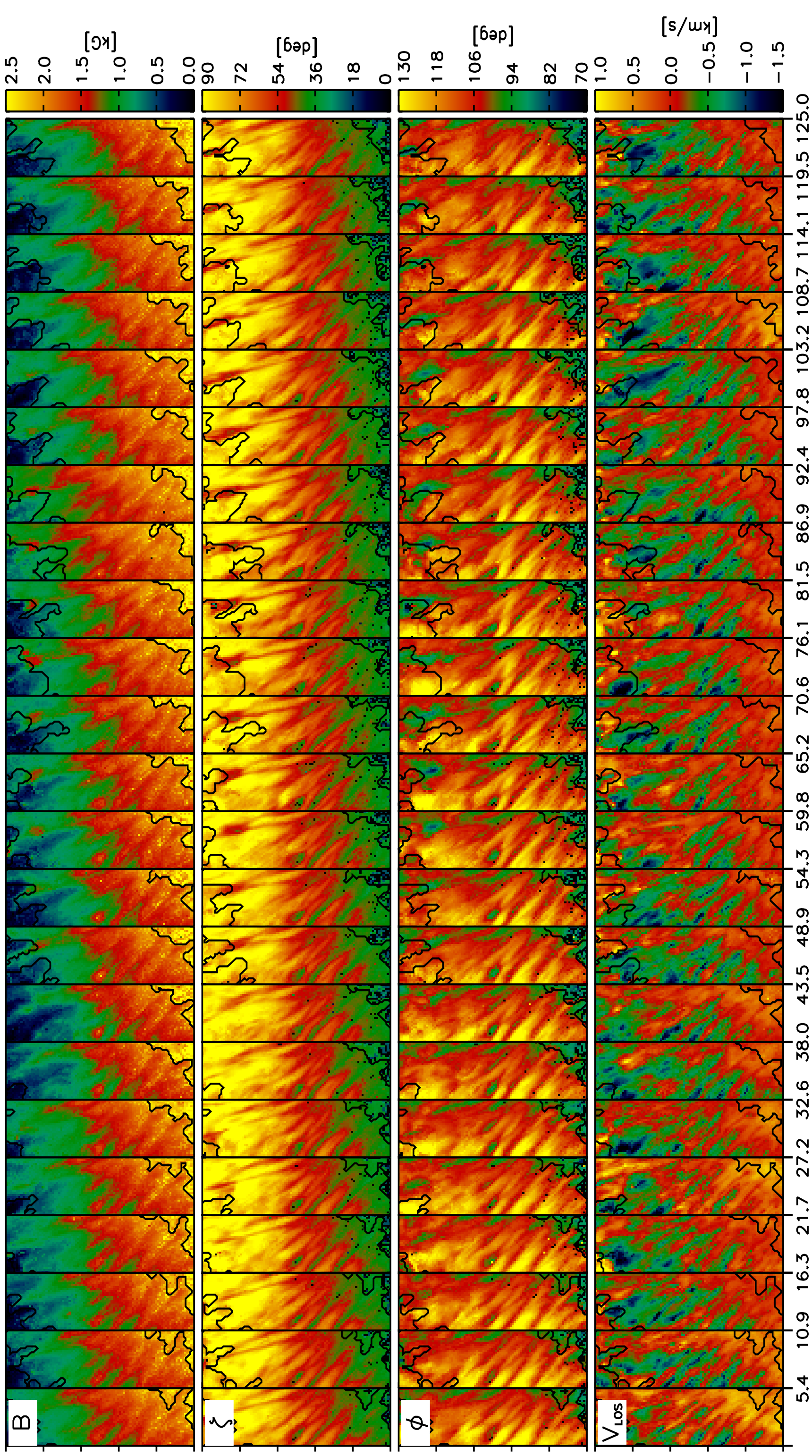

Figure 5.5: Same as Figure 5.3 and 5.4 but the physical parameters have been averaged between the $\log\tau$ = -1.0 and $\log\tau$ = -1.5 layers.

procedure was then adopted to compute the normalized radial distance. For each time, sequence a binary image was made from the G band filtergram, wherein all pixels within the visible penumbra were set to one and those outside it were set to zero. For each penumbral pixel, the nearest pixel on the umbra-penumbra boundary was determined. After calculating the angle between these two points and the vertical, the radial line connecting the points was extended outwards in steps of one pixel. This was carried out till the value of the pixel changed from one to zero, which would imply that the corresponding point on the penumbral-photosphere boundary was reached. For pixels lying in the photosphere the same procedure was used except that the radial vector was incremented inwards. As pointed out by Centeno et al. (2009) the slit of the spectropolarimeter is rotated by 0.26° in the clockwise direction to the vertical axis of the G band image. My analysis, however, is restricted to 90 pixels along the slit which would imply that the relative shift in the G band image is less than half a pixel. Moreover the horizontal direction comprises of only 30 pixels or 30 slit positions, hence constructing a composite G band image from images closest to each slit position was not necessary.

5.5 Results

5.5.1 Penumbral Spine and Intraspine Structure

For each time sequence only the visible part of the penumbra was chosen, within which, pixels exhibiting negative inclination stratifications were avoided. Bad pixels account for less than 3% of the total area. The inclination and azimuth were subsequently transformed to the local reference frame (LRF). The physical parameters retrieved from the inversion were averaged over various optical depths corresponding to $-0.5 < log\tau < 0$, $-1.0 < log\tau < -0.5$, $-1.5 < log\tau < -1.0$ and $-2.0 < log\tau < -1.5$ respectively, as shown in Figure 5.6 for one particular time sequence. As is evident, the fine structure of the penumbra is more prominently seen in the zenith angle and azimuth maps at optical depths of logτ = -1.0 to -2.0 which correspond to the heights where the Fe line is formed (Westendorp Plaza et al., 2001a). As shown in the bottom right panels of Figure 5.6, the

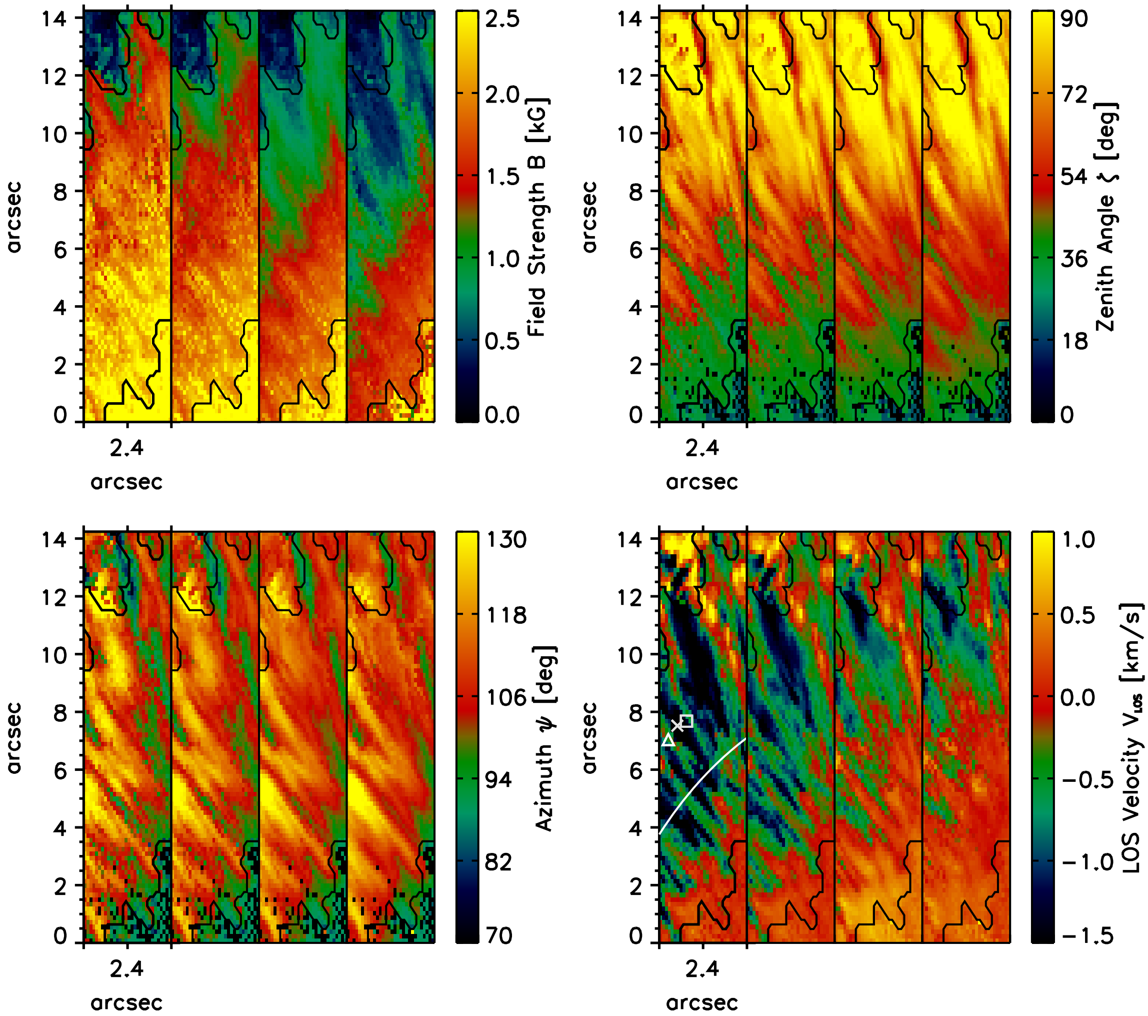

Figure 5.6: The four panels represent the field strength (**top left**), zenith angle (**top right**), azimuth (**bottom left**) and LOS velocity (**bottom right**) respectively of sequence no. 20 that was mapped by the spectropolarimeter from 8:26 UT to 8:32 UT. The 4 sub panels (**from left to right**) correspond to the optical depth ranges of $\log\tau = 0.0$ to -0.5, -0.5 to -1.0, -1.0 to -1.5, -1.5 to -2.0 respectively. The images have been scaled as shown in their respective colour bars. The white *triangle*, *square* and *cross* symbols in the bottom right panel represent the spine, intraspine and Evershed Cloud respectively. The arc marked in white represents a radial distance of $0.33R_P$.

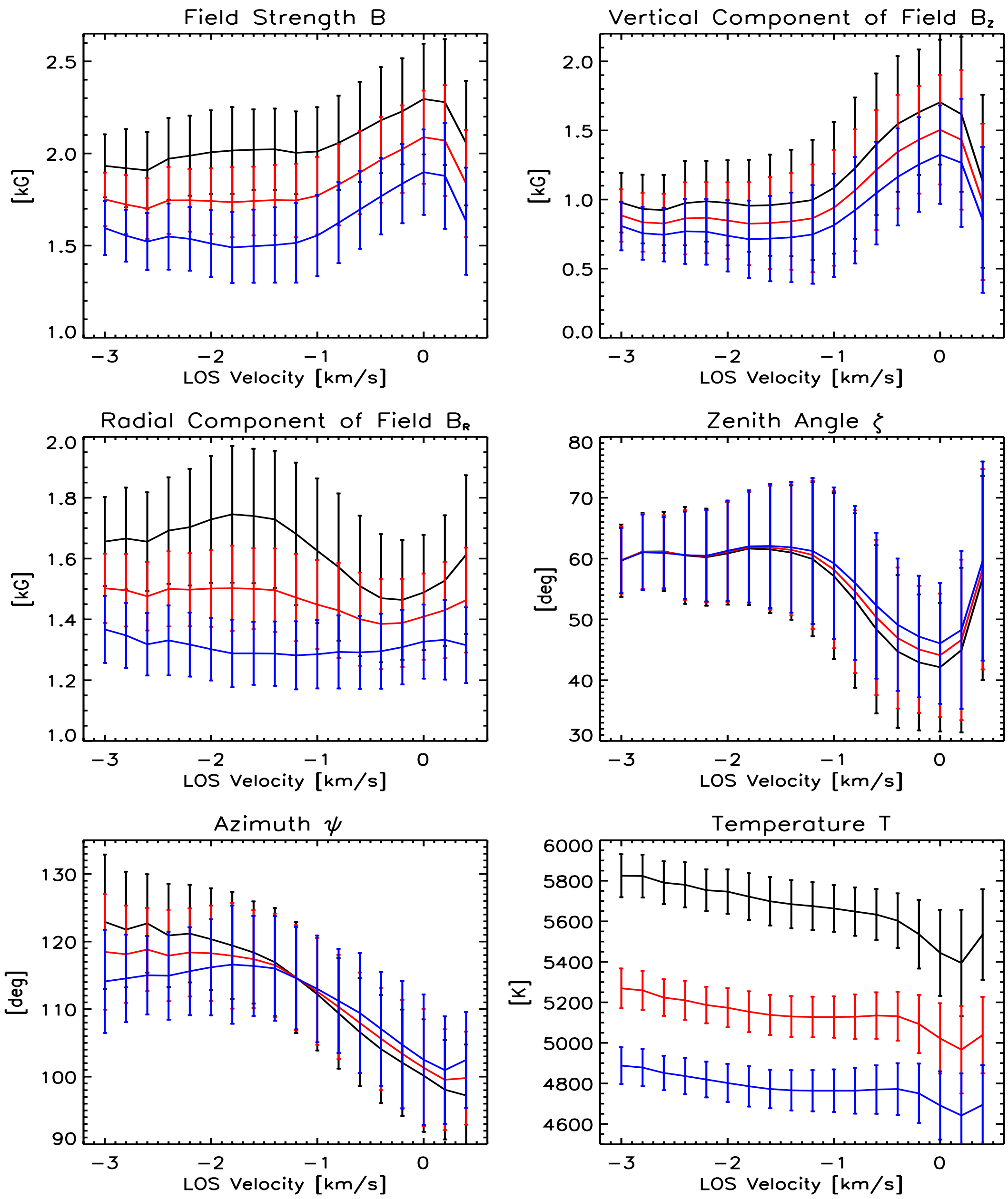

Figure 5.7: Distribution of physical parameters with LOS velocity. Black, red and blue correspond to the parameters averaged over $\log\tau = 0$ to -0.5, -0.5 to -1.0 and -1.0 to -1.5 respectively. The vertical bars correspond to the *rms* values in each velocity bin. Bin size is 200 m s^{-1}.

Table 5.1: Mean errors in the physical parameters at different optical depths.

Parameter	logτ		
	0.0	-0.5	-1.0
Field Strength (G)	182	106	81
Zenith Angle (deg)	6	6	6
Azimuth (deg)	12	11	11
LOS Velocity (m/s)	282	167	140
Temperature (K)	13	29	37

EF is clearly confined to the deep layers particularly in the logτ = 0 to -1.0 region. In order to statistically derive the association of the penumbral intraspines with the EF, the physical parameters namely, field strength (B), the vertical component of the magnetic field (B_z), the radial component of the magnetic field (B_R), zenith angle (ζ), azimuth (ψ) and temperature (T) were averaged between logτ = 0 to -0.5, -0.5 to -1.0 and -1.0 to -1.5 respectively and subsequently binned with the LOS velocity that in turn was averaged between logτ = 0 to -0.5. Figure 5.7 depicts the distribution of the physical parameters with LOS velocity along with the *rms* values in each velocity bin. As is apparent, there exist 2 distinct velocity components in the penumbra. The component that is essentially at rest corresponds to the penumbral spines while the intraspines are characterized by strong upflows greater than 1.5 km s^{-1}. Although the results presented below were derived from a limited region of the penumbra, the 4 hr. observing run, ensures that a satisfactory statistic can be constructed as there are sufficient data points in the large velocity bins.

The mean 1σ error computed from the inversions at various optical depths is summarized in Table 5.1. The large errors associated with the field strength arise as the Stokes profiles are less sensitive to B in the deep layers, which is a characteristic of the Response Functions (Westendorp Plaza et al., 2001a; del Toro Iniesta, 2003a). Table 5.2 illustrates the magnitude of the physical parameters along with their *rms* values for velocity bins corresponding to 0 and -2 km s^{-1} that represent the spine and intraspine structures respectively. The field strength in the spines decreases from $\approx$ 2300 G at $-0.5 < log\tau < 0$ to 1900 G at $-1.5 < log\tau < -1.0$, while for the intraspines, the field strength reduces by 500 G for

Table 5.2: Mean value of physical parameters and their r.m.s values averaged at different heights and binned against mean LOS velocity in the logτ = 0.0 to -0.5 range. The physical parameters correspond to pixels lying in the inner and mid penumbra i.e. $0 < r < 0.6R_P$. The spine and intraspine components refer to quantities corresponding to velocity bins 0 and -2 km s^{-1} respectively.

Parameter	logτ<0.0 to -0.5>		logτ<-0.5 to -1.0>		logτ<-1.0 to -1.5>	
	Spine	Intraspine	Spine	Intraspine	Spine	Intraspine
Field Strength B (G)	2296±301	2007±227	2088± 253	1742± 178	1899±232	1511±181
Vertical Component of Field B_Z (G)	1704±452	976±308	1505±395	848±277	1325±356	738± 258
Radial Component of Field B_{RAD} (G)	1488±190	1729±209	1409±142	1502±126	1327±122	1302± 103
Zenith Angle (deg)	42±11	61±8	44±10	61±8	46±10	61±8
Azimuth (deg)	100±8	120±8	101±9	118±7	103±10	116±7
Temperature (K)	5444±213	5746±110	5022±174	5174±97	4691±168	4803±94

same depth range. The zenith angle and the azimuth practically remain constant for the above mentioned layers for both spines and intraspines. The temperature however reduces by $\approx$ 700 K and 1000 K for the spines and intraspines respectively as illustrated in Table 5.2. In the deep layers ($-0.5 < log\tau < 0$), the intraspine regions of the penumbra that harbor the EF, are 300 G weaker, inclined by 17° and 300 K hotter, relative to the penumbral spines which is in good agreement with the results of Westendorp Plaza et al. (2001a); Bellot Rubio et al. (2005). Downflows of the order of 1 km s^{-1} are seen in some regions, at $\log\tau = 0$, particularly where the fields are fairly horizontal. It is imperative to mention here that the pixels that were used to construct the distribution essentially belong to the penumbral region defined by $0 < r < 0.6R_p$. This was done by changing the penumbral radius gradually from $0.3R_p$ to $1.0R_p$ and selecting the radial distance at which the differences in the spine and intraspine properties became indistinguishable from the computed uncertainties. It should be kept in mind that the errors expressed in Table 5.1 arise from the synthesis of the model atmosphere to fit the observed Stokes profiles whose nature is described in detail in Section 5.5.3.

Figure 5.8 shows the stratifications of the physical parameters corresponding to the spines and intraspines. Only those pixels lying within a radial distance of 0.6 R_P were utilized. The pixels were selected as spines and intraspines if $-0.5 < V_{\rm LOS} < 0.5$ km s^{-1} and $V_{\rm LOS} < -1.5$ km s^{-1} respectively. The field strength reduces monotonically from 2370 G at $\log\tau$=0 to 1606 G at $\log\tau$=-2.0 for the spines while for the same heights the field strength of the intraspines are 2178 G and 1290 G respectively. The zenith angle of the spines becomes relatively inclined by $\approx$ 10° in comparison to the intraspines which practically remains a constant with height. The temperature difference at $\log\tau$ = 0 and $\log\tau$ = -2.0 exceeds 1500 K for the spines as well as intraspines. As can be seen the overall trend in the height variation of the physical parameters is dictated by the model atmosphere that was employed in SIR-2 and the relatively small scatter in the observed quantities is evidence for the same.

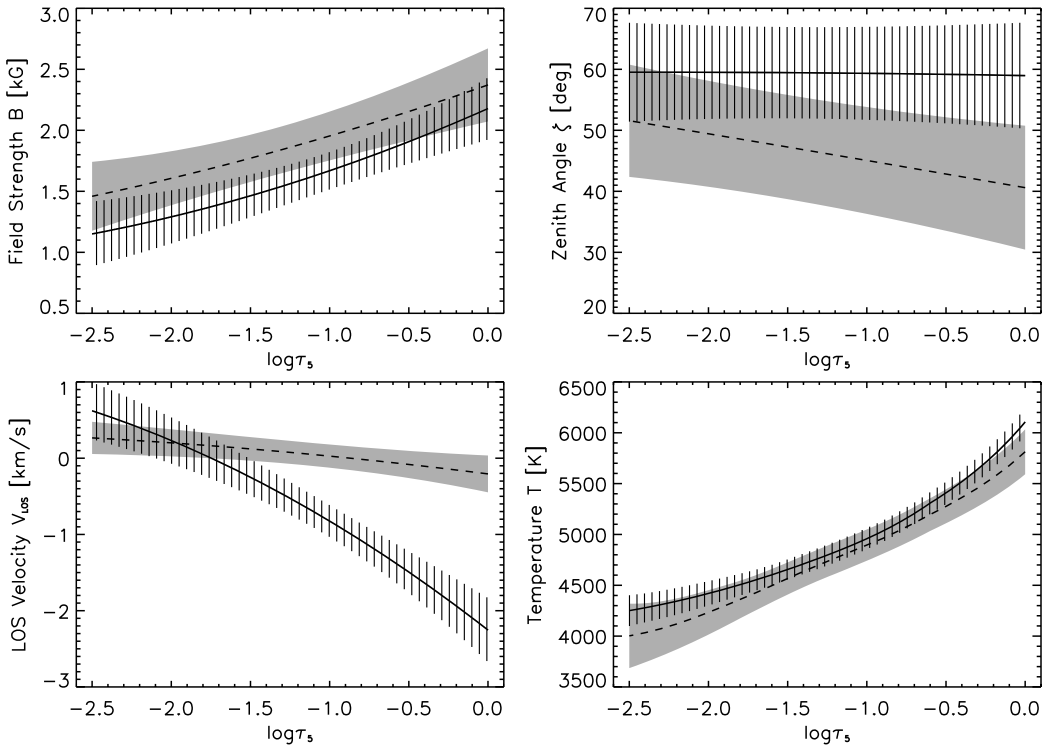

Figure 5.8: Mean Spine (*dashed*) and Intraspine (*solid*) stratifications derived from SIR-2. The vertical bars and grey shaded areas correspond to the *rms* values.

5.5.2 Radial Variation of Parameters

The radial distribution of the physical parameters is shown in Figure 5.9. The radial distance, used for binning the observed quantities, was calculated as described in Section 5.4. As in Figure 5.7, the distribution is shown for three different layers which is depicted in the top left panel of Figure 5.9. The *rms* values in each radial bin, represented as the hatched lines, have been drawn only for $-0.5 < log\tau < 0$ and $-1.5 < log\tau < -1.0$ respectively. The field strength shows a monotonic decrease with radial distance at all heights, from a value of 2374$\pm$213 G at r/R_p=0 to 1056$\pm$401 G at r/R_P=1 corresponding to $-0.5 < log\tau < 0$. A similar trend is seen in the vertical component of the magnetic field which reduces from 1887$\pm$216 G at the umbra-penumbra boundary to 263$\pm$388 G at the penumbra-photosphere boundary respectively. The radial component of the magnetic field (B_R) on the other hand shows an increase from 1432$\pm$152 G at r/R_P=0 to 1678$\pm$251 G at r/R_P=0.4 as shown in the top right panel of Figure 5.9. B_R then gradually falls off to 976$\pm$321 G at the penumbra-photosphere boundary. The increase in the radial component from the umbra-penumbra boundary to the mid-penumbra and the gradual decrease to the periphery of the sunspot is more prominent in the deep layers corresponding to $-0.5 < log\tau < 0$ and the trend diminishes with height.

The zenith angle (ζ) increases monotonically from 37$\pm$4° at the umbra-penumbra boundary to 80$\pm$10° at r/R_P=0.8, after which it nearly remains a constant. This behaviour in the radial variation of ζ is seen in the other higher layers as well. However when a running difference of ζ is taken with consecutive radial bins, one finds an inflection point at $r/R_P = 0.3$ that corresponds to $\Delta\zeta \approx 8°$, which then gradually decreases. When the cosine and sine of $\Delta\zeta$ is computed it is seen that the inflection point stands out very clearly in the latter while it is absent in the former. This explains the increase in the radial component of the magnetic field (B_R) which essentially goes as $\sin\zeta$. The azimuth (ψ) on the other hand practically remains a constant with radial distance for all heights, which is expected since the information is restricted to a small portion of the penumbral region. The large spread in the *rms* values, however, indicate the presence of the spines

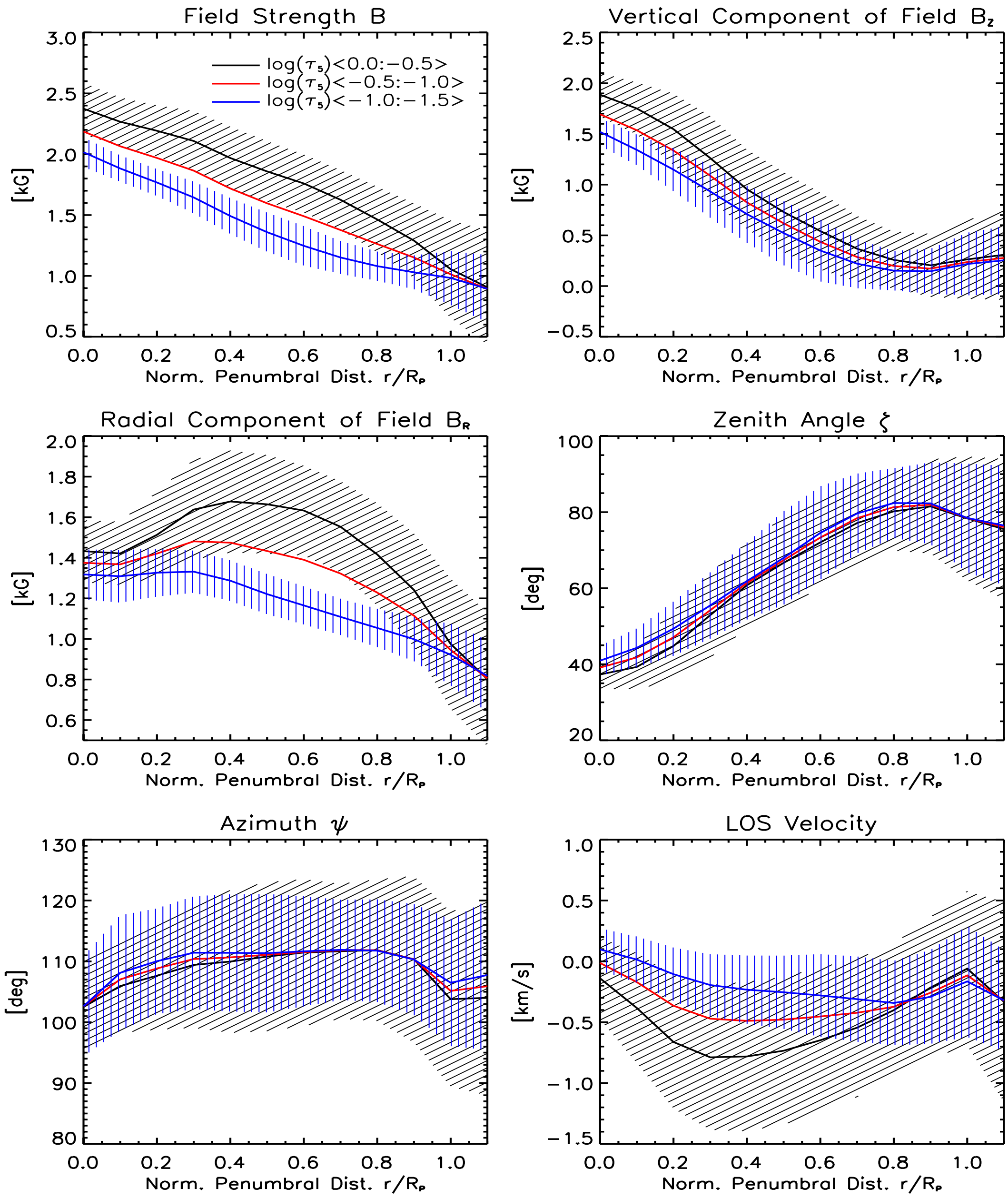

Figure 5.9: Radial variation of physical parameters averaged over different heights. 0 and 1 in the x-axis correspond to umbra-penumbra and penumbra-photosphere boundaries respectively.

and the more radially oriented intraspines. This aspect will be discussed in Section 5.5.3. The lower right panel of Figure 5.9 shows the radial distribution of the LOS velocity at different heights. In the deep layers the LOS velocity increases to 789±595 m s^{-1} at r/R_P=0.3, quite similar to the increase in the radial component of the magnetic field. With increasing radial distance $V_{\rm LOS}$ reduces with a large *rms* value of 635 m s^{-1} at the outer penumbral boundary. In comparison the velocities are much smaller in the subsequently higher layers.

5.5.3 Characteristics of Spines, Intraspines and Evershed Clouds

Three pixels marked in white symbols in Figure 5.6 denote the spine (*triangle*), intraspine (*square*) and Evershed cloud (*cross*) respectively. The qualitative differences between these structures can be inferred from their respective Stokes profiles which is illustrated in Figure 5.10. The linear polarization signals from the spines are much weaker than the intraspines and the Evershed Clouds (ECs), which would imply that the field is relatively vertical. This is also seen in the circular polarization signals which are relatively stronger than those from the intraspines and the ECs. More importantly, the enhanced LOS velocity signals that characterize the ECs, exhibit anomalous Q profiles. The proximity of the model atmosphere used in the inversions, to the physical one is evident from the fit to the Q profile as illustrated in Figure 5.10. The asymmetric Q profiles could possibly arise from a mixing of polarimetric signals from the EC and the spine structure along LOS, which would be the case for the sunspot that is located marginally away from the disk center. This is demonstrated in the large change in azimuth from from 140±5° at logτ = 0 to 99±5° logτ = -2.0, while the spine and intraspine vary from 91±13° to 101±12° and 125±4° to 123±4° respectively. Figure 5.11 depicts the stratification of the spine, intraspine and EC.

In order to compute the flow velocity $V_{\rm FLOW}$ from the LOS component $V_{\rm LOS}$, the relation described by Tritschler et al. (2004) was employed and modified to

$$V_{\rm LOS}(r,\phi) = V_{\rm FLOW}(r,\phi)[\sin\gamma\cos\phi\sin\theta + \cos\gamma cos\theta] \tag{5.1}$$

where γ and ϕ are the inclination and azimuth in the LOS frame and θ is the heliocentric angle. It is assumed that the flow has a variation in the radial

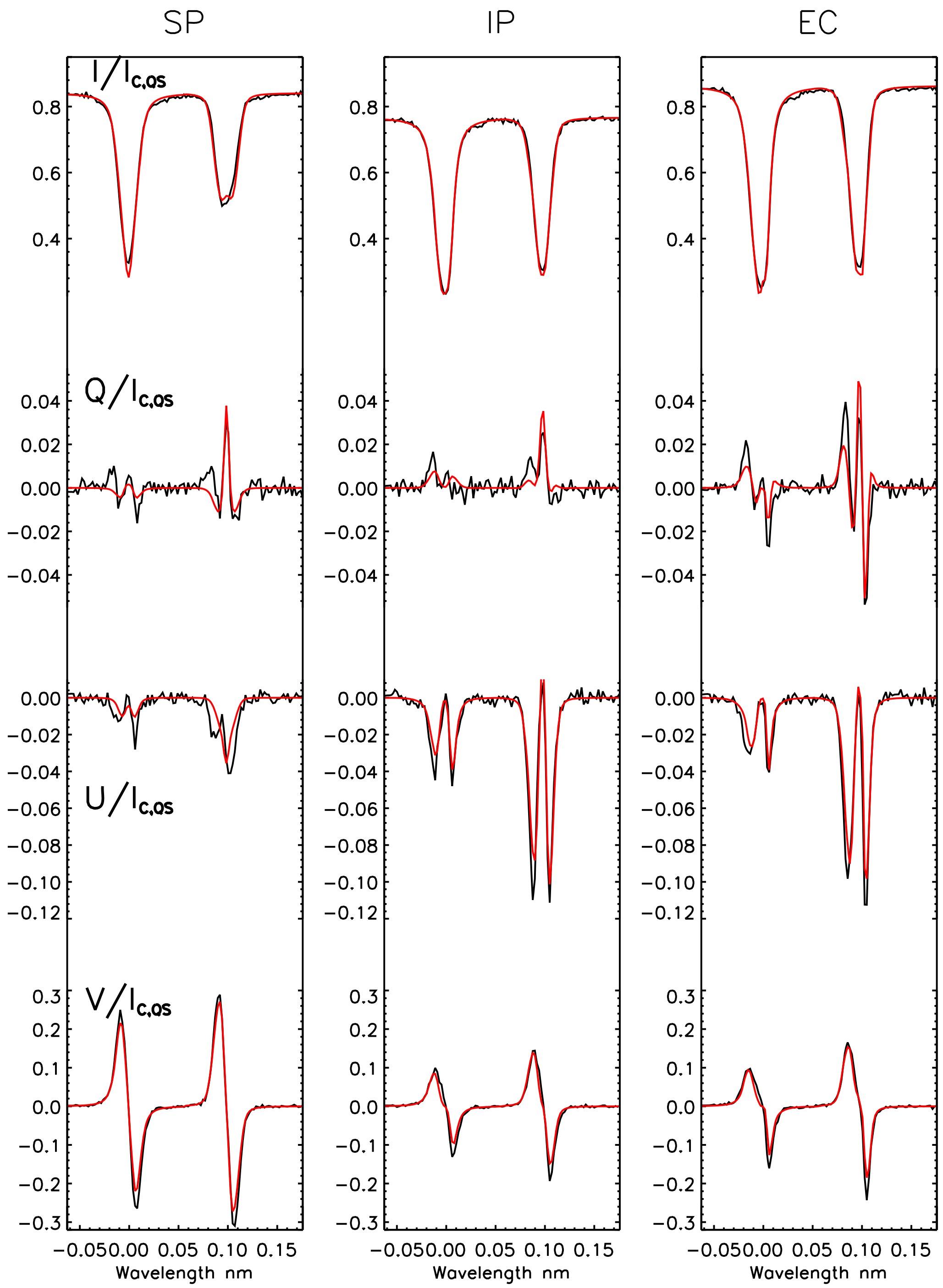

Figure 5.10: Observed (*black*) and Inverted (*red*) profiles corresponding to the spine (**SP**), intraspine (**IP**) and EC (**EC**) pixel marked in Figure 5.6.

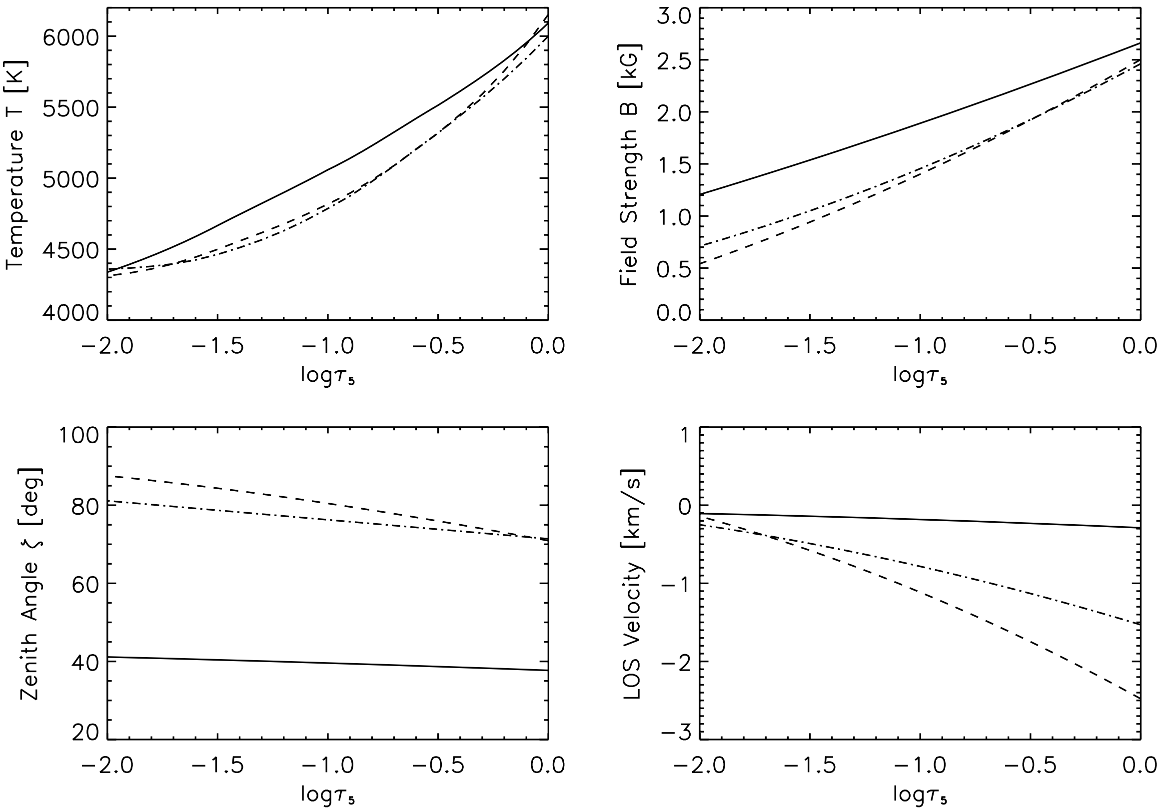

Figure 5.11: Stratification of the spine (*solid*), intraspine (*dashed-dot*) and EC (*dashed*) pixel marked in Figure 5.6.

and azimuthal direction as is evident from the LOS velocities along the arc of constant radius shown in Figure 5.6. In addition the $\sin\phi$ term in Equation 2 of (Tritschler et al., 2004) has been changed to $\cos\phi$, such that the limb and center side penumbra correspond to 0° and 180° respectively, measured in the counterclockwise direction. Equation 5.1 is justified since the plasma is essentially frozen with the field as pointed out by Bellot Rubio et al. (2003a). Using values of -2.5 km s^{-1}, 59°, 148° and 20.7° for V_{LOS}, γ, ϕ and θ respectively for the logτ = 0 layer, it turns out that the flow velocity is supersonic with a value of $\approx$ -11 km s^{-1}. It also appears that the ECs have the same physical properties as the intraspines, with the velocity being the only distinction. This aspect is further discussed in Section 5.5.4.

5.5.4 Perturbative Nature of ECs

The top panel of Figure 5.12 illustrates the temporal evolution of an EC along the penumbral intraspine. The EC is located at $r = 0.37R_P$. Between sequence 17 and 18, it is observed that the EC completely disappears but in the very next sequence it emerges very conspicuously along the intraspine. It appears to move radially in the next sequence. Sequence 20 illustrates a new EC, which in fact occupies the spatial position of the previous one. The period of $\approx$ 23 minutes demonstrates the rapid transition of ECs. The Stokes profiles corresponding to the EC in sequence 18 exhibit highly anomalous Q profiles, an asymmetric U profile and a V profile that has an extended blue lobe, indicative of a faster blue-shifted component along LOS (Figure 5.13). This is in contrast to the regular profiles emanating from the same pixel in the previous sequence. The asymmetric profiles are also seen in sequence 19 but of reduced strength, that may be associated with the trailing of the EC along the intraspine. The LOS velocity, field strength, zenith angle, azimuth and temperature measured in sequence 18 are -3.93±0.5 km s^{-1}, 1770±325 G, 81±10°, 151±11° and 5763±23 K respectively. The values correspond to averages between the logτ = 0 and logτ = -0.5 layer. Substituting these values in equation 5.1, one obtains very large flow velocities exceeding 20 km s^{-1}. For sequence 17 on the other hand the respective values are -1.0±0.44 km s^{-1}, 1832±244 G, 60±8°, 125±10°, 5681±16 K. This

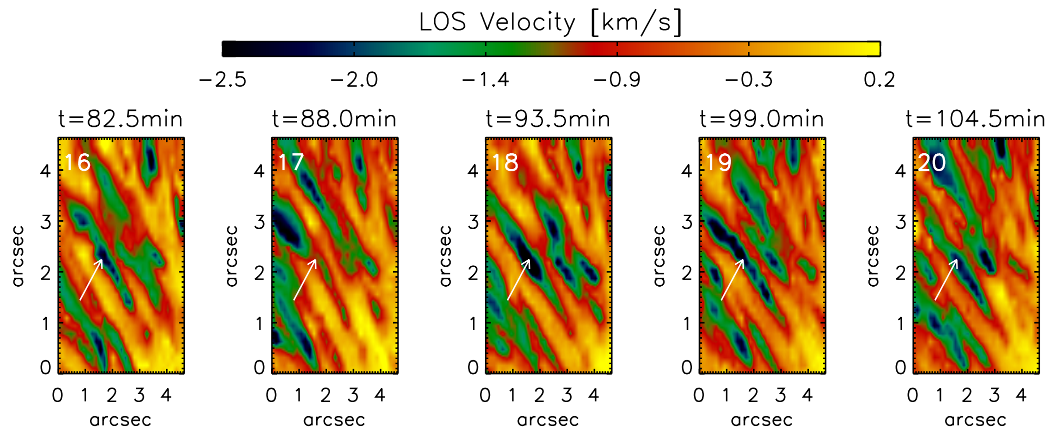

Figure 5.12: Temporal evolution of the EC shown by the white arrow for sequences 16 to 20.

would imply that a change in LOS velocity of 2.93 km s^{-1} is associated with a change of 62±406 G in the field strength, 21±13° in the zenith angle, 26±15° in azimuth and 82±28 K in temperature. Now consider sequence 19, wherein the LOS velocity in the same pixel is -2.9±0.6 km s^{-1} and the field strength, zenith angle, azimuth and temperature are 1622±359 G, 65±10°, 129±11° and 5760±21 K respectively. Although the LOS velocity in sequence 19 is also very large, the corresponding magnetic and thermal parameters are equivalent to those before the passage of the EC. For the layers corresponding to logτ = -1.5 and logτ=-2.0 there are no changes in the magnetic and thermal parameters in time i.e., with the passage of the EC. In order to disambiguate the changes introduced in the physical parameters due to the passage of the EC, I resort to a statistical description of the intraspine and EC properties.

In the first case, the temperature and magnetic field were averaged within the optical depth of logτ = 0 to -0.5 and binned into two categories corresponding to $-1.5 \geq V_{\rm LOS} \leq -1.0$ and $V_{\rm LOS} \leq -2.0$, which represent the intraspines and the ECs respectively. Figure 5.14 shows the histogram of the thermal and magnetic parameters of the intraspines and the ECs. The field strength and azimuth distributions are nearly similar as reflected by the median values, while the small difference in the same for the zenith angle is equal to the computed uncertainty. The temperature distribution too does not show a significant difference, with the

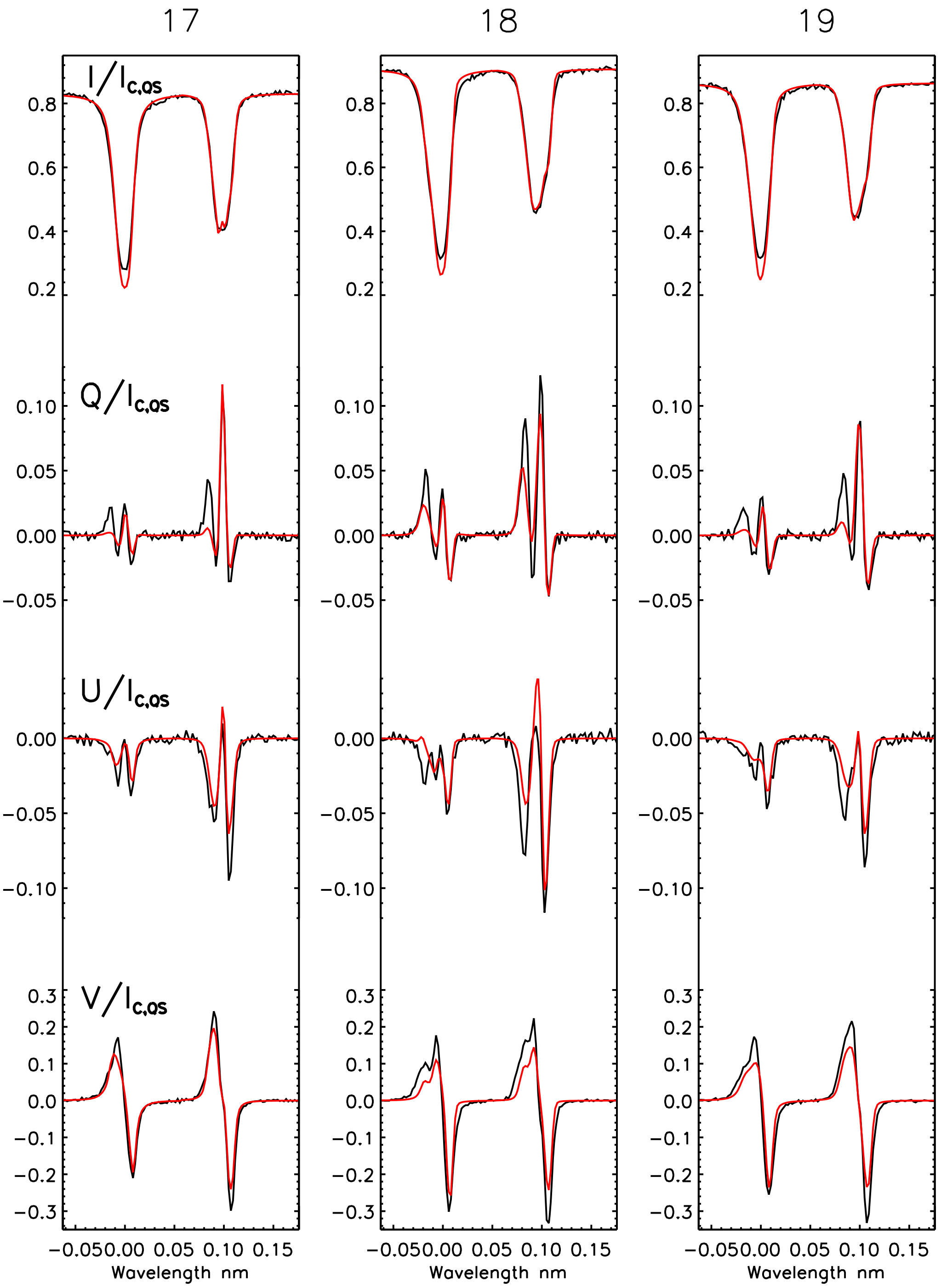

Figure 5.13: Observed (*black*) and Inverted (*red*) profiles corresponding to sequences 17, 18 and 19 for the pixel depicted by the arrow in the top panel.

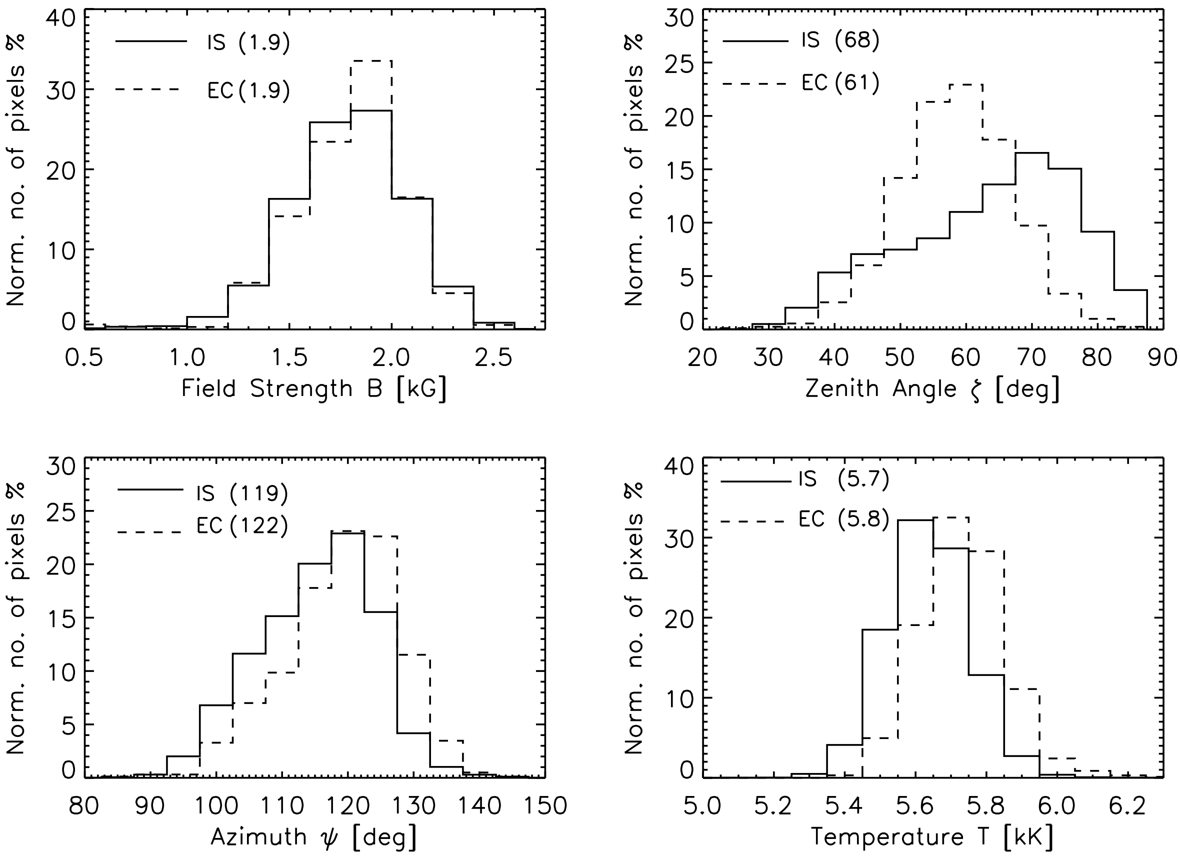

Figure 5.14: Distribution of the physical parameters corresponding to the Intraspines (*solid*) and the Evershed clouds (*dashed*). The numbers in the parentheses indicate median values.

ECs being $\approx$ 60 K hotter than the intraspines.

The second statistical test was to determine the mean radial variation of the physical parameters for the two structures. The field strength of the intraspines and the ECs at the umbra-penumbra boundary are 2.2$\pm$0.16 kG and 2$\pm$0.2 kG respectively, while the values at the penumbra-photosphere boundary are 0.97$\pm$0.35 kG and 1.2$\pm$0.28 kG respectively as shown in the top left panel of Figure 5.15. Similarly the zenith angles for the two structures at $r/R_p = 0$ and $r/R_p = 1$, are 41$\pm$5°, 42$\pm$5° and 75$\pm$7°, 65$\pm$6° respectively. No significant trend is seen in the azimuth as well, which varies from 113$\pm$7° to 121$\pm$14° for the intraspines and 118$\pm$4° to 111$\pm$9° for the ECs. The temperature of the intraspines and the ECs are 5650$\pm$117 K and 5724$\pm$75 K respectively at $r/R_p = 0$ and gradually increases

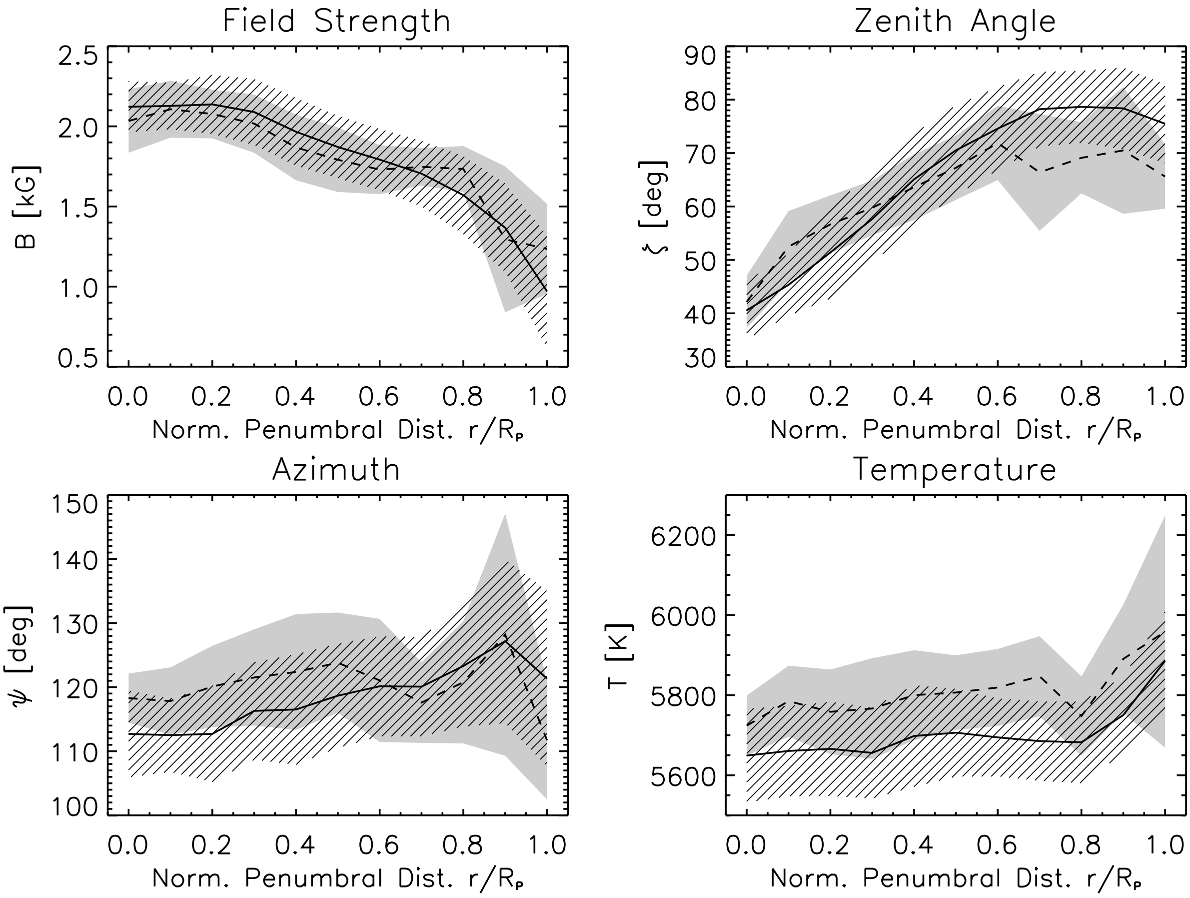

Figure 5.15: Mean radial variation of the physical parameters corresponding to the Intraspines (*solid*) and the Evershed clouds (*dashed*). The *rms* values for the 2 distributions are shown as the hatched lines and the shaded grey area respectively. The radial bin in the x-axis is 0.1.

to 5886±123 K and 5958±290 K respectively at $r/R_p = 1$.

5.5.5 The Long Term Horizontal Flow Field

The time sequence of continuum maps of the sub-region depicted in Figure 5.1 were subjected to Local Correlation Tracking (LCT; November & Simon, 1988; Welsch et al., 2004; Fisher & Welsch, 2008). Each continuum image was unsharp-masked using a 0.″8 boxcar (5×5 pixels) to track the small scale features. A time interval $\Delta t = 5.5$ minutes and an apodizing window with a σ=1.6″ was employed. The uncertainty in the measurement of the transverse speed is $\approx$ 50 m s^{-1}. An average transverse flow map was constructed for a total duration of $\approx$ 3.5 hr. Although LCT suffers from systematic errors that can be $\approx$ 20%, one would like to establish the nature of the long term flow field.

An average continuum and G band image was constructed for the above time period and using the latter, the radial positions in each pixel of the average continuum image were derived using the procedure described in Section 5.4. The computed transverse speed averaged in time was then corrected for the heliocentric angle θ described by Vargas Domínguez et al. (2008) as

$$v'^2 = v^2(\sin^2\phi + \cos^2\phi\cos^2\theta) \tag{5.2}$$

$$\tan\phi' = \frac{\tan\phi}{\cos\theta} \tag{5.3}$$

where v, ϕ are the computed transverse speed and azimuth respectively, while v', ϕ' are the same in the deprojected plane. Figure 5.16 shows the average continuum map with the horizontal flow vectors overlaid on it. As a consequence of averaging over a 4 hr period, the magnitude and orientation of the transverse flow does not appear to have any structuring in azimuthal direction while it is clearly apparent in the radial direction which is suggestive from the two part flow structure of the penumbra as illustrated in Figure 5.16. There is clearly an inward motion of intensity features from a distance of 0.6 R_P while the motion is predominantly outwards from $0.7R_P$ to the outer penumbral boundary. The transverse speeds decrease gradually from 422±32 m s^{-1} at a distance of $0.2R_P$ as shown in Figure 5.17 to 98±40 m s^{-1} at $0.6R_P$ which corresponds to the Dividing Line (DL; Sobotka et al., 1999; Sobotka & Sütterlin, 2001). The

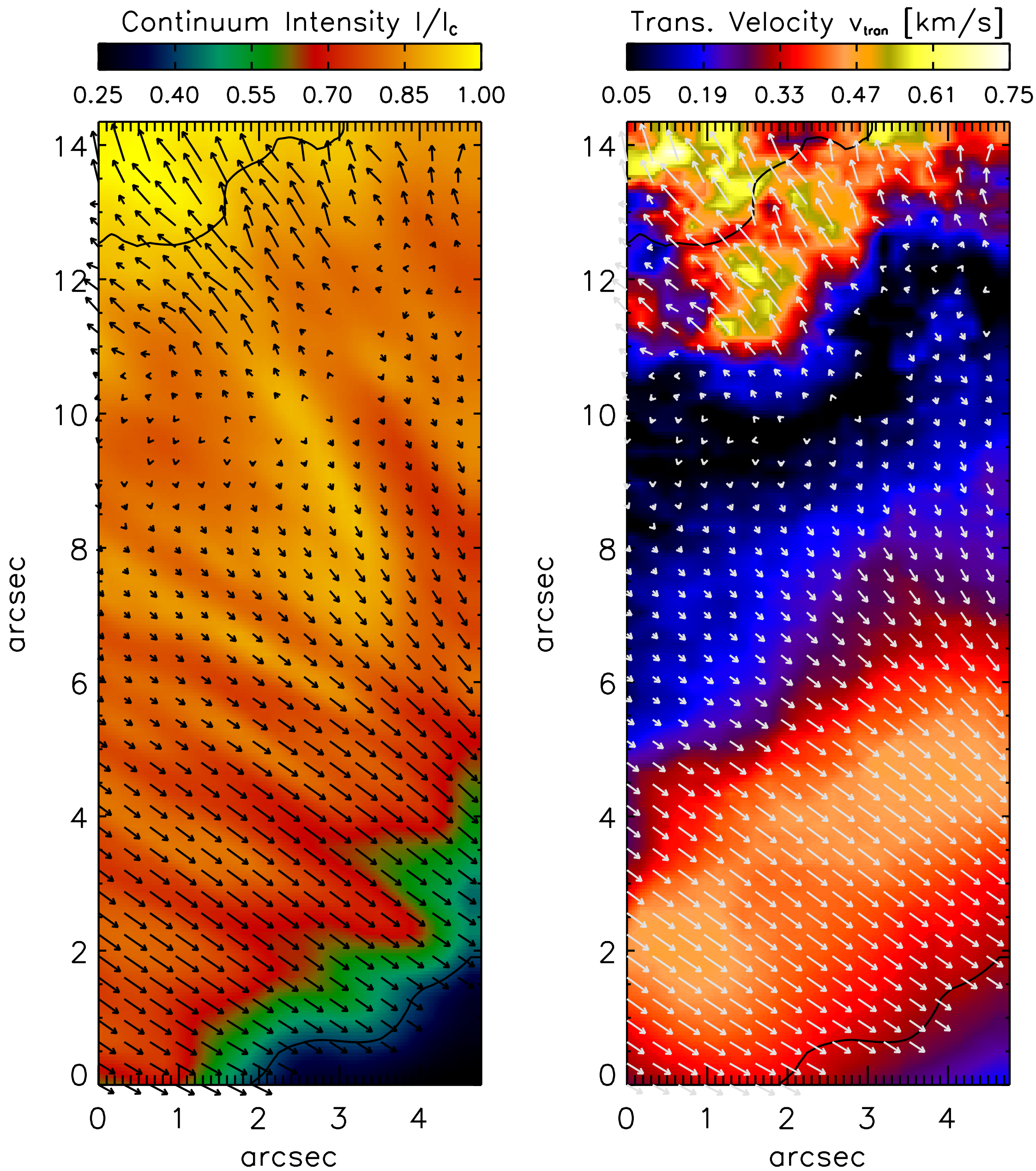

Figure 5.16: Maps of the average continuum (*left*) and transverse speed (*right*). The transverse flow vectors derived from LCT are overlaid on the two images. Both images have been scaled as shown in their respective colour bars. The arrows have been drawn for every alternate pixel wherever the flow velocity exceeds 50 m s^{-1} which is the maximum measurement error.

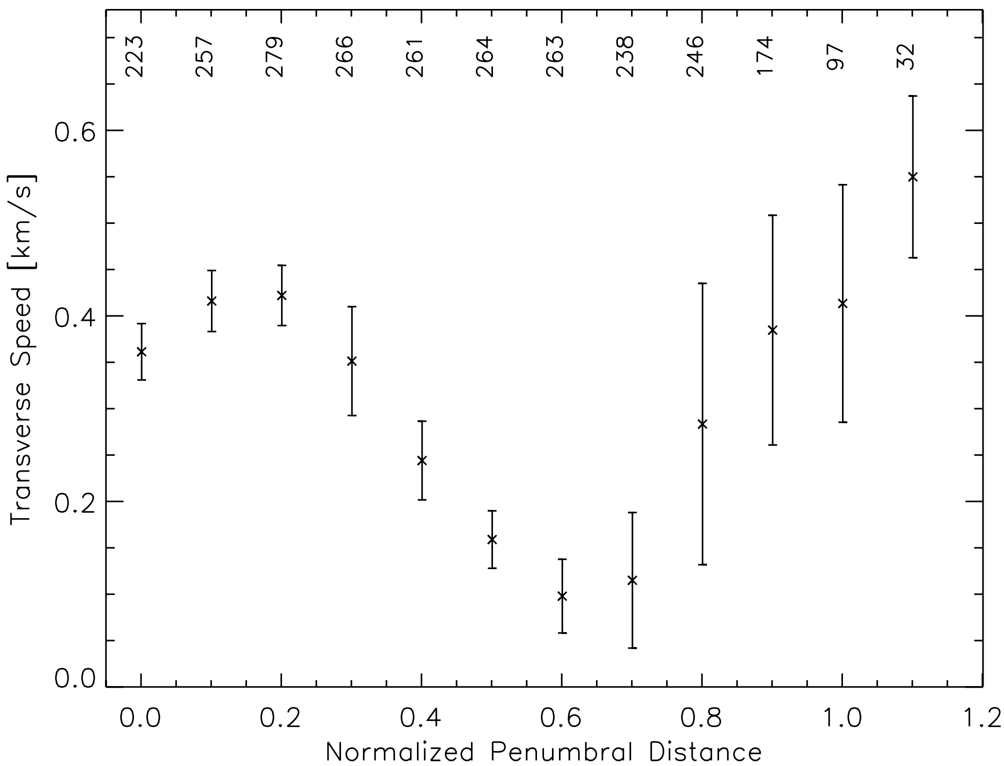

Figure 5.17: Radial distribution of the transverse speed. Vertical bars correspond to *rms* values while the numbers indicate samples in each bin. Bin size is $0.1R_P$.

transverse speeds then steepen to 550±87 m s^{-1} at the outer penumbral boundary. Since the radial position in each pixel depends on the corresponding points on the umbra-penumbra boundary and the penumbra-photosphere boundary, the intensity values defining the two boundaries were changed by ±15 % of the value chosen for the analysis. The resulting distribution appeared to be insensitive to the change in the intensity range.

Based on the feature tracking algorithm of Sobotka et al. (1997a) that was used to trace motions of individual penumbral grains (Sobotka et al., 1999; Sobotka & Sütterlin, 2001) and LCT used in this analysis, it is suggestive that the DL is intrinsic to the penumbral structure. The use of LCT on a regular sunspot as well as on a decaying one depicts the presence of the DL (Deng et al., 2007; Denker et al., 2008). The transverse flow vectors are seen to be well aligned with the average continuum image shown in the left panel of Figure 5.16. In the inner and mid penumbra the flow vectors are radially aligned with the filaments whose structure is coherent even after averaging. The outflow continues beyond the visible part of the penumbra while the flow vectors, lying within the penumbra-photosphere boundary, appear to show a V-shape orientation that coincides with the persistent intensity structure of the penumbra.

5.5.6 Coherence of Penumbral Fine Structure

Figure 5.16 illustrated the presence of the penumbral fine structure as seen from the average continuum image. In the same manner the maps of the average LOS velocity, field strength, zenith angle and azimuth were constructed as shown in Figure 5.18. The magnetic and velocity maps correspond to the logτ = -0.5 layer. The structuring between the filaments is clearly seen in the average continuum image. The same is observed in the LOS velocity maps where the distinction between individual EF channels is quite apparent. The filamentary ordering is equally distinguishable in the maps of the zenith angle and azimuth while average field strength map gives an impression of a long term radial structuring. Having obtained the average maps of the physical parameters, the linear correlation co-efficients (CCs) of the LOS velocity with other quantities such as the field strength, zenith angle, azimuth and continuum intensity were determined. Unlike Ichimoto et al. (2007a), who studied the correlations along arcs at various radial distances in the center and limb side penumbra, I consider sectors of increasing radius in the penumbra and determine the CC between the various parameters for all pixels lying within the sector. This is illustrated in Figure 5.19 which shows the radial variation of the CCs between LOS velocity and the other physical quantities. For the sake of consistency with Ichimoto et al. (2007a), it is assumed that the blue shift is positive.

As seen from Figure 5.19 the field strength, has a strong anti-correlation with the LOS velocity upto a radial distance of $0.6R_P$, with a CC $\approx$ 0.78. Beyond this region the CC starts to reduce becoming close to zero at the penumbra-photosphere boundary. The CC between LOS velocity and ζ increases from 0.5 at $0.1R_P$ to a maximum of 0.75 at $0.4R_P$ after which it reduces with radial distance and eventually becomes very weak at the outer penumbral boundary.

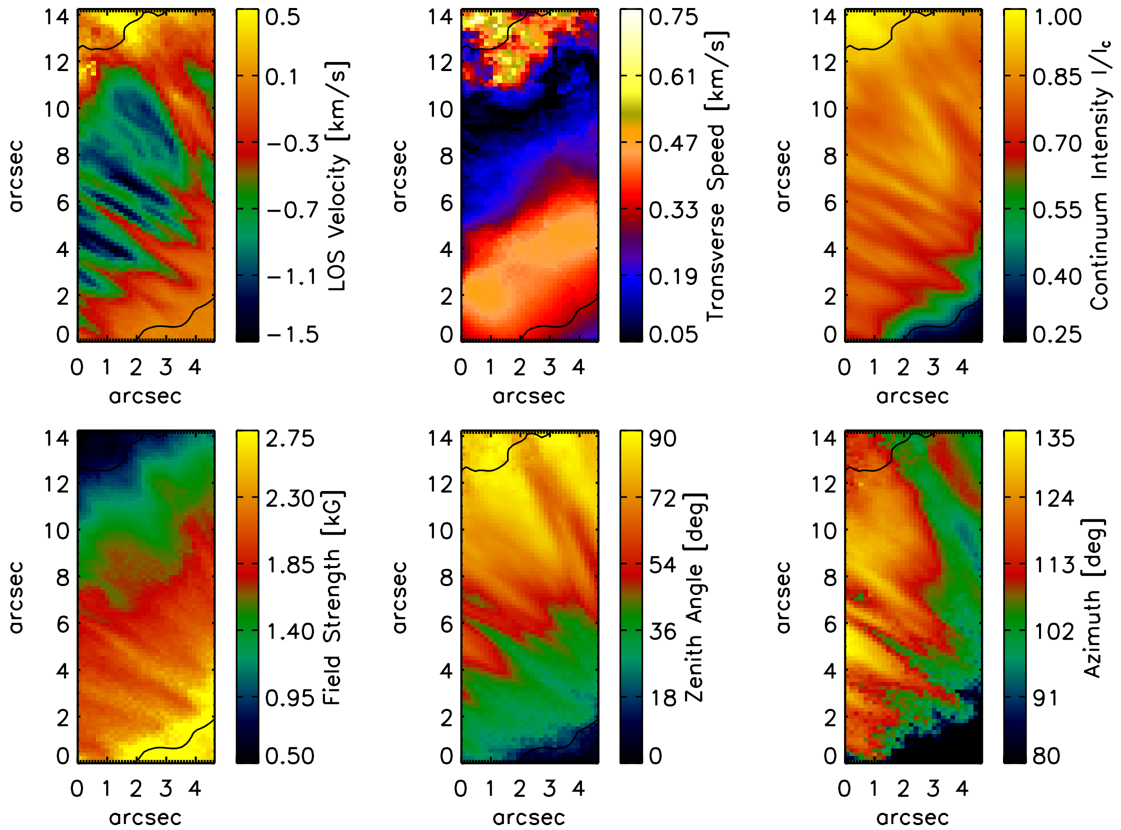

Figure 5.18: Average maps of the physical quantities derived from the entire sequence spanning ≈ 4 hrs. The magnetic field and LOS velocity maps correspond to the logτ = -0.5 layer.

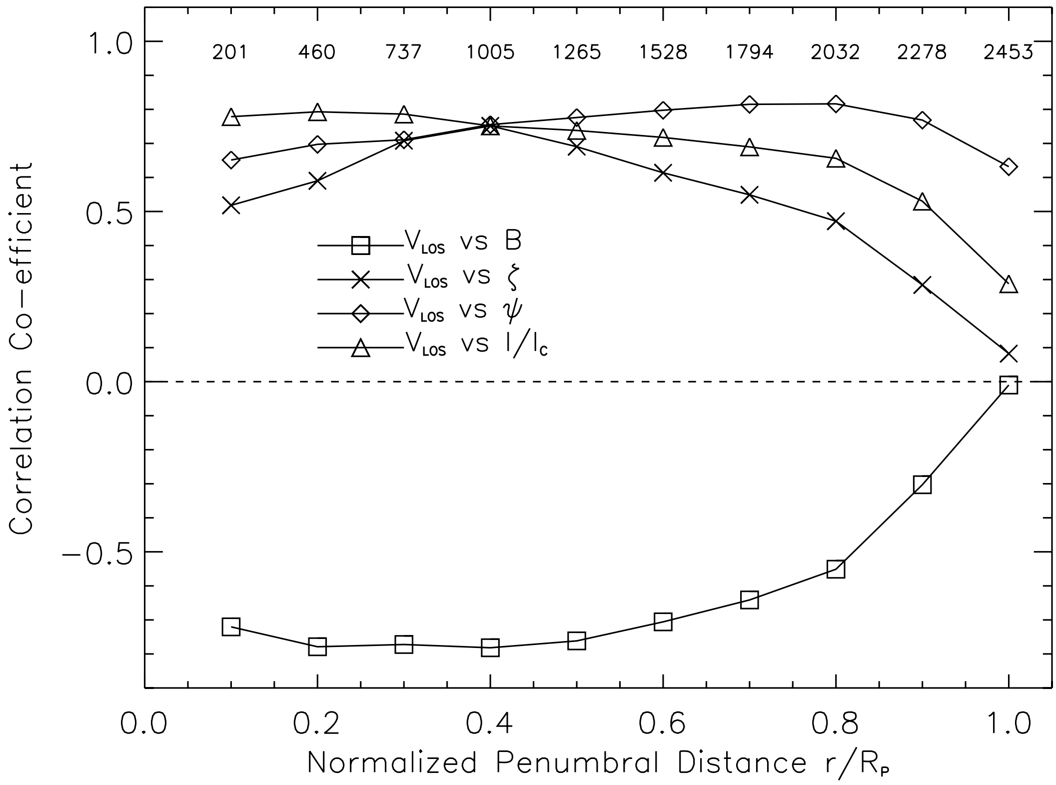

Figure 5.19: Radial distribution of the linear correlation co-efficient between LOS velocity and other physical parameters over various sectors in the penumbra. The numbers denote the pixels in each sector.

The positive correlation of LOS velocity with ζ is due to the positive polarity of the sunspot as against the negative polarity sunspot in NOAA AR 10923 observed by Ichimoto et al. (2008). The azimuth on the other hand appears to be well correlated with LOS velocity throughout the penumbra with an average CC of 0.74, implying that the strong LOS velocities are associated with more radially oriented magnetic fields. The radial variation of the CC between LOS velocity and the continuum intensity indicates that in the inner and mid penumbra the Evershed Flow is confined to the bright filaments. At radial distances beyond $0.8R_P$ the CC sharply falls off to zero. Thus the general scenario that was seen from individual maps emerges from the average picture as well, that the EF is confined to weaker, inclined magnetic fields that are relatively radially oriented. Furthermore, in the inner and mid penumbra the EF is associated with bright continuum features.

5.6 Summary and Conclusion

High resolution spectropolarimetric observations from *Hinode* were used to study the fine structure of a small region of the centre side penumbra of a regular sunspot in NOAA AR 10944 on 2007 March 2. The observed profiles were inverted using the SIR code which assumed a spatially resolved penumbra and gradients in the physical parameters along LOS. At a spatial resolution of $0.''3$ it is assumed that a single magnetic component is present in each pixel. The parameters retrieved from the inversion were averaged within different ranges of optical depth in order to study the spatial variations in the EF, both spatially as well as vertically. It is seen that the EF is predominantly confined to the deep layers pertaining to the $\log\tau = 0$ and $\log\tau =$ -1 layers. The physical parameters, averaged over different heights, were subsequently binned with the LOS velocity which substantiates the existence of 2 distinct components in the penumbra. The spines which are essentially at rest in all heights are magnetically stronger and relatively vertical in comparison to the intraspines which harbor the hot EF. The intraspines are also more radially oriented in contrast to the penumbral spines. These properties of spines and intraspines derived from their velocity signatures appear to be distinct to a radial distance of $0.6R_P$ after which they become indistinguishable from the computed uncertainties. Based on these results the mean atmospheric stratifications for the spines and intraspines was constructed for the two penumbral components.

While the field strength increases with height in the outer penumbra, as reported by Westendorp Plaza et al. (2001a), due to the presence of a canopy, Borrero & Solanki (2008b) observed that the field strength strength can either increase or decrease with optical depth based on inversions of the Fe line at 630 nm using *Hinode* observations of the limb side penumbra. They observed that intraspine pixels, for which $dB/d\tau < 0$, mostly lie in the inner penumbra, while those pixels for which $dB/d\tau > 0$, lie in the outer penumbra. On the other hand, the results of Mathew et al. (2007) illustrate that the field strength decreases with height based on inversions of a sunspot using the infrared Fe lines at 1.56 μm. However, they put forth the argument that a flux tube embedded in a background atmosphere, can in fact, give rise to different atmospheric stratifications depending on the sensitivity of the spectral lines, (visible and infrared) at various heights in the atmosphere. A decrease of the field strength with height in the inner and mid regions of the disc side penumbra are consistent with the results of Borrero & Solanki (2008b) - our differences could stem from the fact that one samples magnetic atmospheres at different geometrical heights for the same optical depth in the centre and limb side of the penumbra. The crucial point between Borrero & Solanki (2008b) and the results obtained in this chapter is the large field strength values seen in the deep layers of the penumbra which poses a challenge for the "gappy" model. Moreover, the model atmospheres used in both cases account for gradients that are relatively smooth, which is not the case, if a flux tube were embedded in a background field. It is thus essential to use a model atmosphere described in Bellot Rubio et al. (2003b) and Jurčák & Bellot Rubio (2008) which will be implemented in future.

Upflows are observed to be a maximum at 0.3 - $0.4R_P$ which is consistent with observations of Lites et al. (1993) and Westendorp Plaza et al. (2001b) and is particularly seen in the deep layers. In this region one also observes an increase in the radial component of the magnetic field (B_R) which is suggestive of the possible injection/emergence of the EF into the penumbra. The conspicuous increase in B_R at $r/R_P = 0.4$ results from an inflection in the radial distribution of the zenith angle. Such a radial trend in B_R is also seen in the middle panel of Figure 9 of Lites et al. (1993). The vertical component B_Z on the other hand, decreases monotonically with radial distance. The zenith angle (ζ) at the umbra-penumbra boundary is $\approx 40°$ from the continuum to logτ=-1.5 and is similar to the values quoted by Westendorp Plaza et al. (2001a). Mathew et al. (2003) measured an average inclination of $\approx 40°$ in the the logτ=-0.5 to logτ=-1.0 layers while in the deeper layers the inclination is only 25° based on inversions of the Fe 1.56 μm infrared lines. The zenith angle tends to flatten out near the penumbra-photosphere boundary beyond a radial distance of $0.8R_P$ which concurs with Lites et al. (1993) and Westendorp Plaza et al. (2001a). This trend in the zenith angle is also seen for the higher layers corresponding to the infrared lines (Mathew et al., 2003). Recent simulations of a sunspot pair by Rempel et al. (2009a) indicate that the radial trend in the inclination is distinct for different penumbral neighbourhoods. Thus the penumbrae of the two sunspots facing each other show a different inclination trend than the penumbra on the other side of the sunspots facing the photosphere.

The spectral nature of some typical spine and intraspine pixels was inspected. Furthermore, Evershed clouds (ECs), display anomalous Q profiles, that are satisfactorily synthesized by the model atmosphere used in the inversions. Results indicate a large change of azimuth along LOS which suggests a possible mixing of the magnetic atmospheres of the EC and the adjacent spine respectively. This scenario is in line with the “uncombed” model of Solanki & Montavon (1993) which was recently confirmed by Borrero et al. (2008a). Based on the realistic assumption that the EF is frozen to the field, I retrieve large flow velocities in the deep layers using the inclination, azimuth, heliocentric angle and LOS velocity. Such large upflows are consistent with the predictions of Schlichenmaier et al. (1998a). Some ECs however, tend to show supersonic flows in the continuum layers that occur well within the inner penumbra. Although supersonic velocities were detected by Bellot Rubio et al. (2004), the unprecedented spatial resolution of *Hinode* allows ECs to be clearly identified along the intraspine channels. The time sequence of observations were used to study the motion of the ECs and in particular the passage of the EC along the penumbral intraspines. It is observed that the ECs can appear quite transiently within a duration of less than 5 minutes. As shown in one example, the passage of the EC is accompanied by a significantly large change in the inclination and azimuth. This would lead to an inference that perhaps ECs perturb the magnetic and dynamic configuration in the penumbra as they move, which was also interpretation of Cabrera Solana et al. (2008) based on a single component inversion, albeit at a much coarser spatial resolution. However if the physical parameters corresponding to the same pixel in the very next time sequence are inspected, it appears that the magnetic and thermal configuration appears to be the same as before the passage of the EC. Clearly, the presence of a large LOS velocity in the same resolution element, ought to be associated with compatible values of inclination and azimuth as in the previous time sequence. The values of the magnetic and thermal parameters of the intraspines and ECs, computed on a larger set reveals that the two are, in general, very similar and their radial variation coincides to a great degree. Thus the scenario compatible with these observations, tends to suggest that the ECs could be associated with different intraspine channels which evolve on time scales of less than 5 minutes. As pointed out by Borrero & Solanki (2008b) that as long as the variations between the ECs and the intraspines is smaller than that between the spines and the intraspines/ECs, the single component atmosphere for determining the penumbral structure holds good. Thus the indistinguishablility of the intraspines and ECs is consistent with the results obtained by Cabrera Solana et al. (2008).

The horizontal flow field was determined by employing LCT on the time sequence of continuum maps and subsequently averaged in time to yield the long term flow field. The penumbra shows two distinct flow regions with inflows from a distance of $0.6R_P$ to the umbra-penumbra boundary, that increase radially inwards and outflows from the Diving Line (DL) at $0.6R_P$, to the penumbra-photosphere boundary. The radial distribution of the flow speeds shows a hump at 0.2-0.3 r/R_P that decreases at $0.6r/R_P$ which is in good agreement with the results of Rimmele & Marino (2006) who observe a much sharper transition of the LOS velocity from an upflow to a radial outflow. The DL could mark the emergence of a new set of penumbral flux tubes (Bellot Rubio et al., 2003b) which would explain why the differences between the spines and intraspines becomes less distinct beyond this radial distance. The inward flow velocities hint at an acceleration while the "moving-tube" model of Schlichenmaier et al. (1998a) predicts an initial acceleration and subsequent deceleration. The results obtained by Sobotka et al. (1999) reveal that only 25% of the bright grains tend to decelerate inward while 30% of them tend to accelerate radially inward.

The organization of the penumbral filamentary structure over the 4 hr observing period strongly exemplifies the coherence and stability of the magnetic and thermal configuration (Balthasar et al., 1996; Sobotka et al., 1999). This is particularly evident in the continuum and LOS velocity maps as well in the zenith angle and azimuth maps. Furthermore, the time averaged magnetic field and continuum intensity is strongly correlated to the LOS velocity within the inner and a little beyond the mid penumbra. I do not find the correlation co-efficient changing sign along the radial direction which could be attributed to the smaller penumbral region considered in the analysis. Thus the association of the EF to relatively weaker, inclined and radially oriented magnetic fields clearly appears to be long-lived despite its non-stationary nature (Schlichenmaier, 2009).

Chapter 6

Results Pertaining to the Development of Adaptive Optics at Udaipur Solar Observatory

6.1 Introduction

We are all familiar with the nursery rhyme "Twinkle, Twinkle little star..." that is often taught to us as little children. In reality, stars do not twinkle, although what seemed magical to us as children, is in fact, a major headache for all ground-based astronomers. The twinkling of stars is not a stellar effect but one introduced by the spatial and time varying turbulent eddies in the Earth's atmosphere. These eddies are a consequence of large warm parcels of air breaking down continuously and randomly, transferring their kinetic energy into smaller parcels. More importantly, the length scales and the distribution of the eddies is random. According to Kolmogorov (1941), the energy of an eddy is proportional to the 5/3 power of its linear size. This condition holds within a range of spatial scales or the 'inertial range', which is limited by the inner (l_0) and outer (L_0) scale of turbulence. While l_0 is the size below which viscous effects are important, L_0 is the size at which turbulence is generated (Tyson, 1991). So what is the nature of the turbulent eddies? They are responsible for causing minute fluctuations in the temperature, which in turn alter the refractive index. These fluctuations in the refractive index, which are random, cause random path length changes in the wave front, arriving from a stellar object. As a consequence, the surface of uniform phase or wave front, which originally was plane, now suffers a global tilt, in addition to small scale corrugations which can be thought of as local tilts. Thus, as a result of star light passing through the Earth's atmosphere, the final image in the focal plane of a telescope would be distorted. To put it into perspective, the presence of atmospheric turbulence introduces aberrations in the image which inhibits us from resolving finer details of the object. According to Rayleigh, the angular resolution of a telescope, having a diameter D is given by

$$\theta_{\mathrm{R}} = \frac{1.22\lambda}{D} \tag{6.1}$$

Equation 6.1 is referred to as the "diffraction-limit" of a telescope. However, the Earth's atmosphere chooses to play spoil sport in this affair and as a result, no matter how large a telescope may be, it is more often than not, "seeing-limited". This is given as

$$\theta_{\mathrm{S}} = \frac{1.22\lambda}{r_0} \tag{6.2}$$

where r_0 is referred to as the Fried's parameter (Fried, 1965), a single value that characterizes the seeing conditions prevalent over the site at a particular wavelength. By definition, it is the size of a telescope for which the *rms* wave front error is about 1 radian.

For solar astronomy, sites with 1 arcsec seeing are considered to be good. Solar granulation is a fair handle that can be used to characterize a site since these structures are typically 1000 km or $\approx$ 1 arcsec in size. The results presented in the earlier chapters unequivocally demonstrate the importance of high resolution observations which is necessary to probe and understand the magnetic and kinematic inhomogeneities which are organized at scales of $0.''2$ to $0.''3$. To achieve this spatial resolution from the ground, it is imperative to combat atmospheric turbulence. As has already been pointed out, space based missions clearly have the advantage of a "seeing-free" environment. Unfortunately, it is a time bound experiment that is also very expensive. In addition the number of instruments that can be flown at any given point is also limited. Since the Sun is a 3 dimensional system wherein the sub-photospheric processes are coupled to dynamics in the corona, it is necessary to carry out multi-wavelength, synoptic observations which are possible only from the the ground. The last decade has witnessed a significant breakthrough in the field of Adaptive Optics coupled with post-processing techniques that has put confidence in solar astronomers to construct large telescopes on the ground in order to probe the Sun with unprecedented spatial resolution (Rimmele et al., 2003; Scharmer et al., 2003a; Keller et al., 2003; von der Lühe et al., 2003; Langhans et al., 2007; Denker et al., 2007; Wöger et al., 2008; Miura et al., 2008). A list of successful solar AO systems currently operational are described in Table 6.1.

Since 1975, the Udaipur Solar Observatory has been associated with the observations and study of energetic phenomena on the Sun, particularly of flares in Hα. This has been carried out using a 15 cm Spar telescope which was gifted by CSIRO, Australia. A Coudé telescope with a 6 inch refractor equipped with a multi-slit spectrograph provided line-of-sight velocities of erupting prominences and surges (Srivastava & Mathew, 1999). A Fabry-Perot based video magnetograph (Mathew et al., 1998) recorded the longitudinal magnetic field, using the photospheric Ca I line, as well as chromospheric filtergrams using Hα. The Razdow telescope on the other hand was used for observing full disk filtergrams in Hα to monitor the activity of the Sun. The Solar Vector Magnetograph is a recent addition to the existing set of instruments which is capable of providing photospheric vector magnetic field measurements using the 6302.5 Å Fe line (Gosain et al., 2006). A dual-beam Hα Doppler System is presently being developed (Joshi et al., 2009) which will analyze and anticipate solar eruptive events directed towards the Earth. In addition to this, a 50 cm MAST (Multi Application Solar Telescope) will be deployed at the island site of the Udaipur Solar Observatory (USO) in the final quarter of 2010 which will be equipped with several back-end instruments. The scientific objectives that MAST will address are:

- The topology and evolution of emerging magnetic flux regions leading to solar activities such as flares and coronal mass ejections.
- Magnetic and velocity structure of sunspots and small scale features such as pores in the photosphere and chromosphere.
- Decay of sunspots and their relation to moving magnetic features.

Table 6.1: A list of successful Adaptive Optics systems. Table adapted from Sankarasubramanian & Rimmele (2008).

Telescope AO	No. of Actuators	WFS Sub-apertures	Camera	Frame rate	Hardware	Deformable Mirror DM	Ref.
76cm DST Lockheed	57	19	-	Analog	-	-	Acton 1992
76cm DST LOAO	97	24	-	<1.6 kHz	24 DSPs	Xenitics Inc.	Rimmele 2000
48cm SVST	19	19	Dalsa CA-D6	955 Hz	566 MHz Alpha	AOPTIX Tech Inc.	Scharmer 2000
76cm DST HOAO	97	76	Custom built CMOS	2.5 kHz	40 DSPs	Xenitics Inc.	Rimmele 2003
70cm VTT KAOS	35	36	Dalsa CA-D6	955 Hz	8X900 MHz Sun	Laplacian Optics	von der Lühe 2003
1.5 m Mc Math Low Cost	37	120-200	Dalsa CA-D6	955 Hz	1 GHz Pentium	Okotech	Keller 2003
97cm SST	37	37	Dalsa CA-D6	955 Hz	1.4 GHz Athlon	AOPTIX Tech Inc.	Scharmer 2003
65cm BBSO HOAO	97	76	Custom built CMOS	2.5 kHz	40 DSPs	Xenitics Inc.	Denker 2007
60cm Hida Obs.[a]	19	20-28	Dalsa CA-D6	955 Hz	-	-	Miura 2008

[a] Recent Addition

- Quantification of helicity in solar active regions and their relation to explosive events.
- Dynamics in small scale structures such as granules and inter-granular lanes.

MAST is proposed to deliver sub-arcsec resolution and will be the first large solar telescope in the Indian longitude to carry out continuous solar observations. In order to achieve the above mentioned goals at a relatively high spatial resolution of $0.''5$ at a site where the median value of r_0 varies between 4 - 4.5 cm (Kumar et al., 2007), it is imperative to have an AO system to compensate for image degradation. The design of the MAST-AO commenced with a prototype system which was installed on the 15 cm Coudé refractor telescope. This chapter details my contribution to the development and characterization of the prototype AO system. The rest of this chapter is organized as follows: Section 6.2 describes the chief components of an AO system and its basic functionality. Section 6.3 deals with the Deformable Mirror's intrinsic and induced aberrations while Section 6.4 illustrates the capability of the Deformable Mirror in compensating real time aberrations created in a controlled environment. In Section 6.5 the performance of the prototype AO system is evaluated through simulations using different lenslet configurations. First light observations with the prototype AO system will be highlighted in Section 6.6.

6.2 Concept of Adaptive Optics

The concept of Adaptive Optics (AO) was introduced by H. W. Babcock as far back as 1953 (Babcock, 1953). It is a system that improves the resolution of ground based imaging systems by correcting the perturbed wave front at the pupil plane by using opto-mechanical components. At that time the technological as well as computing capability was limited and it was nearly 40 years later that the first AO system became operational at the Dunn Solar Telescope of the National Solar Observatory (Acton & Smithson, 1992; Acton & Dunn, 1993). All AO systems essentially comprise of three components, namely, a wave front sensor, wave front corrector and a control computer. The specifications of the components however pertain to the AO system presently being developed at the

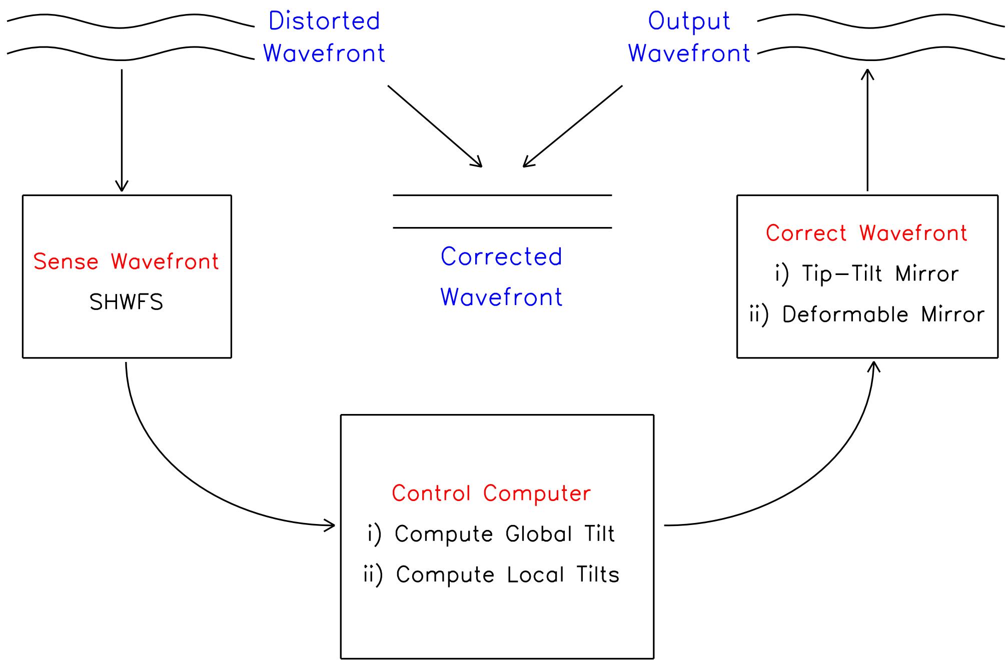

Figure 6.1: Concept of an Adaptive Optics System.

Udaipur Solar Observatory (USO). The AO system has been designed on the same lines as that of the Low Cost Solar AO system at the 1.5 m McMath Pierce Telescope at the Kitt Peak Observatory (Keller et al., 2003, referred hereafter as KPA) since it utilizes off-the-shelf components. All the major hardware components and software implementations are similar to their system except for a few changes owing to developments in the hardware and software industry. The working of an AO system is depicted in Figure 6.1. Each of the AO components and their functionality is described below.

1. **Wave Front Sensor:** The effect of atmospheric turbulence on the incoming plane wave front from a stellar source is to introduce phase perturbations thereby distorting it as shown in the top left hand corner of Figure 6.1. The perturbed wave front can be sensed using a Shack-Hartmann wave front sensor (SHWFS). This wave front sensor comprises of an array of micro-lenses that sample the distorted wave front at discrete locations. Henceforth, the term lenslets and sub-apertures will be used synonymously, wherein the former refers to the individual micro-lenses while the latter is in the context

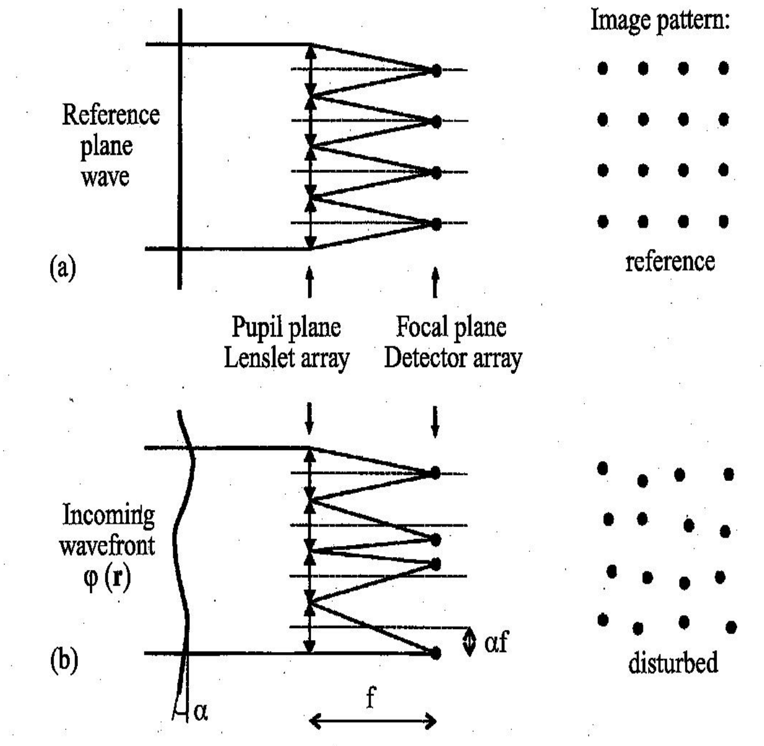

Figure 6.2: The concept of the Shack-Hartmann wave front sensor. Figure adapted from Roddier (1999).

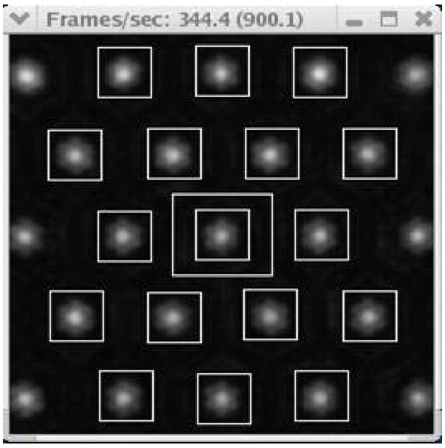

Figure 6.3: Sub-aperture images of a collimated laser beam, produced by a hexagonal lenslet array. A CCD camera is placed at the focal plane of the lenslet array. The pitch of the hexagonal lenslet is 600 μm with a focal length of 145 mm.

of the image formed by the lenslets on the imaging camera. The action of a SHWFS is illustrated in Figure 6.2. Since the wave front is essentially corrugated, the sampling by the lenslets results in a set of sub-aperture images that are shifted with respect to one another. Thus, knowing the shift in the image plane in each sub-aperture is equivalent to measuring the local tilt in the wave front. In case of point sources, the SHWFS can be placed anywhere in the collimated beam while in case of extended sources, such as the Sun, the SHWFS must necessarily be placed at the reimaged telescope pupil. The physical significance of the number of lenslets arises from the seeing conditions prevalent over the site. As mentioned in Section 6.1, the Fried's parameter, r_0, corresponds to a spatial scale for which the phase perturbations have an amplitude of 1 radian. Below this there is no further degradation in the image quality and so the number of lenslets required to sample a wave front is proportional to $(D/r_0)^2$.

It is apparent from Figure 6.2 that a highly accurate alignment of the lenslets as well as high optical quality is required. The manufacturing process of a micro-lenslet array, described by Popovic et al. (1988) consists of depositing a coating of aluminum thin film (250 nm thick) on a quartz substrate and patterned with an array of 15μm diameter holes using a standard

Table 6.2: A list of Shack Hartmann wave front sensors at USO.

Geometry	Pitch μm	Focal Length (mm)	Procured from
Hexagonal	600	145	Smart Micro Optical Solutions, Germany
Hexagonal	600	19	Adaptive Optics Associates, USA
Hexagonal	1000	45	Adaptive Optics Associates, USA
Square	500	45	Adaptive Optics Associates, USA
Square	250	19	Adaptive Optics Associates, USA

photoresist material. The same positive photoresist is subsequently spun on the wafer and exposed to produce a pattern of 30μm diameter circles which are centered on top of the 15μm apertures. After development of the photoresist the wafer is subjected to the process of deep UV hardening, so that pedestals are formed, that become insoluble and stable for temperatures in excess of 1800°C. This is followed by the formation of cylindrical pedestals of photoresist patterned on the 30μm UV baked pedestal. The wafer is then heated to 140° for 15 min in a convection oven which finally yields 15μm diameter lenslets with a spacing of 32μm. The refractive index of quartz at 700 nm is 1.455. This method is more accurate than melting small cylinders of a suitable resin produced by photolithographic techniques in carefully controlled heating conditions, since the molten resin has a tendency to spread, which makes isolation of closely spaced lenses difficult to control. Figure 6.3 depicts the different sub-aperture images produced by a hexagonal lenslet array at USO. A collimated laser beam is incident on the lenslet array which produces the set of spots at the focal plane where a CCD camera is placed. Table 6.2 lists the different lenslet geometries available at USO.

2. **Wave Front Sensing Camera:** The sub-aperture images produced at the focal plane of the Shack-Hartmann wave front sensor are imaged using

Figure 6.4: The wave front sensing camera (WFSC) being used at USO. The WFSC is a 2.6mm×2.6mm CCD and can acquire 955 frames per sec.

the wave front sensing camera (WFSC). The WFSC should be large enough to accommodate the lenslet images corresponding to the sampled pupil and the frame rate should be sufficiently large so as to acquire the images before the temporal evolution of atmospheric turbulence. The dynamic time scale of turbulence can be estimated from the wind speed v and r_0. At Udaipur, where the wind speeds are $\approx$ 5 m/s and the median seeing is 4 cm, the time scale at which the atmosphere evolves is $\sim$ 8 ms.

The wave front sensing camera (WFSC) currently being used at USO is a CCD from Dalsa which is capable of acquiring 955 fps. The CA-D6 sensor is a 260×260 pixel array with each pixel being 10 μm in size. The sensor has four outputs, each of which have a readout speed of 25MHz. The CCD is equipped with a frame transfer architecture with an 8-bit digitization in the LVDS format. The WFSC is shown in Figure 6.4. The image acquisition system is completed by a PC-DIG^{TM} frame grabber card from *CORECO IMAGING*. The images are acquired in a linearly addressed, single-ported 64 bit SGRAM buffer with a 4Mb storage capacity. The device driver for the frame grabber card, available on a Linux platform, called ITIFG^{TM}, was provided freely by GOM *(Gesselleschaft Für Optische Messtechnik) mbH.*

3. **Control Computer:** The Control Computer is a desktop PC that has a 2.4 GHz Intel Pentium IV processor with a Red Hat Linux 8.0 Operating System. The Image Acquisition system and the wave front correctors, namely the Tip-Tilt Mirror and the Deformable Mirror are essentially controlled by the computer. The software for the AO system comprises of two C programs which have been extensively modified from the KPA version. The first C program also called the "correlation tracker" is responsible for communicating with the AO hardware. The main task of this program is to compute the local tilts or the shifts from the sub-aperture images. Once the shifts are determined they are suitably converted to voltages that are fed to the wave front correctors. The second program which is also referred to as the "control program" enables the user to communicate to the "correlation tracker" wherein the reference update time, opening or closing the AO loop, changing PID parameters, recording measurements etc. can be carried out. Both these programs run simultaneously and in real time. The exchange of system dependent parameters is done through the use of Shared Memory which essentially requires "mapping" an area before hand that can be used by both programs. The determination of the shifts in the correlation tracker is described below.

   In the present version of the correlation tracker the shift estimation can be extended to an area as large as 192×192 pixels. This has been possible because of the following two reasons. The first is that the MMX instruction PSADBW (packed sum of absolute difference byte word) allows for finding the sum of absolute difference (SAD) of 8 pixels simultaneously, thus increasing the speed of calculations. The second reason is to do with the way of implementation of the search grid for correlation tracking: To start with, a pixel shift of (1,1) is assumed and the sum of absolute differences is obtained for all the shifts that are two pixels away from (1,1) in all the eight directions. This leads to a search grid size of 25 pixels (but the actual search is for 9 points only). When the minimum is found at a certain pixel, the new search is started in another search grid of 25 pixels surrounding that pixel. When two consecutive searches result in the minimum for the same pixel shift, that pixel shift is assumed to be the actual shift. This procedure leads to the simultaneous estimation of the pixel shift between the images in both x and y directions with ± 2 pixel accuracy. However, this accuracy is further improved to a fraction of a pixel in the present system using a parabolic interpolation (Press et al., 1993; Niblack, 1986) using three points in x and y directions centered at the estimated pixel shift (See Section 6.5.2 for more details on the retrieval of shifts using SAD). The part of the source code wherein the MMX instruction is used to calculate the shift over a 32×32 pixel sub-aperture is given in Appendix - A.

4. **Wave Front Correctors:**

   (a) Tip-Tilt Mirror: The Tip-Tilt mirror (TTM) comprises of a plane mirror glued onto a two channel, three actuator, fast, piezo-electric tilting stage (PZT) procured from *Piezosystem Jena GmbH*. The PZT has a resonant frequency of 1.2 kHz and is capable of providing a maximum tilt of 8 milli-radian. The operating voltage is -10 to +150 V. The operating temperatures are from -20 to +80° C. The voltage to the PZT is provided by a High-Voltage Controller which has an amplification factor of 15.8. The two output channels allow for tilting the mirror in two orthogonal directions. The left-most position of the High-Voltage controller is equal to a base voltage of -10 V. The base voltage for operating the TTM can be controlled both manually as well as through a computer interface. In case of the latter, a 16-bit Digital to analog PCI Interface/DAQboard from *IOTECH* is used to feed voltages from the control computer to the High-Voltage Controller. The DAQboard has several channels of 200 kHz analog to digital outputs and two channels of 200 kHz digital to analog outputs. The software for addressing the PCI interface, initializing it and controlling the voltage are available as C programs compatible with Linux. Figure 6.5 shows the TTM being used at USO.

   (b) Deformable Mirror: A 37 channel Micro Machined Deformable Mirror (Vdovin et al., 1997) from OKO Technologies, Netherlands, is being used at USO similar to the one used by KPA. It consists of a

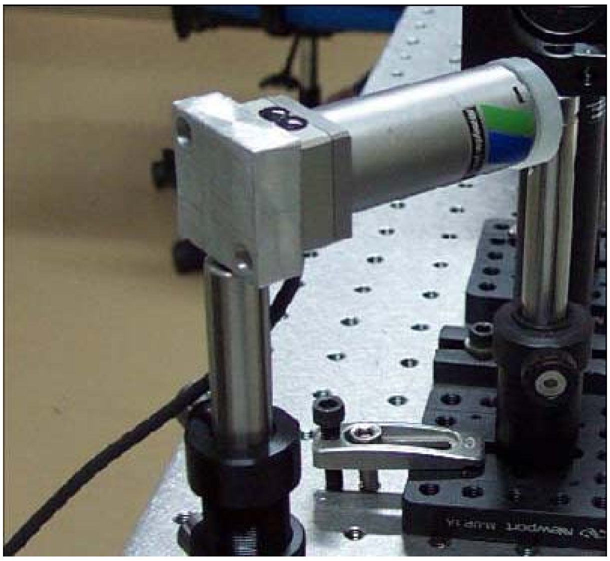

Figure 6.5: Tip-Tilt Mirror used for correcting the global tilt of the wave front.

thin stretched membrane suspended over an array of electrostatic electrodes. The membrane is fabricated by LPCVD (Low Pressure Chemical Vapor Deposition) of a thin $\sim 0.5\ \mu$m layer of tensile stressed silicon nitride Si_nN_m, followed by anisotropic etching of bulk silicon to release the membrane. Pure nitride membranes are sufficiently strong for mirrors with a diameter of up to 25 mm while larger membranes (up to 50 mm) can be fabricated by sandwiching a relatively thick (up to 10 μm) layer of epitaxial polysilicon between two nitride layers (Vdovin, 2003). The DM is coated by a thin layer of aluminum (Al) providing sufficient reflective broadband coatings in the visible while the one used by KPA was gold coated for operating in the infrared wavelengths. In case a higher reflectivity is required (for instance for laser intracavity applications), the membrane can be coated with Cr/Ag composition followed by up to 12 dielectric layers, resulting in reflectivity of up to 99.8% in a narrow spectral region.

The DM has a clear aperture of 15 mm while the inter-actuator spacing is 1.8 mm. The maximum central deflection of the membrane surface is 7 μm while the initial *rms* deviation from plane is less than 0.3 μm. The DM can be operated in a frequency range of 0-500 Hz.

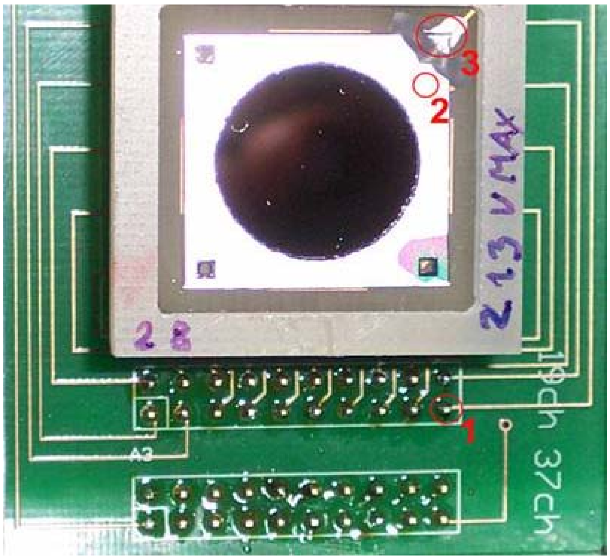

Figure 6.6: 37 channel Micro Machined Deformable Mirror used for correcting the local tilt of the wave front.

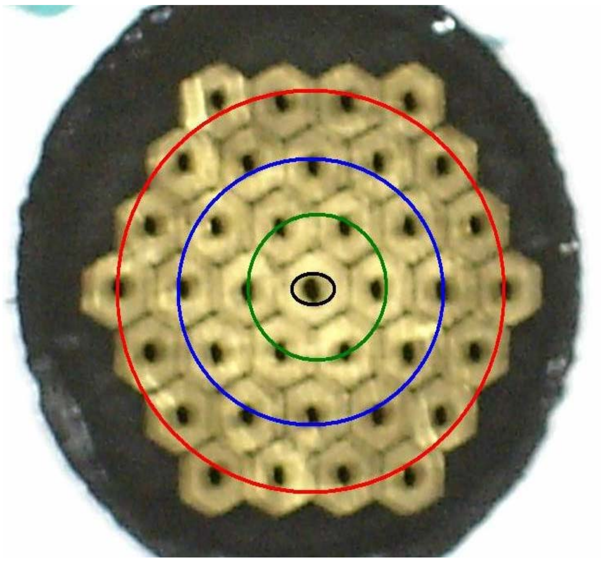

Figure 6.7: Actuator Geometry of the 37 channel Deformable Mirror. The concentric rings shown in different colours represent the numbering scheme of the actuators, with the first actuator being the central one shown in black.

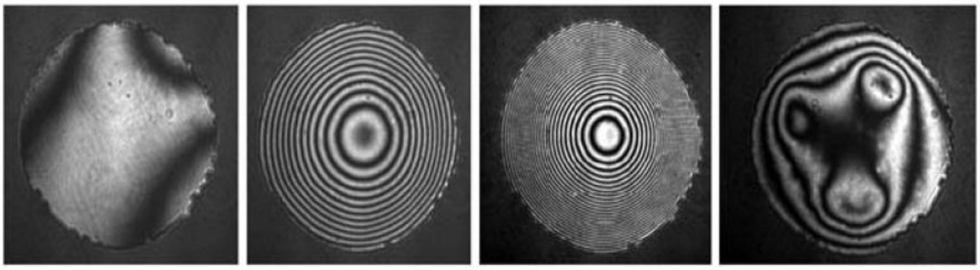

Figure 6.8: Left to right: Typical interferometric pattern of the 37 channel, 15mm MMDM, when zero voltage is applied, control byte 180 applied to all actuators, control byte 255 applied to all actuators and to some actuators respectively. Figure adapted from the MMDM technical passport provided by OKO Technologies.

Figures 6.6 and 6.7 depict the DM and its actuator geometry. The first ring consists of the central actuator, the second ring consists of 6 actuators while the third and fourth comprise of 12 and 18 actuators respectively. The actuators of the DM can be addressed individually from the computer using two 8-bit PCI cards. The voltage from the PCI cards is further boosted using 37 high voltage amplifying cards which provide a maximum operating voltage of the DM of 215 V in each channel. The response of the membrane to the application of different voltages to its actuators is illustrated in the interferometric patterns shown in Figure 6.8.

6.3 Membrane based Deformable Mirror: Intrinsic Aberrations and Alignment Issues

The deformable mirror (DM) is an important component of an Adaptive Optics System. As described in Section 6.2 it is a continuous face sheet with actuators positioned behind the membrane. The mirror boundary is fixed and voltage applied to any one actuator influences the neighbouring surface as well. The surface can also be formed by several, small mirror segments (Roggemann, 1997). Micro Machined Deformable Mirrors (MMDM; Li et al., 2006) are preferred in many AO systems (Zhu et al., 1999; Dayton et al., 2000; Paterson et al., 2000;

Fernández et al., 2001; Theofanidou et al., 2004) because of their low cost and capability of achieving large stroke even though the influence can be as large as 60% (Vdovin & Sarro, 1995). Since the membrane surface of the DM can in principle be deformed in only one direction, it is necessary to bias the DM such that the stroke can be achieved in both positive and negative direction. In general, this can be done by applying a constant voltage to all the actuators. However in case of the MMDM, application of a constant voltage to all the actuators renders a parabolic shape to the membrane[1]. Now it is well known that an on-axis spherical/parabolic optical component, placed at an angle to the incident beam induces defocus and to a great extent, astigmatism in the image plane. While defocus can be compensated by moving the imaging system, astigmatism cannot be corrected by a simple alignment. Hence, the DM surface that is distorted by applying an arbitrary/uniform set of voltages to its actuators, using it in the optical path at an angle to the beam will undoubtedly mimic an on-axis tilted distorted/parabolic surface. Since the DM is also being used to compensate a turbulence-induced curvature term in addition to other aberrations, it is necessary to determine the aberrations induced by such (curved DM surface) an optical element when placed at various angles of incidence in the optical path. In addition to aberrations induced from the optical alignment, intrinsic aberrations are also very important. As the technical passport of the DM states that the initial figure of the DM is astigmatic upto 1.3 fringes (P-V), one would like to study the intrinsic aberrations as well. The aberrations introduced in the optical system as a result of folding the beam using a DM are estimated quantitatively, for various angles of incidence. The results from the simple experiment are then compared with simulations using the optical design software *ZEMAX™* [2] that is described in detail in Bayanna et al. (2010).

[1] *http://www.okotech.com/howtobiasthemmdm*, see also Technical Passport from OKO Technologies for 37-Channel MMDM

[2] ZEMAX Development Corporation, 3001 112th Avenue NE, Suite 202, Bellevue, WA 98004-8017 USA.

6.3.1 Experiment

6.3.1.1 Optical Setup

The f#15 Coudé telescope (Figure 6.9) served as the light feed. Using a set of relay lenses the image was magnified by a factor of 2. At the focal plane of the f#30 beam an artificial target was placed, which was illuminated by sunlight. A lens of focal length 200 mm was used to collimate the light modulated by the target. The DM was placed in the collimated beam which folded the beam towards an imaging lens of focal length 300 mm. The size of the reimaged telescope pupil on the DM is 6.6 mm while the clear aperture of the DM is 15 mm. When the DM is placed at an angle of 45° the projected pupil will be elliptical in the x direction having a size of $6.6/\cos 45^\circ = 9.3$ mm. Thus the pupil is well within the clear aperture of the DM. The difference between the tangential and sagital planes and the circle of least confusion were measured in order to estimate the intrinsic as well as induced astigmatism by placing the DM at different angles of incidence. A 1392×1024 pixel, Cool-Snap HQ CCD with a 12 bit digitization from Roper Scientific was used to image the target. The voltage to the DM was controlled by 2, 8-bit PCI cards whose maximum output voltage to any channel is 5 V. The individual actuators were first assigned a port address as stated in the user manual and the PCI output was checked for each channel. A high voltage amplifier consisting of 2 high voltage amplifier boards, boost the signal from the PCI cards. Each amplifier board contains 20 non-inverting DC amplifiers with a gain of 59. A high voltage stabilized DC supply was used to power the amplifier boards. The maximum operating voltage of the DM is 162 V.

6.3.1.2 Intrinsic Aberrations and Image quality

For measuring the intrinsic aberration, the DM was initially placed at an angle of 0° as shown in Figure 6.10. The target had an **L** shape pattern and it was observed that the vertical line was focused at one location while the horizontal line at another. This difference in the sagital and tangential focus is caused by astigmatism. To see if the astigmatism changed with the curvature of the DM, a uniform voltage was applied to all 37 actuators of DM, starting from 0 to 225 DACs (Digital-to-Analog Counts) in steps of 25 DACs. For every voltage set,

Figure 6.9: f#15 Coudé refractor with a focal length of 2.25 m that is used as the light feed for the prototype AO system. The light is folded and subsequently magnified by a factor of 2 using two relay lenses which produce an image size of 42 mm at the field stop inside the lab.

the tangential, sagital and optimum focal positions were measured and the corresponding images were recorded. The difference between the sagital and tangential focal positions do not vary with voltage (Figure 6.11). It can thus be estimated that the intrinsic astigmatism in the DM is ≈ 6 mm. The optimum focus changes quadratically with voltage as shown in Figure 6.11. As is evident the increase is unidirectional, whose implication will be discussed in the following section. The presence of an intrinsic astigmatism results in a poor image quality which can be judged visually as shown in Figure 6.12 which also shows images taken by a plane mirror kept at the same location of the DM. Astigmatism essentially arises due to different curvatures along different directions. As a first order trial, maximum voltage was applied to a specific line of actuators alone and the corresponding image recorded, as shown in Figure 6.12. As a performance measurement, contrast of the images were estimated before and after application of the above arbitary voltage set, for the entire image as well as for a few selected features as shown in the right most panel of Figure 6.12. Although the improvement in image contrast is nominal, it is evident that a specific voltage set is necessary to com-

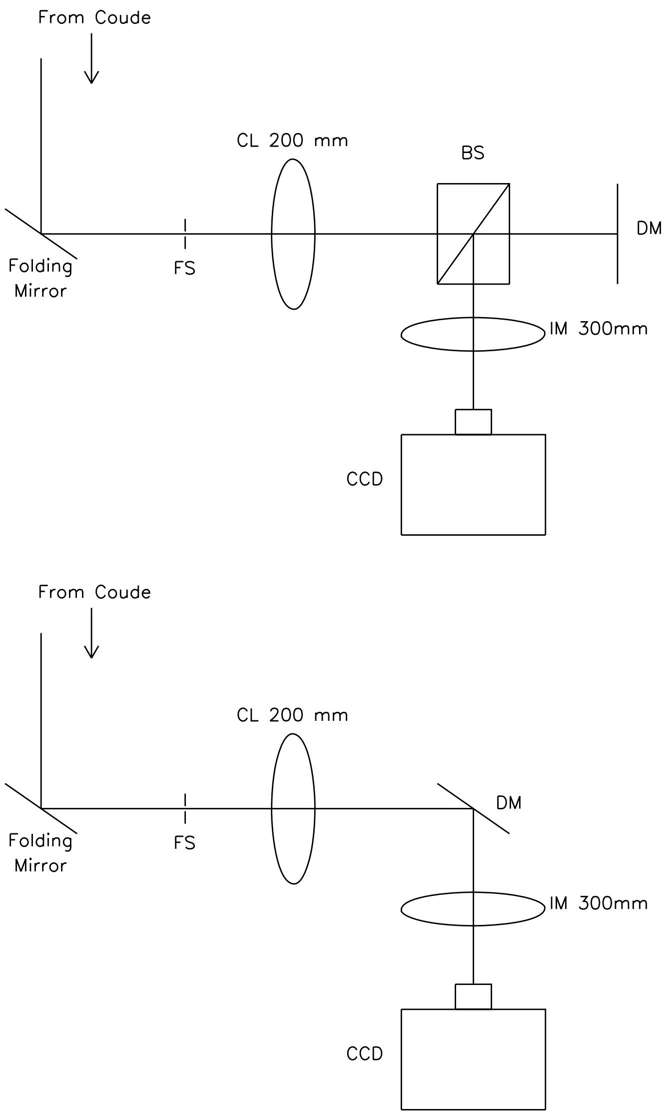

Figure 6.10: Optical setup with the DM at different angles of incidence. **Top:** DM at 0° angle of incidence. **Bottom:** DM at 45° angle of incidence. Intermediate incidence angles were produced by rotating the imaging lens and the CCD in the clockwise direction. FS-Field Stop, CL-Collimating Lens, IM-Imaging Lens, DM-Deformable Mirror, BS-Beam Splitter.

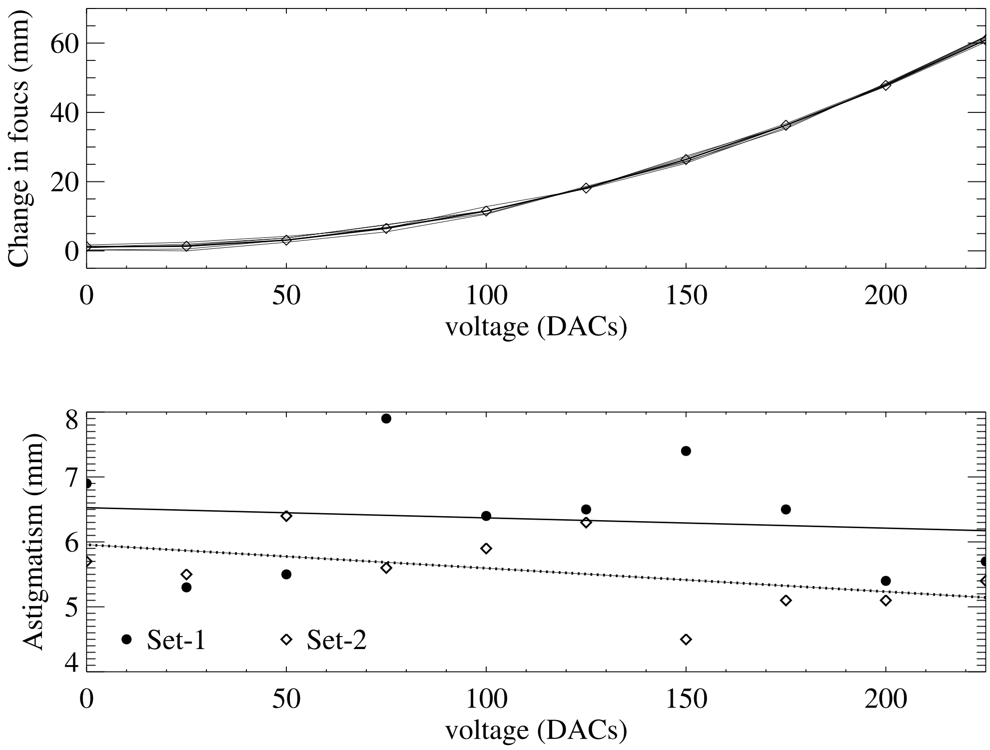

Figure 6.11: Top panel: Change in focus w.r.t change in voltage. **Bottom panel:** Intrinsic astigmatism measured as the difference in the tangential and sagital focus positions. The *solid* line represents the linear fit for data set-1 (filled circles), while the *dotted* line corresponds to data set-2 (open boxes). The difference in the two sets arises due to the error in visual inspection of tangential and sagital focus positions.

pensate for the degradation caused by the intrinsic astigmatism. The experiment was repeated by placing the DM at several angles of incidence and the tangential, sagital and optimum focus positions were measured and the corresponding images were also recorded. The results are displayed in Figure 6.13. Interestingly, for angles less than 10° the astigmatism remains nearly a constant with the applied voltage. Images obtained for different angle of incidence are shown in Figure 6.14. A voltage equivalent to 225 DACs was given to all the actuators.

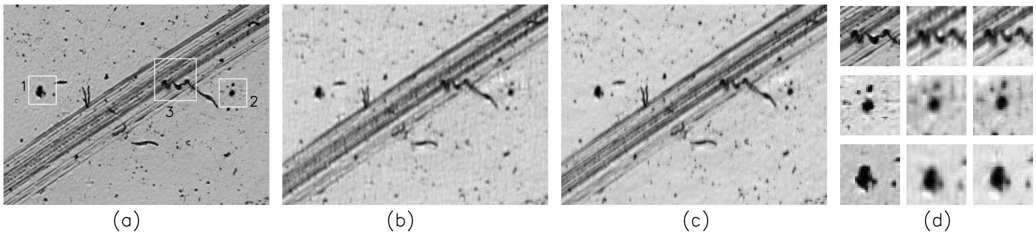

Figure 6.12: Image quality using (a) a plane mirror (along with three features identified for further processing), contrast = 1, (b) DM (plane mirror replaced by a DM), contrast = 0.6, (c) after applying some correction to DM, contrast = 0.64. (d) Three rows corresponds to three features identified in panel (a) shown in white boxes; images along the row are due to plane mirror, DM and correction to the DM respectively; contrast improvement varies from 4% to 10%.

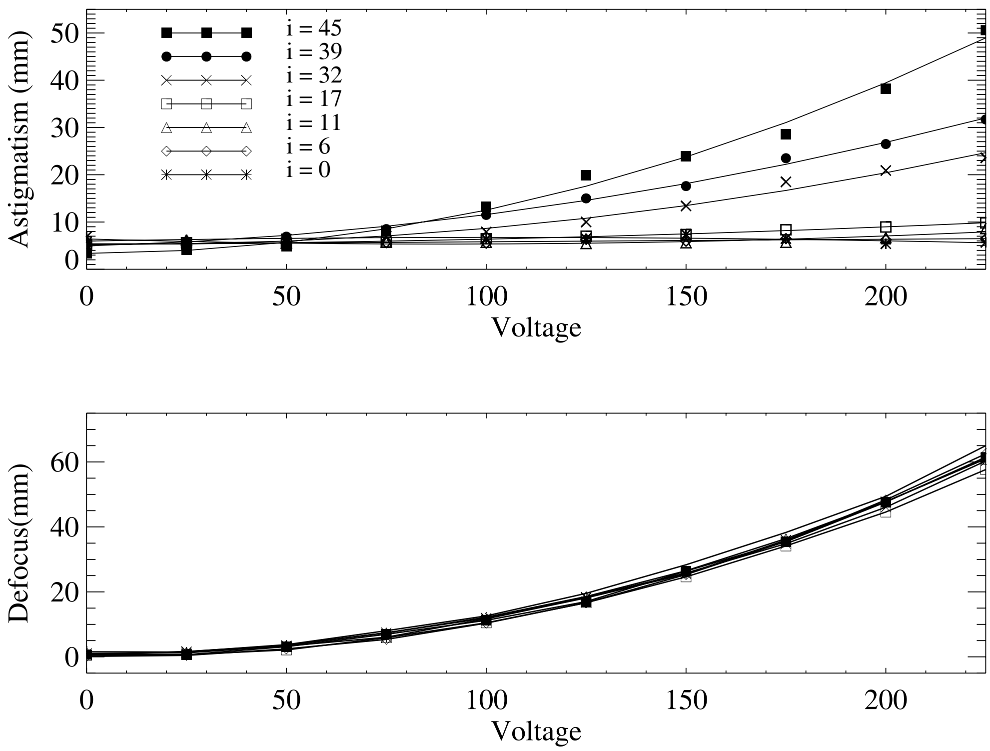

Figure 6.13: **Top** panel shows astigmatism with increase in radius of curvature for different angles of incidence. **Bottom** panel shows the change in focal plane (circle of least confusion) with the increase in radius of curvature.

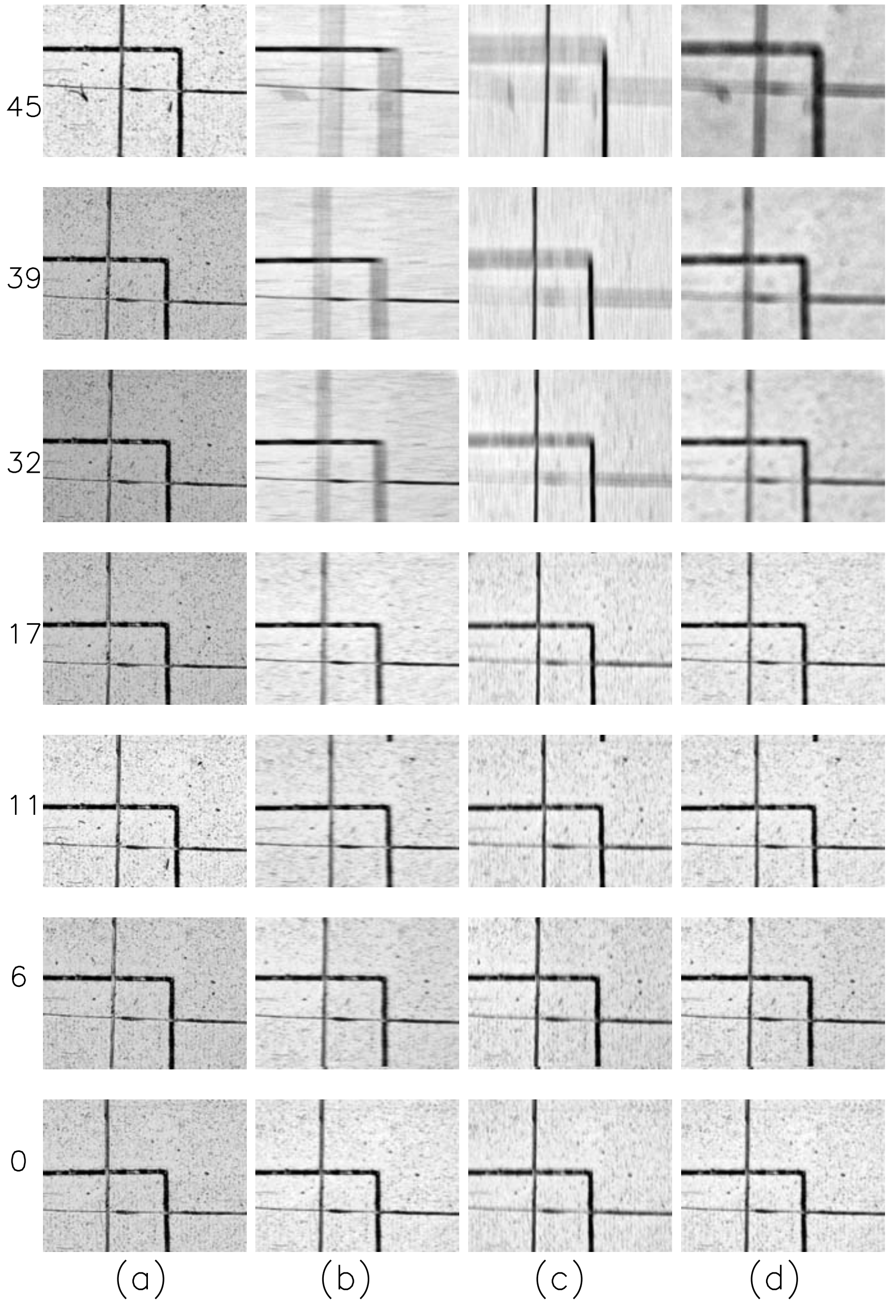

Figure 6.14: Images corresponding to different angles of incidence. Maximum voltage of 225 DACs was applied to all actuators of DM. Images with (a) plane mirror, (b) DM at the sagital plane (c) DM at the tangential plane (d) DM at the plane of least confusion.

6.3.2 Dealing with Induced and Intrinsic Astigmatism

It has been demonstrated from the simple experiment that when the DM is kept at angles greater than 0° and voltages are applied to it, there is an induced astigmatism which increases in general with the angle of incidence. The change in focus and astigmatism varies quadratically with the applied voltage which could be due to the fixed boundaries of the DM. It is also observed that the optimum focal position changes quadratically with voltage and does not exhibit a change of sign which suggests that the DM does not possess any intrinsic curvature that would change sign on application of voltages. In order to deal with the intrinsic astigmatism one must derive a suitable voltage set that will compensate the degradation caused by it. Since the intrinsic astigmatism is independent of voltage, it naturally facilitates using a suitable bias voltage in order to allow the membrane to move in either direction.

6.4 DM Performance in Compensating Real Time Aberrations

In the previous section the intrinsic and induced astigmatism of the DM were determined. In this section I attempt to use the DM for correcting a time changing aberration. The aberrations are produced using a second DM to which voltages can be fed at different time intervals and this is particularly useful to evaluate the DM's performance in compensating real-time aberrations, particularly those introduced by the Earth's atmosphere which vary on a timescale of $\sim$ 10 ms. In addition, the possibility of using Phase Diversity as an off-line processing technique on AO corrected images, is explored through simulations.

6.4.1 Optical Setup

A He-Ne laser operating at 633 nm is collimated using a 150 mm lens (CL) through a spatial filter and a pin-hole combination (SF). The collimated beam size is minimized to 10 mm by an aperture stop. The light is then allowed to pass through a tip-tilt mirror (TTM) and two deformable mirrors (DM-1, DM-2) as shown in Figure 6.15. The TTM is used for correcting the global tilt of

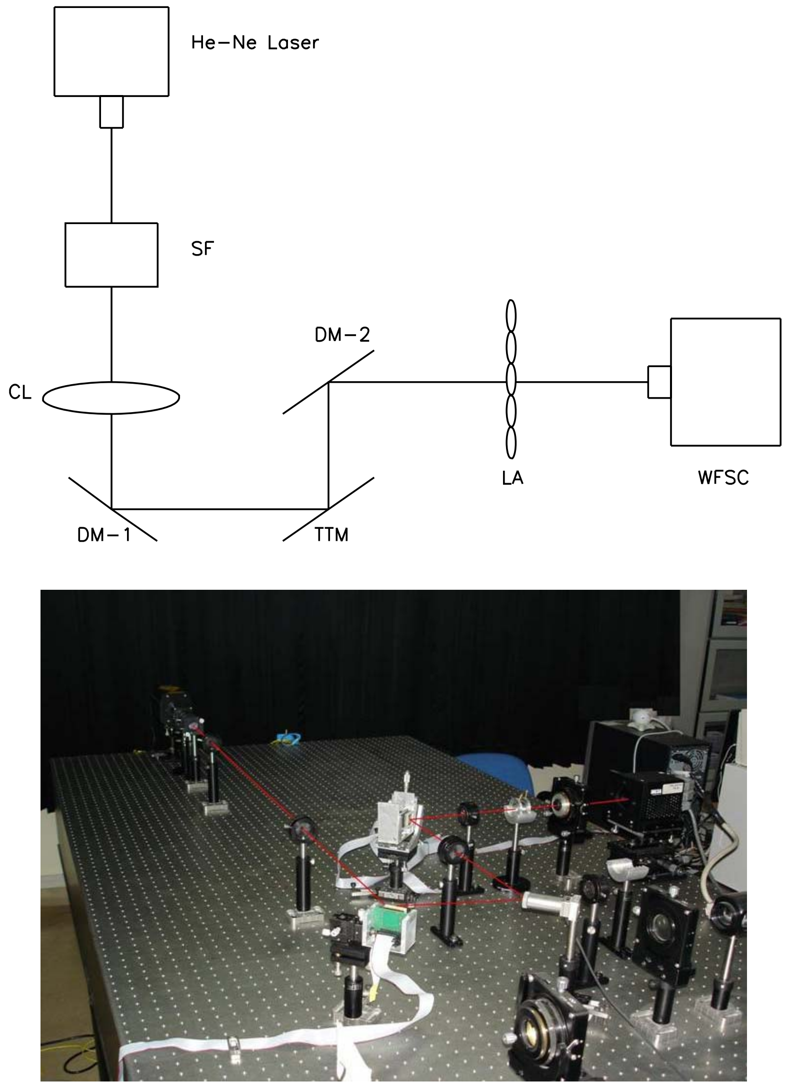

Figure 6.15: Top: Optical setup using one DM as the distorting element and the second DM as the correcting element. SF - Spatial Filter, CL - Collimating Lens, DM-1,DM-2 - Deformable Mirrors, TTM - Tip Tilt Mirror, LA - Lenslet Array, WFSC - Wave Front Sensing Camera. The tip-tilt mirror is used to correct the overall/global tilt of the wave front. **Bottom:** Photograph of the optical setup using the two DMs in the lab.

the wave front. The maximum operating voltage for DM-1 and DM-2 are 162 V and 215 V respectively. One of the deformable mirrors (DM-1) is used for creating distortions while DM-2 is used for correcting the input distortions. A Shack-Hartman wave front sensor and a wave front sensing camera (WFSC) are used for sensing the wave front. The lenslet array (LA) of hexagonal micro lenses is illuminated by the collimated beam and forms multiple images of the laser spot in the sensing camera. The focal length of the lenslet array is 145 mm. As the pitch of the lenslet array and the pixel size of the WFSC are 600 and 10 μm, respectively, only the central 17 lenslets are utilized. Although Section 6.3 described the effect of the astigmatism induced as a result of keeping the DM at large angles of incidence, the aim in this study is to determine the capability of the DM to correct a time varying aberration even in the presence of both an induced as well as intrinsic astigmatism.

6.4.2 Experiment and Results

Before using the DM for correcting the aberrations introduced by the other DM, it is necessary to carry out the following calibration of the DM and the LA. This involves the mapping of the DM actuator geometry with LA and computing the Influence Matrix.

6.4.2.1 Mapping of the DM Actuator Surface with the Lenslet Array

Mapping of the DM actuator surface to the lenslet array involves centering the central actuator onto the central sub-aperture. Thus when a voltage is applied to the first central actuator the subsequent images in the remaining sub-apertures are radially shifted and symmetric about the central sub-aperture, while the image in the central sub-aperture does not move. The deformation produced above is equivalent to a defocus. The motion of the image in the various sub-apertures is due to the fact that voltage to a particular actuator produces a local deformation in the membrane surface. Figure 6.16 shows the disturbance in terms of spot motion vectors created in the sensor plane when a voltage is applied to actuator numbers 1, 2 and 3, respectively.

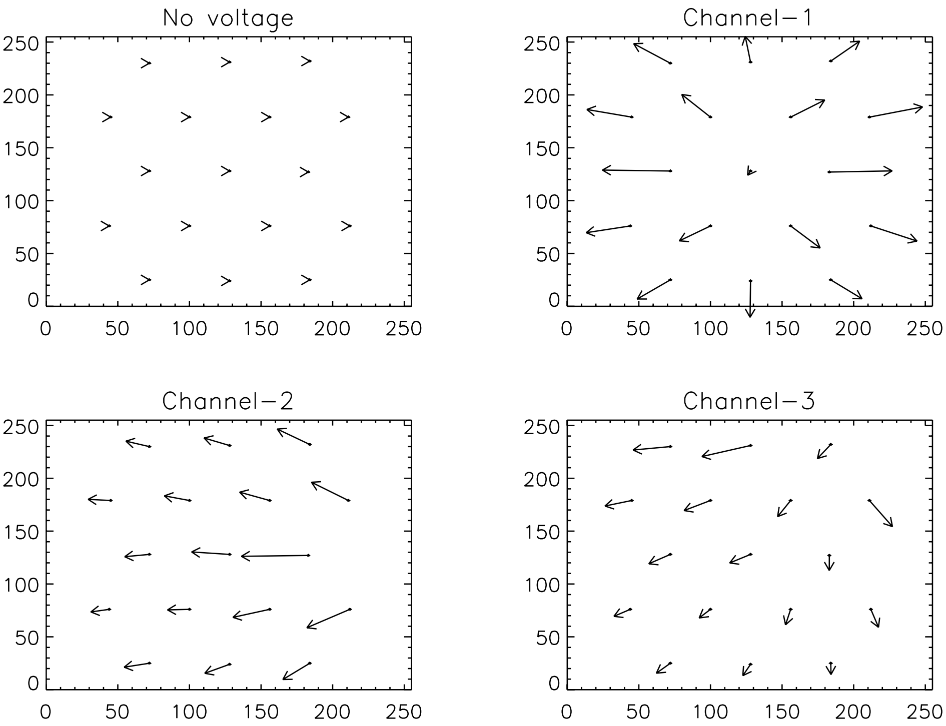

Figure 6.16: Vector representation of image motion observed in the sub-aperture plane: when no voltage was given to any of the actuators (**top left panel**); when voltage was given to the 1st central actuator (**top right panel**), 2nd actuator (**bottom panel left**) and 3rd actuator (**bottom panel right**). When the voltage was applied to the remaining actuators, the sub-aperture shifts follow a similar trend as shown above.

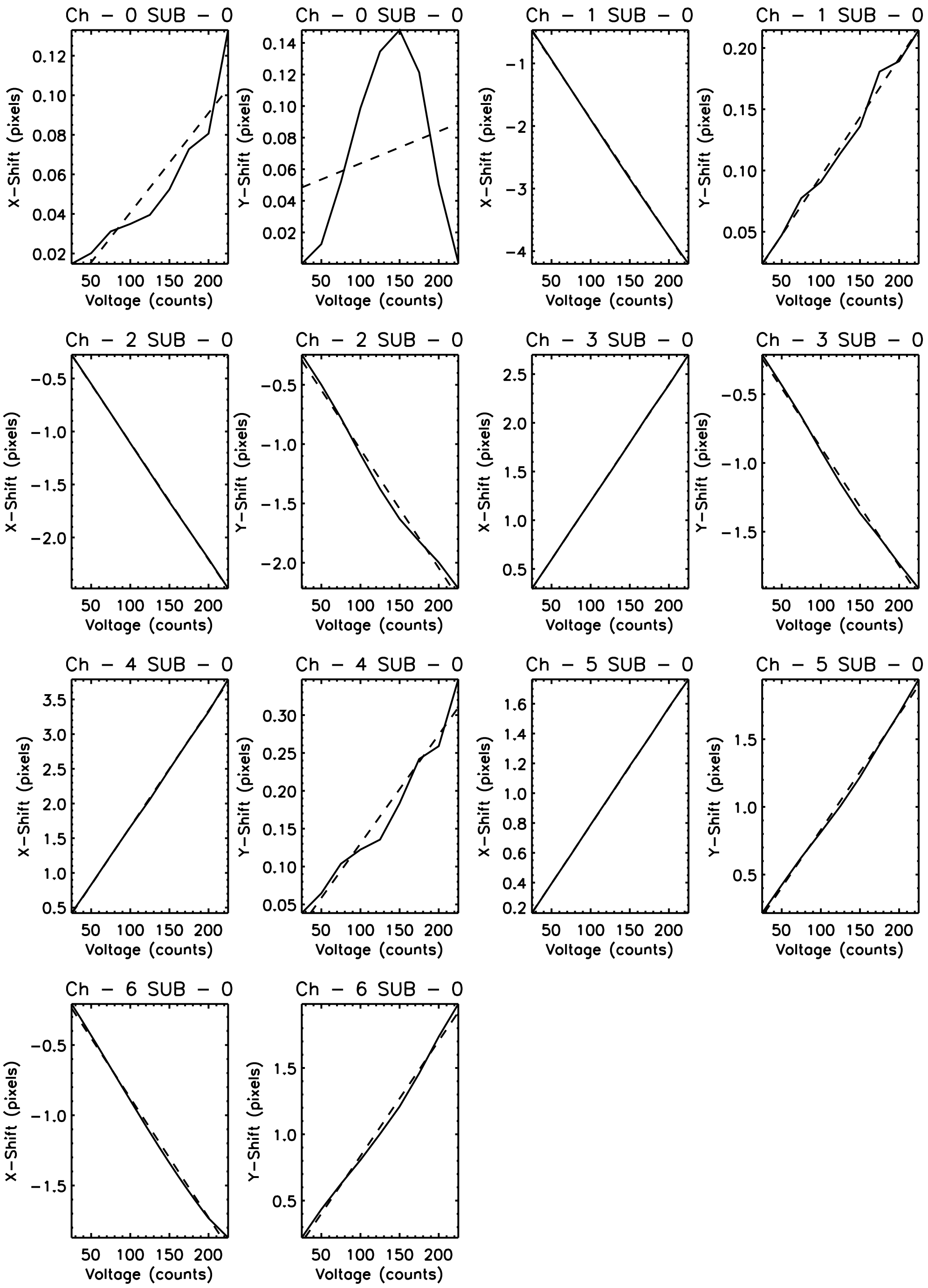

Figure 6.17: Response observed in the central sub-aperture when voltage was applied to the central 7 actuators one by one from 0 to 225 DACs in steps of 25 DACs. The *solid* and *dashed* lines represent the observed shifts for different voltages and the linear fit respectively. Similar curves are obtained for all the remaining sub-apertures of the DM showing almost linear behavior. Shift measured in pixels. CH: actuator number, SUB: Sub-aperture number.

6.4.2.2 Generating the Influence Matrix

The Influence Matrix (IM) is essentially a calibration matrix that allows us to determine the set of voltages to the DM actuators, required to compensate a set of shifts observed in the sub-aperture plane. The relationship between the observed shifts and the voltage to be applied is given as

$$\mathbf{A}.\ \mathbf{x} = \mathbf{b} \tag{6.3}$$

where $\mathbf{A}$ is the influence matrix which has $2M$ rows and N columns. Here M and N refer to the number of sub-apertures and actuators respectively. $\mathbf{x}$ is the voltage vector while $\mathbf{b}$ is the shift vector. The procedure involves applying a set of voltages to a particular actuator and recording the shifts in all the sub-apertures. Using this information, one can determine the shift per unit voltage in each sub-aperture when voltage is applied to that actuator. This measurement is recorded along the column and the procedure is repeated for the remaining actuators. After the IM is determined its inverse is calculated using the SVD (Singular Value Decomposition; Antia, 1991) method. When voltage is applied to the central actuator, the central sub-aperture has negligible shift along both the x and y directions, whereas the shift varies linearly with voltage when applied to other actuators. For a voltage range of 0-225 DACs with an interval of 25 DACs, the shift observed in the sub-apertures are linear with the applied voltage. Figure 6.17 illustrates the shift observed in the central sub-aperture when voltages were applied to all the actuators one by one.

6.4.2.3 DM in Real-Time Correction Mode

To demonstrate the capability of the DM as a local-deformation-correcting element, along with the TTM for global tilt correction, distortions are produced in two ways using DM-1: (a) introducing a defocusing error by applying voltage to the central actuator while changing it with different time delays and (b) by disturbing one of the peripheral actuators to represent a distortion dominated by global tilt. It is well known that the global tilt is taken care by the TTM and local deformations are corrected by the DM.

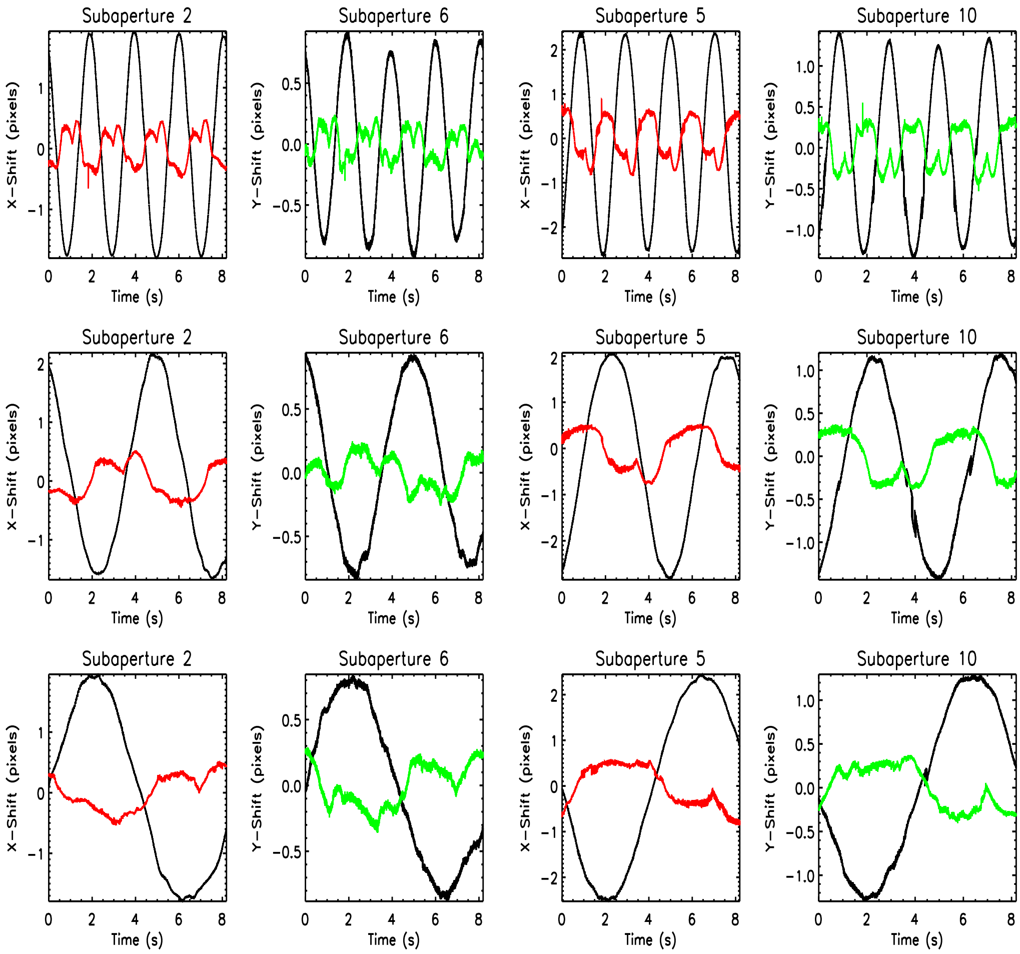

Figure 6.18: First column: Open (*black*) and closed (*red*) loop shift measurements recorded in sub-aperture number 2. The panels from top to bottom represent time delays of 1, 3 and 5 ms respectively. **Columns 2 to 4:** Same as the first column except for measurements in a different sub-aperture. The red and green plots correspond to closed loop measurements recorded in the x and y direction respectively.

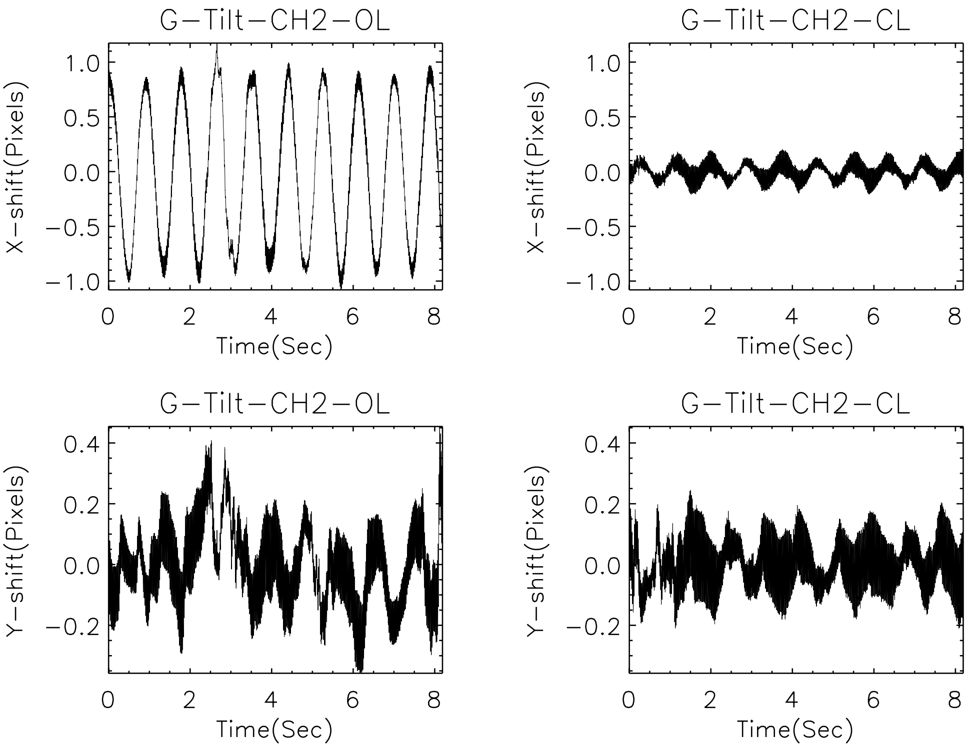

Figure 6.19: The performance of the AO system when voltage was applied to the 2^{nd} actuator alone. Top panels show open-loop and closed-loop shifts respectively along x axis, while the bottom panels are same as above but for the y axis. The global tilt was reduced to a fraction of a pixel.

For the first test, a sine pulse was applied to the central actuator alone. The minimum and maximum of the pulse correspond to 0 and 225 DACs respectively. The pulses were given in intervals of 25 DACs for time delays of 1, 3 and 5 ms respectively. Since this distortion is a radially symmetric one, the global tilt is negligible. The black lines in Figure 6.18 illustrate shifts in each sub-aperture when no correction was done (open-loop). Using the observed shift vector and the Influence matrix, the control voltage vector for the first seven actuators was computed and the same was applied to them. Application of the voltage to these actuators resulted in a reduction in the amplitude of shifts in each sub-aperture to a fraction of a pixel. The same is over-plotted in Figure 6.18 in red and green corresponding to the x and y directions respectively.

The global tilt correction was studied by creating a distortion in two ways:

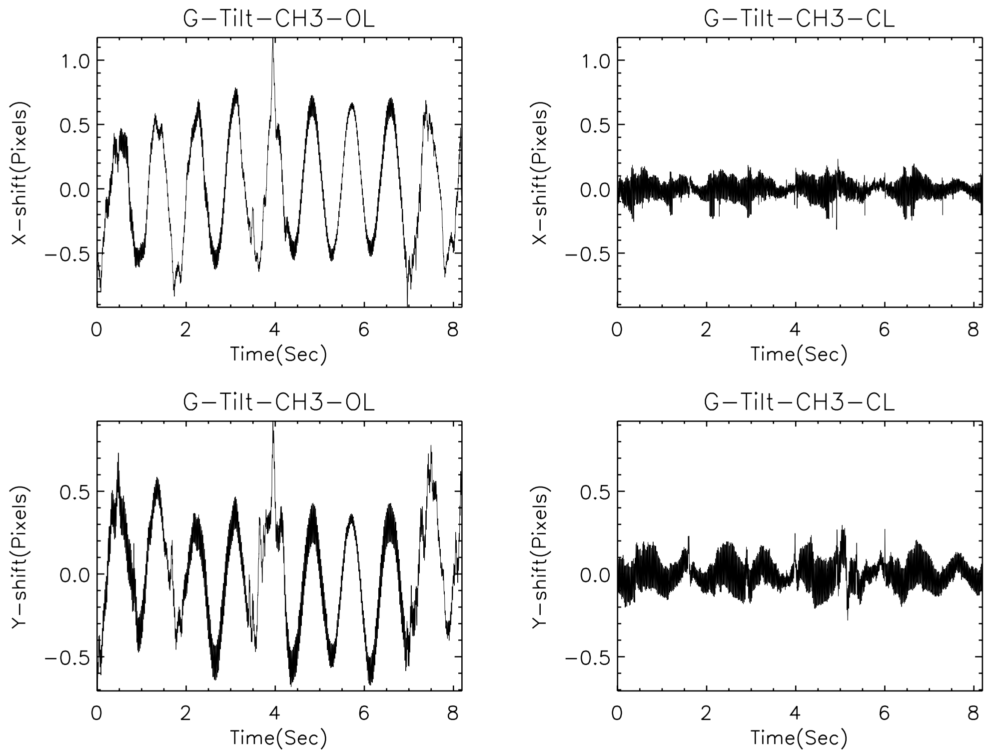

Figure 6.20: The performance of the AO system when voltage was applied to the 3rd actuator alone. Top panels show open loop and closed loop shifts respectively along x axis, while the bottom panels are same as above but for the y axis. The global tilt was reduced to a fraction of a pixel.

1. Voltage was applied to the 2nd actuator of DM-1, which is along the x axis of the actuator surface, the global tilt observed was along the x direction as expected while the same along the y-direction was nominal (Figure 6.19).

2. Voltage was applied to the 3rd actuator of DM-1, the global tilt observed was along both x and y directions as expected (right panel of Figures 6.20). Using suitable tuning parameters, the TTM was able to compensate the image motion in the closed-loop in all the above cases. The residual local shifts correspond to a voltage vector that was fed to DM-2. The residual local shifts being very small, the corresponding voltage vector too is small. Since the DM is insensitive at low voltages, the overall correction was carried out by the TTM alone.

6.4.3 Simulations Demonstrating the Effectiveness of Phase Diversity on AO Corrected Images

This technique involves acquiring two simultaneous images in which one image is focused and the other is defocused by a known amount (Löfdahl & Scharmer, 1994). Phase diversity (PD) is usually employed under fairly good seeing conditions, which is possibly why many astronomical groups apply it on AO corrected images to enhance the resolution of ground based telescopes to their diffraction limit. The atmospheric Point Spread Function (PSF) is the same for both images except that the PSF for the defocused image is also convolved with a defocus term having a finite known amount of defocus. Using a least square fitting method which requires an initial guess value for the Zernike coefficients (see Section 6.5.3.1 for a description of Zernike terms) for a finite number of terms, the object can be retrieved. This method involves computing the partial derivative of the Optical Transfer Function (OTF; Paxman et al., 1992) with respect to the Zernike co-efficients. Since the field of view of the detector is usually larger than the isoplanatic patch, the reconstruction must be applied separately to small segments of the full image, each segment being about the size of the isoplanatic patch (typically a few arcseconds in the visible).

Simulations were performed by using a portion of the image taken from the 1 m Swedish Solar Telescope (Scharmer et al., 2003b) as the reference object. The following studies were carried out to test the code and its effectiveness:(a) Performance of the code under various seeing conditions corresponding to different r_0, (b) Effect of increasing the number of Zernike terms to reconstruct the atmospheric PSF, (c) Effect of the defocusing parameter, and (d) Performance of the code on AO corrected images.

Using phase screens for different r_0 values (Sridharan et al., 2003), the focused and defocused images were obtained for a given defocusing parameter. The first three Zernike terms namely, piston, tip and tilt were removed from the wave front to compensate image motion. The developed phase diversity code was used to retrieve the original object by fitting the atmospheric PSF with 4-15 Zernike terms (Noll, 1976). It is observed that under good seeing conditions ($r_0 > 9$ cm), the code was able to recover the object as shown in Figure 6.21. Table 6.3 illustrates

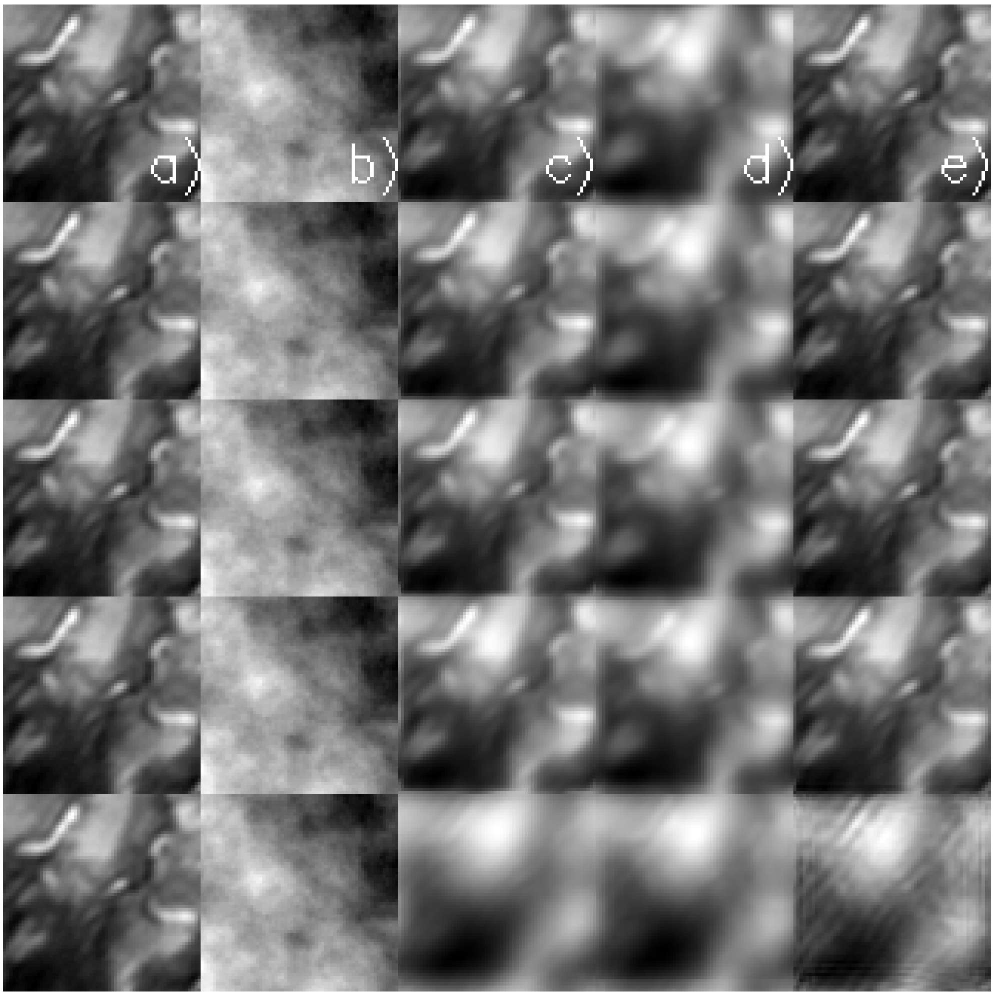

Figure 6.21: a) Object, b) Phase Screen, c) Object convolved with phase screen, d) Object convolved with phase screen and a finite Zernike Defocus term, e) Reconstructed Image. The phase screens used from top to bottom correspond to r_0 equal to 25, 20, 15, 9 and 3 cm respectively.

improvement in contrast, SNR (Signal-to-Noise Ratio) and reduction in rms wave front error (WFE). However, under moderate seeing conditions, corresponding to $r_0 < 5$ cm, artifacts were seen in the reconstructed image. Although, these artifacts could have been removed using a suitable filter which would lead to the loss of information, the performance was subsequently evaluated by increasing the number of Zernike terms. It was observed that as the number of correction terms increased, the signal to noise ratio improved as shown in Table 6.4. Thus the level of artifacts could be reduced, but since the evaluation time increased with the number of terms, only 10-25 terms were utilized to evaluate the code's performance. To obtain the optimum value of the defocus parameter, further simulation runs were carried out on a given phase screen for various values of the defocusing parameter (Zernike co-efficient, z). The actual distance m to be moved along the focus for a given Zernike defocus co-efficient z, can be written in terms of the depth-of-focus df using the following relation.

$$
\begin{aligned}
m &= \frac{4\sqrt{3}}{\pi} z df \\
df &= \frac{\lambda}{2}\left(\frac{f}{r}\right)^2
\end{aligned}
\tag{6.4}
$$

where λ is the wavelength of light, f and r are the focal length and radius of the telescope respectively. It is observed that the defocus parameter should be 2 to 5 times the depth of focus for optimum performance as shown in Table 6.5. However the same exercise should be performed for different input wave fronts of varying WFEs.

The code was applied on AO corrected images to achieve the high resolution imaging under seeing conditions corresponding to $r_0 < 5$ cm. As mentioned earlier, artifacts were seen in the reconstructed image when using phase diversity alone. Using point-wise correction on the input wave front, the coefficients of the first 15 Zernike terms were estimated. As it is impractical to achieve 100% correction with AO alone, 60% correction with AO was assumed and the phase diversity routine was applied on this AO corrected image. Figure 6.22 depicts the difference in the reconstructed image due to phase diversity alone and hybrid

Table 6.3: Performance of the code for atmospheric turbulence of varying wave front error (WFE). The input object contrast is 282 and the number of Zernike terms corrected is 15. The defocusing parameter is 1.5. Foc-focused, Defoc-defocused, Rob-Reconstructed object, TWF, RWF and ReWF - Tilt removed, Reconstructed and Residual wave front respectively.

rms WFE λ	Contrast of			*rms* WFE			No. of iterations	SNR
	Foc	Defoc	Rob	TWF	RWF	ReWF		
0.27	61	25	209	0.14	0.14	0.09	13	339
0.37	42	20	251	0.24	0.24	0.08	18	200
0.48	77	40	229	0.11	0.10	0.09	18	493
0.58	70	20	174	0.12	0.10	0.09	12	212
0.70	50	27	219	0.22	0.21	0.07	16	458
0.82	59	48	175	0.16	0.14	0.07	12	251

Table 6.4: Performance of the code vs no. of corrected terms. The input object contrast is 282 and the *rms* WFE of the wave front is 0.12 waves. The defocusing parameter is 1.5. Here it is shown that as the no. of terms increase the SNR increases.

No. of terms corrected	Contrast of the Rob	Variance		No. of iterations	SNR
		RWF	ReWF		
10	245	0.11	0.10	9	460
15	229	0.10	0.09	19	493
20	216	0.10	0.07	9	568
25	251	0.11	0.07	11	1076

Table 6.5: Performance of the code for various values of the defocusing parameter. The input object contrast is 282 and the *rms* WFE of the wave front is 0.12 waves. The number of terms corrected are 15.

Defocussing parameter z	Contrast		Variance		No. of iterations	SNR
	Foc	Defoc	RWF	ReWF		
0.5	77	214	0.10	0.07	12	511
0.75	70	214	0.10	0.08	18	504
1.0	60	204	0.09	0.08	13	437
1.25	50	288	0.12	0.11	15	320
1.5	40	229	0.10	0.09	19	493
1.75	32	202	0.09	0.08	11	418
2.0	25	195	0.09	0.08	10	382
2.25	19	193	0.09	0.08	12	365
2.5	15	191	0.09	0.07	12	358

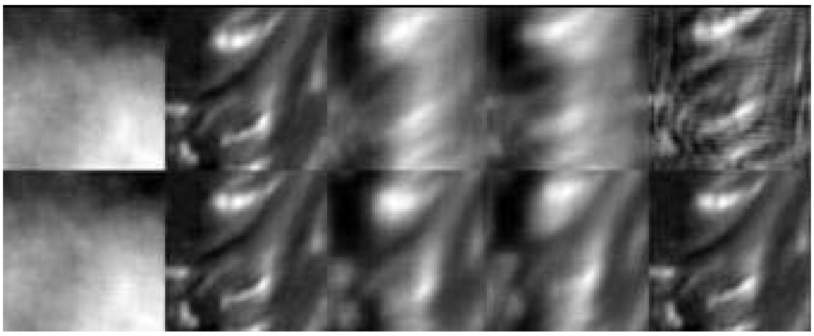

Figure 6.22: From left to right: Phase screen, Object, Focused image, Defocused image, Reconstructed image. The top panel shows image reconstruction using phase diversity alone. In the bottom panel the focused image is AO corrected on which phase diversity was implemented. The reconstructed image is due to the hybrid imaging. The phase screen used here corresponds to an r_0 = 3cm. It is evident that phase diversity is effective when the *rms* WFE is less.

imaging (AO+PD) respectively. The SNR of the reconstructed image using hybrid imaging is significantly larger when employing phase diversity alone. It is evident that the latter is more effective and necessary for high resolution imaging under moderate seeing conditions.

6.5 Choosing the Optimal Shack Hartmann Wave Front Sensor for the Adaptive Optics System at USO

In this Section I aim to arrive at a suitable lenslet configuration from a set of lenslet arrays, in an attempt to evaluate the performance of the prototype AO system under similar site conditions and optimistic corrective limits, through simulations. The telescope size, seeing conditions and the wave front sensing camera are considered as inputs in the simulations. Since SHWFs are inexpensive, can be custom manufactured and easy to procure, it justifies the approach to determine the geometry and configuration of a lenslet array (LA) that would yield desirable results under typical operating conditions.

Section 6.5.1 describes the optical setup for the prototype AO system at USO. Various shift algorithms, which will be required for the simulations, are presented in Section 6.5.2. The different lenslet geometries considered for the analysis and their performance in sensing random wave fronts is discussed in Section 6.5.3. I summarize the findings and present my recommendations for a suitable LA in Section 6.7.

6.5.1 Proposed Optical Setup for the prototype AO System

Figure 6.23 shows the tentative optical setup of the prototype AO system. The light feed is a 15 cm Coudé telescope having an f#15 beam (Figure 6.9). This produces a 21 mm image of the Sun at the prime focus. Using suitable relay lenses, the image of the full Sun at the reimaged focal plane (FS) is magnified to 42 mm inside the lab where the rest of the optical components are housed. For a small sized telescope the global tilt of the wave front is a dominant aberration

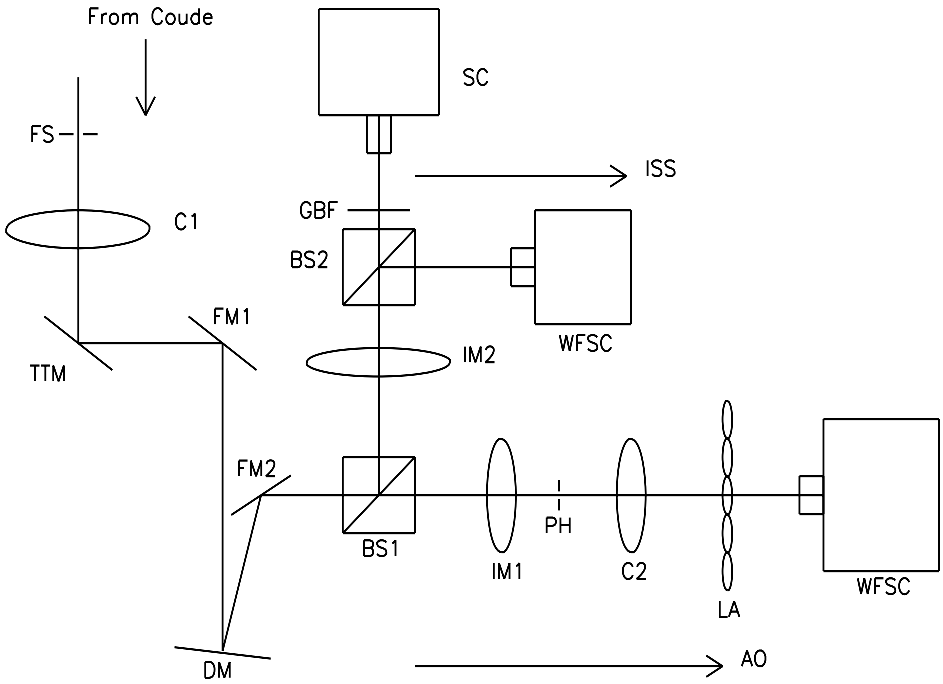

Figure 6.23: Tentative Optical setup of the prototype AO system. FS: Field Stop/Reimaged Focal Plane, C1: Collimating Lens, TTM : Tip-Tilt Mirror, DM: Deformable Mirror, FM1 & FM2: Folding Mirror, BS1 & BS2: Beam Splitter, IM1 & IM2: Imaging Lens, PH: Pin-Hole, C2: Collimating Lens, LA: Lenslet Array, WFSC: Wave Front Sensing Camera, GBF: G band Filter, SC: Science Camera, ISS: Image Stabilization System.

which causes random image motion. It is thus desirable to implement the AO compensation on the tilt-corrected wave front. The image motion is arrested using the Tip-Tilt Mirror (TTM) and the high speed wave front sensing camera (WFSC) which together form the Image Stabilization System (ISS). The ISS is currently operational with a closed loop bandwidth of 70 - 100 Hz with a residual *rms* image motion of ~ 0.1 arcsec (Sridharan et al., 2007). The optical setup shown in Figure 6.23 includes the ISS and the AO modules. Following the results of Section 6.3 the incidence angle on the DM is kept at an angle of less than $10°$ so as to avoid an additional astigmatism. The choice of the remaining collimating and imaging lenses are subject to the pitch and focal length of the Shack-Hartmann wave front sensor which I shall arrive at from the results of the simulation.

6.5.2 Shift Estimation Algorithms

Before setting up the simulations it is necessary to evaluate the accuracy of various shift estimation algorithms implemented on different scenes. There are essentially two algorithms that are used frequently for calculating the shift on extended objects, namely Sum of Absolute Difference (SAD) and Cross-Correlation (CORR; von der Lühe, 1983). SAD is computed as

$$SAD = \sum_{i=0}^{M} \sum_{j=0}^{N} |\mathrm{Ref}_{i,j} - \mathrm{Liv}_{i,j}| \tag{6.5}$$

The instantaneous shift of the live image (Liv) w.r.t a reference image (Ref), of size $M \times N$, is that for which SAD is a minimum.

This algorithm involves shifting the the live image artificially and calculating the SAD. When a minimum is reached, parabolic interpolation between the 2 neighbouring points about the minima, yields a shift accurate to a fraction of a pixel. One of the ways in which this algorithm is implemented is to compute SAD for a range of shifts starting from negative to positive. Naturally, for time critical applications this method is redundant although for the simulations this aspect is not so crucial. A variant of this algorithm called Sum of Absolute Difference Fast (SADF) is also employed (Sridharan et al., 2007). This algorithm is essentially the same as SAD with one minor change. The current image is always shifted within a 3×3 pixel grid corresponding to -1, 0 and 1 pixel respectively, in the x and y directions. The SAD is computed for these 9 points and the current image is subsequently shifted in the direction of the local minima. In general, SAD/SADF works well under better seeing conditions and can be quite fast for small images with relatively small shifts (Sridharan et al., 2005). As is evident, the time taken by SADF to compute the shift is dependent on the magnitude of the shift.

The Cross Correlation routine utilizes the Fast Fourier Transform (FFT) and is estimated as,

$$\text{CORR} = FFT^{-1}\left(\frac{FFT(\text{Ref}) * conj(FFT(\text{Liv}))}{(P_{REF} * P_{LIV})^{1/2}}\right) \tag{6.6}$$

where $conj$ implies complex conjugate while P_{REF} and P_{LIV} represent the total power in the reference and live image respectively. The instantaneous shift $(\delta x_0, \delta y_0)$ is that for which CORR is a maximum. Before computing the correlation the intensity gradient in the images should be removed since image motion is sensitive to high frequency components.

The three algorithms SADF, SAD and CORR were tested with a 1000 random shifts on three different images, namely, a point source, a sunspot and solar granulation. All images were 64×64 pixels in size while the central 32×32 region was considered for the shift calculation. The point source was generated using the standard hanning function in IDL. The image of the sunspot and its neighbouring quiet sun was acquired by the Solar Optical Telescope (SOT) on board the Japanese Space satellite *Hinode* (Tsuneta et al., 2008) on 2007, January 7. The image was taken in the G band at 4305 Å having a bandwidth of 0.8 nm. At USO, the shift estimation routine is not only used during AO correction but also during the calibration of the DM and estimation of the influence matrix.

The results of the random shift estimation using the three routines are shown in Figures 6.24-6.26. Both SAD and CORR retrieve the input shift irrespective of the scene, while there is a large scatter when SADF is used on a solar granulation. The scatter in the estimated shifts is perhaps due to local corrugations in the absolute intensity difference of the two images, arising from the relatively

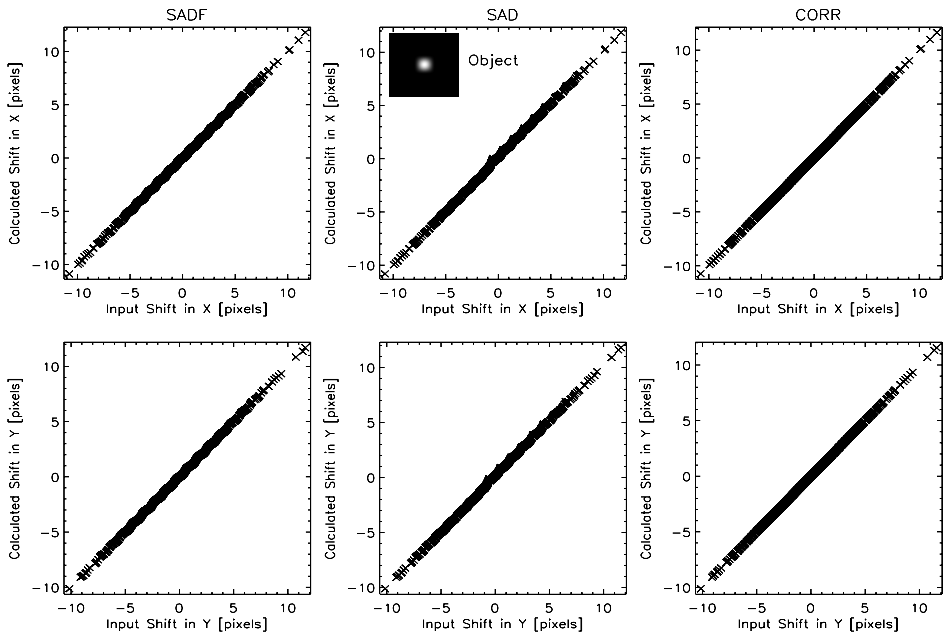

Figure 6.24: Left Column: Calculated X and Y shift using SADF on the point source. **Middle and Right Columns**: Calculated X and Y shifts using SAD and CORR respectively.

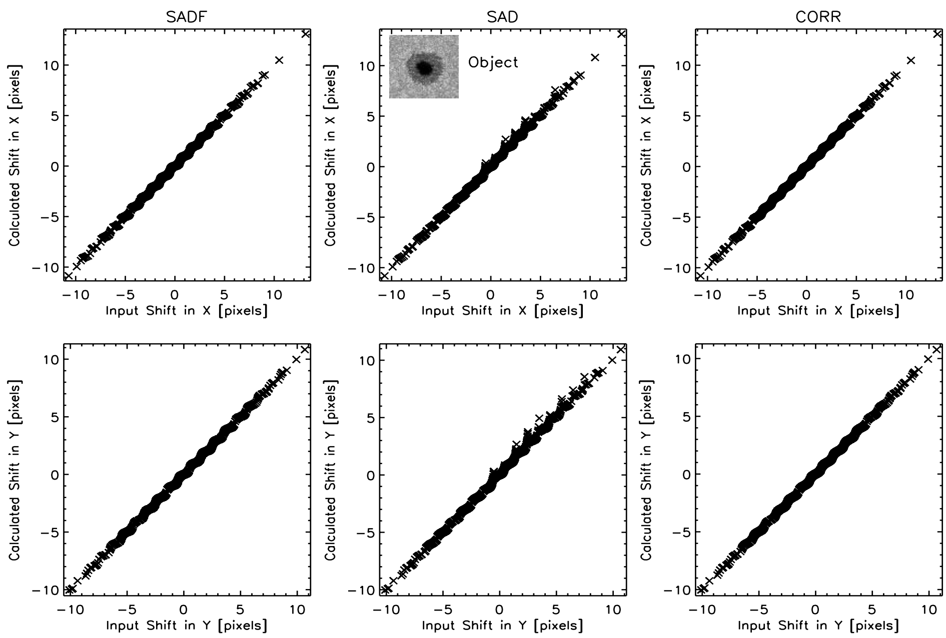

Figure 6.25: Same as Figure 6.24 but with a sunspot as the feature.

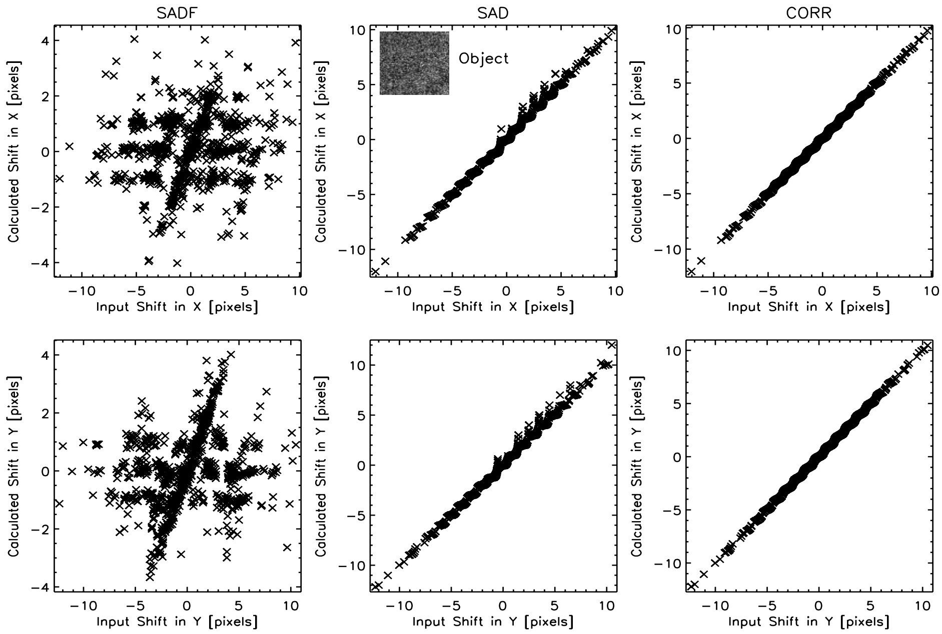

Figure 6.26: Same as Figures 6.24 and 6.25 but with solar granulation as the feature.

low-contrast feature such as granulation, thus biasing SADF. SAD on the other hand, searches for the global minima within a broader shift range and is able to recover the input shift. The reduction in contrast is apparent from the intensity distribution of the 3 images normalized to unity wherein, the minimum and median intensity of the granulation image is 45% and 64% respectively in comparison to 5% and 58% for the image corresponding to the sunspot. For the point source on the other hand, only 5 % of the total number of pixels have an intensity greater than 10%, thereby yielding a high contrast to the image. For the simulations described below, CORR was utitlized for estimating the shifts.

6.5.3 Performance of SH Wave Front Sensors

The size of the pupil on the SH wave front sensor should not exceed 2.6 mm, since this limitation is imposed by the size of the WFSC. The simulations were carried out for four lenslet configurations, namely Sq(340), Sq(460), Hx(360) and Hx(520). 'Sq' and 'Hx' imply square and hexagonal lenslets respectively, while the numbers in parentheses indicate the lenslet pitch in μm. The simulations were carried out in a 260×260 pixel window, each pixel being equivalent to 10

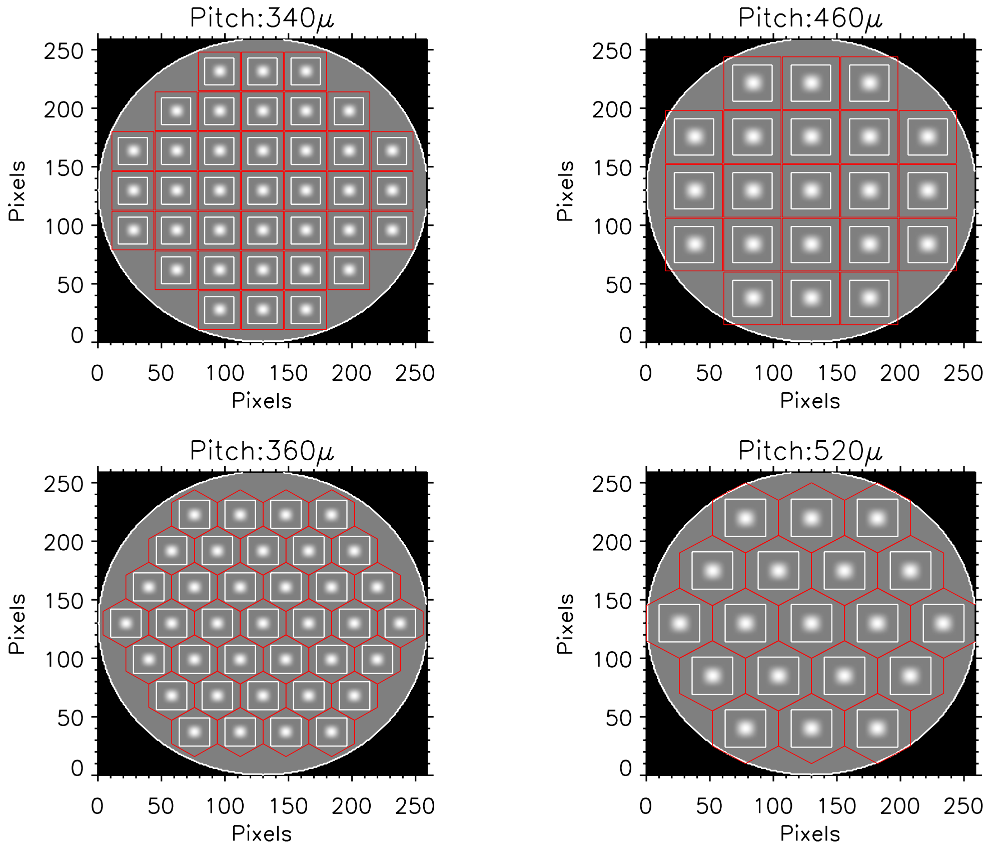

Figure 6.27: Lenslet configurations considered for the simulations. The top and bottom set of panels depict square and hexagonal LAs respectively. The grey area represents the pupil, while the sub-apertures are shown in red. The white boxes denote the central region within which the shift is estimated. The point source has been shown in negative for clarity.

μm. The central window in which the shift estimation was carried out for each LA was 24×24, 32×32, 24×24 and 32×32 pixel respectively. The lenslets were chosen based on the following criteria.

1. The lenslets should have a 100% fill fraction, hence circular lenslets were ruled out.

2. At least 98% of the lenslet area should lie within the pupil.

3. There should be an odd number of lenslets along the central row and column of the pupil.

4. The pitch of the lenslet should be large enough to accommodate a central region of at least 24×24 pixels for calculating the shift and must have clearance for a minimum of ± 5 pixel shift.

Condition 3 is not very crucial, since there are many AO systems in which the central pupil area is obscured by the telescope secondary. However, in our Coudé refractor system as well as the off-axis configuration of the proposed MAST, the central pupil is available and hence it is simply a matter of convenience to consider a symmetric geometry. Once having decided the geometry of the lenslets it is necessary to store the locations of each lenslet/sub-aperture. In our case the numbering of the sub-aperture starts from the lower left-hand corner and progresses from left to right, up to the top right-hand corner. The different LAs are shown in Figure 6.27.

6.5.3.1 Constructing the Influence Matrix

The next step in the simulations is constructing the influence matrix (IM) for each LA. A hanning window occupying 25% of the sub-aperture area was embedded within the central portion of the lenslet. The IM is an $2M \times N$ matrix, where M is the no. of sub-apertures and N the no. of Zernike terms (Noll, 1976; Roddier, 1999). The Zernike terms are orthonormal polynomials within a circle of unit radius (Born & Wolf, 1980). These polynomials describe the aberrations in an optical system. The phase errors introduced by the atmosphere into the incident wave front are equivalent to the phase errors (aberrations) introduced by an imperfect optical system. Thus, any distorted wave front can be decomposed into a sum of several Zernike polynomials. Mathematically these polynomials can be conveniently represented as (Noll, 1976)

$$\begin{aligned} Z_{evenj} &= \sqrt{2*(n+1)}R_n^m(r)\cos(m\theta), \quad m \neq 0 \\ Z_{oddj} &= \sqrt{2*(n+1)}R_n^m(r)\sin(m\theta), \quad m \neq 0 \\ Z_j &= \sqrt{(n+1)}R_n^0(r)\cos(m\theta), \qquad m = 0 \end{aligned} \tag{6.7}$$

where

$$R_n^m(r) = \sum_{s=0}^{(n-m)/2} \frac{(-1)^s(n-s)!}{s![(n+m)/2-s]![(n-m)/2-s]!} r^{n-2s} \tag{6.8}$$

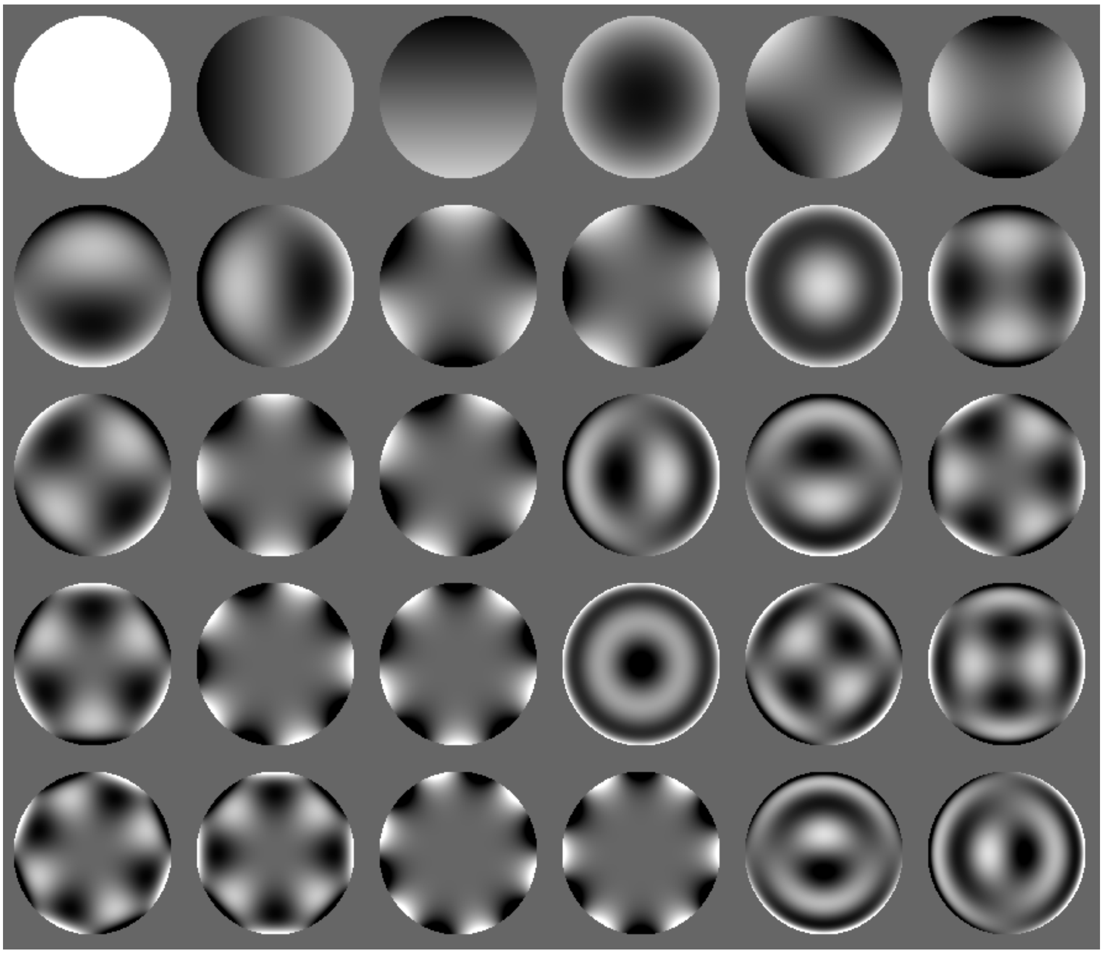

Figure 6.28: Zernike polynomials from 1 (**top left**) to 30 (**bottom right**).

The geometrical shapes of these polynomials are such that higher the mode, the higher the small scale variations in them. Figure 6.28 shows the first 30 Zernike polynomials.

For the simulations only 27 terms were considered starting from the defocus term Z_4. Terms Z_1, Z_2 and Z_3 correspond to piston, tilt in x and tilt in y respectively. Each sub-aperture image was convolved with the equivalent portion of the phase patch given as $\phi_k(x, y) = a_i Z_i^k(x, y)$, where the indices k and i denote the sub-aperture no. and the Zernike term respectively. For each Zernike term, its coefficient (a_i) was increased and the shift of the convolved image from the initial reference in each sub-aperture was recorded. The slope derived from a straight line fit to the plot of a_i vs. observed shift, was placed as an entry in

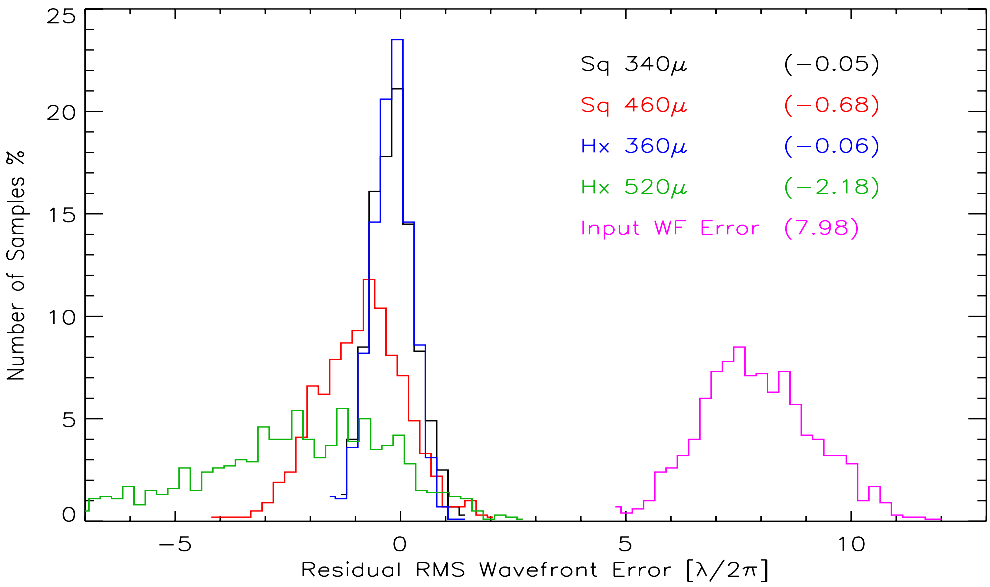

Figure 6.29: Histogram of the residual wave front errors using the four LAs, shown in different colours. The numbers in the parentheses denote median values.

the i^{th} column and the k^{th} row of the IM. This procedure was repeated for all 27 terms and subsequently for all four LAs.

6.5.3.2 Random Test Wave Fronts

To test the effectiveness of the IM for each LA, a linear combination of 20 Zernike terms with random coefficients, were used to construct 1000 realizations of wave fronts. Figure 6.29 depicts the distribution of the residual wave front error for the four LAs. The median residual wave front error for Sq(340), Sq(460), Hx(360) and Hx(520) in units of $\lambda/2\pi$ are -0.05 $\pm$ 0.5, -0.68 $\pm$ 0.98, -0.06 $\pm$ 0.46 and -2.18 $\pm$ 2.69 respectively. A comparison of the input random wave front and the estimated wave front, using Hx(360), is shown in Figure 6.30. It is apparent that irrespective of the geometry a lenslet array with a large number of lenslets is thus far more effective.

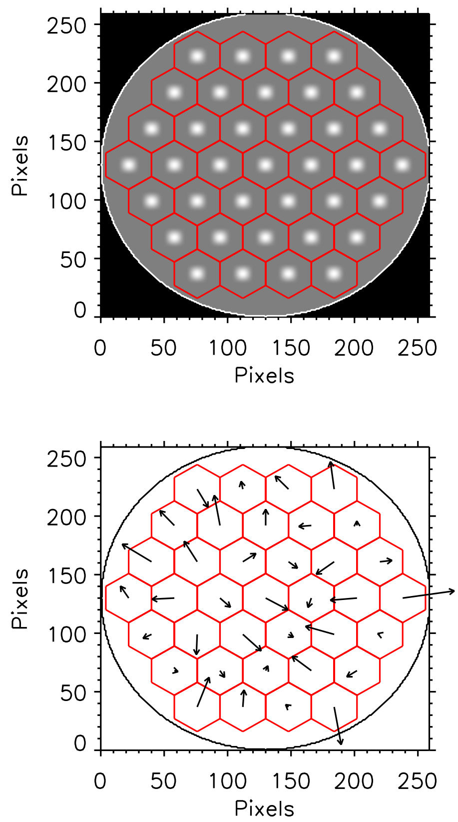

Figure 6.30: Top Left: Initial sub-aperture images using the Hx(360) LA. **Top Right:** Input Random wave front. **Bottom Left:** Sub-aperture shift vectors obtained from the CORR routine between the original image and the convolved image. **Bottom Right:** Wave front estimated from the shift vectors and previously determined Influence Matrix. The residual wave front error is -0.12($\lambda/2\pi$).

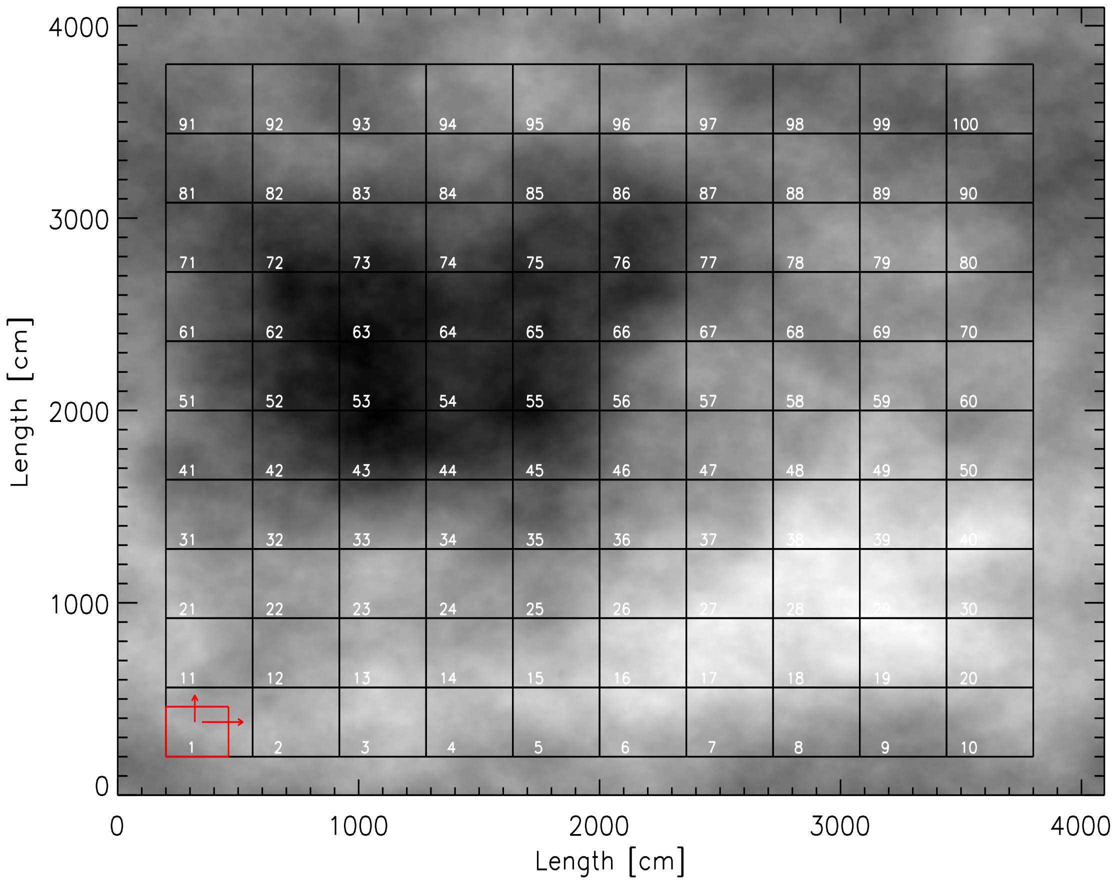

Figure 6.31: 40.96 m× 40.96 m phase screen derived from a Kolmogorov spectrum corresponding to an r_0 of 3 cm. The red box indicates the sub phase screen of size 260×260 pixels. 10000 realizations of the subphase screen are carried out within the larger numbered black grid by shifting the sub phase screen pixel by pixel along the direction shown by the red arrows. From the entire phase screen 100 such sub phase screens were derived.

6.5.3.3 Realistic Seeing Conditions

In this Section I restrict the analysis to LAs Sq(340) and Hx(360), based on the results obtained from the estimation of random wave fronts. The two LAs were used to sense wave fronts arising from realistic phase perturbations similar to that induced by the atmosphere. Two phase screens based on a Kolmogorov spectrum (Tyson, 1991; Roddier, 1999) corresponding to an r_0 of 3 cm and 5 cm were utilized. The generation and validation of the phase screens are described in (Sridharan, 2001; Sridharan et al., 2003; Sridharan & Bayanna, 2004). The phase screens corresponding to an r_0 of 3 cm and 5 cm are 4096×4096 pixel and 8192×8192 pixel respectively, with each pixel equivalent to 1 cm. The phase fluctuations mimic the average seeing conditions prevalent at the site where the 15 cm Coudé telescope is located. Henceforth the 2 large phase screens corresponding to the seeing conditions will be referred to as PHS1 and PHS2 respectively.

Since the aperture considered in our simulations is 260×260 pixels, phase screens of the same size are utilized. As shown in Figure 6.31, each numbered black grid signifies the area within which 10000 realizations of the 260×260 phase patch was averaged. Each of these realizations was generated by shifting the phase patch (shown as the red box) by 1 pixel to the right and subsequently upwards shown by red arrows. A total of 100 such sub-phase screens were generated from PHS1 while 400 sub-phase screens were obtained from PHS2. It is necessary to average over the phase patch (black boxes) in order to obtain a Modulation Transfer Function that falls off smoothly at the spatial frequency corresponding to that value of r_0. This depends on the number of realizations one considers. Since our primary aim is to compare the performance of the 2 LAs, it is not necessary to generate sub-phase screens which strictly have an MTF cut-off at the spatial frequency corresponding to that particular r_0. Hereafter the sub-phase screens belonging to PHS1 and PHS2 will be denoted as PH-1 and PH-2 respectively.

Before testing PH-1 and PH-2 on the 2 two LAs Sq(340) and Hx(360), the global tilt was removed from the wave front. This was done by creating a look-up table similar to the way the IM was created, but using only the tilt terms, namely Z_2 and Z_3. These tilt-corrected wave fronts were then used for testing the two LAs. For each image/frame, the MTF of the following quantities was determined;

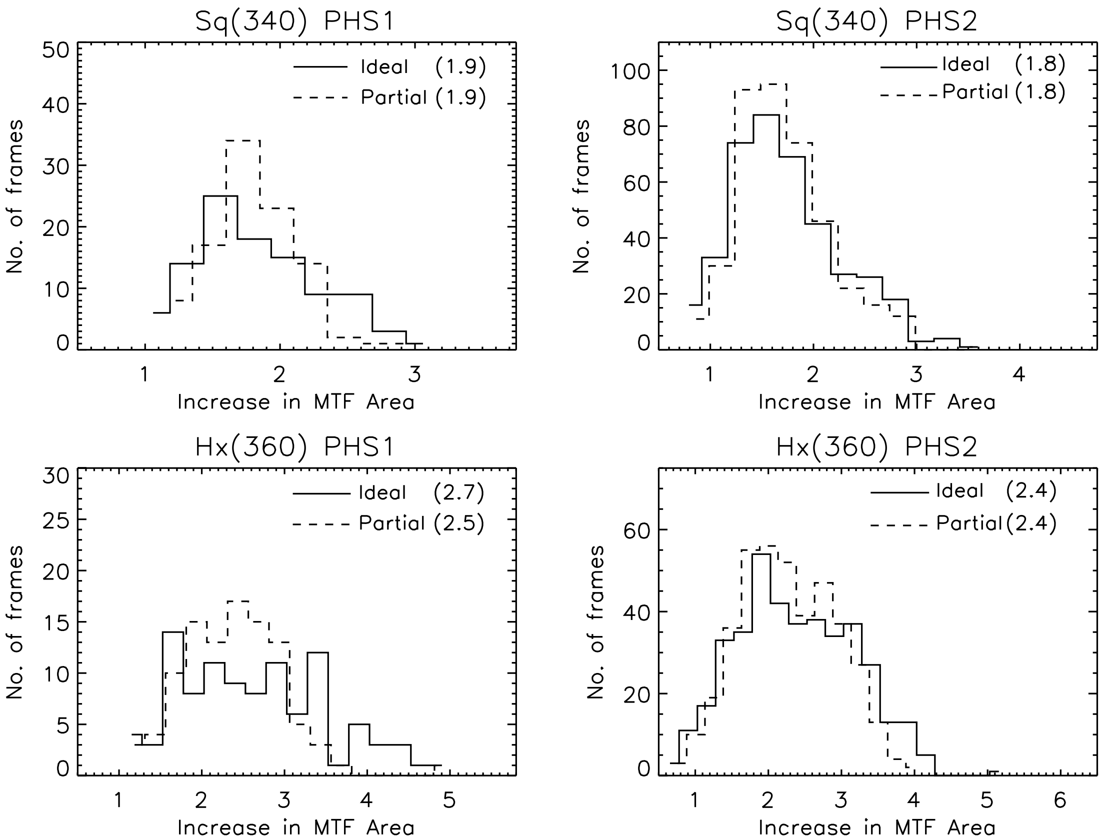

Figure 6.32: Histogram of the fractional increase in the azimuthally averaged MTF area for ideal (*solid*) as well as partial (*dashed*) AO compensation. **Top Left:** AO correction for PHS1 using Sq(340). **Top Right:** AO correction for PHS2 using Sq(340). **Bottom Left:** AO correction for PHS1 using Hx(360). **Bottom Right:** AO correction for PHS2 using Hx(360).The numbers in the parentheses denote median values of the histogram. The bin size is 0.25.

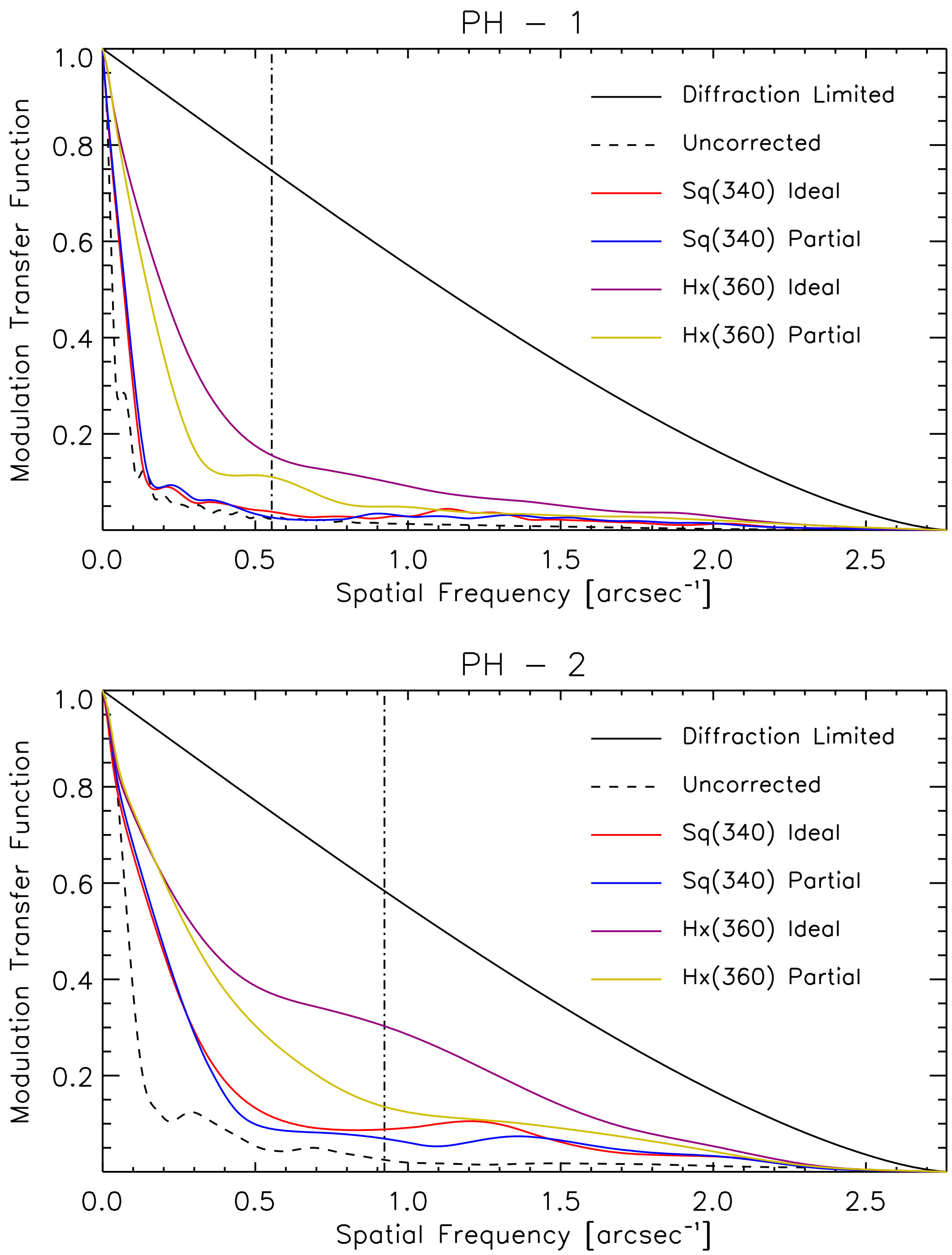

Figure 6.33: Azimuthally averaged MTF before and after AO compensation for phase screens PH-1 and PH-2, using Sq(360) and Hx(360). The vertical *dot–dashed* line in the top and bottom panels corresponds to an r_0 of 3 cm and 5 cm respectively. The theoretical MTF for a 15 cm telescope in the G band is shown as the solid black line. The x-axis represents the spatial frequency, where 2 pixels per diffraction limit has been assumed.

a) the tilt-corrected input wave front, b) the residual wave front after assuming ideal compensation and c) the residual wave front after assuming partial compensation, i.e., 85 % correction. Quantifying the factors contributing to the overall efficiency of the system has to be evaluated. I defer this calculation to the future. The MTF for each of these quantities was then averaged azimuthally over a constant radius corresponding to the cut-off frequency in the Fourier domain. Following this, the ratio of the ideally/partially corrected MTF area to the uncorrected MTF area was determined. The ratio of the MTF areas signifies the extent of sensing in both scenarios and serves as a tool to compare the performance of the two LAs under identical seeing conditions. The distribution of the ratio of the azimuthally averaged MTF areas is shown in Figure 6.32.

The median value of the increase in the MTF area for sensing phase perturbations corresponding to PHS1 and PHS2 using Sq(340) is 1.9 and 1.8 respectively assuming ideal as well as partial compensation. The increase in MTF area can be as high as 3 in both ideal and partial cases for both phase screens although the number of images with ideal correction is only marginally greater than in the partial case. This trend is also seen in the LA Hx(360).

The median value of the increase in the MTF area for sensing phase perturbations corresponding to PHS1 and PHS2 using Hx(360) is 2.7 and 2.4 respectively assuming ideal compensation while with partial compensation the values are 2.5 and 2.4 respectively. The increase in MTF area using Hx(360) can even reach 3.5, in ideal and partial cases for both phase screens. However, it is clearly apparent that even with partial compensation, Hx(360) is ~ 1.3 times more efficient than Sq(340) for both seeing conditions with a 2.5 times increase in the MTF area.

Figure 6.33 demonstrates the improvement in MTF for 2 phase screens PH-1 and PH-2 belonging to PHS1 and PHS2 respectively. For both phase screens the improvement in the MTF amplitude is much greater when using Hx(360) than with Sq(340). The increase in the amplitude at higher spatial frequencies clearly indicates the effectiveness of optimal sensing, even with partial compensation. This is qualitatively demonstrated in Figures 6.34 and 6.35 where the corresponding uncorrected and AO corrected images for both phase screens PH-1 and PH-2 are shown. It is evident that for both LAs, even partial compensation is capable of improving the contrast in the images and with marginally better

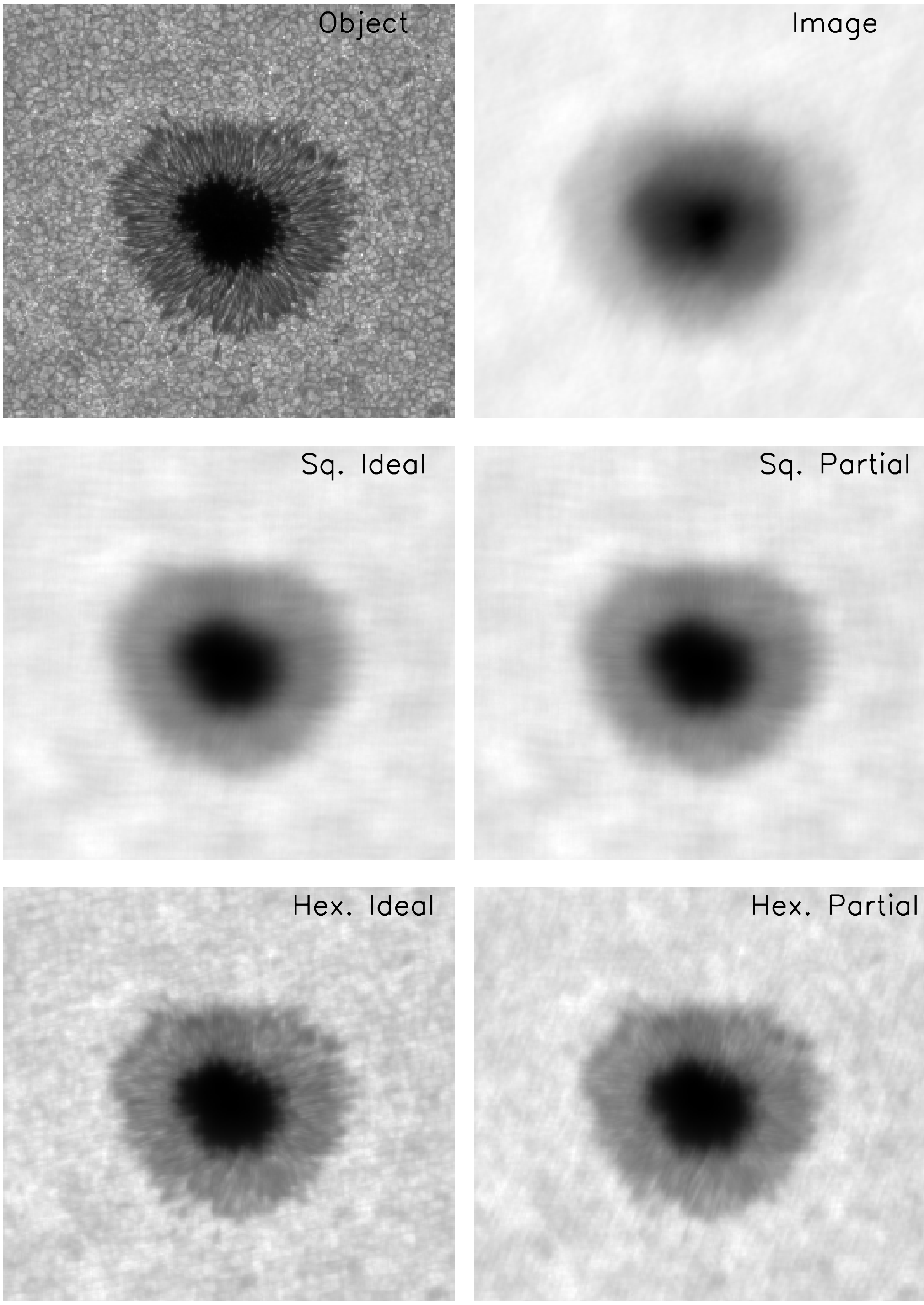

Figure 6.34: AO corrected images using Sq(340) and Hx(360) lenslet arrays for an $r_0 = 3$ cm seeing. Sunspot image (**top left**) and image resulting from convolution with phase screen PH-1 (**top right**). The middle and bottom panels represent ideal and partial AO compensation of shifts using Sq(340) and Hx(360) respectively.

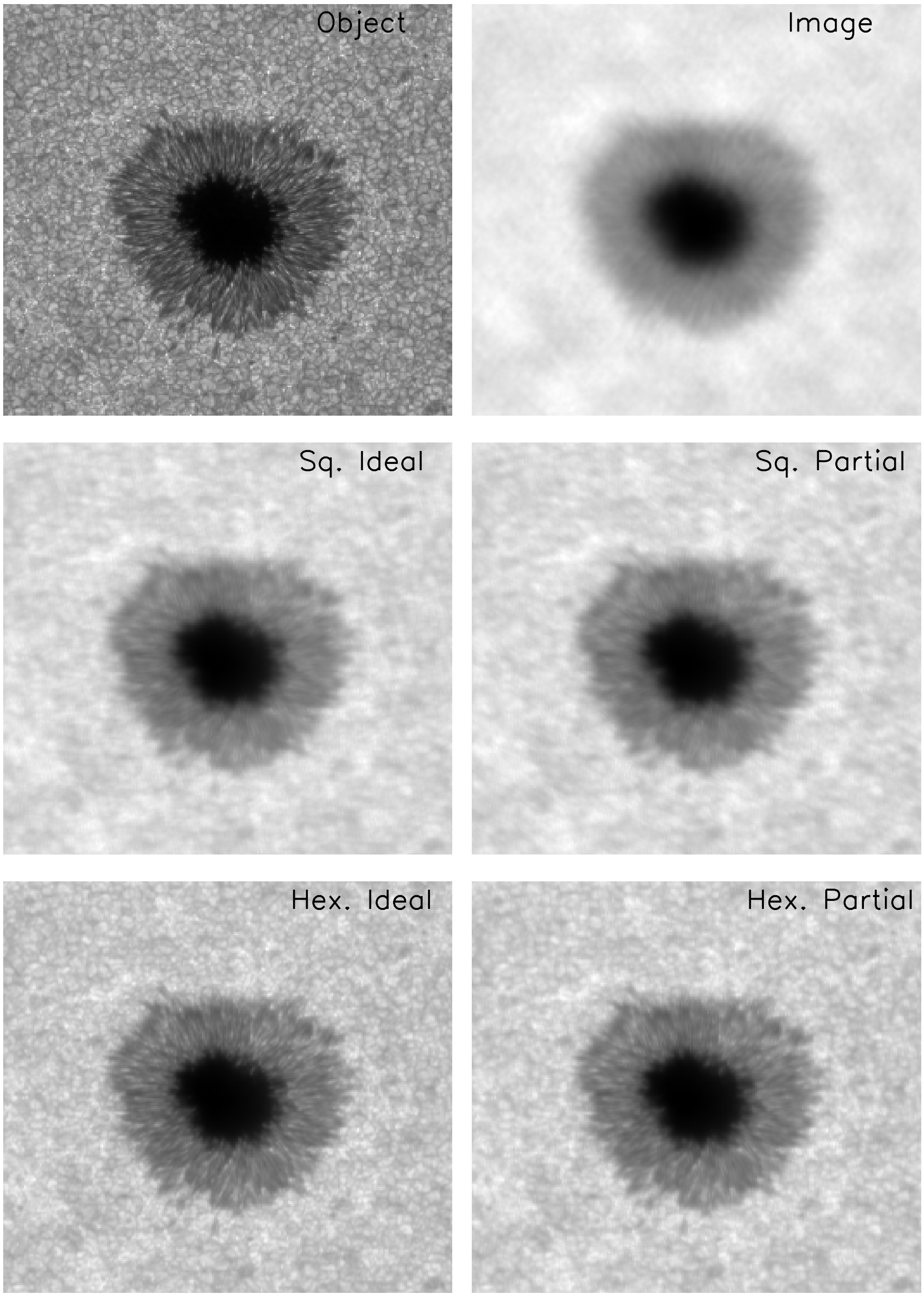

Figure 6.35: Same as Figure 6.34 but for an $r_0 = 5$ cm.

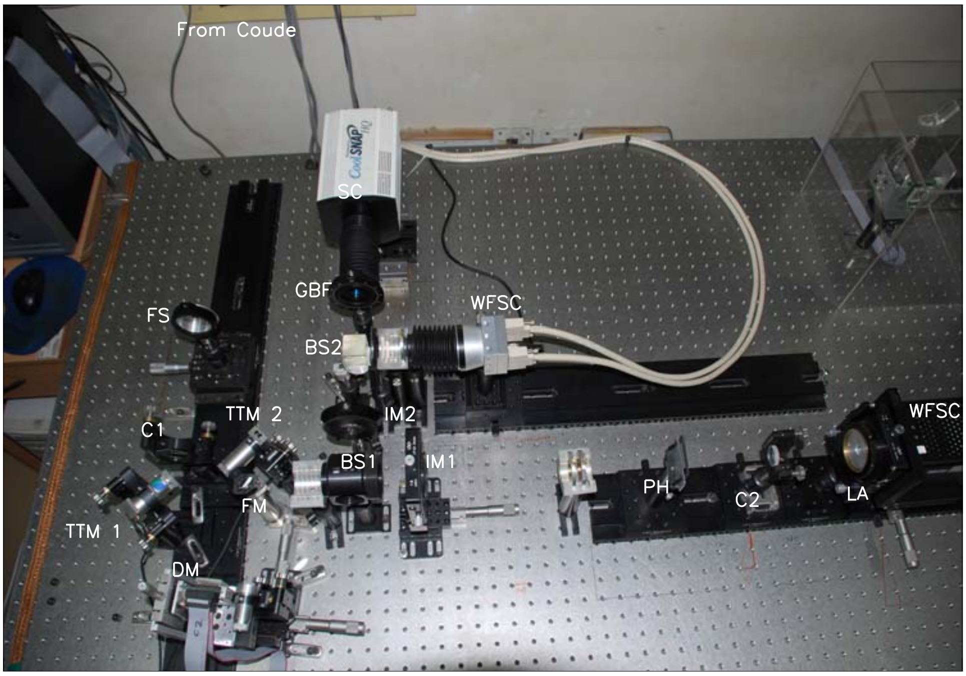

Figure 6.36: Optical setup of the prototype AO system. FS: Field Stop/Reimaged Focal Plane, C1: Collimating Lens, TTM 1 & TTM 2: Tip-Tilt Mirror, DM: Deformable Mirror, FM: Folding Mirror, BS1 & BS2: Beam Splitter, IM1 & IM2: Imaging Lens, PH: Pin-Hole, C2: Collimating Lens, LA: Lenslet Array, WFSC: Wave Front Sensing Camera, GBF: G band Filter, SC: Science Camera.

seeing, as is the case in PH-2, the improvement in image quality is undoubtedly superior.

6.6 First Light Observations using the Prototype Adaptive Optics System

This section describes first light photospheric observations of NOAA AR 11072 taken with the prototype AO system at USO on 2010 May 25 at 7:38 UT. A stand alone Image Stabilization system was developed using a new CMOS based wavefront sensing camera in order to correct for image motion arising from seeing as well as the imperfect telescope tracking. This was done to allow the solar feature to remain within the sub-aperture long enough to switch on the DM.

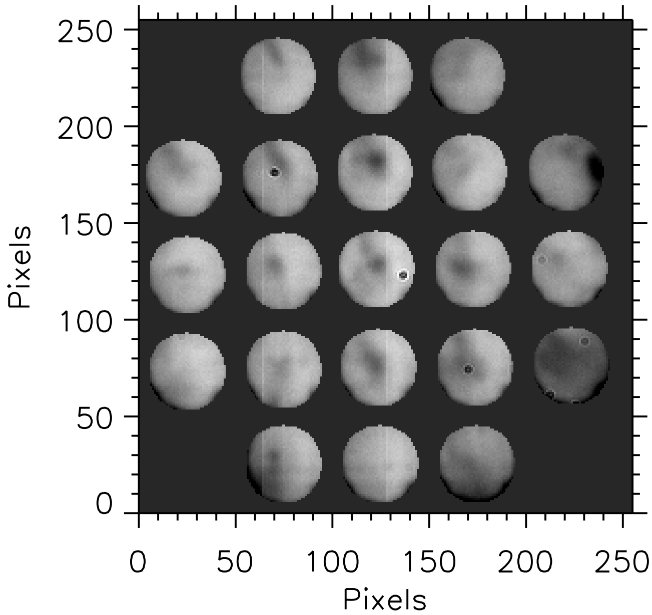

Figure 6.37: Sub-aperture images using the square 500μm lenslet array having a focal length of 45 mm. The raw lenslet images (flat and dark correction not applied) were acquired separately after the AO acquisition program was halted. The background of the image has been scaled suitably to enhance the contrast of the feature within the lenslets.

The optical setup used in the observations is presented in Section 6.6.1. The derivation of the Influence Matrix is described in Section 6.6.2 while the results and preliminary performance of the AO system is discussed in Section 6.6.3.

6.6.1 Optical Setup of the Prototype AO system

The optical setup shown in Figure 6.36 is similar to the one depicted in Figure 6.23 with one of the folding mirrors (FM 1) replaced by a second tip-tilt mirror (TTM 2). The f#15 beam from the Coudé telescope is magnified by two relay lenses placed outside the lab which produce a 42 mm image of the full Sun at the field stop (FS). The collimating doublet C1 has a focal length of 200 mm and produces a 6.7 mm pupil on the deformable mirror (DM). The two tip-tilt mirrors consist of 1 inch mirrors from Newport Corporation^{R} glued onto the piezo stacks. The light reflected from the DM is steered at a small angle using the folding mirror (FM) towards the beam splitter BS1, which diverts half the beam to the wavefront sensing unit for AO correction and the other to the science camera (SC) and the wavefront sensing camera (WFSC) of the Image Stabilization System using another beam splitter (BS2). The imaging doublets IM1 and IM2 have a focal length of 300 and 250 mm respectively. While the former produces a 63 mm image at the pin hole (PH), the latter produces a 52.5 mm image at the two cameras.

A 1.1 mm nearly circular pin hole (PH) covers a 32″ FOV. Using a collimating lens (C2) of focal length 125 mm and a square lenslet array having a pitch of 500μm with a focal length of 45 mm, 21 sub-apertures, each occupying 40 pixels, could be accommodated in the wavefront sensing camera as shown in Figure 6.37. To avoid the edges the central 32×32 pixel area was chosen and the shift estimation was done in the central 16×16 pixel area. The spatial sampling in the DALSA is 0.″8/pixel.

The wavefront sensing camera (WFSC) of the image stabilization system (ISS) is a CMOS based monochrome camera from Optronis GmbH with a MicroEnable-IV PCIe x4 frame grabber board from Silicon Software. The frame grabber has an on-board memory of 512 Mb and a transfer speed of 750 Mbps. The serial communication between the camera and the frame-grabber is carried out by RS-644 over CameraLink having a baud rate of 9600 bits/sec. The camera works with an internal as well as external synchronization.

The camera has a frame rate of 500 fps at the full resolution of 1280×1024 pixels. The pixel size is 14×14μm. The frame format can be selected in steps of 24 and 2 pixels in the x and y-direction respectively. The minimum frame rate with internal synchronization is limited to 16 fps. The maximum frame rate of the camera can vary depending on the camera Link configuration mode (Base, Medium, Full) and the resolution. For correcting image motion, a 256×256 pixel frame with 0.5 ms exposure was utilized with a frame rate of 1000. The SAD algorithm was carried out on a central 96×96 pixel area. The correlation tracker and control program were developed in-house[1] using C on a Windows Vista Basic edition having an Intel Core 2 Duo processor with a 2 Gb RAM. The shifts from

[1]The DLLs and standard functions for camera and frame grabber initialization and image acquisition were combined with the existing AO software developed for DALSA which were subsequently customized to work on a Windows environment. Details are present in the project report prepared by Manish Bansal and Niraj Punjabi.

the WFSC were used to operate TTM 1 (Figure 6.36). Each pixel of the CMOS camera samples $0.''49$.

The science camera (SC) is a 1392×1040 pixel CoolSNAP$_{\mathrm{HQ}}$ CCD from Roper Scientific with a pixel size of 6.45 μm. At full resolution the CCD readout speed is 96 ms with a 20 MHz digitization rate. The CCD communicates with the computer through a 32 bit PCI card. The PCI card also accepts a standard BNC connector for video output. Exposure times, number of frames, region of interest and observing modes can be changed through the camera acquisition software. A 10 Å G band interference filter (GBF) from Spectro-film was placed in front of SC to carry out photospheric observations at 4305 Å. The spatial sampling in the SC is $0.''23$/pixel.

6.6.2 Determination of the Influence Matrix

Before locking onto solar features such as sunspots, the Influence Matrix was determined so as to allow the DM to correct the local tilts using the shifts observed in the 21 sub-apertures. The procedure is similar to the one described in Section 6.4.2.2. Voltages were applied from 0 to 220 DACs in steps of 10 DACs to each actuator and the corresponding shifts in each sub-aperture were noted. This is shown in Figures 6.38 and 6.39 for the central sub-aperture when voltages were applied to the 19 actuators one by one. With 21 sub-apertures, a 42×19 matrix was derived which was then tested to retrieve one of the input recorded shifts corresponding to a set of voltages to a single actuator. As seen in Figure 6.40, the voltages to the specific actuator are nearly equal to the input value and the contribution from other channels is almost nill.

6.6.3 Performance of the Prototype AO system

On 2010 May 25, the prototype AO system was used to lock onto a sunspot that was located at a heliocentric angle of 30°. For a small sized telescope, the global tilt is the dominant aberration. This was one of the reasons why a stand alone tip-tilt system was developed. Proportional and Differential gain values of 20 and 2 were used respectively for both the axes after resolving the direction of the correction. For the DM a gain value of 0.8 was utilized to correct the local

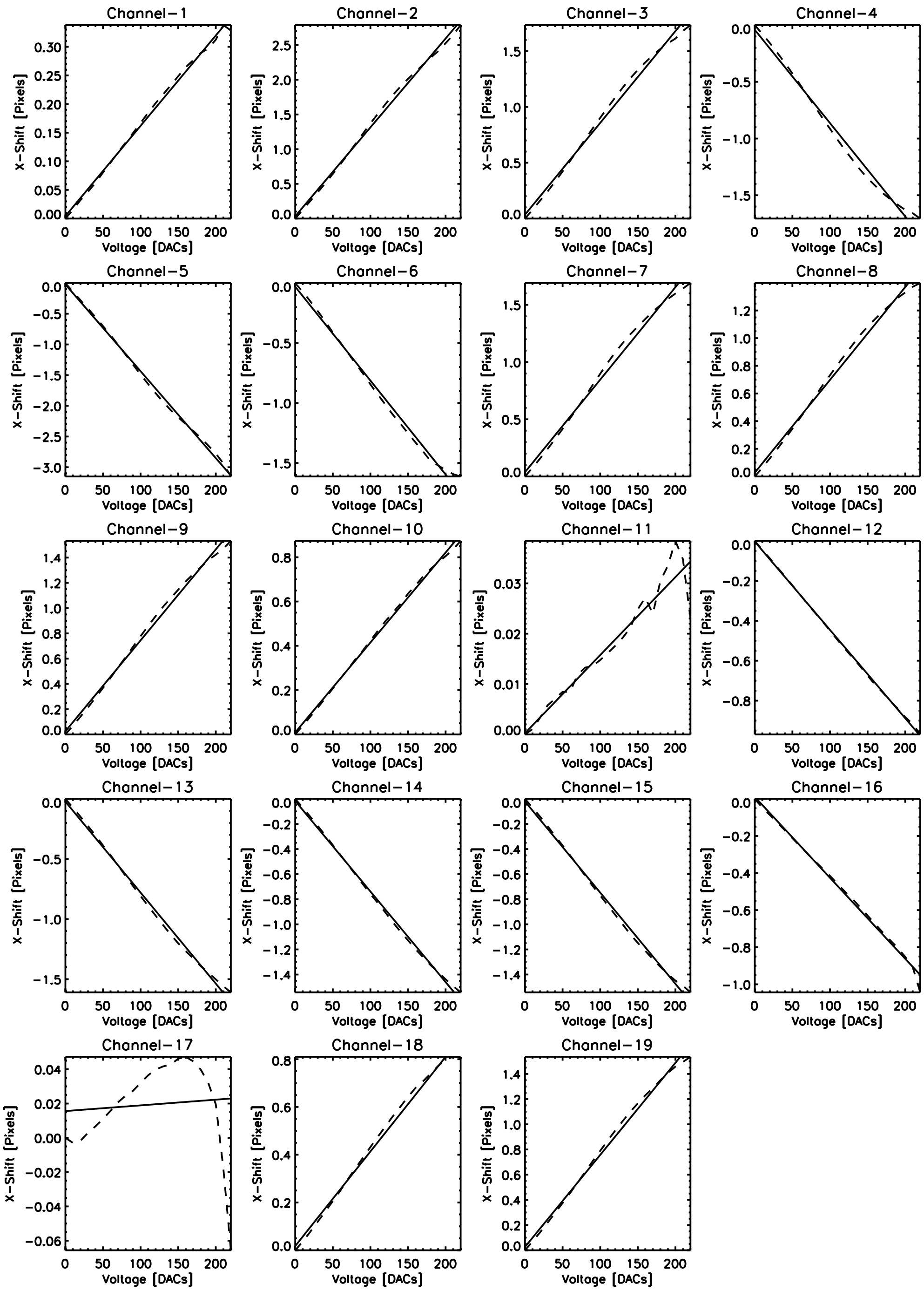

Figure 6.38: Constructing the Influence matrix. Plots show shifts seen along the x-axis of the central sub-aperture when voltages 0 to 220 DACs were applied to each of the 19 actuators in steps of 10 DACs. The *dashed* and *solid* lines are the observed shifts and the linear fit respectively.

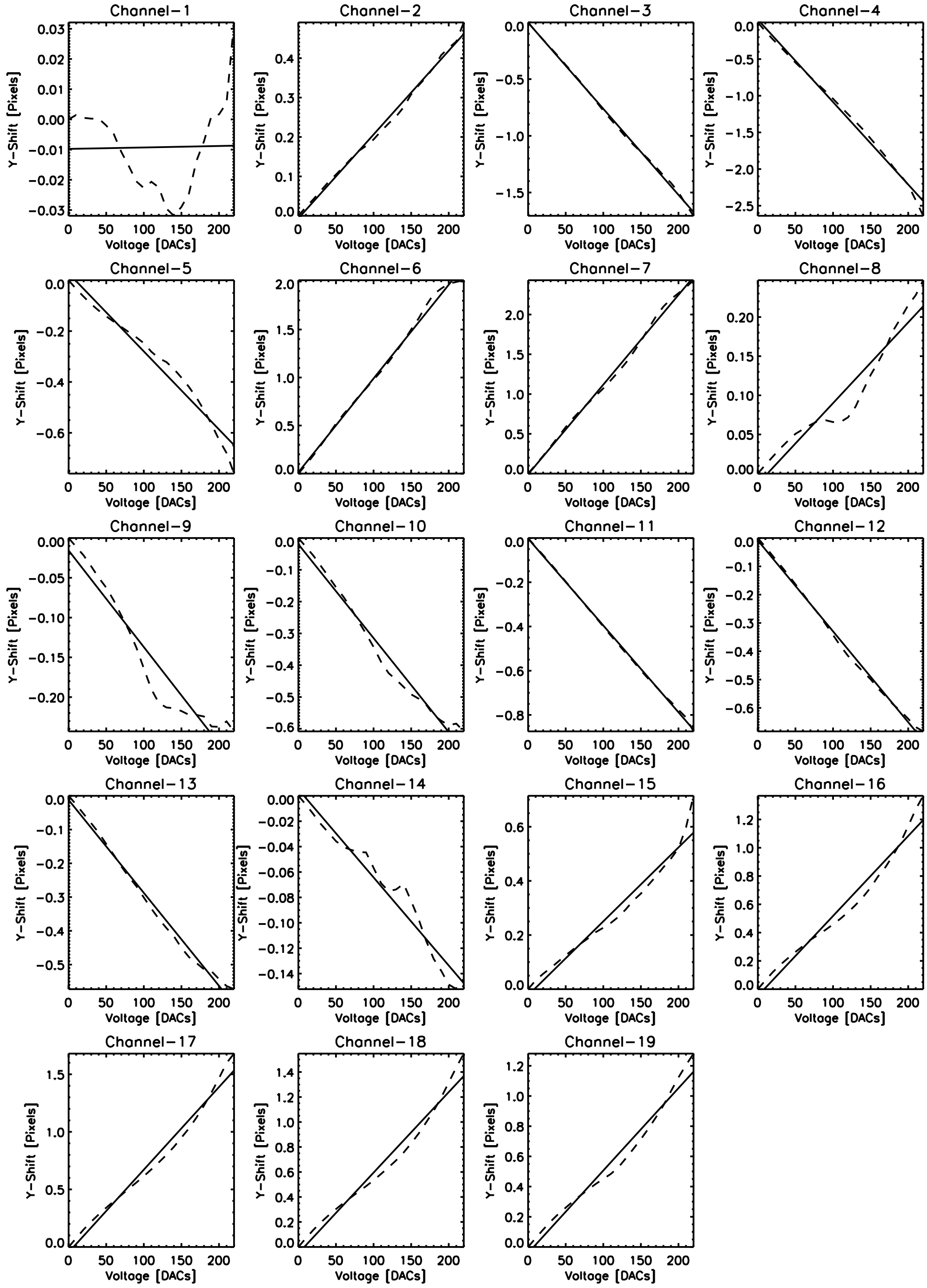

Figure 6.39: Same as Figure 6.38 but for shifts observed along the y-axis in the central sub-aperture.

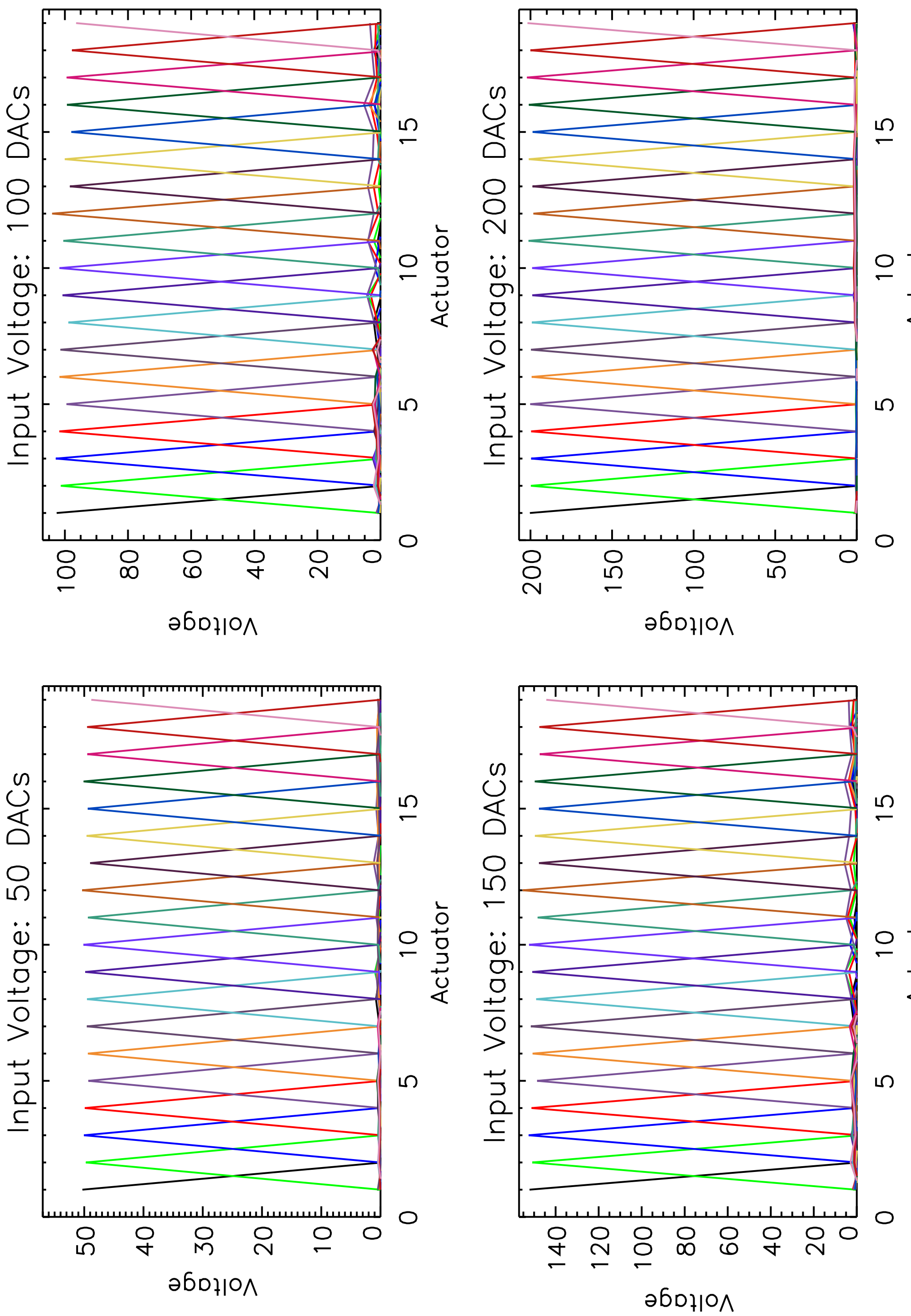

Figure 6.40: Retrieval of the voltage vector using the input shifts and the Influence Matrix to verify the calibration. The colours indicate retrieved voltages in different channels when an input voltage was applied to a single actuator.

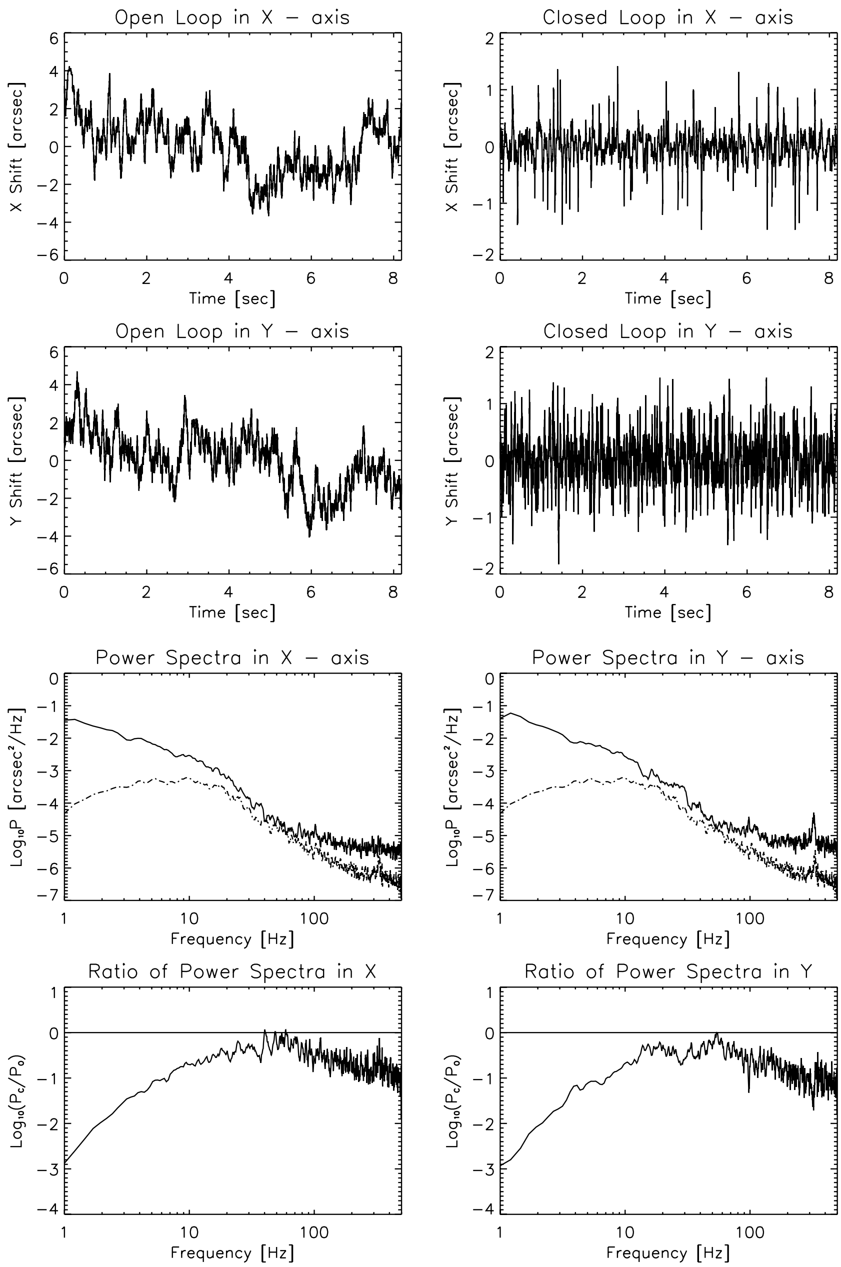

Figure 6.41: First Row: Open and closed loop shifts measured along x-axis using the Image Stabilization system. **Second Row:** Same as above but for shifts in the y-axis. **Third Row:** Log of the power spectra in the open (*solid*) and closed loop (*dot-dashed*) measured along x and y axis. **Bottom Row:** Log of the ratio of the power spectra along x and y axes. The bandwidth of the Image Stabilization System is determined from the frequency at which the ratio becomes unity.

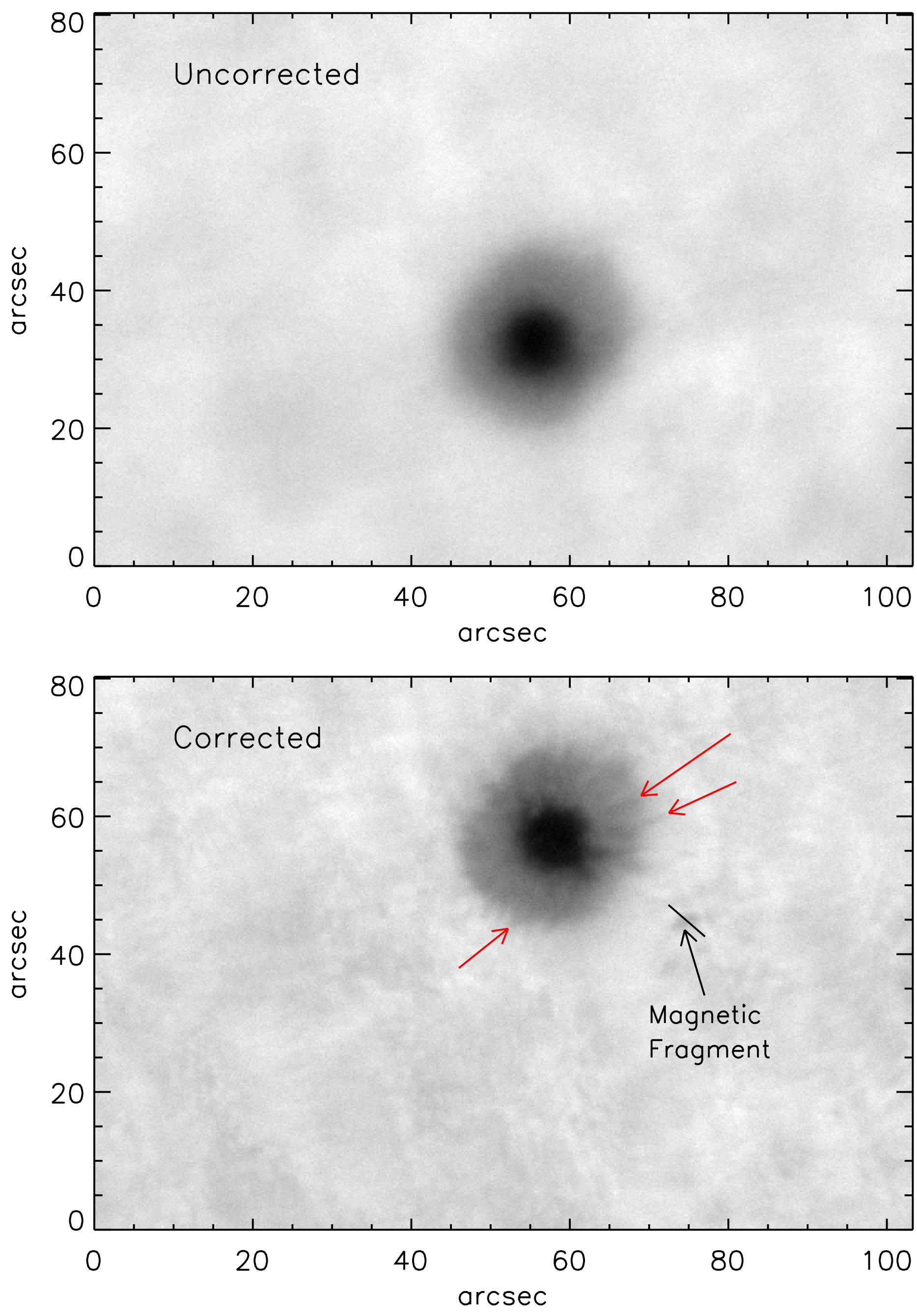

Figure 6.42: Best uncorrected (**top**) and AO corrected (**bottom**) images acquired from the 100 frame burst in the Science Camera. Exposure time was 6 ms. The red arrows indicate the filamentary structure of the penumbra. The solid black line represents a cut across the magnetic fragment to estimate the spatial resolution achieved with the AO correction.

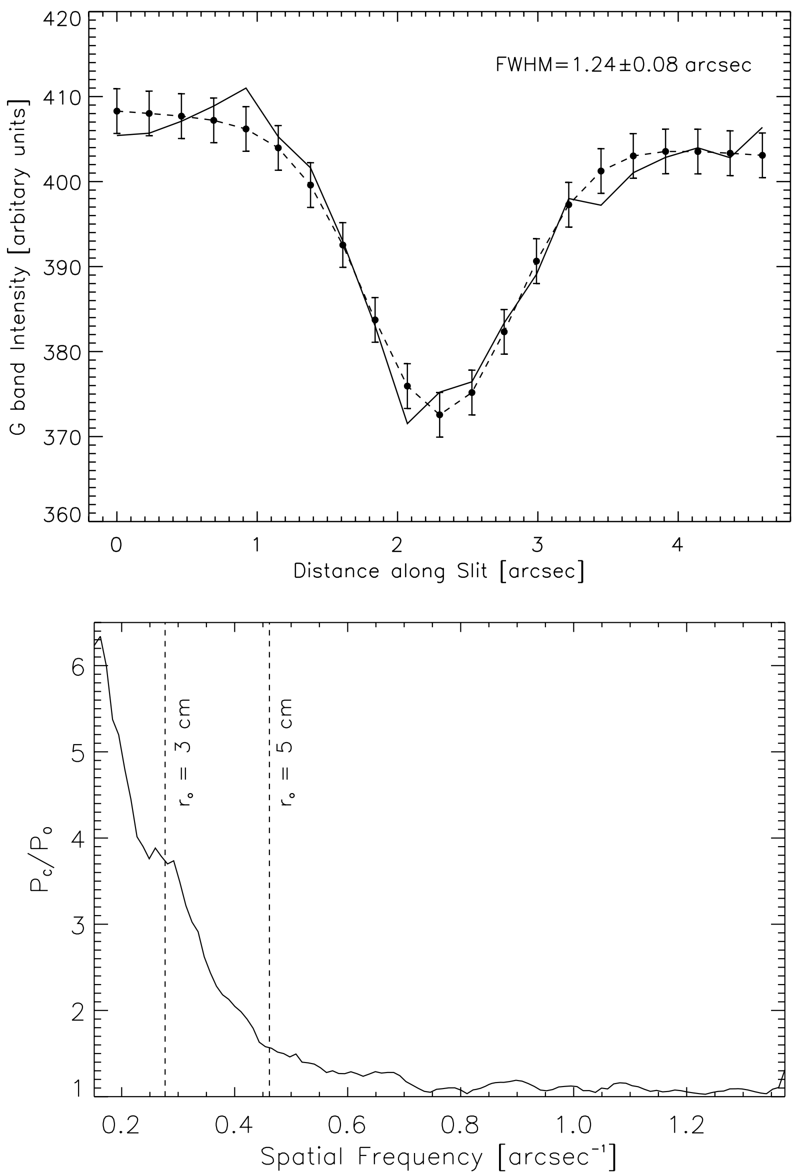

Figure 6.43: Top: The black solid line represents the G band intensity along the slit across the magnetic fragment. The dashed line is the Gaussian fit to the profile joining the black filled circles. The vertical bars correspond to $\pm 1\sigma$ in the estimated values. The FWHM estimated from the fit is inscribed in the top right hand corner. **Bottom:** Ratio of the azimuthally averaged power spectra of the AO corrected and uncorrected image. The distribution has been smoothed by 5 pixels. The x-axis represents the spatial frequency. The cut-off frequency corresponds to a 15 cm aperture at 4305Å. The vertical dashed lines correspond to a spatial resolution of $3.6''$ and $2.1''$ equivalent to a seeing of 3 cm and 5 cm respectively.

tilts from the shifts seen in the sub-apertures. The seeing was extremely poor since it was nearly afternoon (local time) when the observations were carried out. The image motion of the sunspot was first arrested using the ISS. The shifts observed in the open and closed loop are shown in top set of panels of Figure 6.41. In addition to seeing, there is a significant image motion arising from the poor telescope tracking. The improvement in the rms image motion in the closed loop varies from a factor of 6 to 4 for the two channels respectively. The ratio of the power spectra (bottom set of panels of Figure 6.41) illustrates that the ISS is able to correct a broad range of frequencies with a bandwidth exceeding 100 Hz although the ratio becomes unity at a few locations near 40-50 Hz. With better tuning, the rms image motion and the bandwidth can be improved further.

With the image motion arrested and the DM correcting the local tilts, the SC was employed to take 100 frame bursts with an exposure time of 6 ms. The G band images were 700×350 pixels in size. Although uncorrected and AO corrected images could not be acquired simultaneously they were taken in quick succession and the dramatic improvement in resolution is shown is Figure 6.42. The images shown here are the best uncorrected and AO corrected frames from the 100 image burst. While the umbra and penumbra appear defocussed and are the only large scale structures visible in the uncorrected image, one is able to clearly distinguish the umbra-penumbra and penumbra-photosphere boundary. In addition the filamentary structure of the penumbra appears coherent which has been indicated with red arrows. More importantly, a small magnetic fragment outside the sunspot is clearly identified which is also seen in the other AO corrected images. A 20 % increase in image contrast is observed between the AO corrected and uncorrected image. The improvement in image quality with AO correction is evident from the movie of the two sets of observations[1].

In order to make a preliminary estimate of the spatial resolution achieved with the AO correction, an intensity profile along a slit passing through the magnetic fragment was chosen. This is shown as the solid black line in Figure 6.43. A gaussian fit was then carried out to this profile with the fitted points shown as black filled circles with a dashed line joining them. The FWHM (Full Width at Half Maximum) of the magnetic fragment was estimated to be 1.24±0.08 arcsec.

[1]Available in mpeg format at http://www.prl.res.in/∼eugene/AO_USO_MOVIE.mpg

A similar result is obtained with the ratio of the power spectra of the AO corrected and uncorrected images shown in Figure 6.43. The ratio tends to become unity $\approx$ at 0.75 arcsec^{-1} which would imply a resolution of 1.3 arcsec which is in good agreement with the value obtained above.

6.7 Summary and Discussion

At the Udaipur Solar Observatory (USO) a prototype AO system is being designed on a 15 cm Coudé refractor telescope. The AO system is equipped with a Shack-Hartmann lenslet array (LA) and a high-speed camera for sensing the aberrated wave front. A 37 channel Deformable Mirror (DM) and a Tip-Tilt Mirror (TTM) serve as wave front correctors. In this chapter a few results pertaining to the development of the prototype AO system were highlighted. Using a simple optical setup it was found that when the DM is placed at an angle of incidence and a uniform voltage applied to all its actuators, astigmatism is induced, which increases, with the angle of incidence and the voltage (radius of curvature). When the DM is placed at 0° angle of incidence, a finite amount of intrinsic astigmatism is present which does not vary significantly with the radius of curvature. In order to operate the DM it is necessary to a) keep the DM at a very small angle of incidence and b) to derive a suitable voltage set that will compensate the intrinsic astigmatism as well. This voltage set can be simply added to any constant voltage set required to bias the DM surface, since the DM does not possess an intrinsic curvature.

The calibration of the DMs and the lenslet array involves mapping the actuator-lenslet geometry, followed by computing the influence matrix. This was subsequently used to correct input distortions created by another DM for various time delays. The perturbing DM was used to create a defocus error as well as a global tilt by manipulating the voltage to specific actuators. The performance of the AO system in the closed loop has been demonstrated for different input perturbations. However using the above set-up it was not possible to produce aberrations which had both a global tilt as well as local deformations. The tip-tilt mirror was able to compensate the global tilt of the distorted wave front to a fraction of a pixel while the DM was able to correct the defocusing error for different time delays of the perturbing pulse. Simulations were carried out to explore the possibility of employing phase diversity as an off-line technique. The code was tested under various seeing conditions and for a finite number of Zernike terms to model the atmospheric PSF. It is concluded that phase diversity works better under good seeing conditions i.e when the *rms* wave front error is small. The effectiveness of hybrid imaging under moderate seeing conditions was also demonstrated.

Further simulations were carried out to ascertain the optimal wave front sensor for the prototype AO system using various lenslet geometries and sizes. Before determining the effectiveness of the different lenslets, some of the shift estimation routines that are routinely used at USO were described and their accuracy was tested for a point source as well as an extended object such as a sunspot and solar granulation. Four different lenslets were considered with two hexagonal and two square arrays. The influence matrix was derived for each lenslet array using 27 Zernike terms starting from Z_4. 1000 random wave fronts were generated from 20 Zernike terms and subsequently retrieved using the lenslet shift vectors and the influence matrix of each lenslet array. Based on this test it was observed that two lenslets, Sq(340) and Hx(360) were able to satisfactorily estimate the input wave front. These 2 lenslets were further subjected to phase perturbations obeying a Kolmogorov spectrum, similar to the phase errors introduced in the wave front by the atmosphere. Two different seeing conditions were simulated that are nearly equivalent to the prevalent conditions at the site. The MTF resulting from the tilt-corrected wave front was compared with the same for a 100% and 85% corrected wave front. Results from the simulations unequivocally demonstrate the superiority of the hexagonal lenslet over its square counterpart under both seeing conditions. Thus for similar site conditions using a hexagonal LA with 37 sub-apertures can significantly improve the image quality.

Although the 2 LAs, Sq(340) and Hx(360) have the same number of lenslets and are fairly symmetrically placed in the reimaged pupil, the latter is clearly more effective than the former. This could be attributed to the fact that the pupil area sampled per lenslet is smaller for Hx(360) than Sq(340). As can be seen, each lenslet of Hx(360) occupies $\approx 3.5\%$ less area than that of Sq(340) which implies that the former has a marginally better sampling. The results from the simulations clearly emphasize this fact. The simulations are an extension of the work by Sridharan et al. (2003) and Sridharan & Bayanna (2004) who had considered circular lenslets alone. Having decided the Shack Hartmann wave front sensor, the rest of the optical components of the AO system, as shown in Figure 6.23, can be suitably chosen.

Some of the other issues that need to be considered are described below.

1. The wave front sensing in the simulations were carried out in the G band while in the prototype system it will be done in the continuum. As long as there is sufficient contrast and SNR, the shift estimation routine should be fairly accurate. I have ignored the presence of noise in the simulations.

2. In the simulations the small, yet finite, time lag in carrying out the sensing and correction has not been accounted for. For this reason the camera exposure time, shift estimation and correction by the DM must be sufficiently quick, such that the phase fluctuations, at the instant when they were sensed, to the instant when they are corrected, remain correlated.

3. For a 15 cm telescope the global tilt is a dominant aberration. Hence it is imperative to have a stand alone Image Stabilization System as shown in Figure 6.23, so that the AO correction can be applied on the tilt corrected wave front.

Results from the first light observations with the prototype AO system are very encouraging in which the image stabilization system was able to lock onto a sunspot and local tilts were successfully corrected by the deformable mirror. The spatial resolution achieved by the AO system was $\approx 1.3''$ and it is anticipated that with proper tuning, the resolution can be improved to within $1''$. The image contrast showed an improvement of 20 % with the filamentary penumbra and magnetic fragments outside the sunspot clearly visible in the AO corrected frames. The need for a stand alone tip-tilt system has been justified for the small 15 cm aperture where the dominant aberration is the global tilt. The following exercises towards AO development need to carried out: a) improve the tuning of the image stabilization system, b) reduce contribution from local/ground layer turbulence since a part of the optical train lies outside the lab where there is a possibility of further wavefront degradation and c) eliminate unnecessary scattered light. It is anticiapted that the above objectives would be completed before the monsoons and the setup would be subsequently shifted to the island in time for the arrival of MAST.

Chapter 7

Summary, Discussion and Future Work

Sunspots are coherent manifestations of the solar magnetic field and appear as dark objects on the bright photospheric background. Despite the existence of small scale and filament sub-structures, the sunspot on the whole presents a longer-lived and stable configuration. The investigation of sunspot fine structure at the highest spatial resolution is thus imperative to understand the behaviour of the larger scale magnetic field. The first part of the thesis describes the properties and evolution of small scale magnetic and velocity inhomogeneities in light bridges and the Evershed flow. These structures or processes are closely associated and linked to the formation, evolution and subsequent decay of sunspots. In addition, they are manifestations of convection in the presence of inclined magnetic fields, within sunspots. Part I of the thesis describes the investigation and analysis of the fine structure in sunspot light bridges and the Evershed Flow, using high resolution, photometric and polarimetric data from the Japanese space satellite *Hinode*. Simultaneously, the developmental aspects of designing an Adaptive Optics system, to facilitate similar high resolution observations from Udaipur, are also described and forms the second part of the thesis. In this chapter, I summarize my findings in the first four sections and present my conclusions in Section 7.5. Section 7.6 briefly highlights future scientific and instrumentation endeavors.

7.1 Photospheric and Chromospheric Observations of Sunspot Light Bridges

High resolution photospheric and chromospheric observations of a set of four sunspot light bridges (LBs) were compared, using filtergrams taken in the G band and Ca II H line as well as spectropolarimetric data using the neutral Fe line pair at 630 nm, from *Hinode*. These LBs were present in NOAA AR 10953, 10961, 10963 and 10969 and were observed on May 1, June 29, July 12 and August 23, 2007 respectively. After carrying out routine preprocessing on the G band filtergrams, it was observed that the LB in NOAA AR 10953 had the maximum length and minimum radius of curvature in comparison to the others. The sunspot in NOAA AR 10953 also was the largest amongst the four sunspots and was located very close to disc centre.

Local Correlation Tracking (LCT) on the G band images was carried out to determine long term horizontal flows in the LBs. Of the four LBs, the one in NOAA AR 10953 was seen to exhibit a unidirectional, non-uniform flow measuring ≈ 500 m s^{-1} while the other LBs did not show any indication of coherent, long term flows. The absence of long term flows in the other three LBs, was verified with a centre tracking algorithm, which traced the motion of individual bright features. While the trajectory of the grains/features appear irregular, their short lifetimes as well as random appearance at different location in the LB, rendered a very small average horizontal velocity.

Chromospheric observations in the Ca II H line, reveal that brightness enhancements appear to be common to all LBs, although the magnitude and frequency of these phenomena vary from one to the other. In particular, the LB in NOAA AR 10953 exhibits very strong and a highly complex set of brightenings which last for three days, while the events are relatively subdued and sporadic in the other LBs. I also found that some events could last a single frame thereby requiring a faster cadence to track these events from the beginning till their disappearance. The variety of chromospheric activity is seen in the form of an arch-type brightening that spans across the LB, as brightness fronts which propagate along the LB occasionally leading to secondary enhancements, as localized enhancements which are directed along the axis of the LB and as tiny jets along the length of the LB which are oriented nearly perpendicular to the axis of the LB.

Magnetograms of the LBs, derived from the far blue and red wings of the Stokes V signal serve as a useful diagnostic to detect small scale magnetic and velocity inhomogeneities. The magnetograms show that there are extended regions in the vicinity of the LB in NOAA AR 10953, wherein the Stokes V signal resembles a Q or U profile thereby producing a positive signal of $\approx$ 2% at -215 mÅ from the line centre at 6302.5Å. Such a feature was not observed in the other LBs, with the exception of the LB in NOAA AR 10969 wherein the positive V signals are confined to a very small region. Moreover, the blue wing magnetograms far from line centre, do not indicate any strong negative signal in any of the LBs studied here. The far red wing magnetograms of NOAA AR 10953 display patches of positive polarity even at wavelength positions 13 and 14 corresponding to 279.5 mÅ and 301 mÅ respectively, while a relatively weaker patch of a similar kind is seen in the other LBs but they are not observed beyond 236.5 mÅ.

7.2 Detailed Investigation of a Chromospherically Active Sunspot Light Bridge

Following the results obtained in Chapter 3, the global magnetic and dynamic properties of the LB in NOAA 10953 were determined from the inversion of Stokes profiles observed by *Hinode*. Observations were made at two different times on the same day which show important changes during the evolution of the LB. A one-component model atmosphere with height-independent parameters was used in the inversions to derive maps of the physical parameters. Continuum images of the LB, corresponding to the two instances of time, indicate a rapid change in the structure of the LB wherein the onset of the decay of the LB is seen in the latter. The reduction in field strength in the LB, which was initially confined to a larger area both along the axis as well as along its width, dramatically disappears in time. There are very small, isolated regions of extremely weak fields which are $<$ 700 G seen in the two SP scans. The weak field region stands out clearly despite the model atmosphere, employed in the inversion, being very simple.

There exist patches of very strong downflows exceeding 4 km s^{-1} in the LB, which are associated with complex Stokes V spectra having double red lobes. These patches correspond to the areas in the far red wing magnetograms described in Chapter 3. Two-component inversions of these profiles indicate supersonic velocities of 10 km s^{-1} or more which have not been reported earlier. Anomalous linear polarization signals are observed close to this region where the umbral fields meet the LB fields, but only when the field is relatively horizontal. During the decay of the LB, similar supersonic downflows are observed at the umbra-penumbra boundary, close to the LB while the LB itself did not exhibit any strong downflows.

The supersonic downflows in the LB as well as at the umbra-penumbra interface are sometimes associated with transient, chromospheric brightenings. This was seen in both sets of observations using event maps. Although co-temporal chromospheric filtergrams were not available during the second SP scan, the event maps clearly show that the chromospheric enhancements lie very close to the downflows. This is seen in both instances of time during the evolution of the LB. Light curves, using the G band and Ca II H filtergrams, show an increase in the Ca intensity, that coincides with that in the G band, for a pixel lying close to the entrance of the LB. The photospheric and chromospheric filtergrams acquired during the latter half of May 1, indicate that the evolution of the LB affects the photometric brightness in the chromosphere. This was appropriately illustrated in the set of filtergrams taken while the LB was fragmenting. The results of the analysis suggest that the LB could perhaps account for an additional brightness of sunspots higher up in the atmosphere, particularly in the chromosphere. As the LB decays, it fragments into a number of umbral dots that appear brighter than the decaying LB. Even in the decay phase, the chromosphere displays a wide variety of brightenings both on the LB as well as in its immediate neighborhood although it is much more subdued in the LB as compared to observations seen by Louis et al. (2008), nearly 18 hrs earlier.

7.3 Penumbral Fine Structure in the Context of the Evershed Flow

The penumbral fine structure and evolution of the Evershed Flow was investigated using high resolution spectropolarimetric *Hinode* observations of a small region of the centre side penumbra of a regular sunspot in NOAA AR 10944. The observed profiles were inverted using the SIR code which assumed a spatially resolved penumbra with gradients in the physical parameters along LOS. Maps of the parameters retrieved from the inversion were subsequently averaged at different ranges of optical depth in order to study the variations in the EF, both spatially as well as vertically. It is seen that the EF is predominantly confined to the deep layers pertaining to the $\log\tau$ = 0 and $\log\tau$ = -1 layers. The variation of the physical parameters with LOS velocity at different heights in the solar atmosphere substantiates the existence of two distinct magnetic, thermal and kinematic components in the penumbra. The "spines" which are essentially at rest at all heights are magnetically stronger and relatively vertical in comparison to the "intraspines" which harbor the hot EF. The intraspines are also more radially oriented in contrast to the penumbral spines. Based on these results the mean atmospheric stratifications for the spines and intraspines was constructed for the two penumbral components. Upflows are observed to be a maximum at 0.3 - 0.4R_P and is particularly seen in the deep layers. In this region one also observes an increase in the radial component of the magnetic field B_R which is suggestive of the possible injection/emergence of the EF into the penumbra. The conspicuous increase in B_R at $r/R_P = 0.4$ results from an inflection in the radial distribution of the zenith angle.

The Stokes profiles of Evershed clouds (ECs), which are blobs of enhanced LOS velocity, comprise of anomalous Q signals, that are satisfactorily synthesized by the model atmosphere used in the inversions. The appearance of an EC can be quite rapid, with some of them disappearing in less than 5 minutes. The values of the magnetic and thermal parameters of the intraspines and ECs, computed for a number of EC pixels, reveals that the two are, in general, very similar and whose radial variation coincides to a great extent, although there are instances when the passage of an EC along the penumbral intraspine is accompanied by a large change in the field inclination.

The horizontal flow field was determined by employing LCT on the time sequence of continuum maps and subsequently averaged in time to yield the long term flow field. The penumbra shows two distinct flow regions with inflows from a distance of $0.6R_P$ to the umbra-penumbra boundary that increase radially inwards and outflows from the Diving Line (DL) at $0.6R_P$ to the penumbra-photosphere boundary. The organization of the penumbral filamentary structure over the 4 hr observing period strongly exemplifies the coherence and stability of the magnetic and thermal configuration (Balthasar et al., 1996; Sobotka et al., 1999). This is particularly evident in the continuum and LOS velocity maps as well as in the zenith angle and azimuth maps. Furthermore, the time averaged magnetic field and continuum intensity is strongly correlated to the LOS velocity within the inner and a little beyond the mid penumbra. Thus the association of the EF to relatively weaker, inclined and radially oriented magnetic fields clearly appears to be long-term despite its dynamic and transient nature (Schlichenmaier, 2009).

7.4 Results Pertaining to the Development of Adaptive Optics at Udaipur Solar Observatory

A new 50 cm Multi Application Solar Telescope (MAST) will be deployed at the island site of USO by the end of this year. The scientific goals have been drafted with a desire that MAST will deliver a spatial resolution of $0.''4$ in polarimetry as well as imaging. With the seeing conditions at USO often worse then $2''$, it necessitates an Adaptive Optics (AO) system to compensate for the image degradation introduced by atmospheric turbulence. In view of this, a prototype AO is being designed using a 15 cm Coudé refractor telescope. The prototype AO system is equipped with a Shack-Hartmann lenslet array (LA) and a high-speed camera for sensing the aberrated wave front. A 37 channel Deformable Mirror (DM) and a Tip-Tilt Mirror (TTM) serve as wavefront correctors. The developmental aspects of the AO project consisted of working on individual components first, to assimilate their performance as well as limitations, which were subsequently assembled together for the final AO system.

The intrinsic and induced aberrations of the DM were estimated from a simple experiment, by keeping the DM at different angles of incidence and applying a uniform voltage to all 37 actuators. It was observed that astigmatism is induced in the mirror, which increases, in general, with the angle of incidence and the applied voltage (radius of curvature). When the angle of incidence is $0°$, a finite amount of intrinsic astigmatism is present which does not vary significantly with the radius of curvature.

The estimation of the intrinsic aberrations of the DM was followed by the mapping of the actuator-lenslet geometry and determination of the influence matrix (IM). The IM serves as a look-up table that was subsequently used to correct input distortions created by a second DM. A sinusoidal perturbing pulse with various time delays was applied to the second DM. The perturbing DM was used to create a defocus error as well as a global tilt by manipulating the voltage to specific actuators and the performance of the AO system in the closed loop was demonstrated. The tip-tilt mirror was able to compensate the global tilt of the distorted wavefront to a fraction of a pixel while the DM was able to correct the defocusing error for different time delays of the perturbing pulse. The above set-up was however, inadequate to create aberrations in which a a global tilt as well as local deformations were present. Simulations were carried out to explore the possibility of employing phase diversity as an off-line technique in tandem with AO. The code was tested under various seeing conditions and for a finite number of Zernike terms to model the atmospheric PSF. It is observed that phase diversity works better under good seeing conditions i.e. when the *rms* wave front error is small. The effectiveness of hybrid imaging under moderate seeing conditions was also demonstrated.

Further simulations were carried out to evaluate the performance of the prototype AO system using various lenslet geometries and sizes keeping the reimaged pupil size on the wave front sensing camera as an input. Four different lenslets were tested with two hexagonal and two square arrays. These lenslet arrays (LAs) were first used to sense 1000 random wave fronts that were generated from 20 Zernike terms and it was observed that two lenslets, Sq(340) and Hx(360) were able to satisfactorily estimate the input wave front. These two lenslets were further subjected to phase perturbations obeying a Kolmogorov spectrum, similar to the phase errors introduced in the wave front by the atmosphere. Two different seeing conditions were simulated that are nearly equivalent to the prevalent conditions at Udaipur. The MTF resulting from the uncorrected, tilt-compensated wave front was compared with the same for a 100% and 85% corrected wave front. Results from the simulations unequivocally demonstrate the superiority of the hexagonal lenslet over its square counterpart under both seeing conditions. Thus for similar site conditions, using a hexagonal LA with 37 sub-apertures can significantly improve the image quality.

Improvement in spatial resolution and image quality of a sunspot was demonstrated with an independent tip-tilt system with a CMOS based camera, 21 square lenslets for sensing the wavefront and 19 channels of the deformable mirror. The AO corrected images depict features within and outside the sunspot having scales of $\approx 1.3''$ which were otherwise washed out due to poor seeing conditions.

7.5 Synthesis

Magnetic fields are ubiquitous on the Sun and are organized on a large range of spatial scales. Sunspots are the largest and most conspicuous manifestation of magnetic fields on the Sun. Although the small scale structures within sunspots have lifetimes much shorter than the evolution time scale of a sunspot, their thermal, kinematic and dynamic properties make each sunspot unique from the other. Sunspot light bridges represent an inhomogeneity within sunspots, but perhaps the extent of this perturbation is seen in the localized confinement of very weak fields which evolve with time. The fact that weak and strong fields coexist in a light bridge very close to one another could imply one of two possibilities. Firstly, the Fe lines may not sample the field free/weak field region that could be present deep in the photosphere. As a result, field free/weak fields do not leave their imprint on the polarization signals emanating from the pixel. A possible solution to this issue would be the use of additional lines, such as the infrared Fe lines at 1.56μm which probe the deeper layers of the photosphere. Secondly, there could be field free intrusions as well as channeled flows since the light bridge appears to be magnetically and dynamically connected to the penumbra. Moreover, this organization of inhomogeneities within light bridges extends to other locations in the same sunspot. Observations by Louis et al. (2008) illustrate two LBs with non-identical morphology and chromospheric activity in the same sunspot. One of the LBs is an extension of the penumbra while the other comprises of a central dark lane with bright granular-like cells/grains. A simple analytical radiative transfer model by Giordano et al. (2008) reproduces dark lanes in a light bridge that result from a higher opacity below the field free cusp, when the hot convective material is confined by the umbral magnetic wall. The absence of the dark lane on one of the LBs could thus reflect the presence of two different dynamic sub-photospheric processes which power the light bridge.

The extent of the light bridge perturbation in the umbra is revealed by the mixing of polarization signals from the two respective domains. This mixing or merging of umbral and light bridge fields could trigger reconnection whose signatures are the supersonic downflows in the photosphere as well as the brightness enhancements in the chromosphere. The amplitude of the perturbation could decide the nature, frequency and strength of the chromospheric activity, since the latter is a common property to all light bridges. The excess chromospheric brightness above sunspots is modulated by the evolution of the light bridge which could serve as a means to heat the lower chromosphere. The chromospheric enhancements/jets on a light bridge can sometimes spawn catastrophic events such as a filament eruption as observed by Guo et al. (2010) who reported an M2.5 two ribbon flare and a CME with speeds of 600 kms^{-1}, following the eruption of the filament.

The temporal evolution of the light bridge, particularly in the decay phase, illustrates its association with the penumbral filaments and umbral dots. High resolution observations by Langhans (2006) demonstrate a smooth transition between the dark cores in a light bridge to a penumbral filament, thereby hinting at a common convective origin. The results obtained in Chapter 5 of this thesis, based on the assumption that the penumbra is spatially resolved, show the clear filamentation and its association with the Evershed flow. The Evershed flow is confined to the penumbral intraspines which are relatively weaker and more inclined than the spines. The phenomena of the Evershed flow is also seen to be dominant in the deep layers pertaining to the logτ = 0 and logτ = -1 layers while being practically absent in the higher layers. Moreover, the Evershed flow channels appear to be wrapped by the surrounding spine field. At the present junction, the results support the “uncombed” model of Solanki & Montavon (1993) although the model atmosphere used in the inversions do not appropriately consider a flux tube geometry embedded in a background field which should be the case for the above model. Moreover, the absence of weak fields in the deep layers of the penumbra pose a challenge for the “gappy” model of Spruit & Scharmer (2006). The results are in good agreement with the recent work of Puschmann et al. (2010) who derived the stratification of physical parameters in terms of geometrical height. According to Ruiz Cobo & Bellot Rubio (2008), penumbral dark cores are the result of nearly horizontal flux tubes carrying the Evershed flow which causes an enhancement in opacity that shifts the unit optical depth to higher layers. Scharmer (2009) on the other hand argues that the dark cores are a combination of increased opacity associated with a strongly reduced field strength and an overall drop of temperature with height in the “gappy” model. As pointed out by Schlichenmaier (2009), the inadequacy of the two models in explaining heat transport over the entire penumbra and the absence of a magnetized Evershed flow respectively could imply that the penumbral fine structure is a superposition of channeled flows as well as convective rolls. Thus even with *Hinode's* spatial resolution, the mechanism for the Evershed flow remains open and only spectropolarimetric measurements at $0.''1$ could shed light on this enigmatic phenomena.

The scientific results presented in this thesis are based on high resolution observations taken by a 50 cm telescope in space. The quality of data, sets a benchmark for achieving the same from ground and is one of the prime objectives of the Multi Application Solar Telescope (MAST) which will be equipped with Adaptive Optics (AO) to compensate image degradation. The developmental aspects in this project include realization of an Image Stabilization system; lab characterization of the Deformable Mirror; simulations for obtaining the optimal wave front sensor and finally demonstrating the AO performance with real time solar observations. The above have been incremental in our efforts to achieve high spatial resolution at Udaipur and the prototype system is the first of its kind for solar astronomy in India. The results obtained in the process will be significant for obtaining even higher spatial resolution with MAST. In summary, the organization of magnetic and velocity inhomgeneities in a sunspot at scales of $0.''3$ and their subsequent evolution are evidence for the anistropy of the interaction between magnetic fields and dynamic processes beneath the photosphere. The investigation of such processes at the highest spatial resolution from space as well as the ground is imperative to determine the overall structure and stability of sunspots.

7.6 Future Work

This section briefly describes future scientific and instrumentation projects.

1. In a recent work, Puschmann et al. (2010) derived the 3D penumbral structure by converting the stratification of the physical parameters from the optical depth scale to geometric height. This technique will be employed to determine the same in sunspot LBs to probe their magnetic nature with ultra high resolution. Earlier studies by Louis et al. (2009, 2010a) indicate the presence of extremely weak fields confined to localized regions on a LB. I wish to carry out the above study for a large sample of sunspots, preferably with observations spanning large to small heliocentric angles. The study would focus on the 3 dimensional magnetic field distribution of weak-field regions with respect to the umbral and sunspot magnetic fluxes. Since SIR inversions are much slower than their Milne-Eddington counterpart, it would be useful to do optimize the inversion code for parallel processing thereby reducing the time taken to retrieve maps of a large area. Preliminary work on this aspect is presented in Appendix - B.

2. The capability of *Hinode's* spatial resolution will be utilized to investigate sub-surface flows under sunspot light bridges using time-distance helioseismology. While a preliminary work by Zhao et al. (2010) shows the existence of divergent sub-surface flows, arising from a convective upwelling, this is not in agreement with the motion of intensity features observed by Louis

et al. (2008). The sub-surface flows could determine the nature and extent of the destabilizing effect of the light bridge on the adjacent umbra.

3. The recent work by Borrero & Solanki (2010) illustrates a flux tube based penumbral model which is capable of producing the azimuthal variations of the net circular polarization (NCP) at different heliocentric angles while the contribution of convective motions to the same is negligible, thus making the "gappy" model (Spruit & Scharmer, 2006) unsuitable for explaining the penumbral fine structure. I intend to carry out inversions of sunspot penumbra using polarimetric observations at very high spatial resolution in order to investigate the fine scale inhomogeneities within the penumbral dark cores by employing a discontinuous model atmosphere, such as the one employed by Bellot Rubio et al. (2003b); Cabrera Solana et al. (2008) and Jurčák & Bellot Rubio (2008), in the inversions, which would be consistent with the flux tube scenario.

4. A crucial aspect in the open ended discussion on the Evershed flow is the detection of small-scale overturning convective motions in the penumbra, i.e. overturning downflows at the edges of the penumbral filaments. While this scenario has been observationally suggested by Zakharov et al. (2008) and Rimmele (2008) using Dopplergrams, the associated velocities are much weaker than those associated with the Evershed Flow. Numerical simulations on the other hand (Rempel et al., 2009b) reproduce these downflows with larger velocities. Such overturning downflows however, have not yet been observed spectroscopically neither at disc centre nor at heliocentric angles $\sim 20°$, even at a spatial resolution of $0.''2$ (Bellot Rubio et al., 2005).

5. Off-line image restoration techniques such as speckle image masking (Denker, 1998) would be integrated with Adaptive Optics corrected images at Udaipur Solar Observatory to improve image quality. It has been shown by Sridharan & Bayanna (2004), that for a telescope aperture of 60 cm, hybrid imaging (Adaptive Optics + Speckle Interferometry) can yield a Strehl ratio of 0.3 for a site with a median seeing of 5 cm.

6. A narrow band imager using two Fabry-Perot etalons is being developed at present at USO which will serve as a back end instrument for MAST. The imager is intended to observe in the photospheric Fe I 6173Å and chromospheric Ca II 8542 Å lines. The substrate of the etalons is made of Lithium Niobate electro-optic crystal wherein the refractive index and wavelength tuning can be achieved by the application of voltages. I wish to assist in the preparation and testing of the data acquisition software which will combine the CCD, blocking filter wheel and the digital-to-analog controller for tuning the etalons.

Appendix-A

The SAD algorithm that utilizes the MMX instruction to calculate the shift over a 32×32 pixel sub-aperture.

```
#define NS 17 /* number of subapertures */
#define AX 60 /* size of reference subaperture in x */
#define AY 52 /* size of reference subaperture in y */
#define SX 32 /* size of subapertures in x */
#define SY 32 /* size of subapertures in y */
#define RX (AX-SX)/2
#define RY (AY-SY)/2

uint8_t cimag[NS*SX*SY] __attribute__ ((aligned (32)));
uint8_t refim[RX*RY] __attribute__ ((aligned (32)));

int sae(int dx, int dy, int sn)
{

/* calculate sum of absolute differences for one subaperture */
/* dx, dy: current shift vector
sn: subaperture number */

int iy;
int csae = 0;
uint8_t *ip, *rp; /* pointers to appropriate rows */
uint32_t c1;

   for(iy=0;iy<SY;iy++)
   {
   ip = &crimag[sn*SX*SY+iy*SX];
   /* start at first pixel of each subaperture */
   rp = &refim[(iy+AY+dy)*RX+AX+dx];
```

```
    /* reference is loaded unaligned with movq*/

    /* assembler code for one subaperture */

    asm("movq   (%1),   %%mm1 \n\t"
    /* load 8 reference pixels unaligned */

    "psadbw (%2),   %%mm1 \n\t"
    /* sum of absolute differences */

    "movq   8(%1),  %%mm0 \n\t"
    /* reference is 8 pixels wide, skip */

    "psadbw 8(%2),  %%mm0 \n\t"
    /* by 8 pixels per row */

    "paddw  %%mm0,  %%mm1 \n\t"
    /* add to previous sum in MMX register */

    "movq   16(%1), %%mm0 \n\t"
    "psadbw 16(%2), %%mm0 \n\t"
    "paddw  %%mm0,  %%mm1 \n\t"
    "movq   24(%1), %%mm0 \n\t"
    "psadbw 24(%2), %%mm0 \n\t"
    "paddw  %%mm0,  %%mm1 \n\t"
    "movd   %%mm1,  %0 \n\t"
    "emms \n\t"
    : "=g" (c1)
    : "r" (rp), "r" (ip)
    );
    csae = csae + c1;
    }
    return csae;
}
```

Appendix-B

The following code calls the shell script 'sirinv' and keeps a track on the total time taken to complete the job.

```
#define _GNU_SOURCE
#include <unistd.h>
#include <sys/syscall.h>
#include <stdio.h>
#include<math.h>
#include<sched.h>
#include<sys/time.h>
#include<time.h>

main()
{
struct timeval th_st,th_et;
const char* comm="./sirinv";
gettimeofday(&th_st,NULL);
system(comm);
gettimeofday(&th_et,NULL);
timersub(&th_et,&th_st,&th_et);
printf("\nTotal time taken:%f min.\n",
(th_et.tv_sec + (th_et.tv_usec/1000000.0))/60.0);
}
```

The shell script 'sirinv' copies two input stokes profiles at any given instant from the input_stokes directory into the current directory where the SIR control file, initial guess file, PSF profile, abundance file and line files are kept and renames them as input-profile1.per and input-profile2.per respectively. If a 100×100 pixel map is to be inverted then the parallel processing is carried out for the two halves simultaneously.

```
for ((i=0;i<=99;i++))
do
for ((j=0;j<=49;j++))
do
k=`expr $j + 50`
cp ~/input_stokes/modelin-$i-$j.per input-profile1.per
cp ~/input_stokes/modelin-$i-$k.per input-profile2.per

./sirexe

cp initial-guess1_3.mod ~/output_stokes/modelout-$i-$j.mod
cp initial-guess1_3.err ~/output_stokes/modelout-$i-$j.err
cp initial-guess1_3.per ~/output_stokes/modelout-$i-$j.per

cp initial-guess2_3.mod ~/output_stokes/modelout-$i-$k.mod
cp initial-guess2_3.err ~/output_stokes/modelout-$i-$k.err
cp initial-guess2_3.per ~/output_stokes/modelout-$i-$k.per
done
done
```

The ‘sirexe’ C-executable is then called which will carry out the inversion of the two profiles in a parallel manner by using threads as illustrated below.

```
#include <pthread.h>
#define _GNU_SOURCE
#include <unistd.h>
#include <sys/syscall.h>
#include <stdio.h>
#include<math.h>
#include<sched.h>

#include<sys/time.h>
#include<time.h>

void *call1();
void *call2();

main()
{
```

```
pthread_t thread1, thread2;
int  iret1,iret2;

int old_sch,new_sch;
struct sched_param sp;
sp.sched_priority=40;
old_sch=sched_setscheduler(0,SCHED_RR,&sp);
new_sch=sched_getscheduler(0);
printf("The old scheduler is :%d\n",old_sch);
printf("\nMain new scheduler is :%d\n",new_sch);

iret2 = pthread_create( &thread2, NULL, call1,NULL);
iret1 = pthread_create( &thread1, NULL, call2,NULL);
pthread_join( thread1, NULL);
pthread_join( thread2, NULL);
}

void *call1()
{
  long new_mask=1,cur_mask;
  int len=sizeof(new_mask);
  pid_t tid=syscall(SYS_gettid);
  sched_setaffinity(tid,len,&new_mask);
  const char* comm1="echo sir1.trol | /root/sir/program1/./sir.x";
  system(comm1);
}

void *call2()
{
  long new_mask=2,cur_mask;
  int len=sizeof(new_mask);
  pid_t tid=syscall(SYS_gettid);
  sched_setaffinity(tid,len,&new_mask);
  const char* comm2="echo sir2.trol | /root/sir/program2/./sir.x";
  system(comm2);
}
```

Bibliography

Acton, D. S., Smithson, R. 1992, Appl. Opt., 31, 3161 158

Acton, D. S., Dunn, R. B. 1993, in Society of Photo-Optical Instrumentation Engineers (SPIE) Conference Series, 1920, 348 158

Antia, N. M. 1991, *Numerical methods for Scientists an Engineers*, Tata McGraw-Hill Publications, New Delhi 181

Asai, A., Ishii, T. T., Kurokawa, H. 2001, ApJ, 555, L65 8

Babcock, H. W. 1953, PASP, 65, 229 158

Balthasar, H., Wöhl, H. 1983, Sol. Phys., 88, 71 2

Balthasar, H. 1988, A&AS, 72, 473 120

Balthasar, H., Schleicher, H., Bendlin, C. Volkmer, R. 1996, A&A, 315, 603 11, 153, 228

Bayanna, A. R., Louis, R. E., Mathew, S. K., Venkatakrishnan, P. 2010, in preparation 169

Beck, C. 2008, A&A, 480, 825 118

Bello González, N., Okunev, O. V., Domínguez Cerdeña, I., Kneer, F., Puschmann, K. G. 2005, A&A, 434, 317 21

Bellot Rubio, L. R., Ruiz Cobo, B. Collados, M. 1996, A&A, 306, 960 29

Bellot Rubio, L. R., Ruiz Cobo, B. Collados, M. 1998, ApJ, 506, 805 30

Bellot Rubio, L. R., Balthasar, H., Collados, M., Schlichenmaier, R. 2003a, A&A, 403, L47 116, 138

Bellot Rubio, L. R. 2003b, ASPC, ed. J. Trujillo-Bueno and J. Sánchez Ameida (San Fransisco), 307, 301 13, 150, 152, 234

Bellot Rubio, Balthasar, H., Collados, M. 2004, A&A, 427, 319 2, 12, 112, 118, 151

Bellot Rubio, L. R., Langhans, K., Schlichenmaier, R. 2005, A&A, 443, L7 12, 117, 131, 234

Bellot Rubio, L. R., Schlichenmaier, R., Tritschler, A. 2006a, A&A, 453, 1117 12

Bellot Rubio, L. R. 2006b, ASPC, 358, 107 13

Bellot Rubio, L. R., Tsuneta, S., Ichimoto, K., Katsukawa, Y., Lites, B. W., Nagata, S., Shimizu, T., Shine, R. A., Suematsu, Y., Tarbell, T. D., Title, A. M., del Toro Iniesta, J. C. 2007, ApJ, 668, L91 12, 112, 117

Bellot Rubio, L. R. 2010, ASSP, 193 12

Berger, T. E., Berdyugina, S. V. 2003, ApJ, 589, L117 8, 50, 75

Bharti, L., Rimmele, T., Jain, R., Jaaffrey, S. N. A., Smartt, R. N. 2007a, MNRAS, 376, 1291 50, 90

Bharti, L., Joshi, C., Jaaffrey, S. N. A. 2007b, ApJ, 669, L57 8

Böhm-Vitense, E. 1997, *Introduction to Stellar Astrophysics*, Vol. 2, Cambridge University Press 54

Born, M., Wolf, E. 1980, *Principles of Optics*, Pergamon, Oxford 197

Borrero, J. M., Bellot Rubio, L. R. 2002, A&A, 385, 1056 120

Borrero, J. M., Solanki, S. K., Bellot Rubio, L. R., Lagg, A., Mathew, S. K. 2004, A&A, 422, 1093 118

Borrero, J. M., Lagg, A., Solanki, S. K., Collados, M. 2005, A&A, 436, 333 118

Borrero, J. M., Bellot Rubio, L. R., Müller, D. A. N. 2007, ApJ, 666, L133 13, 116

Borrero, J. M., Lites, B. W., Solanki, S. K. 2008a, A&A, 481, L13 117, 151

Borrero, J. M., Solanki, S. K. 2008b, ApJ, 687, 668 118, 150, 152

Borrero, J. M., Solanki, S. K. 2010, ApJ, 709, 349 234

Bumba V. 1965, in Stellar and Solar Magnetic Fields, R. Lüst (Ed.), North-Holland Pub. Co., IAU Symp. 22, 305 17

Cabrera Solana, D., Bellot Rubio, L. R., del Toro Iniesta, J. C. 2005, A&A, 439, 687 13

Cabrera Solana, D., Bellot Rubio, L. R., Beck, C., Del Toro Iniesta, J. C. 2006, ApJ, 649, L41 14

Cabrera Solana, D., Bellot Rubio, L. R., Beck C., Del Toro Iniesta, J. C. 2007, A&A, 475, 1067 14, 118

Cabrera Solana, D., Bellot Rubio, L. R., Borrero, J. M., Del Toro Iniesta, J. C. 2008, A&A, 477, 273 14, 118, 152, 234

Carrington, R. C. 1858, MNRAS, 19, 1 3

Centeno, R., Lites, B. W., de Wijn, A. G., Elmore, D. 2009, ASPC, ed. B. Lites, M. Cheung, T. Magara, J. Mariska, and K. Reeves (San Francisco), 415, 323 126

Choudhuri, A. R. 1986, ApJ, 302, 809 8, 50, 75

Choudhuri, A. R. 1998, *Physics of Fluids and Plasmas*, Cambridge: Cambridge Univ. Press 2

Choudhary, D. B., Balasubramaniam, K. S. 2007, ApJ, 664, 1228 14

Collados, M., Martínez Pillet, V., Ruiz Cobo, B., del Toro Iniesta, J.C., & Vázquez, M. 1994, A&A, 291, 622 29

Culhane, J. L., Harra, L. K., James, A. M., Al-Janabi, K., Bradley, L. J., Chaudry, R. A., et al. 2007, Sol. Phys., 243, 19 114

Dayton, D. S., Restaino, S., Gonglewski, J., Gallegos, J., MacDermott, S., Browne, S., Rogers, S., Vaidyanathan, M., Shilko, M. 2000, Opt. Comm., 176, 339 168

del Toro Iniesta, J. C., Tarbell T. D., Ruiz Cobo B. 1994, ApJ, 436,400 29

del Toro Iniesta, J. C., Bellot Rubio, L. R., Collados, M. 2001, ApJ, 549, L139 12, 112, 118 del Toro Iniesta, J. C. 2003a, *Introduction to Spectropolarimetry*, Cambridge University Press 28, 129

del Toro Iniesta, J. C. 2003b, AN, 324, 383 13

del Toro Iniesta, J. C., Orozco Suárez, D., Bellot Rubio, L. R. 2010, ApJ, 711, 312 13

Deng, N., Choudhary, D. B., Tritschler, A., Denker, C., Liu, C., Wang, H. 2007, ApJ, 671, 1013 145

Denker, C. 1998, Sol. Phys., 180, 81 16, 234

Denker, C., Mascarinas, D., Xu, Y., Cao, W., Yang, G., Wang, H., Goode, P. R., Rimmele, T. 2005, Sol. Phys., 227, 217 16

Denker, C., Tritchler, A., Rimmele, T. R., Richards, K., Hegwer, S. L., Wöger, F. 2007, PASP, 119, 170 16, 156

Denker, C., Tritschler A., Deng, N., Verdoni, A. P. 2008, AN, 329, 773 10, 145

De Rosa, M. L., 2005, ASPC, ed. K. Sankarasubramanian, M. Penn and A. Pevtsov, 346, 337 4, 15

Dikpati, M., Gilman P. A. 2006, ApJ, 649, 498 2

Evershed, J. 1909, MNRAS, 69, 454 11, 116

Fernández, E. J., Iglesias, I., Artal, P., 2001, Opt. Lett., 26, 746 169

Fisher, G. H., Welsch, B. T. 2008, ASPC, ed. R. Howe, R. W. Komm, K. S. Balasubramaniam, K.S. and G. J. D. Petrie (San Fransisco), 383, 19 57, 143

Franz, M., Schlichenmaier, R. 2009, A&A, 508, 1453 12

Fried, D. L. 1965, J. Op. Soc. Am., 55, 1427 155

García de La Rosa, J. I. 1987, Sol. Phys., 112, 49 8, 17, 49

Gary, G. A., Hagyard, M. J. 1990, Sol. Phys., 126, 21 56

Giordano, S., Berrilli, F., Del Moro, D., Penza, V. 2008, A&A, 489, 747 231

Gosain, S. Venkatakrishnan, P., Venugopalan, K. 2006 J. Astrophy. Astron., 27, 285 156

Guo, J., Liu, Y., Zhang, H., Deng, Y., Lin, J., Su, J. 2010, ApJ, 711, 1057 231

Hagenaar, H. J. 2001, ApJ, 555, 448 4

Hagenaar, H. J., Shine, R. A. 2005, ApJ, 635, 659 14

Hale, G. E. 1908, ApJ, 28, 315 2

Hale, G. E., Ellerman, F., Nicholson, S. B., Joy, A. H. 1919, ApJ, 49, 153 3

Hartkorn, K., Rimmele, T. 2003, ASPC, ed. A. Pevtsov and Han Uitenbroek (San Francisco), 286, 281 8

Harvey, K., Harvey, J. 1973, Sol. Phys., 28, 61 14

Komm, R. W., Howard, R. F., Harvey, J. W., Forgach, S. 1992, ASPC, 27, 325 3

Hirzberger, J., Bonet, J. A., Sobotka, M., Vázquez, M., Hanslmeier, A. 2002, A&A, 383, 275 50, 60

Ichimoto, K., Shine, R. A., Lites, B., Kubo, M., Shimizu, T., Suematsu, Y., Tsuneta, S., Katsukawa, Y., Tarbell, T. D., Title, A. M., Nagata, S., Yokoyama, T., Shimojo, M. 2007a, PASJ, 59, S593 12, 68, 118, 146

Ichimoto, K., Suematsu, Y., Tsuneta, S., Katsukawa, Y., Shimizu, T., Shine, R. A., Tarbell, T. D., Title, A. M., Lites, B., Kubo, M., Nagata, S. 2007b, Science, 318, 1597 10

Ichimoto, K., et al. 2008, Sol. Phys., 249, 233 22, 77, 120, 149

Isobe, H., Kubo, M., Minoshima, T., Ichimoto, K., Katsukawa, Y., Tarbell, T. D., Tsuneta, S., Berger T. E., Lites, B. W., Nagata, S., Shimizu, T., Shine, R. A., Suematsu, Y., Title, A. M. 2007, PASJ, 59, S807 113

Jahn, K., Schmidt, H. U. 1994, A&A, 290, 295 117

Jones, H. P. 2005, ASPC, ed. K. Sankarasubramanian, M. Penn, and A. Pevtsov 346, 229 1

Joshi, A. D., Mathew, S. K., Srivastava, N., Martin, S. F., Gupta, S. K. 2009, arXiv0905.3037J 156

Jurčák, J., Martínez Pillet, V., Sobotka, M. 2006, A&A, 453, 1079 8, 50, 75, 80, 111

Jurčák, J., Bellot Rubio, L. R. 2008, A&A, 481, L17 150, 234

Katsukawa, Y., Yokoyama, T., Berger, T. E., Ichimoto, K., Kubo, M., Lites, B. W., et al. 2007a, PASJ, 59, 577 50, 75, 111, 114

Katsukawa, Y., et al. 2007b, Science, 318, 1594 74, 113

Keller, C. U., Plymate, C., Ammons, M. 2003, in Society of Photo-Optical Instrumentation Engineers (SPIE) Conference Series, 4853, 351 16, 156, 159

Keppens, R., Martínez Pillet, V. 1996, A&A, 316, 229 17

Kitai, R., Watanabe, H., Nakamura, T., Otsuji, K., Matsumoto, T., Ueno, S., Nagata, S., Shibata, K., Muller, R., Ichimoto, K., Tsuneta, S., Suematsu, Y., Katsukawa, Y., Shimizu, T., Tarbell, T. D., Shine, R. A., Title, A. M., Lites, B. W., 2007, PASJ, 59, S585 7

Kolmogorov, A. N. 1941, DoSSSR, 30, 301 154

Korobova, Z. B. 1966, Astron. Zh., 43, 480 49

Kosugi, T., et al. 2007, Sol. Phys., 243, 3 4, 15, 21, 50, 77, 120

Kubo, M., Shimizu, T., Tsuneta, S. 2007a, ApJ, 659, 812 14

Kubo, M., Ichimoto, K., Shimizu, T., Tsuneta, S., Suematsu, Y., Katsukawa, Y., Nagata, S., Tarbell, T. D., Shine, R. A., Title, A. M., Frank, Z. A., Lites, Elmore, D. 2007b, PASJ, 59, 607 14

Kumar, B., Venkatakrishnan, P., Bayanna, A. R., Venugopalan, K. 2007, Sol. Phys., 241, 427 158

Lagg, A., Woch, J., Krupp, N., Solanki, S. K. 2004, A&A, 414, 1109 47

Landi Degl'Innocenti, E., Landolfi, M. 2004, *Polarization in Spectral Lines*, ASSL, 307, Kluwer Academic Publishers 28

Langhans, K. 2006, ASPC, ed. R. Casini and B. W. Lites, 358, 3 231

Langhans, K., Scharmer, G. B., Kiselman, D., Löfdahl, M. G. 2007, A&A, 464, 763 16, 117, 156

Lee, J. W. 1992, Sol. Phys., 139, 267 14

Leka, K. D. 1997, ApJ, 484, 900 8, 50, 80

Leka, K. D., Skumanich, A. 1998, ApJ, 507, 454 17

Leka, K. D., Steiner, O. 2001, ApJ, 552, 354 68

Li, E., Dai, Y., Wang, H., Zhang, Y. 2006, Appl. Opt., 45, 5651 168

Lites, Q. W., Elmore, D. F., Seagraves, P., Skumanich, A. P. 1993, ApJ, 418, 928 12, 116, 150, 151

Lites, B. W. 1996, Sol. Phys., 163, 223 21

Lites, Q. W., Elmore, D. F., Streander, K. V. 2001, ASPC, ed. by M. Sigwarth (San Francisco), 236, 33 22, 77, 120

Lites, B. W., Scharmer, G. B., Berger, T. E., Title, A. M. 2004, Sol. Phys., 221, 65 8, 50

Löfdahl, M. G., Scharmer, G. B. 1994, A&AS, 107, 243 16, 185

Louis, R. E., Bayanna, A. R., Mathew, S. K., Venkatakrishnan, P. 2008, Sol. Phys., 252, 43 8, 64, 80, 97, 100, 115, 226, 231, 233

Louis, R. E., Bellot Rubio, L. R., Mathew, S. K., Venkatakrishnan, P. 2009, ApJ, 704, L29 233

Louis, R. E., Bellot Rubio, L. R., Mathew, S. K., Venkatakrishnan, P. 2010a, in preparation 233

Louis, R. E., Bellot Rubio, L. R., Mathew, S. K., Venkatakrishnan, P. 2010b, to be submitted to ApJ 114

Martínez Pillet, V. 2000, A&A, 361, 734 117

Martínez Pillet, V., Katsukawa, Y., Puschmann, K. G., Ruiz Cobo, B. 2009, ApJ, 701, L79 118

Mathew, S. K., Bhatnagar, A., Prasad, C. D., Ambastha, A. 1998, A&AS, 133, 285 156

Mathew, S. K., Lagg, A., Solanki, S. K., Collados, M., Borrero, J. M., Berdyugina, S., Krupp, N., Woch, J., Frutiger, C. 2003, A&A, 410, 695 12, 116, 151

Mathew, S. K., Solanki, S. K., Lagg, A., Collados, M., Borrero, J. M., Berdyugina, S., 2004, A&A, 422, 693 2

Mathew, S. K., Martínez Pillet, V., Solanki, S. K., Krivova, N. A. 2007, A&A, 465, 291 57, 150

Matthews, S., Baker, D., Domínguez Vargas, S. 2010, ASPC, in Press 114

Milne, E. A. 1921, MNRAS, 81, 361 54

Miura, N., Noto, Y., Kato, S., Kuwamura, S., Baba, N., Hanaoka, Y., Nagata, Y., Ueno, S., Kitai, R., Takami, H. 2008, in Society of Photo-Optical Instrumentation Engineers (SPIE) Conference Series, 7015, 188 16, 156

Mihalas, D. 1967, ApJ, 149, 169 30

Montesinos, B., Thomas, J. H. 1993, ApJ, 402, 314 117

Montesinos, B., Thomas, J. H., 1997, Nature, 390, 485 112, 117

Muller, R. 1979, Sol. Phys., 61, 297 8, 49

Niblack, W. 1986, *An Introduction to Digital Image Processing*, Prentice Hall, NJ, 139 165

Noll, R. J. 1976, J. Op. Soc. Am., 66, 207 185, 197

November, L. J. 1986, Appl. Opt., 25, 392 57

November, L. J., Simon, G. W. 1988, ApJ, 333, 427 57, 143

Ortiz Carbonnel, A. N., Bellot Rubio, L. R., van der Voort, L. R. 2010, ApJ, 713, 1282 8

Orozco Suárez, D., del Toro Iniesta, J. C. 2007, A&A, 462, 1137 47

Parker, E. N. 1955, ApJ, 122, 293 2

Parker, E. N. 1979, ApJ, 234, 333 7, 8, 50, 75

Parker, E. N. 1983, ApJ, 264, 642 4

Parker, E. N. 1992, ApJ, 390, 290 17

Parnell, C. E., DeForest, C. E., Hagenaar, H. J., Johnston, B. A., Lamb, D. A., Welsch, B. T. 2009, ApJ, 698, 75 4, 15

Paterson, C., Munro, I., Dainty, J. C., 2000, Opt. Expr., 6, 175 168

Paxman, R. G., Timothy, J. S., James, R. F. 1992, J. Op. Soc. Am., 9, 1072 185

Popovic, Z. D., Sparague, R. A., Neveille Connell, G. A. 1988, Appl. Opt., 27, 1281 161

Press, H. W., Teukolsky, S. A., Vellerling, W. T., and Flannery, B. P. 1993, *Numerical Receipes in FORTRAN; The art of scientific computing*, Second edition, Cambridge University Press, New Delhi 29, 34, 165

Priest, E. R., Heyvaerts, J. F., Title, A. M. 2002, ApJ, 576, 533 4

Puschmann, K. G., Ruiz Cobo, B., Martínez Pillet, V. 2010, 720, 1417 232, 233

Rachkovsky, D. N. 1967, Izv. Krymsk. Astrofiz. Obs. 37, 56 47

Ravindra, B., Venkatakrishnan, P., Kumar, B. 2004, Sol. Phys., 225, 47 14

Ravindra, B. 2006, Sol. Phys., 237, 297 14

Rempel, M., Schüssler, M., Knölker, M. 2009a, ApJ, 691, 640 117, 151

Rempel, M., Schüssler, M., Cameron, R. H., Knölker, M. 2009b, Science, 325, 171 12, 117, 234

Riethmüller, T. L., Solanki, S. K., Lagg, A. 2008a, ApJ, 678, L157 7

Riethmüller, T. L., Solanki, S. K., Zakharov, V., Gandorfer, A. 2008b, A&A, 492, 233 7

Rimmele, T. 1994, A&A, 290, 972 116

Rimmele, T. 1995, ApJ, 445, 511 118

Rimmele, T. R. 1997, ApJ, 490, 458 8, 75

Rimmele, T. R., Richards, K., Hegwer, S., Ren, D., Fletcher, S., Gregory, S., Didkovsky, L., Denker, C., Marquette, W., Marino, J., Goode, P., 2003, in Society of Photo-Optical Instrumentation Engineers (SPIE) Conference Series, 4839, 635 16, 156

Rimmele, T. R. 2004, ApJ, 604, 906 8, 50, 75

Rimmele, T. R., Marino, J. 2006, ApJ, 646, 593 118, 152

Rimmele, T. 2008, ApJ, 672, 684 8, 234

Roddier, F. 1999, *Adaptive Optics in Astronomy*, Cambridge University Press 160, 197, 202

Roggemann, M. C., Welsh, B. M., Fugate, R. Q. 1997, Rev. Mod. Phys., 69, 437 168

Rouppe van der Voort, L. H. M. 2003, A&A, 397, 757 116

Rouppe van der Voort, L. H. M., Löfdahl, M. G., Kiselman, D., Scharmer, G. B. 2004, A&A, 414, 717 10

Rüedi, I., Solanki, S. K., Livingston, W. 1995, A&A, 302, 543 8, 50, 90

Ruiz Cobo, B., Del Toro Iniesta, J. C. 1992 ApJ, 398, 375 29, 34, 80, 121

Ruiz Cobo, B., del Toro Iniesta, J. C., Rodríguez Hidalgo, I., & Collados M., Sánchez Almeida, J. 1996, ASPC, ed. R. Pallavicini and A. K. Dupree (San Fransisco), 109, 155 29

Ruiz Cobo, B., Rodríguez Hidalgo, I., & Collados M. 1997, ApJ, 488, 462 29

Ruiz Cobo, B. 2007, Modern Solar Facilities - Advanced Solar Science, 287 43

Ruiz Cobo, B., Bellot Rubio, L. R. 2008, A&A, 488, 749 10, 117, 232

Ryutova, M., Shine, R., Tile, A., Sakai, J. I. 1997, ApJ, 492, 402 14

Ryutova, M., Tarbell, T. D., Shine, R. 2003, Sol. Phys., 213, 231 113

Ryutova, M., Berger, T., Title, A. 2008a, ApJ, 676, 1356 113

Ryutova, M., Berger, T., Frank, Z., Title, A. 2008b, ApJ, 686, 1404 113

Sainz Dalda, A., Martínez Pillet, V. 2005, ApJ, 632, 1176 14

Sainz Dalda, A., Bellot Rubio, L. R. 2008, A&A, 481, L21 12, 14

Sankarasubramanian, K., Rimmele, T. 2008, J. Astrophy. Astron., 29, 329 157

Sánchez Almeida, J. 2005, ApJ, 622, 1292 13, 117

Scharmer, G. B., Gudisen, B. V., Kiselman, D., Löfdahl, M. G., Rouppe van der Voort, L. H. M. 2002, Nature, 420, 151 10, 117

Scharmer, G. B., Bjelksjo, K., Korhonen, T. K., Lindberg, B., Petterson, B. 2003a, in Society of Photo-Optical Instrumentation Engineers (SPIE) Conference Series, 4853, 341 156

Scharmer, G. B., Dettori, P., Löfdahl, M. G., Shand, M. 2003b, in Society of Photo-Optical Instrumentation Engineers (SPIE) Conference Series, 4853, 370 16, 21, 185

Scharmer, G. B., Nordlund, Å., Heinemann, T. 2008, ApJ, 677, L149 117

Scharmer, G. B. 2009, Space Sci. Rev., 144, 229 117, 232

Scherrer, P. H. et al. 1995, Sol. Phys., 162, 129 3

Scherrer, P. H., Hoeksema, J. T. and the HMI Team, 2006, 36th COSPAR Scientific Assembly, 1469 15

Schleicher, H., Balthasar, H., Wöhl, H., 2003, Sol. Phys., 215, 261 50, 90

Schlichenmaier, R., Jahn, K., Schmidt, K. U. 1998a, ApJ, 493, L121 13, 112, 117, 151, 153

Schlichenmaier, R., Jahn, K., Schmidt, K. U. 1998b, A&A, 337, 897 112, 117

Schlichenmaier, R., Schimdt, H. U. 1999, A&A, 349, L37 116

Schlichenmaier, R., Solanki, S. K. 2003, A&A, 411, 257 118

Schlichenmaier, R., Bellot Rubio, L. R., Tritschler, A. 2005, AN, 326, 301 12

Schlichenmaier, R. 2009, Space Sci. Rev., 144, 213 4, 153, 228, 232

Schlichenmaier, R., Rezaei, R., Bello González, N., Waldmann, T. 2010, A&A, 512, L1 17

Schüssler, M., Vögler, A. 2006, ApJ, 641, L73 8

Sheeley, N. R. 1969, Sol. Phys., 9, 347 14

Shepard, D. 1968, Proceedings of the 23rd ACM National Conference, 517 56

Shimizu, T., et al. 2009, ApJ, 696, L66 64, 97, 112, 115

Skumanich, A., Lites, B. W. 1987, ApJ, 332, 473 29

Sobotka, M. 1989, Sol. Phys., 124, 37 49

Sobotka, M., Bonet, J. A.,Vázquez, M. 1993, ApJ, 415, 832 111

Sobotka, M., Bonet, J. A.,Vázquez, M. 1994, ApJ, 426, 404 50, 111

Sobotka, M., Brandt, P. N., Simon, G. W. 1997a, A&A, 328, 682 7, 145

Sobotka, M., Brandt, P. N., Simon, G. W., 1997b, A&A, 328, 689 7

Sobotka, M., Vázquez, M., Bonet, J. A., Hanslmeier, A., and Hirzberger, J. 1999, ApJ, 511, 436 10, 11, 143, 145, 153, 228

Sobotka, M., Sütterlin, P. 2001, A&A, 380, 714 10, 143, 145

Sobotka, M., Jurčák, J., 2009, ApJ, 694, 1080 7, 11

Socas-Navarro, H. 2001, ASPC, ed. M. Sigwarth (San Francisco), 236, 487 47

Solanki, S. K., Montavon, C. A. P. 1993, A&A, 275, 283 12, 13, 68, 116, 151, 232

Solanki, S. K. 2003a, A&ARv, 11, 153 2, 16, 116

Solanki, S. K., Gandorfer, A. M., Schüssler, M., Curdt, W., Lites, B. W., Martínez Pillet V., Schmidt, W., Title, A. M., and the SUNRISE Team, SUNRISE: A Balloon-borne Telescope for High Resolution Solar Observations in the Visible and UV, 2003b, Proceedings of the Society of Photo-Optical Instrumentation Engineers (SPIE), 4853, 129 15

Spruit, H. C., Title, A.M., Van Ballegooijen, A. A. 1987, Sol. Phys., 110, 115 14

Spruit, H. C., Scharmer, G. B. 2006, A&A, 447, 343 8, 13, 49, 117, 232, 234

Sridharan, R. 2001, Techniques for Achieving Higher Spatial Resolution, Ph.D Thesis, Bangalore University, Bangalore, India. 16, 202

Sridharan, R., Bayanna, A. R., Nandita, S., Kumar, B., Ravindra, B., Gupta, S. K., Jain, N., Ambastha, A., Venkatakrishnan, P. 2003, BASI, 31, 455 185, 202, 221

Sridharan, R., Bayanna, A. R. 2004, Telescopes and Instrumentation for Solar Astrophysics, Fineschi, S., Gummin, M. A., (eds.), Proceedings of the Society of Photo-Optical Instrumentation Engineers (SPIE), 5171, 219 202, 221, 234

Sridharan, R., Bayanna, A. R., Venkatakrishnan, P. 2005, Science with Adaptive Optics, Proceedings of the ESO Workshop, Brandner, W., and M. E. Kasper (eds.), 132 193

Sridharan, R., Raja Bayanna, A., Louis, R. E., Kumar, B., Mathew, S. K., Venkatakrishnan, P. 2007, in Society of Photo-Optical Instrumentation Engineers (SPIE) Conference Series, 6689, 29 192

Srivastava, N., Mathew, S. K. 1999, Sol. Phys., 185, 61 156

Stix, M. 2002, *The Sun: An Introduction*, Berlin: Sringer 1

Su, J. T., Sakurai, T., Suematsu, Y., Hagino, M., Liu, Y. 2009, ApJ, 697, L103 10

Suematsu, Y., Tsuneta, S., Ichimoto, K., Shimizu, T., Otsubo, M., Katsukawa, Y., Nakagiri, M., Noguchi, M., Tamura, T., Kato, Y., Hara, H., Kubo, M., Mikami, I., Saito, H., Matsushita, T., Kawagachi, N., Nakaoji, N., Nagae, K., Shimada, S., Takeyama, T., Yamamuro, T. 2008, Sol. Phys., 249, 197 22

Tan, C., Chen, P. F., Abramenko, V., Wang, H. 2009, ApJ, 690, 1820 54

Tarbell, T. D. et al. 2008, Sol. Phys., to be submitted 22

Theofanidou, E., Wilson, L., Hossack, W. J., Arlt, J. 2004, Opt. Comm., 236, 145 169

Thévenin, F. 1989, A&AS, 77, 137 39

Thomas, J. H., Montesinos, B. 1993, ApJ, 407, 398 112, 117

Tritschler, A., Schmidt, W. 2002, A&A, 388, 1048 7, 10

Tritschler, A., Schlichenmaier, R., Bellot Rubio, L. R. and the KAOS Team 2004, A&A, 415, 717 135, 138

Tsuneta, S., Suematsu, Y., Ichimoto, K., Shimizu, T., Otsubo, M., Nagata, S., et al. 2008, Sol. Phys., 249, 167 21, 22, 51, 77, 120, 193

Tyson, R. K. 1991, *Principles of Adaptive Optics*, Academic Press Inc. 154, 202

Unno, W. 1956, PASJ, 8, 108 47

van Noort, M., Rouppe van der Voort, L., Löfdahl, M. 2005, Sol. Phys., 228, 191 16

Vargas Domínguez, S., Rouppe van der Voort, L., Bonet, J. A., Martínez Pillet, V., Van Noort, M., Katsukawa, Y. 2008, ApJ, 679, 900 143

Vdovin, G., Sarro, P. M. 1995, , 34, 2968 169

Vdovin, G. V., Middelhoek, S., Sarro, P. M. 1997, Opt. Engg., 36, 1382 165

Vdovin, G. 2003, Adaptive Optics for Industry and Medicine, Proceedings of the 4th International Workshop Münster, Germany, 102, 3 166

Vernazza, J. E., Avrett, E. H., Loeser, R. 1981 ApJS, 45, 635 114 von der Lühe, O. 1983, A&A, 119, 85 192

von der Lühe, O., Soltau, D., Berkefeld, T., Schelenz, T. 2003, Proceedings of the Society of Photo-Optical Instrumentation Engineers (SPIE), 4853, 187 16, 156

Vrabec, D. 1971, in IAU Symp. 43, Solar Magnetic Fields, ed. R. Howard(Dordrecht: Reidel), 329 14

Watanabe, H., Kitai, R., Ichimoto, K. 2009, ApJ, 702, 1048 7

Weiss, N. O., Thompson, M. J. 2009, Space Sci. Rev., 144, 53 2

Welsch, B. T., Fisher, G. H., Abbett, W. P., Reginer, S. 2004, ApJ, 610, 1148 57, 143

Westendorp Plaza, C., del Toro Iniesta, J. C., Ruiz Cobo, B., Martínez Pillet, V., Lites, B. W., Skumanich, A. 1997, Nature, 389, 47 12, 29, 118

Westendorp Plaza, C., del Toro Iniesta, J. C., Ruiz Cobo, B., Martínez Pillet, V., Lites, B. W., Skumanich, A. 1998, ApJ, 494, 453 29, 121

Westendorp Plaza, C., del Toro Iniesta, J. C., Ruiz Cobo, B., Martínez Pillet, V., Lites, B. W., Skumanich, A. 2001a, ApJ, 547, 1130 12, 126, 129, 131, 150, 151

Westendorp Plaza, C., del Toro Iniesta, J. C., Ruiz Cobo, B., Martínez Pillet, V. 2001b, ApJ, 547, 1148 12, 116, 150

Wilson, P. R., Cannon, C. J. 1968, Sol. Phys., 4, 3 2

Wilson, P. R. 1973, Sol. Phys., 32, 435 14

Wöger, F., von der Lühe, O., Reardon, K. 2008, A&A, 488, 375 16, 156

Yurchyshyn, V. B., Wang, H., Goode, P. R. 2001, ApJ, 550, 470 14

Zakharov, V., Hirzberger, J., Reithmüller, T., Solanki, S. K., Kobel, P. 2008, A&A, 488, L17 117, 234

Zhao, J., Kosovichev, A. G., Sekii, T. 2010, ApJ, 708, 304 233

Zhang, J., Solanki, S. K., Wang, J. 2003, A&A, 399, 755 14

Zhang, J., Solanki, S. K., Woch, J., Wang, J. 2007, A&A, 471, 1035 14

Zhu, L., Sun, P. C., Bartsch, D. U., Freeman, W. R., Fainman, Y. 1999, Appl. Opt., 38, 6019 168

List of Publications

I. In Refereed Journals:

1. **Louis, R. E.**, Bellot Rubio, L. R., Mathew, S. K., Venkatakrishnan, P., "Supersonic Downflows in a Sunspot Light Bridge", 2009, *Astrophys. J. Lett.*, 704, L29

2. Nandita, S., Mathew, S. K., **Louis, R. E.**, Wiegelmann, T., "Source region of the 18 November 2003 coronal mass ejection that led to the strongest magnetic storm of cycle 23", 2009, *J. Geo. Res.*, 114, A3107

3. **Louis, R. E.**, Bayanna, A. R., Mathew, S. K, Venkatakrishnan, P., "Dynamics of Sunspot Light Bridges as Revealed by High-Resolution Images from *Hinode*", 2008, *Sol. Phys.*, 252, 43

II. In Proceedings:

1. **Louis, R. E.**, Bellot Rubio, L. R., Mathew, S. K., Venkatakrishnan, P., "Supersonic Downflows in a Sunspot Light Bridge as Revealed by *Hinode*", 2010, *Astron. Soc. Pacific Conference Series*, in Press

2. Sridharan, R., Raja Bayanna, A., **Louis, R. E.**, Kumar, B., Mathew, S. K., Venkatakrishnan, P.,"An Image Stabilization System for Solar Observations", 2007, in Society of Photo-Optical Instrumentation Engineers *(SPIE)* Conference Series, 6689

3. Bayanna, A. R., **Louis, R. E.**, Kumar, B., Mathew, S. K., Venkatakrishnan, P., "High Resolution Imaging System for Udaipur Solar Observatory", 2007, in Society of Photo-Optical Instrumentation Engineers *(SPIE)* Conference Series, 6689